Fracture Behavior of Particulate Polymer Composites (PPCs) and Interpenetrating Polymer Networks (IPNs): Study of Filler Size, Filler Stiffness and Loading Rate Effects

by

Kailash Chandra Jajam

A dissertation submitted to the Graduate Faculty of
Auburn University
in partial fulfillment of the
requirements for the Degree of
Doctor of Philosophy

Auburn, Alabama
August 03, 2013

Keywords: experimental mechanics, optical metrology, dynamic fracture, nanocomposites, particulate polymer composites, interpenetrating polymer networks

Approved by

Hareesh V. Tippur, Chair, McWane Professor of Mechanical Engineering
Jeffrey C. Suhling, Quina Distinguished Professor of Mechanical Engineering
Barton C. Prorok, Associate Professor of Materials Engineering
Maria L. Auad, Associate Professor of Polymer and Fiber Engineering

Abstract

Particulate Polymer Composites (PPCs) generally consist of nano- or micro-fillers of various sizes and shapes randomly dispersed in a polymer matrix. Introduction of second phase fillers of different stiffness and alteration of filler-matrix adhesion characteristics offer a cost effective way of tailoring strength, stiffness and fracture toughness of such composites. However, filler size, filler stiffness and loading rate (static or dynamic) could vary the mechanical response in general and fracture behavior in particular. Furthermore, failure of PPCs is intrinsically linked to the interactions of a matrix crack with foreign particles. Accordingly, an in-depth understanding of the fracture behavior of PPCs is essential for design and safety of the mechanical members made of these materials.

The first part of this research investigates the role of nano- and micro-filler size, and loading rate effects on silica-filled epoxy PPCs. The digital image correlation method in conjunction with high-speed photography (250,000 – 300,000 frames/sec) is used to quantify crack-tip deformation histories during impact loading. The measured displacement fields are analyzed to extract stress intensity factor histories for dynamically propagating cracks. The quasi-static fracture tests show improved fracture toughness of ~170% for nanocomposites and ~55% for micro-particle filled ones at 10% volume fraction, relative to the neat epoxy. The dynamic crack initiation toughness, on the other hand, is consistently lower for nanocomposites than the micro-filler counterparts. The post-mortem analyses of fracture surfaces reveal higher surface

ruggedness for nanocomposites under quasi-static loading. However, the opposite is evident for inertial loading cases. Next, the synergistic effects of amino-functionalized multi-walled carbon nanotubes and polyol diluent on fracture of two- and three-phase (hybrid) epoxy nanocomposites are investigated at quasi-static and impact loading conditions. Measurements show improved crack initiation toughness in modified-epoxies relative to the neat resin with the highest enhancement of ~90% in case of hybrid nanocomposites. Fractography reveals a combination of toughening mechanisms including shear yielding, crack deflection, CNT bridges and pull-outs.

In the second part, to gain fundamental understanding of the counterintuitive loading rate effects on fracture responses of PPCs, experimental simulations of dynamic crack growth past inclusions of two different elastic moduli, stiff (glass) and compliant (polyurethane) relative to the matrix (epoxy), are carried out. The crack growth behavior as a function of inclusion-matrix interfacial adhesion strength and the inclusion eccentricity relative to the initial crack path is studied. The measurements show that the crack front is arrested by a symmetrically located compliant inclusion for half of the duration needed for complete specimen fracture. The dynamically growing crack is attracted and trapped by the weak inclusion-matrix interface in case of both stiff and compliant inclusions when located symmetrically, whereas it is (i) deflected by the stiff inclusion and (ii) attracted by the compliant inclusion, when located eccentrically and strongly bonded to the matrix. The compliant inclusion cases show higher fracture toughness than the stiff inclusion counterparts. Measured crack-tip mode-mixities correlate well with the observed crack attraction and repulsion mechanisms. Fracture

surfaces reveal much higher surface roughness and ruggedness after crack-inclusion interaction for the compliant inclusion case than the stiff counterpart.

Lastly, the fracture behavior of transparent Interpenetrating Polymer Networks (IPNs) with poly(methyl methacrylate) (PMMA) as the stiff phase and polyurethane (PU) as the ductile phase and varying PMMA:PU ratios in the range of 90:10 to 70:30 are studied. Quasi-static and dynamic fracture tests show that an optimum range of PMMA:PU ratio in the IPNs can produce enhanced fracture toughness (~60%) when compared to PMMA. All IPNs show higher impact energy absorption capability (a 3 to 4 fold increase) relative to PMMA. The impact damage features reveal shear-crazing and through-the-thickness cracking as the dominant failure modes responsible for greater energy absorption in IPNs.

Acknowledgements

I would like to thank my advisor, Dr. Hareesh V. Tippur, for his guidance and motivation throughout my PhD program. I am immensely grateful to him for providing excellent experimental facilities and for showing complete trust in my abilities to work in an experimental environment. I also thank him for encouraging me to present the research work at various forums and giving me an opportunity to teach an undergraduate course. My sincere thanks to Dr. Jeffrey C. Suhling, Dr. Barton C. Prorok and Dr. Maria L. Auad for their willingness to serve on my committee as well as teaching me various courses which greatly helped me in my research work. I especially thank Dr. Virginia A. Davis for serving as the external reader for my dissertation. I am deeply indebted to my school and college teachers for educating and inspiring me to pursue higher studies.

I gratefully acknowledge the National Science Foundation (NSF-CMMI-0653816), the US Army Research Office (DAAD19-02-10126), the Defense Threat Reduction Agency (HDTRA1-09-1-0023) and the National Aeronautics and Space Administration (NASA-NNX10AN26A) for extending financial and equipment support for this research. I would like to thank the Alabama Commission on Higher Education for granting me the AL-EPSCoR GRSP Round-7 Fellowship. I wish to thank my colleagues and friends in Auburn for the memorable time I spent with them.

Finally, I would like to express my gratitude to my grandparents, parents, uncles, aunts, brothers, sisters and my wife Bhavana for their love and support which enabled me to reach to this joyous achievement. I dedicate this dissertation to them.

Table of Contents

List of Tables

List of Figures

CHAPTER 1

INTRODUCTION

Polymer-based materials have entered nearly all facets of daily life due to their superior properties, cost, as well as ease of processing. A few polymers are known to occur in nature in the form of human/animal skin, cellulose, proteins, and silk, while many others, including polyester, nylon, polyurethane, acrylic, and polycarbonate are man-made. The origin of polymer synthesis may be traced back to the development of vulcanization process in 1830s by Charles Goodyear who modified the sticky latex natural rubber to a more useful elastomer for tires [1]. Since then, researchers have synthesized a wide variety of polymers including thermoplastics (polyethylene, polypropylene, PVC, polystyrene, polyamide, etc.) and thermosets (bakelite, epoxies, urea-formaldehyde, duroplast, polyimides, melamine resins, etc.). Due to their low density and high specific strength, polymers are commonly used as matrix materials for composites. In its simplest form, a composite material is one that is made by combining two or more constituent phases with significantly different physical or chemical properties to obtain a new product with characteristics different and/or better than the individual constituents. The concept of a composite material can be seen in nature in both the plant and animal worlds. Wood, palms and bamboo are few prehistorically natural composites still used by the mankind in construction and scaffolding. Wood consists of cellulose held together by lignin, a natural polymer, forming the woody cell walls where the molecules of cellulose are oriented along the axis of the fibers so that maximum

strength is in that direction. The human bone is also a composite where the collagen acts like the resin and the nano-sized hydroxyapatite mineral crystals (~20 nm long) serve as the reinforcement. These mineral crystals are exceptionally strong in tension and flexure. Silky threads spun by spiders are another example of natural composite consisting of a gel core encased by a solid structure of aligned molecules, and are as strong as steel. The earliest man-made composite materials may have been the adobe bricks, fashioned by the ancient Egyptians by mixing clay with water and straw, resistant to both compression and tearing, making them excellent building blocks [1]. Plywood is another ancient composite made by gluing wood at different angles to enhance the strength by exploiting grain structure and resistance to hygrothermal expansion. Figure 1.1 shows some examples of natural and first man-made composite materials.

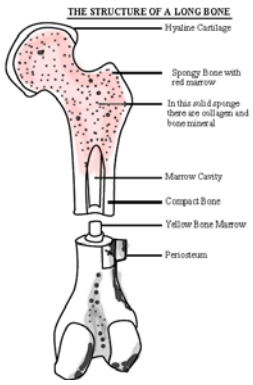

(Ref: http://resources.edb.gov.hk)

Natural composite: bone

(Ref: http://www.solidearth.co.nz/adobe-brick-technique.php)

The first man-made composite: Adobe bricks

Fig. 1.1: Examples of natural and first man-made composite materials.

Inspired by natural composites and introduction of polymers, the mid-20th century witnessed a tremendous progress in the development of polymer matrix composites (PMCs) that compete favorably with more traditional materials, such as metals and

concrete, for structural, automotive and aerospace applications where high strength-to-weight ratio is an important factor. Figure 1.2 depicts the increasing use of composite materials in aerospace industry in the last few decades. For example, the composites content in the B787 and A350 aircrafts is about 35-50% by weight.

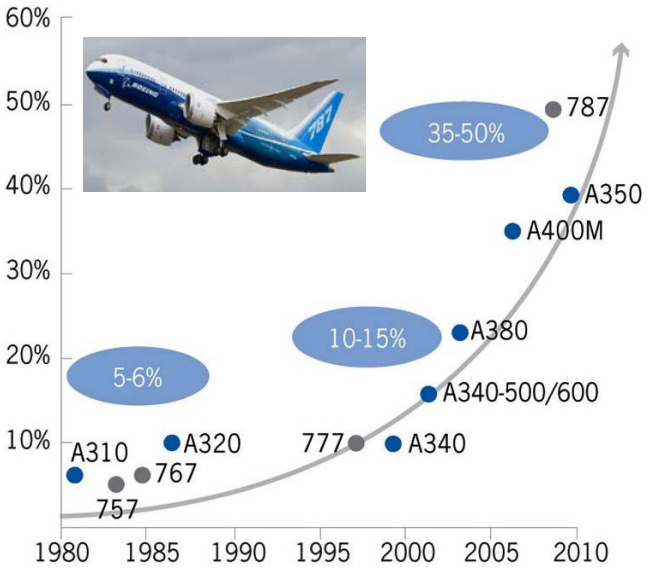

Fig. 1.2: Composites content (by weight %) in commercial aerospace in the last few decades. (Source: Grant Thornton and Hexcel Corporation)

Typically, PMCs are multiphase materials having physical mixtures of a host polymer and one or more secondary phases at the macro-, micro- or molecular scale. The secondary phase can be in the form of particulates of different sizes and shapes, and could be another polymer network or domain. Over the years, there has been an increasing demand for lightweight, fracture-resistant, stiffer, stronger and tougher materials. Fillers play a vital role in tailoring the desirable properties of polymers. In this regard, particulate polymer composites have attracted growing interest in a vast number of engineering applications. Also, in recent years, the search for transparent, impact resistant, energy absorbing materials as alternatives to glass, polycarbonate, and acrylics

has led to studies on molecular composites for use in a variety of civilian and military applications.

Particulate polymer composites (PPCs) generally consist of metallic or nonmetallic particles dispersed in either organic or inorganic matrices. Syntactic structural foams, dental fillers, bone cements, self-healing materials, underfills in electronic packages, surface coatings for thermal insulation, scratch, erosion and corrosion resistance are few examples that fall into this category. Among these, syntactic foams (filled polymers with thin walled *hollow* microballoons) exhibit excellent compressive strength, low moisture and high energy absorption capabilities, and are increasingly used as core materials in sandwich structures, buoyancy modules, offshore platforms, aerospace and military applications. As shown in Fig. 1.3, particulate composites such as silica-filled epoxies are often used as underfill materials in electronic packages to minimize thermal expansion and hence, stress gradients in electrical interconnects between the flip-chip solder ball grid arrays and the substrate.

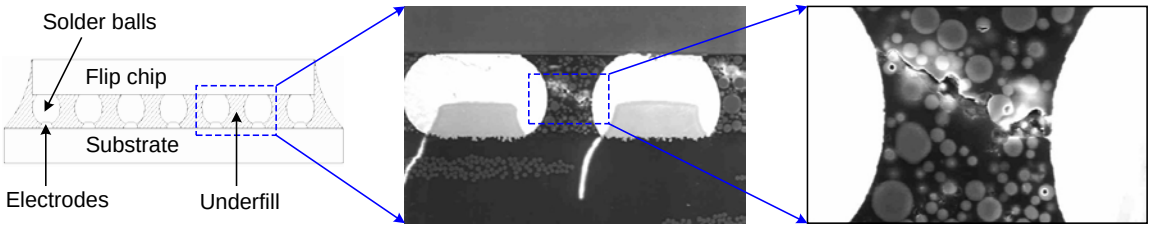

Fig. 1.3: Application of particulate polymer composite as underfill material in electronic packaging. The magnified view shows failure in a silica particle-filled epoxy [2].

Molecular composites are combinations of two or more polymers in a co-continuous network crosslinked at the molecular scale under controlled reaction kinetics. An example of molecular composites could be one that combines a thermoplastic with a

thermoset where each contributes its inherent characteristics. Thermoplastics offer higher toughness but have lower elastic modulus and glass transition temperature (T_g), while thermosets are generally stiffer, stronger and offer higher T_g but are relatively brittle. Interpenetrating Polymer Networks (IPNs) are a class of molecular composites where one polymer is synthesized and/or crosslinked in the immediate presence of the other(s). The concept behind transparent IPNs is to combine the best features of constituent phases in order to engineer a new material with optimum toughness, strength and stiffness while preserving the much needed optical "transparency" intact. The potential usages of these composites include aerospace, military armor, automotive, hurricane resistant windows, offshore and many electronics applications where impact resistance and energy absorption characteristics are of primary importance. Figure 1.4 shows some potential areas where transparent IPN molecular composites can be useful.

Aircraft canopies | Hurricane resistant windows | Helmet visors | Cellphone screens

Fig. 1.4: Potential applications of transparent interpenetrating polymer network (IPN) molecular composites. (Source: https://www.google.com/imghp?hl=en&tab=wi)

1.1 Motivation and Literature Review

In most PMCs, composite matrices are thermosets due to their high stiffness, strength and glass transition temperature relative to the thermoplastics. The most important class of thermosets for structural composites is epoxies as they are relatively inexpensive and easy to process. However, their relative brittleness often leads to

structural damage due to poor crack growth resistance. A common approach to improve damage tolerance is to incorporate secondary phases, as filling polymers with particles of different size-scale, aspect ratio, stiffness, and filler-matrix interfacial strength offers a cost effective way of functionalizing a polymer. It further allows optimization of material performance in terms of physical, thermo-mechanical and dielectric attributes. Effective stiffness, strength and fracture toughness of the multiphase system can be tailored using stiff or compliant fillers relative to the matrix. From a mechanical characteristics perspective, addition of relatively stiff phases to a polymer increases the overall stiffness, strength and creep resistance at the expense of ductility. On the other hand, compliant fillers show the opposite effect of decreasing the effective stiffness with an improvement in effective toughness. In addition to the properties of the constituent phases (filler and matrix), the material behavior, in general, is fundamentally linked to loading rate. In many circumstances, structural members and their material constituents experience an expansive range of loading conditions. Specifically, the rate at which the structural loading occurs can vary from being virtually static to being almost instantaneous. Figure 1.5 shows some real life examples where stress-wave loading dominates.

Aerospace
(Source: avioners.net)

High-speed trains
(Source: ambafrance-sg.org)

Automotive
(Source: autospies.com)

Sporting goods
(Source: junebugoutlets.com)

Fig. 1.5: Possible scenarios where materials encounter stress-wave dominated loading.

The literature review presented in the following sections shows that most studies on quantifying stiffness, strength and toughness have been generally made under quasi-static

loading conditions and dynamic loading responses are largely unknown. However, a recent work by Kitey and Tippur [3] on the dynamic fracture behavior of glass-filled epoxy with a variety of spherical particles of mean diameter (7 - 200 μm) and adhesion strengths (weak and strongly bonded) at a fixed volume fraction (10%), reveal a few counterintuitive behaviors such as the existence of an optimum particle size (~35 μm) relative to which either an increase or a decrease of particle size only results in a reduction of steady state dynamic fracture toughness. As shown in Fig. 1.6, their results also show that reinforcements with higher adhesion strength with matrix produce consistently lower fracture toughness when compared to the weakly bonded ones.

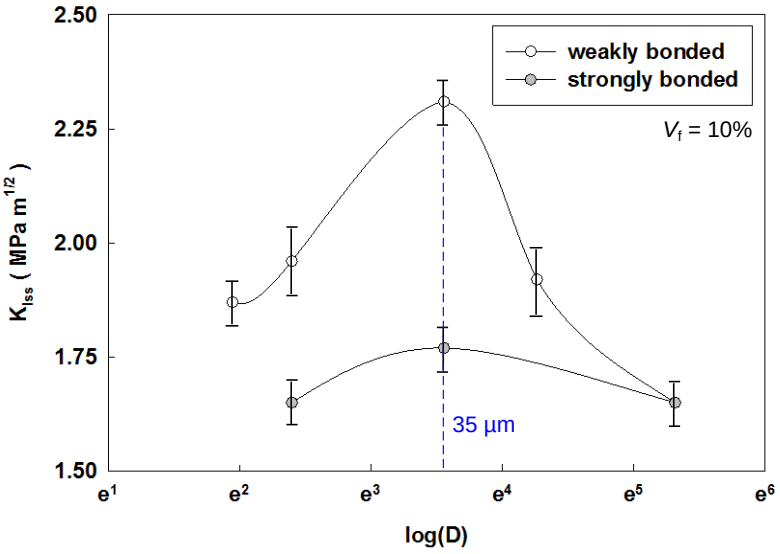

Fig. 1.6: Variation of measured steady-state stress intensity factor (K_{Iss}) as a function of average particle diameter (D) in glass-filled epoxy at 10% volume fraction (V_f). Reproduced from [3].

The micrographs in Fig. 1.7 show two different fracture surface morphologies. In the case of weakly bonded filler, the separation between glass particles and matrix can be seen whereas in the case of strongly bonded filler, the particles are rigidly held within the matrix. Closer examination reveals that the propagating crack front frequently

circumvents the strongly bonded filler particles in contrast to being attracted by the weakly bonded particles causing the crack front to lodge into the crack-particle interface arresting it momentarily before re-initiation. Therefore, the bond strength between the fillers and matrix plays a vital role in the fracture behavior of filled polymers.

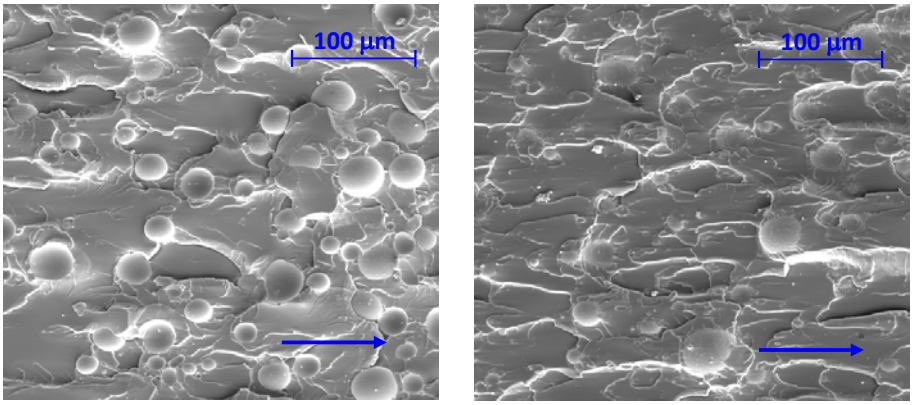

Weakly bonded filler Strongly bonded filler

Fig. 1.7: Fracture surface morphology of glass-filled epoxy composites (10% V_f and 35 µm particles). The arrow shows crack growth direction. Reproduced from [4].

It should be noted that their work describes the role of particle size in the micron range and limited to stiff fillers. However, other factors such particle size in the nano-scale with low and high aspect ratios, as well as incorporation of compliant phases and plasticizers could vary the mechanical response in general and fracture behavior in particular depending upon the nature of mechanical loading, quasi-static or dynamic. The present dissertation is essentially motivated by the work of Kitey and Tippur [3], to gain an in depth understanding of failure behaviors of particulate polymer composites (PPCs) made using nano-scale particles of ultra-high surface areal densities (silica nano-particles and carbon nanotubes) and to compare the fracture responses with micron-size stiff and sub-micron size compliant fillers and their hybrid counterparts in terms of loading rate effects. In general, failure of PPCs is intrinsically linked to the fundamental problem of

matrix crack encountering a second phase inhomogeneity in or near its path. Thus, to understand the underlying physics of fast fracture in PPCs, experimental simulations of dynamic crack growth past cylindrical inclusions of two different elastic moduli, stiff (glass) and compliant (polyurethane) relative to the matrix (epoxy), are carried out. The current work also studies the development and characterization of IPN molecular composites in terms of tensile, fracture and impact energy absorption behaviors due to their potential use in engineering applications.

In the following, the literature review for various aspects of the current research is provided in five parts. In the first part, works on failure characterization of PPCs with nano- and micro-size spherical fillers is reviewed. In the second part, reviews on multi-walled carbon nanotube (MWCNT) reinforced nanocomposites are provided. The third part reviews the works on PPCs with stiff and compliant fillers. The literature review on crack-inclusion interaction studies is presented in the fourth part. In the fifth part, investigations pertaining to mechanical and fracture behaviors of molecular IPN composites are reviewed.

1.1.1 Literature review of PPCs with nano- vs. micro-fillers

Investigations pertaining to mechanical and fracture behaviors of particulate composites with nano- and micro-fillers, and the associated toughening mechanisms reported in the literature are briefly reviewed in the following. Past studies [5-9] on PPCs with micron-size fillers suggest that fracture toughness is essentially governed by filler particle shape, size, volume fraction and filler-matrix interfacial strength. Recently, Hsieh et al. [10] have studied the toughening mechanisms of epoxies modified with silica nanoparticles of 20 nm mean diameter. They have reported steady increase in elastic

modulus, quasi-static fracture toughness, K_{Ic}, and fracture energy, G_{Ic}, with particle volume fraction (V_f) and identified localized shear bands and debonding of particles leading to void growth as the main toughening mechanisms. Reynaud et al. [11] used in-situ polymerization technique to produce nanocomposites consisting of nano-silica (12-50 nm) embedded in polyamide 6. They observed enhanced tensile yield strength with smaller particle size. Boesl et al. [12] and Liu et al. [13] noted enhanced fracture response of nano-size ZnO (53 nm) and nano-silica (20 nm) modified epoxies, respectively. Rosso et al. [14] examined the effect of 5% V_f silica nanoparticles (~50 nm) on quasi-static fracture of Araldite-F epoxy and noted 70% and 140% improvement in K_{Ic} and G_{Ic}, respectively. The incorporation Al_2O_3 (13 nm) and TiO_2 (200-500 nm) nanoparticles in epoxy by Wetzel et al. [15] showed improved flexural stiffness and strength as well as quasi-static fracture toughness and fracture energy. Their work pointed out crack-tip blunting, crack deflection and crack pinning as major sources of toughening. Liang and Pearson [16] incorporated two particle sizes of nanosilica (20 and 80 nm) to study the size effect on toughening mechanisms of epoxy-silica nanocomposites. They demonstrated that both particle sizes improved K_{Ic} and G_{Ic} with volume fraction due to matrix plastic deformation led zone shielding mechanism. However, particle size showed negligible effect on the variation of fracture toughness. Tsai et al. [17] noted enhanced mechanical properties and fracture toughness for nanosilica (25 nm) reinforced epoxies. The fracture response of bidispersed nano- and micro-filler epoxies examined by Kwon et al. [18] found to be dependent on the particle-matrix interactions as well as on temperature. Johnsen et al. [19] carried out mechanical and fracture studies on nanosilica (20 nm) filled-epoxies up to 13% V_f and observed enhanced K_{Ic} and G_{Ic} due to void

growth and particle-matrix debonding. A review by Jordan et al. [20] on experimental trends in polymer nanocomposites highlights issues associated with processing and mechanical responses of nano- *vs.* micron-sized particulate composites. They summarized that nanocomposites serve better in some mechanical aspects than the micron-sized counterparts. However, no universal trends were established as nanocomposites showed large deviations in properties due to physical and chemical differences between the constituent phases and processing challenges. Similarly, more recent reviews by Sun et al. [21] and Fu et al. [22] suggest that energy absorption characteristics of nanocomposites under quasi-static or impact loading conditions depends on key parameters such as shape, dimension of nano-particles, mechanical properties of the filler and the host matrix, filler-matrix interfacial strength, as well as volume fraction and the degree of particle dispersion in the matrix.

A few comparative studies have also been carried out to understand the effects of size-scale and particle volume fraction on the fracture behavior and fracture toughness of nano- and micro- particulate composites under quasi-static loading conditions. For example, Singh et al. [23] reinforced polyester resin with aluminum particles of nano- (100 nm) and micron-sizes (3.5 and 20 μm). They noted monotonic increase in K_{Ic} with volume fraction for a given particle size and higher K_{Ic} in case of nanocomposites than the micron-sized ones up to a volume fraction of 2.3%. Adachi et al. [24] studied quasi-static fracture behavior of nano- and micro-spherical silica-filled epoxies and observed improved K_{Ic} in the nano-filler cases than the micron-size counterparts. Mechanical response of nano- and micron-size TiO_2 (32 nm and 0.24 μm) particle loaded epoxies was

compared by Ng et al. [25, 26]. They indicate that nano-particle filled epoxy show higher stiffness, failure strain and toughness when compared to the micron-sized ones.

Among the few dynamic fracture investigations reported on particulate composites include the study of filler particle size on the mode-I fracture behavior of glass-filled epoxy studied by Kitey and Tippur [3]. In regards to nanocomposites, dynamic fracture work has been reported by Shukla et al. [27] using TiO_2 (35 nm) and Al_2O_3 (14 nm) nanoparticles. Their results indicate improved fracture toughness and higher crack velocity in nano-filler cases when compared to the neat resin. Evora and Shukla [28] performed quasi-static and dynamic fracture studies on TiO_2 (36 nm) nanoparticle filled-polyester nanocomposites and observed higher fracture toughness under dynamic loading cases compared to the quasi-static cases. In a similar dynamic fracture work using TiO_2 (36 nm) nanoparticles in polyester resin, Evora et al. [29] reported a relationship between mode-I dynamic stress intensity factor and crack velocity and noted higher crack velocity and enhanced crack arrest toughness for nanocomposites than the virgin polyester.

1.1.2 Literature review of PPCs with stiff and compliant fillers

It has been well established that rigid inorganic fillers provide macroscopic isotropy as well as enhanced fracture toughness and high energy absorption capabilities to brittle polymers [30-33]. Hussain et al. [34] investigated fracture behavior of particle-filled epoxy composites by varying TiO_2 filler volume fraction and particle size (20 nm and 1μm) and found that the micron size particles led to higher fracture toughness with increasing volume fraction than the nanoparticle counterparts. Early works on compliant fillers have been reported by Kinloch et al. [35-37] on deformation and fracture behavior of rubber-toughened epoxies. They performed microstructural and fracture studies on

unmodified and CTBN rubber modified epoxies and proposed that localized cavitation at the particle-matrix interface, plastic shear yielding in the matrix and crack-tip blunting are the main sources of energy dissipation and increased toughness in the rubber-modified epoxy. Geisler and Kelley [38] used rubbery and rigid fillers as well as a combination of both types to improve fracture toughness of epoxy resins and found that both rubbery and rigid particle-filled epoxies showed higher fracture energies than the neat epoxy. In addition, cured resins prepared with an optimum loading of both rubbery and rigid particles resulted in greater fracture energies than those with rubbery or rigid particles alone. The crack front impedance is said to have toughened the rigid particle composites and localized plastic deformation ahead of the crack front to have contributed in the hybrid composites. The work of Tirosh et al. [39] focused on detailed stress analysis around compliant rubber inclusion particles in a brittle epoxy matrix and a brittle inclusion (styrene-acrylonitrile copolymer, SAN) in a compliant polycarbonate matrix. They found that the tensile strength of a brittle matrix with a soft inclusion continuously degraded as the inclusion size increased whereas the tensile strength of a soft matrix reinforced with stiff inclusions could be maximized with respect to the matrix properties using an optimum particle size.

1.1.3 Literature review of nanocomposites with carbon nanotubes (CNTs)

A common approach to improve damage tolerance is to incorporate rubber particles [35, 40, 41], thermoplastics [37, 42, 43] or stiff fillers [14, 31, 32] that alter the overall mechanical and fracture performances favorably [21, 44]. The rubbery or thermoplastic phases, however, generally improve ductility but diminish stiffness of thermoset resins whereas the rigid inorganic inclusions such as silica and alumina improve stiffness and

strength often at the expense of ductility. In addition to the type of fillers, other studies [3, 7, 22, 33] on particulate PMCs suggest that fracture toughness can be affected by various factors such as filler size, shape, volume fraction, filler-matrix adhesion strength and the loading rate.

An alternative approach to counteract the reduction in thermo-mechanical properties of PMCs is simultaneous addition of compliant and stiff phases where each contributes its inherent characteristics to produce optimum stiffness, strength and toughness. Previous works on such hybrid composites [38, 45, 46] have shown enhanced fracture toughness and energy absorption. In the recent years, a number of polyol based reactive diluents has been considered as a good choice for improving the fracture resistance of brittle epoxies [46, 47]. In addition to the toughening effect, the lower viscosity and the extended pot life of polyols generally increase the level of filler loading as well as the resin wetting action without a substantial decrease in curing rate and thermal stability. These properties make polyols suitable for modification of epoxy resins to achieve improved peel and impact strengths, and facilitate processing of particle-filled and fiber-reinforced PMCs. For instance, the use of polyether polyol as a toughener for epoxy resins by Isik et al. [46] provided 160% enhancement in impact strength. In the past few decades, researchers have also successfully tailored the matrix properties by using nano fillers [20]. Since their discovery in 1991 by Iijima [48], carbon nanotubes (CNTs) have emerged as potential candidates for matrix modification because of their exceptional strength and stiffness [49], resilience, diameter dependent specific surface area and high aspect ratio with low density [50]. These remarkable features of CNTs make them to act as bridges between crack faces and induce interlocking with the matrix material.

However, to incorporate CNTs as effective reinforcements, good dispersion and interfacial adhesion between matrix and CNTs is desirable. Previously, it has been shown that surfactant treatment and amino-functionalization of CNTs enhance their dispersibility in the epoxy matrix [51-55]. Furthermore, multi-walled carbon nanotubes (MWCNTs) exhibit better dispersion than single walled carbon nanotubes (SWCNTs) because of lower specific surface area in the former than the latter.

Nanocomposites modified with CNTs as reinforcements in polymer matrices have been extensively investigated over the years [50, 56]. The dispersion of 0.1 wt% of amino-functionalized double-wall carbon nanotubes (DWCNTs) in epoxy using a calandering technique by Gojny et al. [57] resulted in improved tensile strength, Young's modulus and quasi-static fracture toughness. A thermo-mechanical study by Fidelus et al. [58] showed 70% improvement in tensile impact strength at 0.5 wt.% of randomly oriented MWCNTs in epoxy resin. In an another thermo-mechanical investigation, Zhou et al. [59] noted 90% improvement in storage modulus and an optimum flexural strength with 0.3 wt% MWCNT/epoxy system. Seyhan et al. [60] used 3-roll milling to disperse CNTs into vinyl-ester-polyester hybrid resin. They found that nanocomposites containing MWCNTs and NH_2-MWCNTs exhibited higher tensile modulus, fracture toughness and fracture energy values relative to DWCNTs and NH_2-DWCNTs counterparts. Hsieh et al. [61] noted improved tensile, fracture and fatigue performances with increasing MWCNTs content in an anhydride-cured epoxy. Some efforts to enhance the fracture toughness of CNT/epoxy nanocomposites by simultaneous addition of a third phase filler such as rubber and/or nanosilica particles have also been made [62, 63].

1.1.4 Literature review of crack-inclusion interactions

The works reviewed in the previous sections mainly address the effect of filler size in micron (rigid and/or rubbery) and nano-scale range on the fracture behavior of particulate composites. A few investigations also report fracture characteristics with macro size fillers of spherical and cylindrical shapes to rigorously explain the underlying failure process in filled polymers through analytical, numerical and/or experimental/modeling. Early analytical study by Tamate [64] focused on complex potentials to analyze stress fields and stress intensity factors for mode-I cracks due to interactions between a compliant matrix crack and a stiff circular inclusion and *vice versa*. Evans [65] reported the effect inclusions have on the fracture of ceramics by evaluating the local stresses around inclusions due to thermal expansion and elastic modulus mismatch and calculated approximate magnitude of stress intensity factors at interface cracks. Erdogan et al. [66] developed expressions for mode-I and mode-II stress intensity factors by using asymptotic values of density functions of integral equations in terms of crack face displacements for interactions between a circular inclusion and an arbitrarily oriented crack. Bush [67] used boundary element method to model interactions of a matrix crack with a single inclusion and a cluster-of-inclusions in order to study crack trajectories and crack driving forces for weakly and strongly bonded inclusion-matrix interfaces. Symmetric-Galerkin boundary element method was adopted by Kitey et al. [68] to simulate two dimensional mixed-mode quasi-static crack growth near strongly bonded stiff particle clusters. They observed differences in crack trajectories with respect to the cluster orientation and concluded that the crack driving force is affected much earlier than the perceivable crack deflection and energy release rate

increases with increase in the inclusion eccentricity relative to the crack. Li and Chudnovsky [69, 70] examined the effects of an elastic inclusion on the energy release rate for crack extension and showed that the crack-tip is shielded from far field stresses when it approaches a rigid inclusion and stresses get amplified when it propagates past the inclusion. More recently, a theoretical model based on the application of a coupled stress and energy criterion for the prediction of the crack onset at the interface between a stiff cylindrical inclusion and a compliant unbounded matrix subjected to a remote uniaxial transverse tension is developed by Mantic [71].

Although information in terms of analytical and numerical perspectives can be noted from previous reports, experiments are relatively few. Among the experimental investigations on this topic, O'Toole and Santare [72] studied crack-inclusion interactions by bonding two identical elliptical steel inclusions on the two faces of a cracked thin polymer plate. Li and Chudnovsky [73] realized perfectly bonded second phase circular inclusion by introducing stiff and compliant circular inclusion in photodegradable plastic material specimens by selectively irradiating with ultraviolet radiation. They studied fatigue crack growth behavior and analyzed fracture surface morphology qualitatively. Savalia and Tippur [74] carried out an experimental-numerical study of crack-inclusion interactions under quasi-static loading conditions using moiré interferometry and finite element analysis. As noted earlier, most of the experimental studies on this topic found in the literature are limited to quasi-static loading conditions with the exception of the one reported by Kitey and Tippur [75]. They investigated the dynamic crack growth behavior in the vicinity of an isolated stiff inclusion using the method of reflection-mode Coherent Gradient Sensing (CGS). Being a surface slope detection method, reflection CGS fringes

heavily localized near the regions of stress concentration and could not be analyzed satisfactorily when the crack tip was in the inclusion vicinity. Moreover, they extracted stress intensity factors (SIF) using governing equations for a monolithic material and the SIF values at the crack-inclusion interface need to be analyzed using bimaterial field equations by fully taking into account velocity effects. The present work on crack-inclusion interaction essentially builds on the work of Kitey and Tippur and extends their observations to study the role of elastic mismatch and interfacial strength between a dynamically growing matrix crack and a stationary stiff or compliant inclusion by directly measuring more readily interpretable full-field surface displacement components both before and after crack-inclusion interaction with an eventual goal of evaluating field quantities in the matrix as well as the inclusion.

1.1.5 Literature review of Interpenetrating Polymer Networks (IPNs)

The term IPN was first coined by Millar [76] in 1960, however, Aylsworth and Edison were likely the first to synthesize such a material in 1914 by mixing a crosslinked phenol formaldehyde resin with rubber and sulphur [77-79]. Following these historic works, a great deal of research [79-85] has been reported in this area over the last few decades. Polyurethane-epoxy based semi-IPNs were synthesized by Cascaval et al. [86] to study thermal degradation. Kim et al. [87-90] studied the synthesis, morphology, density, T_g, viscoelastic, and volume resistivity behaviors of a series of PMMA-PU IPNs. They found optimum Young's modulus and shear storage modulus for 85/15 wt% IPN category among all the IPNs configurations. In a similar study, Lee and Kim [91] prepared 50/50 wt% PMMA-PU IPNs under varying pressures of up to 20000 kg/cm^2. They noted changes in phase continuity with synthesis pressure and observed better

optical transparency in the IPNs synthesized at a higher pressure than the ones at a lower pressure. The effect of ultraviolet (UV) radiation on vinyl ester resin-modified lignin based semi-IPNs was examined by Rosu et al. [92]. They concluded that the synthesized networks undergo photosensitive degradation under UV radiation of wavelengths higher than 300 nm. The kinetics of network formation and inter-network grafting of PMMA-PU IPNs was studied by Djomo et al. [93]. Synthesis of transparent interpenetrating organic/inorganic networks have been performed by Widmaier and Bonilla [94] and Bonilla et al. [95]. They prepared PMMA-PU IPNs with the addition of silica generated in-situ by sol-gel process during the IPN formation.

Apart from synthesis and chemistry aspects, there exist a few investigations pertaining to mechanical behavior of IPNs. The mechanical properties of simultaneous IPNs based on PMMA-PU networks were studied by Akay and Rollins [96]. In their work, the storage modulus and damping (tan δ) values from dynamic mechanical analysis (DMA) were found to be optimum for 80/20 wt% IPNs. The work of Chen et al. [97] on thermal, mechanical, and damping studies of castor oil-based polyurethane-epoxy graft IPNs modified with hydroxyl-terminated liquid nitrile rubber showed improved tensile and impact strengths when the rubber content was 5%. Chou and Lee [98] mechanically characterized polyurethane-unsaturated polyester IPNs as a function of change in reaction temperature and reaction rates. Chakrabarty et al. [99, 100] conducted morphological, mechanical and thermal studies on epoxy-poly(ethyl methacrylate) IPNs and observed a gradual decrease in stiffness and tensile strength with a consequent gain in failure strain and toughness with poly(ethyl methacrylate) amount. The effects of blend morphology on mechanical and fracture behaviors of dicyanate ester-polyetherimide semi-IPNs were

investigated by Harismendy et al. [101]. They noted increased fracture toughness and fracture energy without any improvement in the elastic modulus and yield strength relative to neat bisphenol-A dicyanate matrix. Although many studies have been reported on IPNs, most have resulted in opaque or translucent networks and very limited work exists from the perspective of transparent IPNs for potential use in civilian and military applications.

1.2 Objectives

The literature review suggests that much of the research to date on failure characterization of nanocomposites, particulate composites with stiff and compliant fillers, and molecular composites has been performed quasi-statically and very limited data exists from the perspective of dynamic crack growth caused by rapid loading. These gaps need to be bridged if these materials are to find engineering applications in diverse areas such as aerospace and automotive structures, sporting equipment, high speed trains, armored vehicles, and explosive ordinance disposal gear where stress-wave loading dominates. The stiff fillers such as glass particles, nano-silica, carbon nanotubes and compliant phases including CTBN rubber and polyol diluents are readily available commercially. However, the dispersion of these fillers in the polymers is rather challenging, especially nano-particles due to their large surface-to-volume ratio. If these second phase inhomogeneities can be dispersed into polymeric matrices uniformly and consistently, one can characterize and examine their failure behaviors under laboratory conditions. The material preparation challenges are also involved in the synthesis of molecular composites due to their complex reaction kinetics and processing parameters.

Considering all these aspects and the available resources, the following are the primary objectives of the present research:

- Fabricate PPCs with epoxy matrix modified with nano-silica, micron-size glass particles, CTBN rubber, multi-walled carbon nanotubes, polyol diluent, and their hybrid counterparts.
- Fabricate specimens for studying crack-inclusion interactions by embedding isolated cylindrical, macro-size stiff and compliant inclusions to understand the implications on the fracture behavior of filled polymers.
- Synthesize IPN molecular composites made of PMMA and PU phases for fracture studies.
- Measure dynamic elastic and physical properties of aforementioned composites using ultrasonic pulse-echo method.
- Perform microstructural characterization to check the quality of exfoliation of filler particles using optical, SEM and TEM microscopy tools.
- Conduct controlled experiments under quasi-static and dynamic loading conditions to characterize failure characteristics and loading rate effects.
- Bridge the microscopic failure characteristics from post-mortem analyses with the macroscopic optical measurements.

1.3 Organization of Dissertation

This dissertation is organized into eight chapters including the current one. In Chapter 2, the optical method of digital image correlation and its working principle are briefly described. The details of different experimental setups and test procedures employed to study quasi-static, dynamic fracture behavior, and impact energy absorption characteristic are provided in Chapter 3. This chapter also presents the details of various experimental tools used for materials characterization and post-mortem analyses of fractured specimens.

Chapter 4 and 5 deal with quasi-static and dynamic fracture investigations of particulate polymer composites (PPCs) made of nano- and micron-size silica particles, as well as epoxy nanocompoistes modified with carbon nanotubes (CNTs) and polyol diluent. In these chapters, the details of particulate composites fabrication, characterization, specimen geometry, and the methodology to evaluate various fracture parameters are provided. The effects of filler size, filler stiffness and loading rates on fracture toughness of PPCs as well as the associated toughening mechanisms are discussed.

In Chapter 6, the experimental investigations of dynamic crack growth past inclusions of two different elastic moduli, stiff (glass) and compliant (polyurethane) relative to the matrix (epoxy), are described in order to understand the underlying physics of stress-wave dominated fracture in PPCs. Implications of dynamic crack-inclusion interactions are also demonstrated on dynamic fracture of micron-size stiff and compliant particle filled epoxies.

Chapter 7 presents failure characterization of transparent interpenetrating polymer networks (IPNs) synthesized using poly(methyl methacrylate) (PMMA) as the stiff phase and polyurethane (PU) as the tough phase. The effect of PMMA-PU compositions on tensile, fracture and impact energy absorption behavior of IPNs is discussed.

Finally, Chapter 8 summarizes major conclusions of this dissertation, followed by future directions related to this research.

CHAPTER 2

EXPERIMENTAL METHOD OF DIGITAL IMAGE CORRELATION

In this chapter, the optical method of 2D Digital Image Correlation (DIC), used to study crack tip deformations in various particulate polymer composites under stress-wave loading conditions, is described. The experimental techniques for evaluating fracture parameters in real-time in a dynamic failure event involving crack initiation and propagation were somewhat limited to full-field optical methods such as photoelasticity, optical caustics, Coherent Gradient Sensing (CGS), and moiré interferometry. All interferometric techniques have stringent surface preparation requirements such as preparation of birefringent coatings in reflection photoelasticity, transfer of gratings in moiré interferometry and preparation of specularly reflective surface for CGS. However, recent progress in image processing methods, high-speed computations and the advent of ultra high-speed digital photography with relatively high spatial and temporal resolutions have made it possible to use DIC method. This method offers the convenience of minimum surface preparation and does not require coherent optics, and ordinary incoherent light is sufficient. These aspects have motivated adopting the DIC technique coupled with high-speed digital photography to carry out dynamic fracture studies in this research.

2.1 Working Principle of Digital Image Correlation (DIC)

The principles of DIC and its applications to the field of experimental mechanics were laid out in the early 1980s [102, 103]. In concept, DIC is a gray scale (intensity) pattern matching method. It is based on the principle of locating a target pattern (a point or a small region) in the deformed state of an object relative to its location in the undeformed state. In this method, the surface of the specimen is covered with a fine, stochastic pattern (also called a random speckle pattern or white light speckles) by spraying a fine mist of black and white paints to achieve a broad range of gray scales. This procedure provides a whole field of unique speckles where each speckle has a unique shape, size and intensity and serves as an ideal target.

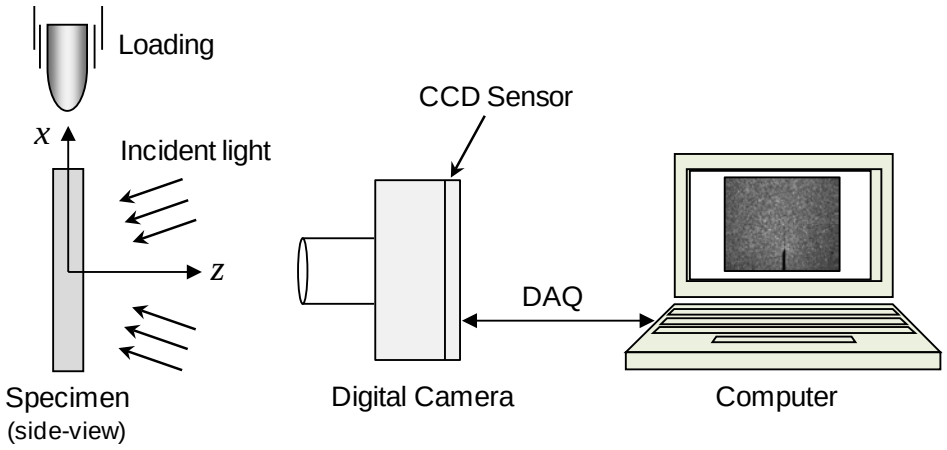

Fig. 2.1: Typical experimental arrangement used for digital image correlation method.

Figure 2.1 shows a typical experimental setup used for 2D DIC method. The surface of the specimen, decorated with a random speckle pattern, is uniformly illuminated using ordinary white light sources. A digital camera with a relatively high pixel count (typically 1-4 megapixels to achieve a good spatial resolution) is employed to photograph the speckle pattern before and after the specimen is deformed. The speckle pattern recorded

under no-load condition serves as the reference image (undeformed image). With the application of load, the speckle pattern distorts and this distorted pattern recorded by the camera serves as the deformed image. The recorded images contain intensity measurements in a discrete form at each pixel location on the CCD array. It should be noted that in general the algorithms used for image correlation are not based on the intensity matching about a single speckle in its two states; instead they are based on matching the intensity field of many speckles in the region-of-interest [104]. Hence, if the target pattern is appropriate to identify a number of unique points and their precise locations in each of the images, the 2D displacement components over the field of view can be evaluated.

Figure 2.2 depicts the working principle of DIC method. As shown in Fig. 2.2(a), the undeformed image (or the reference image) of size, say 2000 x 2000 pixels is segmented into sub-images of size, say 30 x 30 pixels. Each sub-image represents an intensity distribution. Now, for every sub-image in the undeformed image, the corresponding speckle pattern (intensity distribution) is searched in the deformed image by performing grayscale correlation operation. For simplicity, the planar deformations of an isolated undeformed sub-image are schematically depicted in Fig. 2(b). After deformation, the undeformed sub-image centered at $O(x, y)$ is displaced to $O'(x + u, y + v)$ by moving u and v distances in the x- and y-directions, respectively. The displacements components u and v can be obtained using affine transformations to relate $O'(x + u, y + v)$ with $O(x, y)$. This is accomplished by using an interpolation method to express intensity variation within the sub-image. It should be noted that the digitized image of an object consists of thousands of pixels with abruptly varying gray-scale values from one pixel to

the next. These abrupt variations in the grayscale values from one pixel to the neighboring pixels produce significant computational difficulties when mapping displacements from undeformed to deformed state [104]. Hence, to overcome these difficulties, the intensity data is smoothed using an interpolation function for each facet/sub-image over the entire field in both the states.

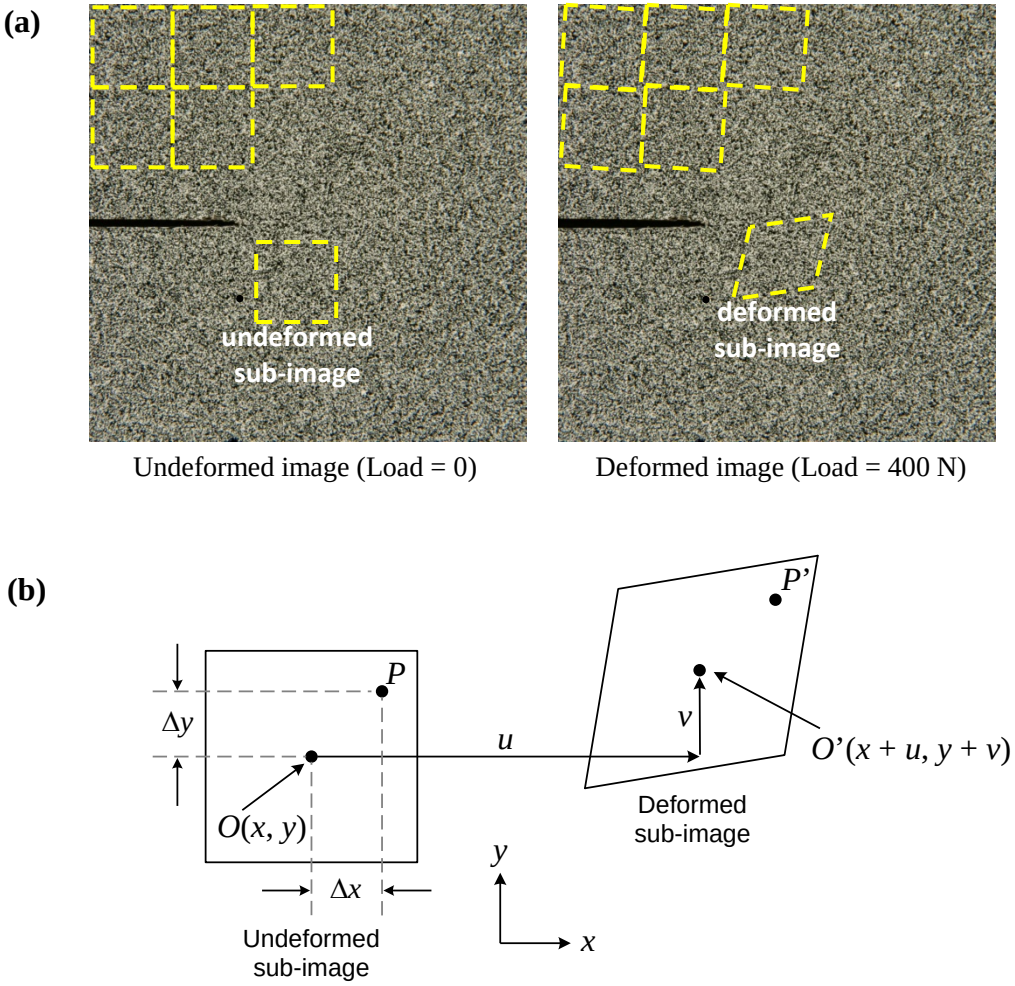

Fig. 2.2: Working principle of DIC. **(a)** A pair of undeformed and deformed speckle images recorded by the digital camera being segmented into sub-images. **(b)** Displacement mapping scheme: undeformed sub-image point $O(x, y)$ translates to a new location $O'(x + u, y + v)$ in the deformed sub-image and the difference between these coordinates gives the sliding (u) and opening (v) displacements for the sub-image.

2.2 The Correlation Procedure

The DIC method compares the intensity (grayscale) data from two pixel fields captured in two states, undeformed and deformed. In digital imaging, the analog light intensity field $I(x, y)$ is converted into a discrete field $D(x, y)$. Typically, the digital image is a 2D array of grayscales, denoted as $D(i, j)$ where i and j denote rows and columns, respectively. For a sub-image centered at point O in the undeformed state (Fig. 2.2(a)), the discretely sampled intensity variations can be represented using interpolation functions at O and its neighborhood including point P as [105],

$$\begin{aligned} D(O) &= D(x, y) \\ D(P) &= D(x + dx, y + dy) \end{aligned} \tag{2.1}$$

where, the neighboring point P is located at an incremental distance from origin O. After deformation, the discretely sampled intensity variations at new locations (denoted by the primed symbols) are given by,

$$\begin{aligned} D'(O') &= D(x',\ y') \\ D'(P') &= D(x' + dx',\ y' + dy') \end{aligned} \tag{2.2}$$

where $x' = x + u(x,\ y),\ y' = y + v(x,\ y)$

For small deformations,

$$\begin{aligned} D'(x',\ y') &= D\left[x + u(x,\ y),\ y + v(x,\ y)\right] \\ D'(x' + dx',\ y' + dy') &= D\left[x + dx + u(x + dx,\ y + dy),\ y + dy + v(x + dx,\ y + dy)\right] \end{aligned} \tag{2.3}$$

Alternatively,

$$D'\left(x'+dx',\ y'+dy'\right)=D\left[x+u\left(x,\ y\right)+\left(1+\frac{\partial u}{\partial x}\right)dx+\frac{\partial u}{\partial y}dy,\ y+v\left(x,\ y\right)+\frac{\partial v}{\partial x}dx+\left(1+\frac{\partial v}{\partial y}\right)dy\right] \tag{2.4}$$

If the sub-image is sufficiently small and displacements are therefore constant within the sub-image, then the mapping parameters u, v, $\frac{\partial u}{\partial x}$, $\frac{\partial v}{\partial y}$, $\frac{\partial u}{\partial y}$, $\frac{\partial v}{\partial x}$ can be evaluated. This process is repeated for all sub-images over the field of view. (Note that overlapping of pixels of neighboring pixels can be used to enhance the number of measurement points and possibly the quality of measurement.)

The matching of a sub-image of the undeformed and deformed states to determine local displacements is done using one of the following measures:

(1) Magnitude of intensity difference:

$$\sum_i\left[\left|D'\left(O'\right)-D\left(O\right)\right|\right] \tag{2.5}$$

(2) Sum of the squares of the intensity value difference:

$$\sum_i\left[D'\left(O'\right)-D\left(O\right)\right]^2 \tag{2.6}$$

(3) Normalized cross-correlation:

$$\frac{\sum_i D'\left(O'\right)D\left(O\right)}{\sqrt{\sum_i D'\left(O'\right)}\sqrt{\sum_i D\left(O\right)}} \tag{2.7}$$

(4) Cross-correlation:

$$\sum_{i} D'(O')D(O) \tag{2.8}$$

Minimizing measures (1) and (2), and maximizing (3) and (4) will provide the optimal estimation of all displacement and displacement gradients. Since minimization algorithms are generally more stable for implementation, the popular method of normalized cross correlation can be implemented alternatively as,

$$C\left(u,\ v,\ \frac{\partial u}{\partial x},\ \frac{\partial v}{\partial y},\ \frac{\partial u}{\partial y},\ \frac{\partial v}{\partial x}\right)=1-\frac{\sum_{i=1}^{N}\sum_{j=1}^{M} D\left(x_i,\ y_j\right)D'\left[x_i+u\left(x_i,\ y_j\right),\ y_i+v\left(x_i,\ y_j\right)\right]}{\sum_{i=1}^{N}\sum_{j=1}^{M} D^2\left(x_i,\ y_j\right)D'^2\left[x_i+u\left(x_i,\ y_j\right),\ y_i+v\left(x_i,\ y_j\right)\right]} \tag{2.9}$$

for minimization. The best estimates of displacements and their gradients can be obtained when the value of correlation coefficient $C\rightarrow 0$. The result of $C=0$ is a perfect match. Note that the correlation coefficient C is a function of displacement components $(u,\ v)$ and their gradients $(\partial u/\partial x,\ \partial u/\partial y,\ \partial v/\partial x,\ \partial v/\partial y)$. Therefore, a search has to be performed for optimum values of these mapping parameters such that C is minimized. To do this, a number of optimization methods including Newton-Raphson, Coarse-Fine search, and Lavenburgh-Marquardt (L-M) methods can be used. Among these, the L-M method offers very good convergence characteristics and is as fast as Newton-Raphson method. Like other minimization algorithms, the L-M method is an iterative procedure and requires initial guess values to start a minimization procedure.

In the current work, an approach developed at Auburn [106] as an in-house software suite on a MATLAB^{TM} platform has been used to estimate in-plane surface displacement

components. In the first step, displacements were estimated by performing a 2D cross-correlation of gray scales in the Fourier domain and the peak of the correlation function detected to a sub-pixel accuracy using bicubic interpolation. This process was repeated for the entire image to obtain full-field in-plane displacements. In the second step, an iterative approach based on nonlinear least-squares minimization was used to minimize the 2D cross-correlation function in the spatial domain to refine the previously computed displacements as an initial guess. In this step, minimization was carried out in a six variable space (displacements and their gradients) rather than in a two variable space as it minimizes a significant amount of noise present in the initial estimation of displacements obtained from the first step, and hence improves the displacement measurement accuracy.

CHAPTER 3

EXPERIMENTAL AND TESTING DETAILS[1]

In this chapter, different experimental setups and test procedures used for studying quasi-static and dynamic fracture behavior, and impact energy absorption characteristics, are described. The various experimental tools used for material characterization and post-mortem analyses of failed surfaces are also presented.

3.1 Quasi-static Tensile and Fracture Tests Setup

The uniaxial quasi-static tensile tests were carried out in an Instron 4465 testing machine to measure properties such as elastic modulus, tensile strength, percent elongation at break. Dogbone-shaped specimens were prepared according to ASTM D638 test method [109]. All the experiments were conducted at room temperature under displacement controlled conditions at a constant crosshead speed of 2 mm/min.

In order to characterize the fracture toughness in terms of the critical stress intensity factor, K_{Ic}, quasi-static fracture tests were performed in accordance with ASTM D5045-96 guidelines [110]. The single edge notched 3-point bend specimens were loaded in displacement control mode at a cross-head speed of 0.25 mm/min using Instron 4465 testing machine. The load-deflection data was recorded up to crack initiation and during stable crack growth, if any. The crack initiation toughness, K_{Ic}, was calculated using the load (P) at crack initiation.

[1] Parts of this chapter appear in Refs. [107, 108].

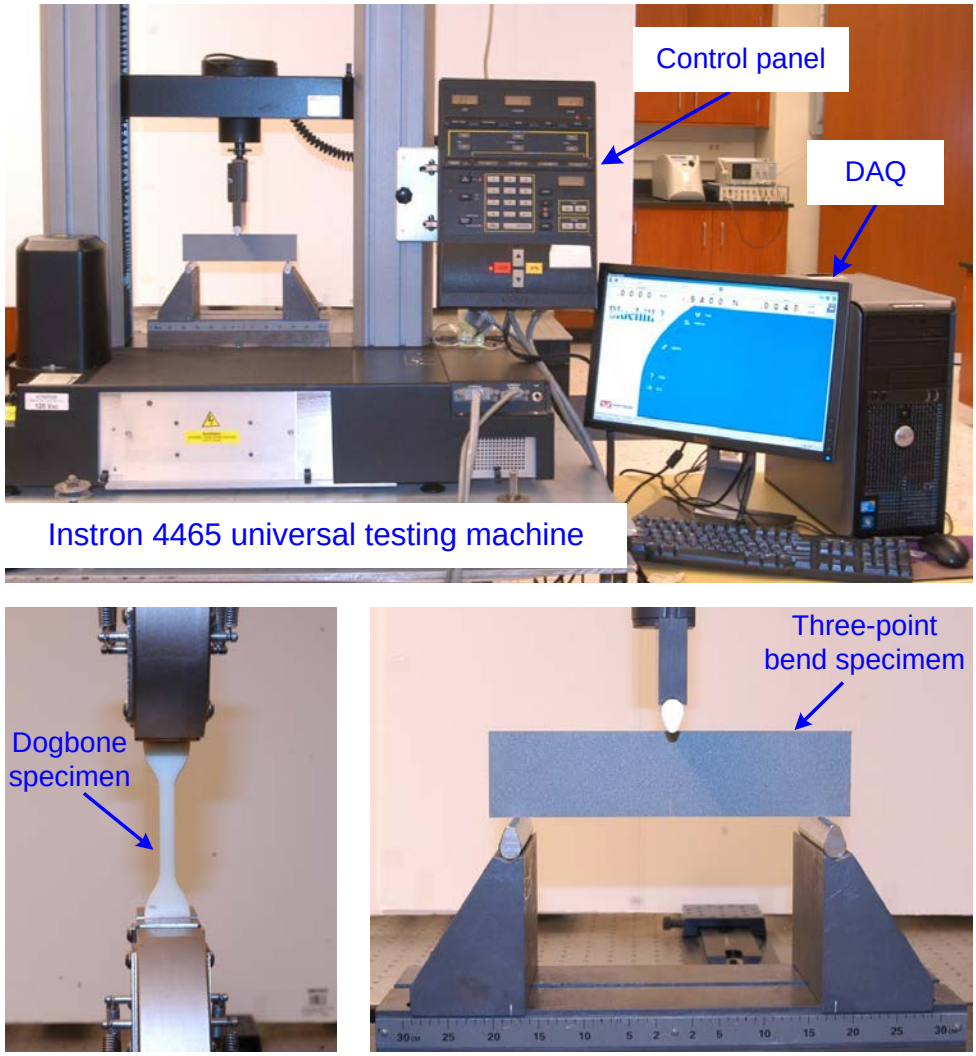

Fig. 3.1: Photographs of the experimental setup for quasi-static tensile and fracture tests.

The photographs in Fig. 3.1 show the experimental setup as well as specimen loading configurations for both quasi-static tensile and fracture tests. Typically, for each type of test and material category at least four sets of experiments were performed.

3.2 Dynamic Fracture Experimental Setups

In this research, the dynamic fracture behavior was studied using 2D digital image correlation (DIC) method in conjugation high-speed photography. As discussed in chapter 2, in this method the decorated random speckle patterns on a specimen surface

were monitored during a fracture event. The speckle patterns were recorded before and after deformation. The images from the deformed and undeformed sets were paired and analyzed using image correlation methodology. Conceptually, a sub-image in an undeformed image was selected and its location in the corresponding deformed image was searched to find its local displacements. In the current study, for dynamic fracture characterization, two types of experimental setups were employed depending upon the specimen geometry, and are described in the following.

3.2.1 Drop tower and high-speed camera setup

The schematic of the experimental setup used for studying surface deformations of relatively large specimens of dimensions 212 mm x 50 mm x 8 mm, is shown in Fig. 3.2.

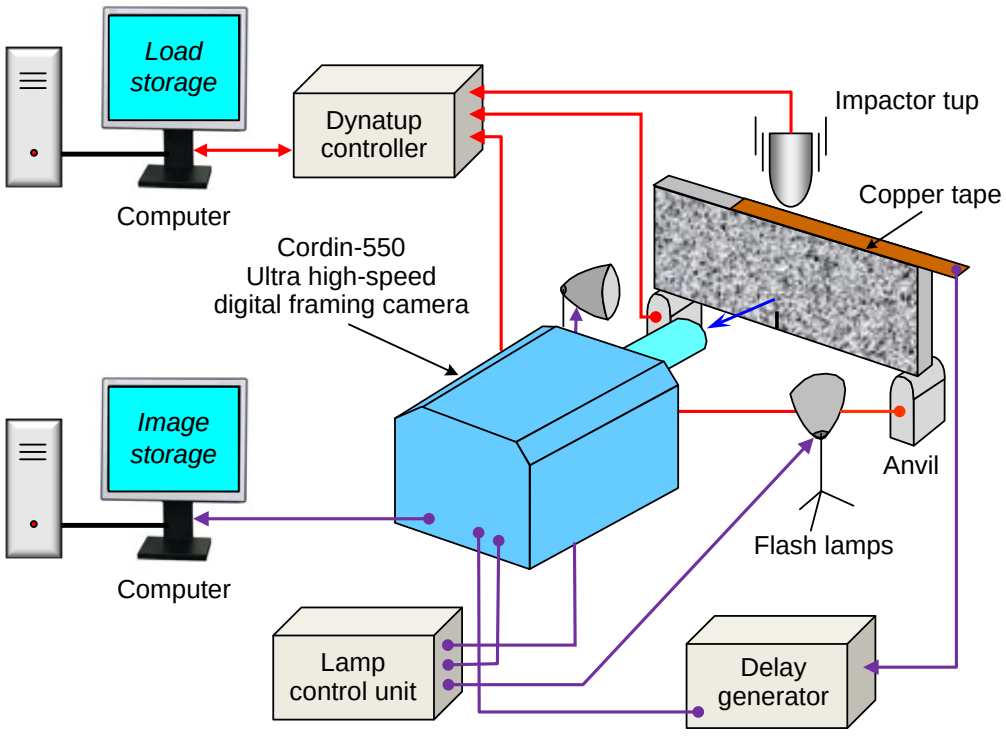

Fig. 3.2: Schematic of the experimental setup used for dynamic fracture study.

The setup included a drop-tower (Instron-Dynatup 9250HV, USA) for impact loading the specimens and a Cordin 550 ultra high-speed digital framing camera (Cordin Scientific Imaging, USA) for recording speckle images during the fracture event. The drop-tower was equipped with an instrumented tup (hemispherical profile) and a pair of instrumented anvils for recording force and support reaction histories, respectively. The setup also included instrumentation to produce a delayed trigger pulse when the impactor contacted the specimen (time, $t = 0$). Two high-energy flash lamps, triggered by the camera and a pulse generator, were employed to illuminate the sample surface. Also, two separate computers, one to record the impact force and anvil reaction histories, and the other to control the high-speed camera and store the images, were used. The light intensity from the specimen surface in the region of interest was recorded. The actual photographs of the dynamic fracture experimental setup, specimen loading device, and the instrumentation used to control drop-tower, high-speed camera, high energy flash lamps and trigger delay are shown in Fig. 3.3.

The Cordin 550 ultra high-speed digital camera is equipped with a combination of CCD based imaging technology and a high-speed rotating mirror optical system. Figure 3.4 shows the internal optical arrangement of Cordin 550 camera. It is capable of recording images at rates of up to 2 million frames per second on 32 individual 1000 x 1000 pixel (pixel size: 7.4 μm square) CCD sensor array positioned circumferentially around a five-facet rotating mirror which reflects and sweeps light over these sensors. The specimen decorated with random speckles was initially rested on two instrumented anvils and the camera was focused on a 30 x 30 mm^2 region-of-interest in the crack-tip vicinity.

Fig. 3.3: Photographs of the experimental setup used for dynamic fracture study.

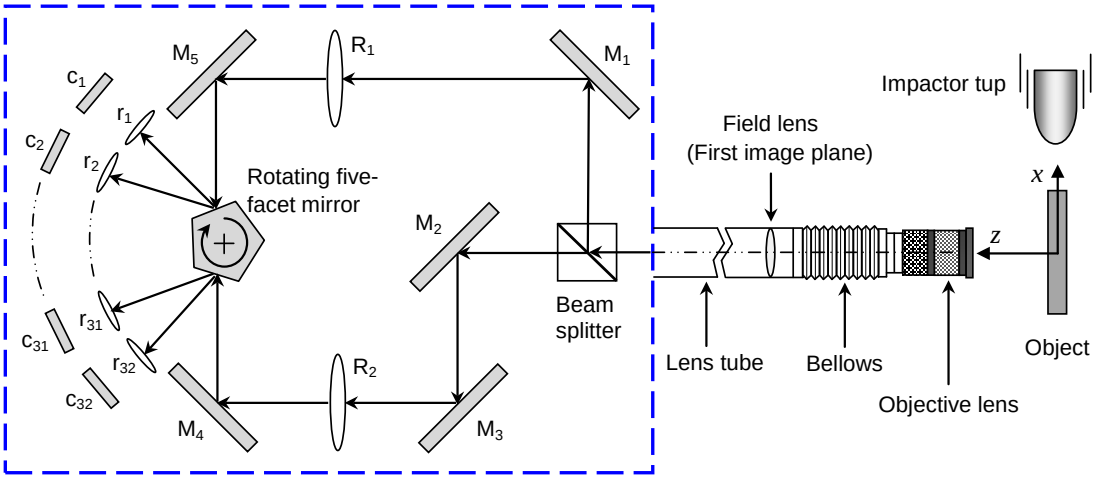

Fig. 3.4: Schematic showing internal optical arrangement of Cordin-550 high-speed camera: M_1-M_5 are mirrors; R_1 and R_2 are relay lenses; r_1-r_{32} are relay lenses for CCDs; c_1-c_{32} are CCD sensors.

Prior to impacting the specimen, a set of 32 images were recorded at a chosen framing rate. While keeping all the camera settings the same, a second set of 32 images was captured when the specimen was impacted at a velocity of 4.5 m/s. A total of 32 images were recorded for undeformed and deformed sets. The corresponding two images of each sensor were paired from the undeformed and deformed sets and analyzed.

3.2.2 Long-bar impactor setup

In order to study dynamic fracture behavior of IPN molecular composites having relatively smaller specimen dimensions (particularly the span), a long-bar impactor setup was employed. The schematic of the experimental setup for studying crack initiation and propagation in symmetric 1-point loading configuration using DIC and high-speed photography is shown in Fig. 3.5. The setup consisted of a long-bar impactor to deliver load to the specimen dynamically and a Cordin-550 high-speed camera for recording

reflected light intensity from the specimen surface decorated with random speckle pattern.

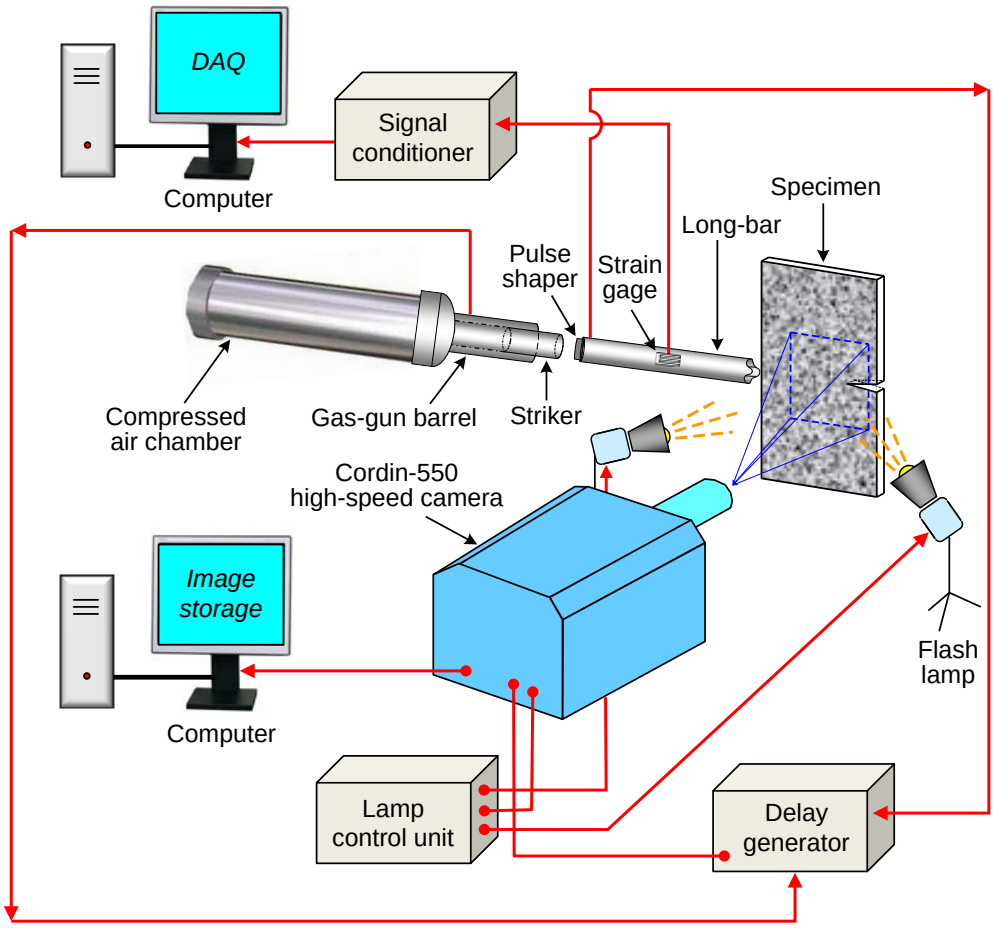

Fig. 3.5: Schematic of the experimental setup for dynamic fracture study of IPNs.

The setup also included instrumentation to produce a delayed trigger pulse when the striker contacted the long-bar. Two high-energy flash lamps, triggered by the camera and a pulse generator, were employed to illuminate the specimen surface. The loading device included an aluminum long-bar (strain-rate independent Al-7075-T6, 6.5 feet long, 1 inch diameter) with a cylindrical head, a compressed air chamber with a gun barrel containing a cylindrical striker (Al-7075-T6, 12 inch long, 1 inch diameter), and a data acquisition system (DAQ) with a signal conditioning unit. (An Al-1100 pulse shaper was used

between the striker and long-bar to control the loading rate.) The strain gage (CEA-13-062UW-350 from Vishay Micro-measurements) on the long-bar, connected to DAQ system via a signal conditioner (Ectron), was used to record the strain history in the long-bar. The edge cracked specimen decorated with random speckle pattern was positioned on an adjustable micromechanical stage with a layer of putty, above and below the specimen edges (see Fig. 3.6 for a close-up view). The specimen was then registered against the cylindrical head of the long-bar, thus, causing a simple 1-point impact loading. Putty was used to ensure symmetry of the reflected stress waves from the top and bottom edges of the specimen, and hence loading the crack symmetrically to achieve mode-I fracture conditions. The computer connected to the high-speed camera was used to control parameters such as trigger delay, flash duration, framing rate, and image storage.

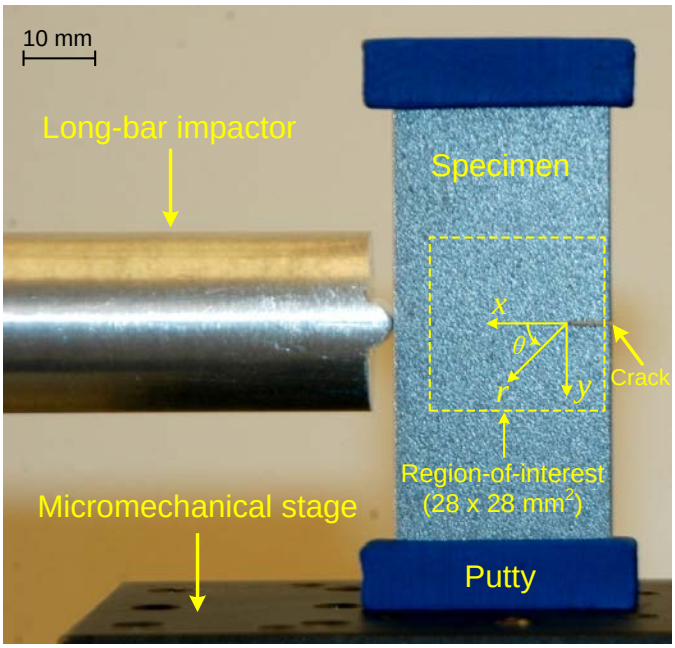

Fig. 3.6: Close-up view of the long-bar imapctor loading the specimen decorated with random speckles.

As shown in Fig. 3.5, the camera was focused on a 28 x 28 mm^2 region-of-interest in the crack-tip vicinity. Prior to impacting the specimen, a set of 32 reference (undeformed set) images were recorded at a chosen framing rate. While keeping all the camera settings the same, the striker was launched. When the striker impacted the long-bar, it generated a compressive stress wave that propagated the length of the bar before imparting a transient load to the specimen edge. The compressive stress waves then entered the specimen, reflected back as tensile waves from its far edge and loaded the crack-tip. When the striker contacted the long-bar, an electrical circuit was closed to activate the camera with a user-specified delay to trigger the two high energy flash lamps. This time delay provided sufficient time for the compressive stress wave to travel the length of the long-bar to the specimen crack-tip as well as enough time for the flash lamps to ramp up to their full intensity levels to provide uniform illumination. The second set of 32 images (deformed set) was captured in real-time during the specimen failure. In order to capture the entire fracture event, a framing rate ranging from 250,000-300,000 frames per second was used. A total of 32 images were present in each undeformed and deformed sets. The corresponding images recorded by each sensor were paired and analyzed to get crack-opening and crack-sliding displacement fields.

3.3 Low-velocity Impact Test Setup

In order to quantify energy absorption characteristics of IPNs in structural configurations, low-velocity impact tests were carried out in accordance with ASTM D5628-96 test method [111]. The IPNs were subjected to impact tests using a drop-tower (Instron Dynatup 9250HV) shown in Fig. 3.7(a). The drop-tower is equipped with Impulse data acquisition software which can acquire a total of 8192 data points at an

acquisition rate of up to 5.0 MHz. It is capable of recording transient load, impact velocity and impact energy absorbed by the specimens. The machine is also fitted with a velocity detector to measure the velocity of the falling tup just before it strikes the specimen. The velocity detector operates in conjunction with a flag mounted on the drop-weight, and triggers data collection when the flag passes through it. Using this setup, the impact energy and impact velocity can be varied by changing the mass and height of the falling weight. The drop-tower has an instrumented tup (hemispherical head, 12.7 mm diameter) with a load cell capacity of 22.2 kN to record the transient response of the specimens. The specimen support fixture (developed in-house) at the bottom of the drop-tower facilitates circular clamp condition with a clear aperture of 76.2 mm in diameter. The close-up view of the striker head and the fixture are shown in Fig. 3.7(b).

All the impact tests were performed at a fixed energy level (E) of 60 J with a constant drop-mass (m) of 4.85 kg, drop-height (h) 1.27 m, and impact velocity (v_{impact}) 5 m/s. The drop-height is the distance between the tip of indenter and the top surface of the clamped specimen, and can be calculated using equation $E=mgh$, where g is the acceleration due to gravity. The impact velocity can be measured using energy conservation ($mgh=½\,mv_{impact}^2$). The energy level E=60 J and impact velocity 5 m/s were arrived at after performing a series of benchmark experiments in order to avoid multiple rebounds and fail the specimens in a single drop/impact. As a general rule, the energy delivered from the drop-weight must be significantly greater than the energy absorbed by the material being tested, so that there is no appreciable slowdown of the striker during the impact event [112].

Fig. 3.7: Experimental setup for low-velocity impact tests for energy absorption studies: **(a)** Instron Dynatup 9250HV drop-tower, **(b)** Close-up view of the impactor tup and the specimen support fixture.

Prior to testing, the load cell was calibrated. The specimen was securely clamped into the specimen support fixture. Using the jog keys and fine position thumbwheel on the drop-tower control panel, the drop-weight cross-head assembly was moved down until the striker head contacted the specimen. The bottom edge of the velocity detector was aligned with the bottom edge of the flag, and at this point the current position of the drop-weight was set to zero height. Next, the drop-weight assembly was raised to a desired height, and released to impact the specimen. The transient load and energy

absorbed by the specimen during the entire impact event was recorded. It should be noted that the Impulse data acquisition software equipped with the drop-tower internally performs energy calculations using,

$$TE(t) = KE(t) + PE(t) + Ea(t) = \text{constant} \tag{3.1}$$

where $TE(t)$ is the total energy in the system which remains constant by the conservation principle, $KE(t)$ is the kinetic energy of the drop-weight, $PE(t)$ is the potential energy of the drop-weight, and $Ea(t)$ is the impact energy absorbed by the specimen up to time t. Graphically, $Ea(t)$ is simply the area under the load-deflection curve and is calculated using the mass (m), velocity ($v(t)$), and position ($x(t)$) of the drop-weight in Eq. (3.2),

$$Ea(t) = \frac{1}{2} m\left[v_{impact}^2 - v^2(t)\right] + mgx(t) \tag{3.2}$$

where the quantities $v(t)$ and $x(t)$ are evaluated using trapezoidal approximations.

3.4 Material Characterization Tools

3.4.1 Ultrasonic pulse-echo method

The dynamic elastic properties of particulate polymer composites and transparent IPNs were determined using a non-destructive method implemented through ultrasonic wave propagation. Figure 3.8 shows the photograph of the setup used for ultrasonic pulse-echo measurements. The setup consists of a digital oscilloscope (Model: Gould DSO 450) and an ultrasonic analyzer (Model: Panametrics 5052UA) equipped with a pulser, receiver, stepless gate, a gated peak detector and appropriate transducers.

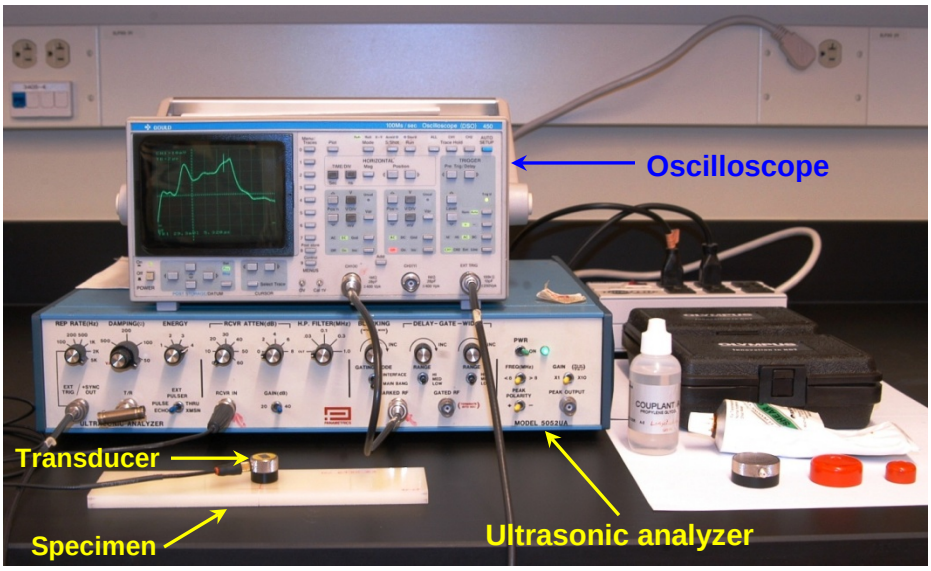

Fig. 3.8: Photograph of the setup for ultrasonic pulse-echo measurements.

The ultrasonic pulse-echo measurements were performed at several discrete locations of the cured sheets. The longitudinal (C_L) and shear (C_S) wave speeds were determined by measuring transit time for the elastic pulse to travel twice the thickness of the sample using a longitudinal wave transducer (Panametrics V129RM; 10 MHz) and a shear wave transducer (Panametrics V156RM; 5 MHz), respectively. The mass density, ρ, of each composition was also determined. The values of dynamic elastic modulus (E_d) and Poisson's ratio (ν_d) were then calculated using measured wave speeds and mass density using,

$$C_L = \sqrt{\frac{E_d(1-\nu_d)}{\rho(1+\nu_d)(1-2\nu_d)}}, \qquad C_S = \sqrt{\frac{E_d}{2\rho(1+\nu_d)}}$$

3.4.2 Microscopy and fractography

Microscopic studies were undertaken to get an insight of the quality of exfoliation of filler particles into epoxy. For micron-size particulate composites, samples with cross-sectional area 15 mm x 8 mm were cut and polished sequentially using 600, 1000 and 2000 grit wet emery papers. The polished surfaces of these samples were viewed using Nikon Eclipse L150 optical microscope as shown in Fig. 3.9. The optical microscope was also used to view global representation of fractured surfaces at low magnifications in order to cover maximum region of failed surfaces.

Fig. 3.9: Photograph of Nikon Eclipse L150 optical microscope used for checking particle distribution in micron-size glass filled PPCs.

The particle distribution in nano-silica and carbon nanotubes modified PPCs were examined using a transmission electron microscope (TEM). Figure 3.10 shows the photograph a ZEISS EM10 TEM used to check particle dispersion and a Leica UltraCut T Microtome used for TEM sample preparation. In the case of nanocomposites, thin film slices (80-90 nm thick) for TEM were microtomed using Leica UltraCut T Microtome.

These slices were then mounted on copper grids as shown in Fig. 3.10 and the associated through-the-thickness morphologies were viewed in a TEM at an accelerating voltage of 70 kV.

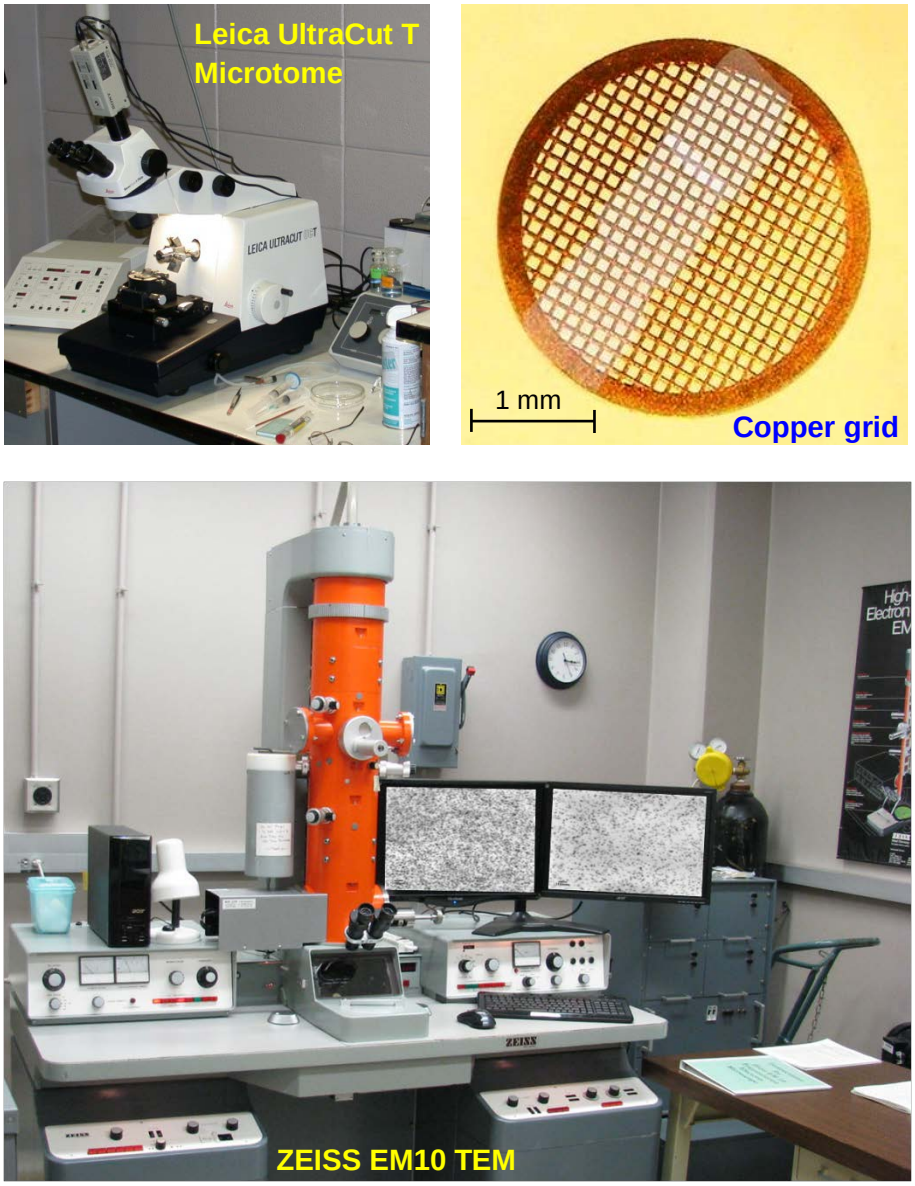

Fig. 3.10: Photograph of Transmission Electron Microscope (TEM) used to check nano-filler dispersion. (Top left image: Leica UltraCut T Mircotome for TEM sample preparation; Top right image: Copper grid for TEM sample mounting.)

It has been well recognized that fracture surface topography reveals inherent details of deformation and the associated energy dissipation mechanisms that govern the fracture process. Accordingly, the fracture surfaces were examined both qualitatively and quantitatively. In most parts of this research, scanning electron microscopy was performed for qualitative examination of fracture surfaces of quasi-statically and dynamically failed specimens. Figure 3.11 shows the photograph of a scanning electron microscope (Model: JEOL JSM-7000F) used to study fracture surface morphologies of PPCs and IPNs. The fracture surfaces were sputter coated with a thin layer of gold to make them conductive in order to prevent charge build up. The inset in Fig. 3.11 shows the photograph of a gold sputtering unit (Model: PELCO SC-6) used for SEM sample preparation.

Fig. 3.11: Photograph of Scanning Electron Microscope (Model: JEOL JSM-7000F) used to study fracture surface morphologies of particulate polymer composites. The top left inset shows the photograph of a gold sputtering unit (Model: PELCO SC-6) used for SEM sample preparation.

The quantitative micro-measurements of fractured surfaces were conducted to further understand the surface morphologies. In view of this, the roughness measurements were performed using a Dektak-150 profilometer (see Fig. 3.12(a)) with a stylus of root radius 2 and 12.5 µm depending on the degree of the surface roughness of the failed material and the lateral resolution needed for improved accuracy in the roughness parameters.

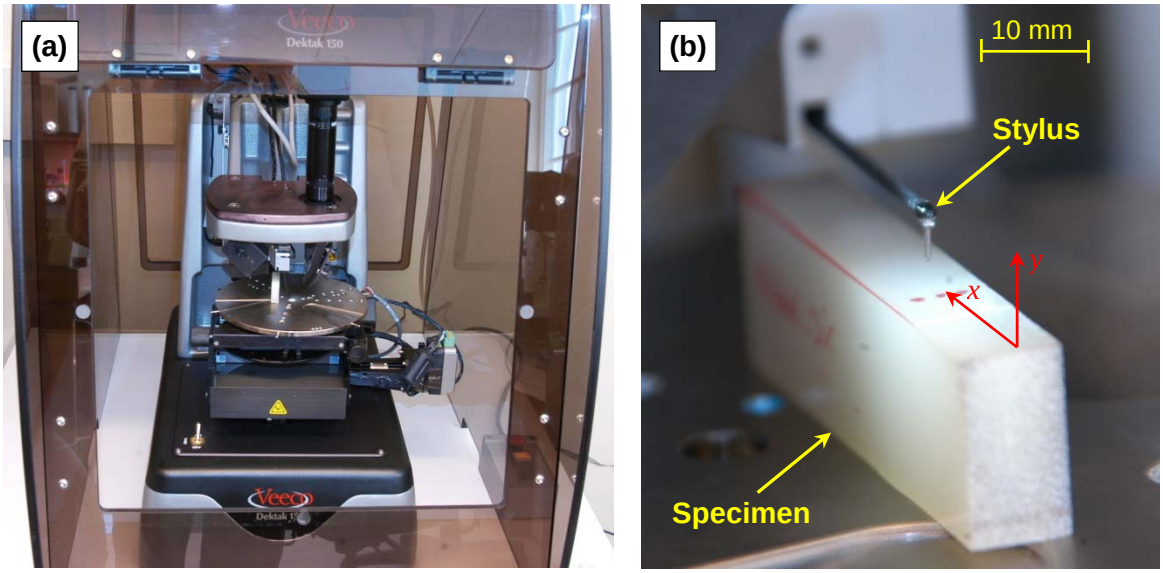

Fig. 3.12: (a) Dektak 150 stylus profiler for fractured surface roughness measurements, **(b)** Close-up view of the stylus and specimen.

Figure 3.12(b) shows a close-up view of the stylus and a failed specimen. The fracture surface profiles were scanned in the stable crack growth zone and will be discussed later in the next chapter.

CHAPTER 4

FRACTURE BEHAVIOR OF PPCs: NANO- VS. MICRO-FILLERS[1]

This chapter deals with quasi-static and dynamic fracture investigation of particulate polymer composites (PPCs) made of nano- and micron-size silica filler in epoxy. The effects of particle size-scale (nano- *vs.* micro-) and loading rate on the fracture behavior of silica-filled epoxy PPCs are studied under both quasi-static and stress-wave dominant loading conditions. In the following section, the details of material preparation, characterization, and specimen geometry are provided. Next, the methodology to evaluate various fracture parameters is briefly described. This is followed by a detailed description of experimental results in a comparative manner for all categories of specimens in terms of load-deflection responses, quasi-static crack initiation toughness (K_{Ic}), dynamic fracture parameters such as crack tip velocity (V) histories, mode-I dynamic stress intensity factor (K_I^d) histories, K_I^d-V relationships. Subsequently, the results are supported qualitatively and quantitatively by microscopic examination of fractured surfaces and roughness measurements.

4.1 Materials Processing and Characterization

4.1.1 Materials

Two sizes of spherical rigid fillers, one nano-sized silica particles of average diameter 20 nm (Nanopox F400 from Nanoresins, Germany) and the other micron-sized

[1] Parts of this chapter appear in Refs. [107, 113].

glass particles of mean diameter 35 μm (Spheriglass®, Potters Industries Inc.) were used in this study. The choice of the latter was based on work of Kitey and Tippur [3] that offered the largest gain in fracture toughness under dynamic loading conditions. Further, silica/glass spheres are smooth, hard, and offer excellent chemical resistance and low oil absorption. Unlike fibers and irregular particles, the solid spheres generally show uniform, regular stress distribution with less localized stress concentrations, and provide high abrasion and creep resistance as well as better dimensional stability to composites due to low shrinkage and warpage.

The Nanopox F400 consisted of 40 wt% (~26 vol% [10, 19]) silica nanoparticles supplied as colloidal silica gel in a diglycidyl ether of bis-phenol A (DGEBA) resin whereas the micro-filler were received in powder form. A low viscosity epoxy system (Epo-Thin™ from Beuhler, Inc. USA) consisting of DGEBA resin and an amine-based hardener in the ratio of 100:39 was employed as the matrix material. This epoxy system offers low shrinkage and relatively long duration room temperature curing characteristics.

4.1.2 Particulate composites preparation

Prior to mixing the constituents, each type of filler was pre-heated in an oven at 70 °C for an hour in order to release any trapped moisture and then cooled gradually to ambient temperature. The nanocomposites and the micron-size particle filled composites were loaded with 3%, 5%, 7%, and 10% of fillers (by volume). Care was exercised to ensure uniform distribution of each type of filler throughout the matrix. It should be noted that the Nanopox F400 resin pre-loaded with silica nanoparticles was diluted first by the required amount of DGEBA resin in such a way that the end product had the appropriate content of nanosilica for the desired volume fraction. The material was mixed

using a magnetic stirrer for 20 min at 50 °C to obtain a homogenous mixture. While the mixture remained at a relatively low viscosity at 50 °C, degassing was done every 30 min for 2 h to remove any trapped air bubbles generated during mixing. This ensured full degassing of the mixture. This also allowed sufficient time for the mixture to reach room temperature. After degassing, the stoichiometric amount of the hardener was added to the mixture, which was again magnetically stirred for 5 min and degassed for 20 min. The mixture was then poured into molds coated with a release-agent as shown in Fig. 4.1.

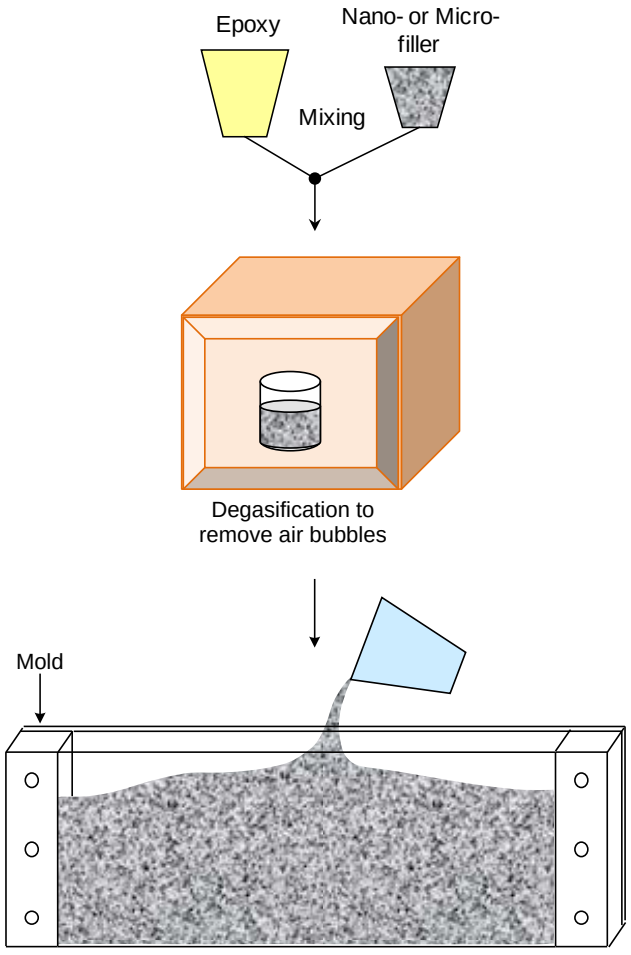

Fig. 4.1: Schematic showing particulate composites preparation.

For the preparation of micro-particle filled composites, the predetermined amounts of filler particle volume fractions were added into DGEBA epoxy resin followed by mixing and degassing steps as mentioned above. However, in this case, after mixing of hardener and degassing, the mixture was continuously stirred until the mixture showed a tendency to gel before pouring into molds. This helped to eliminate sedimentation of the filler particles during subsequent curing. The poured mixtures were allowed to cure for 96 h at room temperature. The cured sheets were removed from the molds and further rested for a week prior to machining and testing.

4.1.3 Microstructural characterization

The particle distribution in nano- and micro-particle filled composites was examined using transmission electron microscope (TEM) and optical microscope, respectively, as described in Chapter 3. The micrographs in Fig. 4.2 depict particle distribution in nano- and micro-particle filled composites. It can be seen that particle agglomeration is absent in all micrographs. The TEM images in Figs. 4.2(a) and (b) show a very uniform distribution of nanoparticles throughout the epoxy matrix with 3% and 10% V_f, respectively. Note that the bigger and darker spots in the TEM images indicate overlapping of two or more particles in the thickness direction. *As noted in section 3.3.2, the TEM specimens were ~90 nm thick, and hence, the apparent volume fraction of nanoparticles is higher than the true volume fraction.* The optical images in Figs. 4.2(c) and (d) show well-dispersed micro-particles with 3% and 10% V_f, respectively. It should be noted that unlike TEM images the optical micrographs show particle distribution imaged only at zero thickness. The dark spots in these micrographs are debris due to polishing and the dark lines are scratch marks.

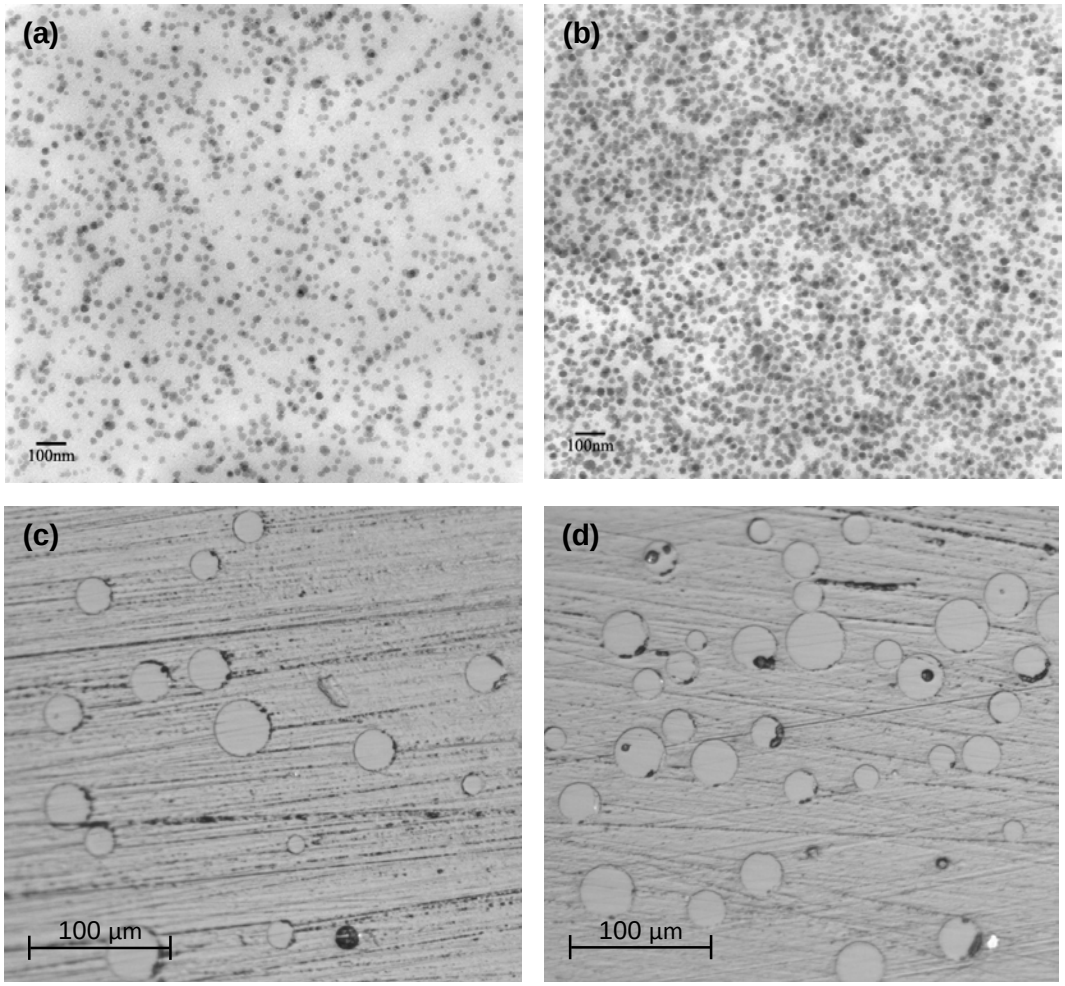

Fig. 4.2: Micrographs showing particle dispersion: **(a)** TEM image of 3% V_f nano-filler, **(b)** TEM image of 10% V_f nano-filler, **(c)** Optical micrograph of 3% V_f micro-filler, **(d)** Optical micrograph of 10% V_f micro-filler.

4.1.4 Elastic characterization

The elastic and physical characteristics of filled composites as a function of volume fraction of the dispersant were determined by indirect means of ultrasonic pulse-echo method as described in section 3.4.1 of the previous chapter. The longitudinal (C_L) and shear (C_S) wave speeds were determined by measuring transit time for the pulse to travel twice the thickness. The values of dynamic elastic modulus (E_d) and Poisson's ratio (ν_d) were calculated using measured wave speeds and mass density (ρ). The measured elastic

and physical properties of nano- and micro-particle filled-composites are shown in Tables 4.1 and 4.2, respectively.

V_f (%)	Density, ρ (kg/m^3)	Longitudinal wave speed, C_L (m/s)	Shear wave speed, C_S (m/s)	Dynamic elastic modulus, E_d (GPa)	Poisson's ratio, ν_d	Impedance, $\rho.C_L$ (MPa.s/m)
0	1124	2487	1136	3.97	0.368	2.80
3	1156	2547	1188	4.44	0.360	2.94
5	1181	2577	1233	4.85	0.352	3.04
7	1218	2604	1250	5.14	0.350	3.17
10	1272	2634	1268	5.52	0.348	3.35

Table 4.1: Measured dynamic material properties of *nano*-particle filled epoxies at different volume fraction (V_f).

V_f (%)	Density, ρ (kg/m^3)	Longitudinal wave speed, C_L (m/s)	Shear wave speed, C_S (m/s)	Dynamic elastic modulus, E_d (GPa)	Poisson's ratio, ν_d	Impedance, $\rho.C_L$ (MPa.s/m)
3	1151	2543	1194	4.46	0.359	2.93
5	1184	2569	1216	4.76	0.356	3.04
7	1223	2591	1239	5.08	0.352	3.17
10	1279	2627	1257	5.46	0.351	3.36

Table 4.2: Measured dynamic material properties of *micro*-particle filled epoxies at different volume fraction (V_f).

The effect of particle volume fraction on measured properties is quite evident. It can be seen that in both types of filled-composites, as the particle volume fraction increases, the density, longitudinal and shear wave speeds, and elastic modulus increase in a monotonic fashion with a negligible change in the Poisson's ratio. It should be noted here that for any given volume fraction (3%, 5%, 7%, 10%), the particle size-scale (nano- *vs.* micro-) does not affect the elastic and physical characteristics. That is, the values of each

measured property are the same for both nano- and micro-filler cases within the measurement error.

4.2 Experimental Details

4.2.1 Specimen fabrication and geometry

The cured composite sheets were machined into rectangular coupons of nominal dimensions 106 mm x 20 mm x 8 mm for quasi-static fracture tests (span 90 mm) and 212 mm x 50 mm x 8 mm for dynamic fracture experiments (span 196 mm) as shown in Figs. 4.3(a) and (b), respectively. An edge notch of 4 mm and 10 mm in length was first cut using a diamond impregnated wafer blade (thickness ~300 μm) into the samples for quasi-static and dynamic fracture tests, respectively. The notch tip was manually sharpened using a razor blade in order to have a naturally sharp crack tip to achieve a relatively quiescent crack initiation followed by a steady growth. A magnified view of the sharpened crack tip is shown in Figs. 4.3(c) and (d) with front- and back-side views of the specimen, respectively.

The dynamic fracture experiments were performed using the method of digital image correlation (DIC) to quantify crack tip deformations and hence the crack growth parameters. (The details of this method are provided in Chapter 2) To facilitate this, a stochastic speckle pattern was created on the surface of the sample by spraying a fine mist of black and white paints alternatively. Figure 4.3(b) depicts the specimen geometry, dimensions and loading configuration along with the crack tip coordinate system with an illustration of random speckle pattern. The region in the dotted box represents 30 x 30 mm^2 region-of-interest.

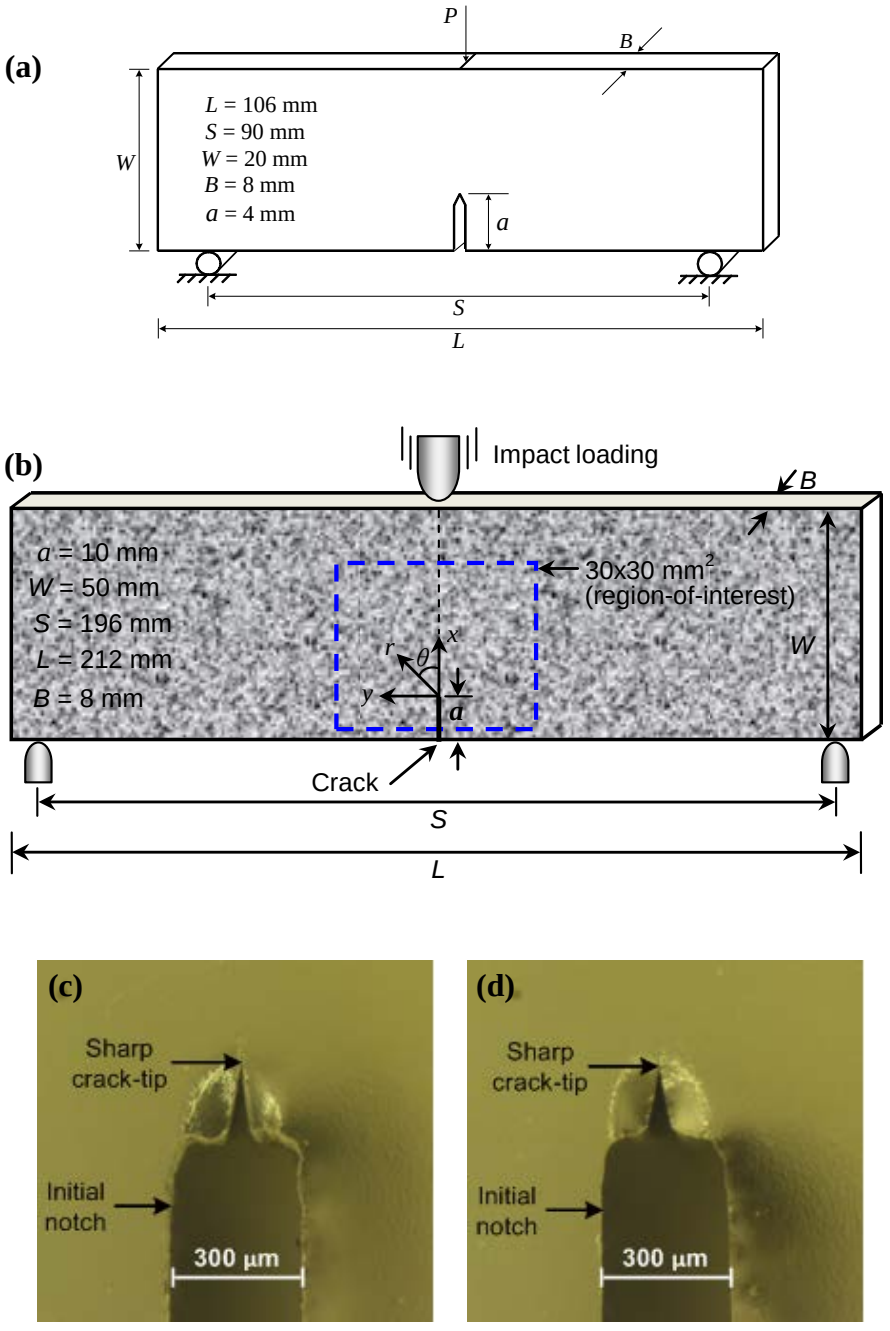

Fig. 4.3: Specimen geometry and loading configurations: **(a)** Quasi-static fracture, **(b)** Dynamic fracture, **(c)** Sharp crack tip: front-side view of the specimen, **(d)** Sharp crack tip: back-side view of the specimen.

4.2.2 Quasi-static fracture tests

Symmetric three-point bending tests were conducted to measure quasi-static crack initiation toughness, K_{Ic}. The load-deflection data was recorded up to complete fracture and K_{Ic} was calculated using the load at initiation and specimen geometry using,

$$K_{Ic} = \frac{3\frac{PS}{BW^2}\sqrt{a}}{2\left(1+2\frac{a}{W}\right)\left(1-\frac{a}{W}\right)^{3/2}}\left[1.99-\frac{a}{W}\left(1-\frac{a}{W}\right)\left\{2.15-3.93\left(\frac{a}{W}\right)+2.7\left(\frac{a}{W}\right)^2\right\}\right] \qquad (4.1)$$

where P, S, B, W and a are the load at fracture, span, thickness, width and crack length of the specimen, respectively (see Fig. 4.3(a)).

4.2.3 Dynamic fracture tests

The dynamic fracture tests were performed using the setup as shown in Fig. 3.2 in Chapter 3. The specimen decorated with random speckles was initially rested on two instrumented anvils and the camera was focused on a 30 x 30 mm^2 region-of-interest in the crack tip vicinity. Prior to impacting the specimen, a set of 32 images were recorded at a chosen framing rate. While keeping all the camera settings the same, a second set of 32 images was captured when the specimen was impacted at a velocity of 4.5 m/s. In order to capture the entire fracture event, the images in the case of micro-particle filled composites were recorded at a rate of 250,000 frames per second whereas framing rates ranging from 250,000-300,000 frames per second were used for nanocomposite specimens. A total of 32 images were recorded in each undeformed and deformed sets. The corresponding two images of each sensor were paired from undeformed and deformed sets and analyzed.

4.2.4 Image analysis details

As noted earlier, the recorded speckle images corresponded to a 30 x 30 mm^2 region on the specimen surface. The size of the decorated speckles and the optical magnification used were such that each speckle occupied 4-6 pixels on the image plane. Care was also exercised regarding electronic gain setting of the high-speed camera sensors and intensity of the flash lamps to produce a near Gaussian distribution of gray scales for each image in the mid-range of 0-255 (8 bit) intensities. That is, saturation or underexposure of pixels was avoided by trial and error prior to carrying out the actual experiment. Each resulting image was segmented into sub-images consisting of 26 x 26 pixels for analysis. While analyzing images, no overlapping of sub-images was used. This resulted in 37 x 37 array of data points in the region-of-interest.

4.2.5 Evaluation of crack tip velocity and stress intensity factors (SIFs)

The position of the current crack-tip from each digitized image was used to measure the instantaneous values of crack length. However, the presence of digitizing errors often manifests in the crack extension data. To minimize this error, the crack length data at an instant *i* was smoothed using a quadratic Bézier curve [114],

$$a_i(s) = (1-s)^2 d_i + 2s(1-s) d_{i+1} + s^2 d_{i+2}, \quad 0 \le s \le 1 \tag{4.2}$$

where *s*, *d* and *a* are the smoothing parameter, the digitized data, and the smoothed crack length data, respectively. In the above expression d_i, d_{i+1}, d_{i+2} are the control points of $a_i(s)$. A smoothing parameter of 0.5 was chosen so that the smoothed data point is located at midway from a data point to an adjacent point. Subsequently, the crack

velocity (V) was estimated from the smoothed crack length histories using forward difference method,

$$V_i = \left(\frac{da}{dt}\right)_i = \frac{a_{i+1} - a_i}{t_{i+1} - t_i} \tag{4.3}$$

where a and t are crack length and time, respectively, at a given instant i.

The mode-I and mode-II stress intensity factors (SIFs) were evaluated using an over-deterministic least-squares analysis of crack-opening and crack-sliding displacements, respectively. The governing asymptotic expressions for crack-opening (v) and crack-sliding (u) displacement fields near the tip of a dynamically loaded stationary crack are expressed as follows:

$$\begin{Bmatrix} u(r,\theta) \\ v(r,\theta) \end{Bmatrix} = \sum_{n=1}^{\infty} \frac{\left(K_{\mathrm{I}}^{d}\right)_n}{2\mu} \frac{r^{n/2}}{\sqrt{2\pi}} \begin{Bmatrix} \kappa \cos\frac{n}{2}\theta - \frac{n}{2}\cos\left(\frac{n}{2}-2\right)\theta + \left\{\frac{n}{2}+(-1)^n\right\}\cos\frac{n}{2}\theta \\ \kappa \sin\frac{n}{2}\theta + \frac{n}{2}\sin\left(\frac{n}{2}-2\right)\theta - \left\{\frac{n}{2}+(-1)^n\right\}\sin\frac{n}{2}\theta \end{Bmatrix}$$
$$+ \sum_{n=1}^{\infty} \frac{\left(K_{\mathrm{II}}^{d}\right)_n}{2\mu} \frac{r^{n/2}}{\sqrt{2\pi}} \begin{Bmatrix} \kappa \sin\frac{n}{2}\theta - \frac{n}{2}\sin\left(\frac{n}{2}-2\right)\theta + \left\{\frac{n}{2}-(-1)^n\right\}\sin\frac{n}{2}\theta \\ -\kappa \cos\frac{n}{2}\theta - \frac{n}{2}\cos\left(\frac{n}{2}-2\right)\theta + \left\{\frac{n}{2}-(-1)^n\right\}\cos\frac{n}{2}\theta \end{Bmatrix} \tag{4.4}$$

where r and θ are the polar coordinates defined at the current crack-tip, κ is $(3-\nu_{\mathrm{d}})/(1+\nu_{\mathrm{d}})$ for plane stress where ν_{d} is the Poisson's ratio and μ is the shear modulus. In the above expressions, the coefficients $\left(K_{\mathrm{I}}^{d}\right)_n$ and $\left(K_{\mathrm{II}}^{d}\right)_n$ of the dominant terms $(n=1)$ are the so-called mode-I and mode-II dynamic SIFs, respectively. The above in-plane displacement fields implicitly assume that the inertia effects are accounted

for by the coefficients while maintaining the functional form of the quasi-static counterpart. However, when the crack initiates, the in-plane displacement components v and u for a steadily growing crack are given by [115],

$$\begin{Bmatrix} u(r,\theta) \\ v(r,\theta) \end{Bmatrix} = \sum_{n=1}^{\infty} \frac{\left(K_{\mathrm{I}}^{d}\right)_n B_{\mathrm{I}}(V)}{2\mu} \sqrt{\frac{2}{\pi}} (n+1) \begin{Bmatrix} r_1^{n/2} \cos\frac{n}{2}\theta_1 - h(n) r_2^{n/2} \cos\frac{n}{2}\theta_2 \\ -\beta_1 r_1^{n/2} \sin\frac{n}{2}\theta_1 + \frac{h(n)}{\beta_2} r_2^{n/2} \sin\frac{n}{2}\theta_2 \end{Bmatrix}$$
$$+ \sum_{n=1}^{\infty} \frac{\left(K_{\mathrm{II}}^{d}\right)_n B_{\mathrm{II}}(V)}{2\mu} \sqrt{\frac{2}{\pi}} (n+1) \begin{Bmatrix} r_1^{n/2} \sin\frac{n}{2}\theta_1 - h(\bar{n}) r_2^{n/2} \sin\frac{n}{2}\theta_2 \\ \beta_1 r_1^{n/2} \cos\frac{n}{2}\theta_1 + \frac{h(\bar{n})}{\beta_2} r_2^{n/2} \cos\frac{n}{2}\theta_2 \end{Bmatrix} \tag{4.5}$$

where

$$r_m = \sqrt{x^2 + \beta_m^2 y^2}, \quad \theta_m = \tan^{-1}(\beta_m y / x), \ m = 1, 2, \quad \beta_1 = \sqrt{1 - (V/C_{\mathrm{L}})^2}, \quad \beta_2 = \sqrt{1 - (V/C_{\mathrm{S}})^2}$$

$$C_{\mathrm{L}} = \sqrt{\frac{(\kappa+1)\mu}{(\kappa-1)\rho}}, \quad C_{\mathrm{S}} = \sqrt{\frac{\mu}{\rho}}, \quad \kappa = \begin{cases} (3-\nu_{\mathrm{d}})/(1+\nu_{\mathrm{d}}): \text{ plane stress} \\ (3-4\nu_{\mathrm{d}}): \text{ plane strain} \end{cases}$$

$$h(n) = \begin{cases} 2\beta_1\beta_2/(1+\beta_2^2): \ n \text{ odd} \\ (1+\beta_2^2)/2: \ n \text{ even} \end{cases} \quad \text{and} \quad h(\bar{n}) = h(n+1)$$

$$B_{\mathrm{I}}(V) = \frac{(1+\beta_2^2)}{D}, \quad B_{\mathrm{II}}(V) = \frac{2\beta_2}{D}, \quad D = 4\beta_1\beta_2 - (1+\beta_2^2)^2.$$

In the above equations, (x, y) and (r, θ) are the instantaneous Cartesian and polar coordinates, respectively, aligned at the current crack-tip, V is the crack-tip velocity, C_{L} and C_{S} are homogenized longitudinal and shear wave speeds of the material, ρ is the mass density, μ and ν_{d} are the shear modulus and the Poisson's ratio, respectively. Again, the coefficients $\left(K_{\mathrm{I}}^{d}\right)_n$ and $\left(K_{\mathrm{II}}^{d}\right)_n$ of the dominant terms $(n=1)$ are the mode-I and mode-II dynamic SIFs respectively. Further, the Eq. (4.5) can be reduced to the form of a dynamically loaded stationary crack in the limit the crack velocity $V \to 0$.

In order to extract SIF history, the crack-opening and crack-sliding displacement fields were digitized by identifying the current crack-tip location in the image. The displacement data used in the analysis was collected in the vicinity of the crack-tip and limited to the region $0.4 < r/B < 1.5$ and ($-150^{\circ} \leq \theta \leq -90^{\circ}$ and $90^{\circ} \leq \theta \leq 150^{\circ}$) to minimize 3D effects on least-squares analysis [116]. At each data point, v and u displacement values as well as the location of these points were stored. The digitized data were used in Eqs. (4.4) and (4.5) along with an over-deterministic least-squares analysis scheme to estimate the SIFs. This process was carried out for all image pairs and the SIF histories were generated.

4.3 Results

4.3.1 Experimental repeatability

In order to verify repeatability in fracture behaviors and measurements, multiple experiments were performed for both nano- and micro-filler composites under quasi-static and dynamic loading conditions. Figures 4.4(a) and (b) show results for multiple quasi-statically fractured specimens. An excellent repeatability in load-deflection responses of four specimens can be seen at 10% volume fraction for each category. At this volume fraction, the nanocomposite specimens fractured at a peak load of 1158±45 N, whereas the specimens with micro-filler failed at 687±12 N. A noticeable departure from linearity of global load-deflection response close to fracture is evident in Fig. 4.4(a) whereas the plots remain linear in Fig. 4.4(b) up to fracture.

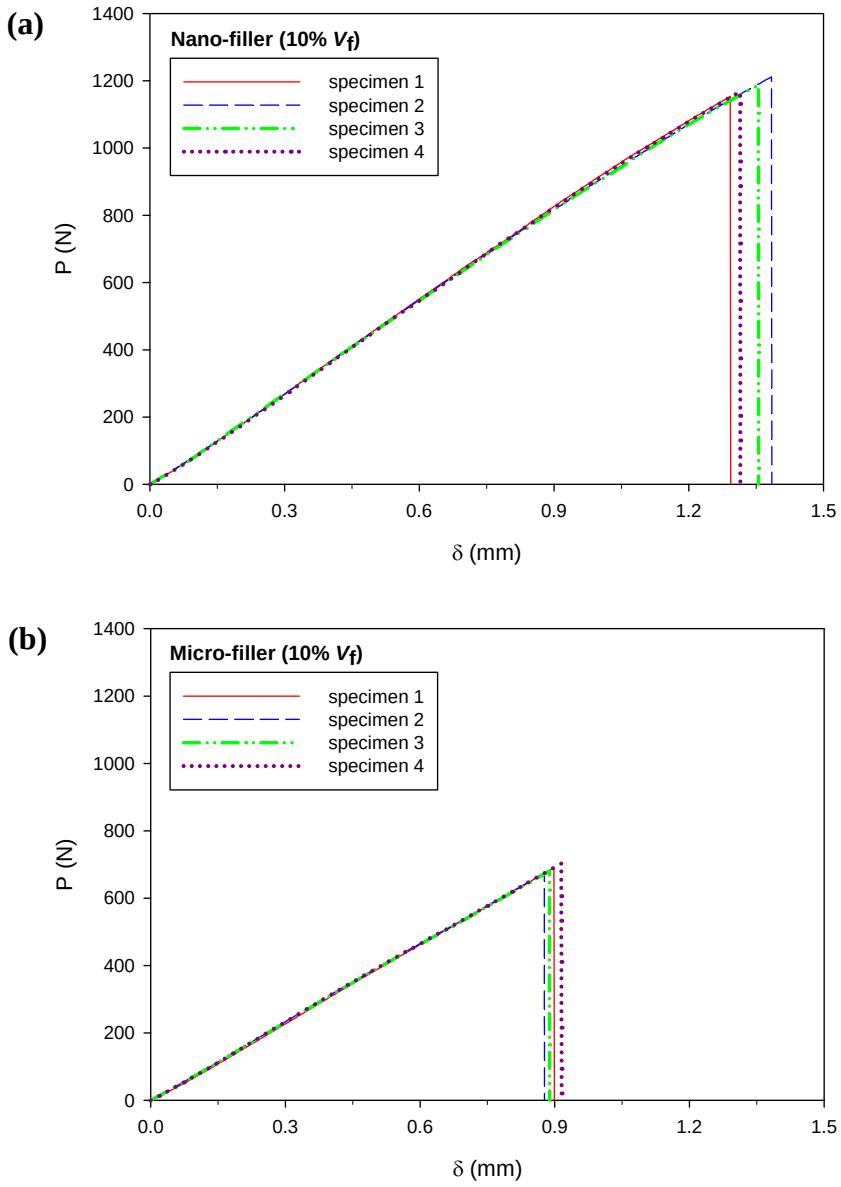

Fig. 4.4: Experimental repeatability in quasi-static fracture tests: **(a)** Load-deflection response of 10% V_f nano-filler modified epoxy, **(b)** Load-deflection response of 10% V_f micro-filler modified epoxy.

Figures 4.5 and 4.6 show repeatability in dynamic fracture behavior in terms of mode-I SIF and load histories at 10% V_f for nano- as well as micro-filler composites. Figs. 4.5(a) and (b) depict repeatability in mode-I SIF, K_I^d histories in three specimens for each type of filler.

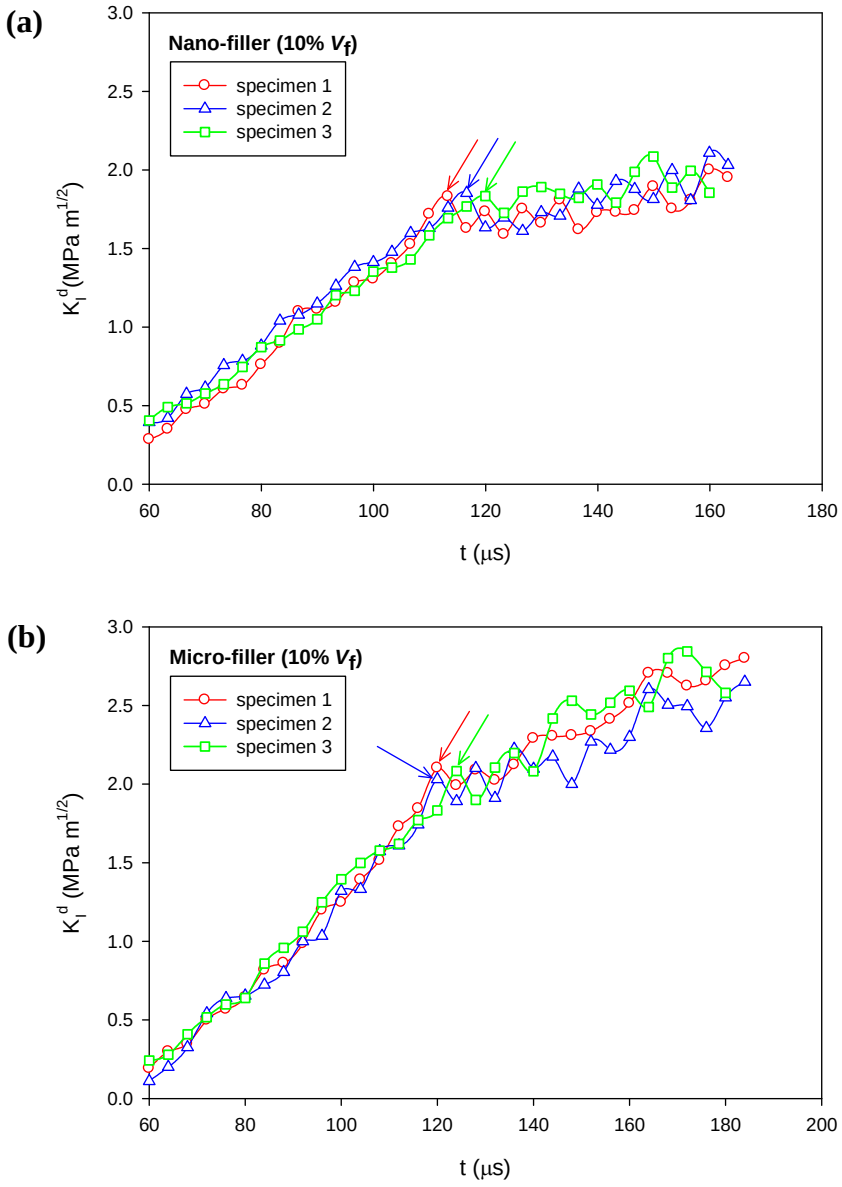

Fig. 4.5: Experimental repeatability in dynamic fracture tests: **(a)** Mode-I dynamic SIF histories of 10% V_f nano-filler modified epoxy, **(b)** Mode-I dynamic SIF histories of 10% V_f micro-filler modified epoxy. The crack-initiation value is indicated by an arrow for each specimen. Note that post initiation K_I^d values are increasing more slowly in nano-filler case compared to micro-filler counterpart.

The K_I^d at crack initiation is indicated by an arrow for each specimen. For nano-filler specimens the crack initiation (after impact) time range is 113-120 μs whereas for micro-filler ones it is 120-124 μs. From the perspective of dynamic fracture experiments,

it is important to note that the K_I^d profiles show excellent repeatability of the entire fracture event for each type of filler. Again, for both types of composites, the SIF increases monotonically up to crack initiation and pre-initiation SIF histories essentially coincide for all three specimens. For nano-filler specimens, the value of K_I^d at initiation is ~1.85 MPa $m^{1/2}$ whereas it is ~2.13 MPa $m^{1/2}$ for micro-filler specimens. Following crack initiation, a noticeable drop in K_I^d can be seen in each specimen for both filler categories due to unloading near the initial notch tip. This is followed by a gradual increase in K_I^d until the fracture is complete for both filler types. The rise in post initiation K_I^d values is smaller in the nano-particle filled epoxy (dK_I^d/dt ~5.3x10^3 MPa $m^{1/2}$/s) when compared to the micron-size filler counterpart (dK_I^d/dt ~13x10^3 MPa $m^{1/2}$/s).

The tup and anvil load histories were recorded for each experiment and are shown in Figs. 4.6(a) and (b) for the same three specimens in each filler category. In these plots, again an excellent repeatability in tup load as well as in left and right support reaction histories is quite evident for all three specimens. In these experiments, the complete fracture of the specimen occurred within ~200 μs after impact. Thus, only the dominant first peak of the tup load history is significant. Note that the peak impact force (compressive) recorded by the tup in case of micro-filler specimens is slightly higher than the nano-filler counterparts, suggesting the role of particle size. It can also be seen that supports register the reaction force only after ~300 μs by which time the crack had already traversed the specimen width. This shows that reaction forces from support anvils do not contribute to the crack initiation and crack growth in the specimens, suggesting

that a free-free cracked beam should suffice analytical or computational modeling of these experiments.

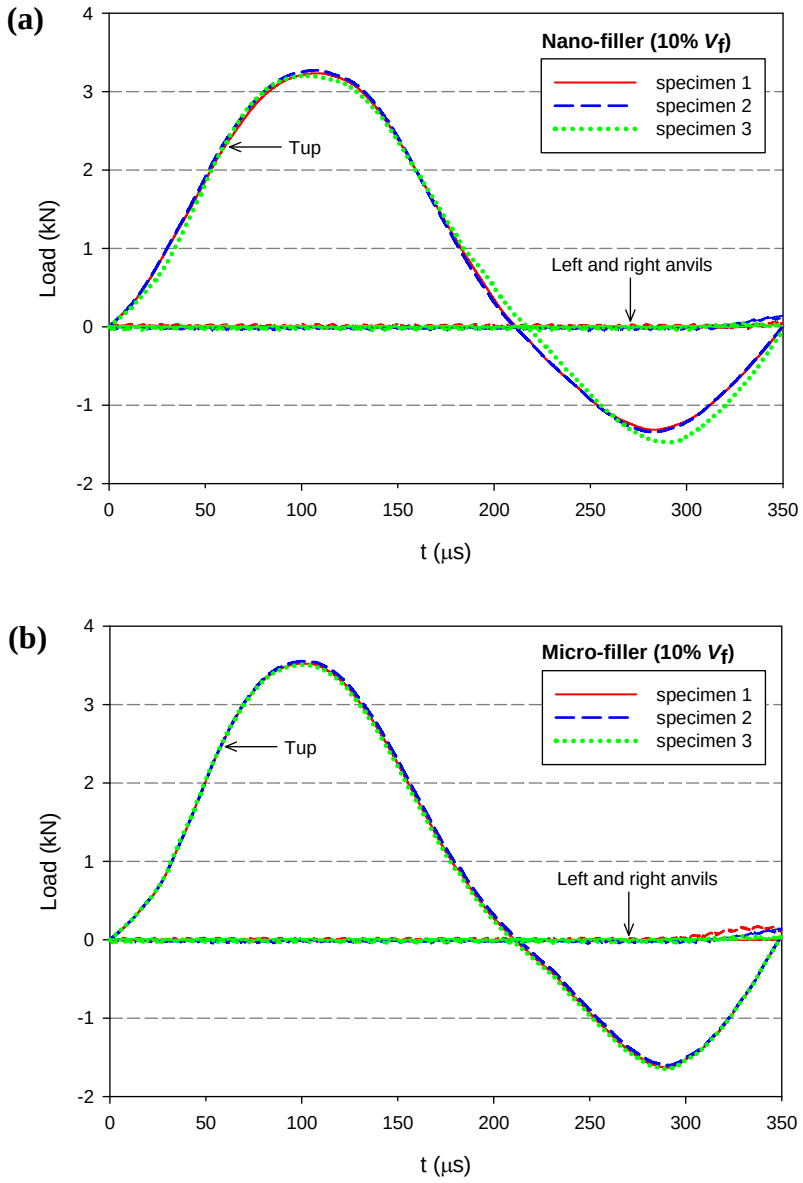

Fig. 4.6: Experimental repeatability of load histories for dynamic fracture tests: **(a)** 10% V_f nano-particle filled epoxy, **(b)** 10% V_f micro-particle filled epoxy. (Note that the tup loads are plotted as positive values for compression.)

4.3.2 Quasi-static fracture behavior

The quasi-static fracture test results are summarized in Figs. 4.7 and 4.8. The load versus deflection responses at different volume fractions are plotted in Figs. 4.7(a) and (b) for nano- and micro-filler epoxies, respectively.

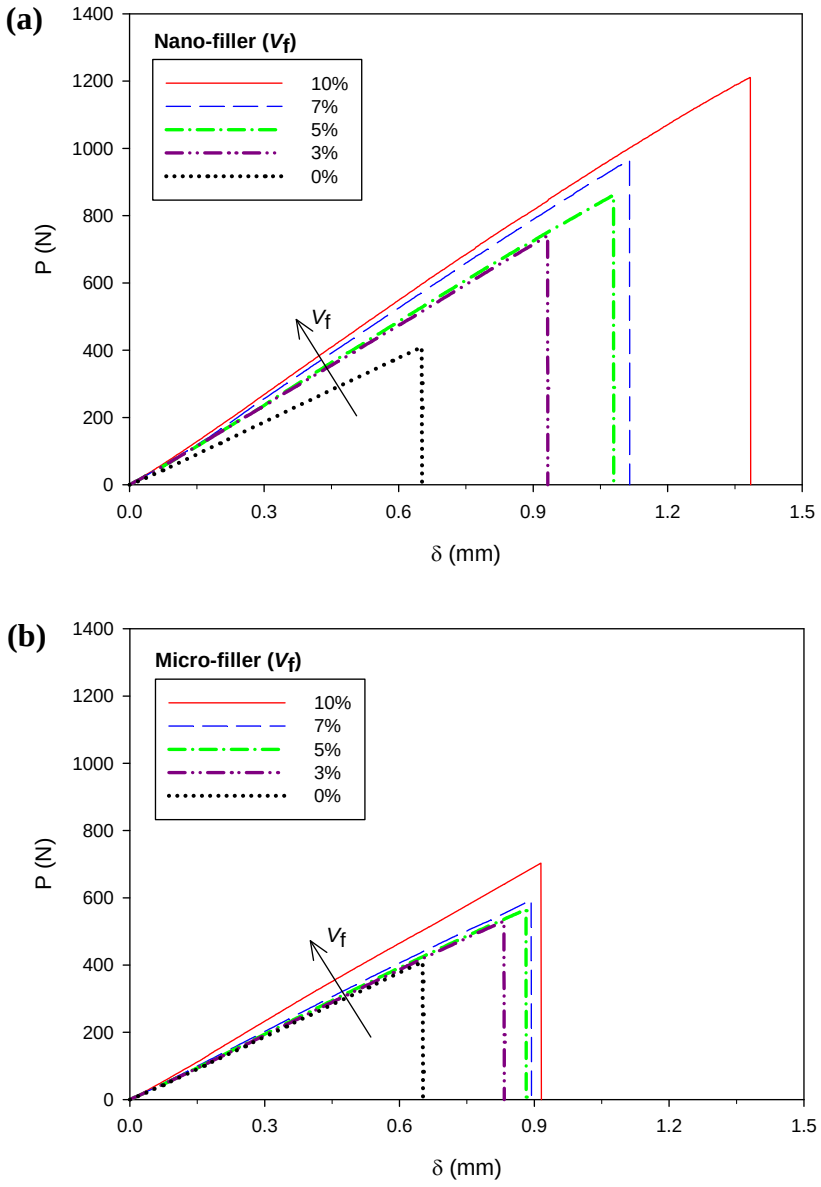

Fig. 4.7: Load-deflection response for quasi-static fracture tests at different volume fractions: **(a)** Nano-filler modified epoxies, **(b)** Micro-filler modified epoxies.

It can be seen that for both filler loadings, the load rises linearly (except 7% and 10% V_f nanocomposites showing noticeable nonlinearity prior to fracture) up to a point at which abrupt crack growth ensues causing a sudden drop in the load. It can also be observed that the peak loads and the corresponding load-point deflections show increasing trends, suggesting that the work needed for crack initiation (area under the load-deflection curve), increases with filler volume fraction. Further, note that in both types of fillers the stiffness of the filled-composites generally increase with filler volume fraction. Moreover, for any given volume fraction the nano-filler specimens sustained higher loads as well as deflections up to failure when compared to micro-filler counterparts.

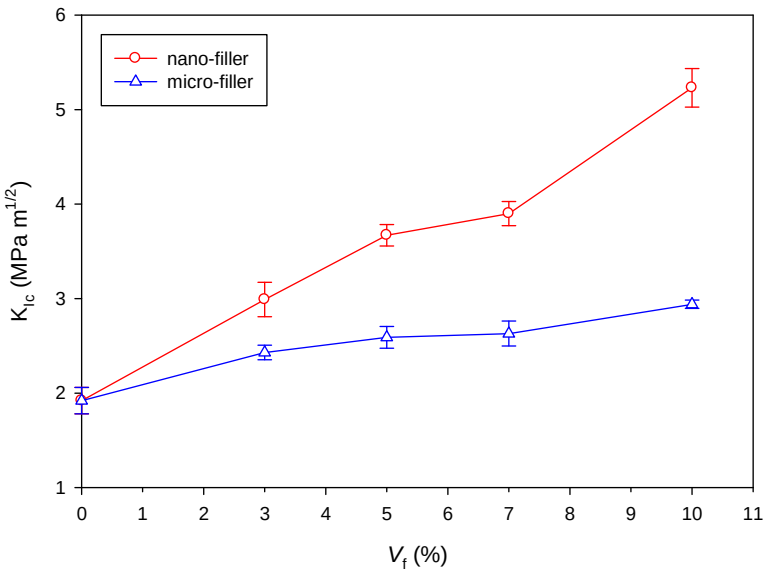

Fig. 4.8: Variation of quasi-static fracture toughness (K_{Ic}) with filler volume fraction (V_f) for nano- and micro-filler modified epoxies.

The quasi-static fracture toughness, K_{Ic}, measured at the onset of crack growth in each case and the variation of K_{Ic} as a function of volume fraction of nano- and micro-fillers is plotted in Fig. 4.8. Each data point represents an average of four measured

values of K_{Ic} and the error bars indicate their standard deviations. For both types of filler loadings, the fracture toughness increases relative to neat epoxy as V_f increases. The observed trends in K_{Ic} for both types of filler loadings are in agreement with previous works on nanosilica filled [12-17] and micro-particle filled [5, 31-33] epoxies. Figure 4.8 also shows that the fracture toughness of nano-particle filled specimens increases dramatically with volume fraction relative to the micro-filler counterparts. Furthermore, the enhancement in K_{Ic} is significantly higher than the micro-filler cases for any given volume fraction. For example, a ~42% and ~78% enhancement in K_{Ic} values at 5% and 10% V_f, respectively, for nano-sized filler relative to micro-filler case is evident.

4.3.3 Dynamic fracture response

4.3.3.1 Surface deformation histories

A sequential arrangement of a few selected speckle images of 30 x 30 mm^2 region-of-interest where surface deformations were monitored optically during the dynamic fracture of specimens with 10 % V_f for nano- and micro-filler cases is shown in Fig. 4.9. The first and second rows of speckle images are for nano- and micro-filler specimens, respectively. The specimens were subjected to symmetric impact loading and the initial notch as well as the sharp growing crack is visible. The time instant (t) after impact at which the images were recorded is also shown and the current crack-tip is indicated by an arrow. In order to compare the effect of particle size-scale on the extent of crack growth, the speckle images in each column for nano- and micro-fillers are shown here for nearly same time instants. It can be seen that at approximately same time instant, crack propagation in the nano-filler specimen is more than the micro-filler counterpart. Further, the crack extension is about twice in the former compared to the latter.

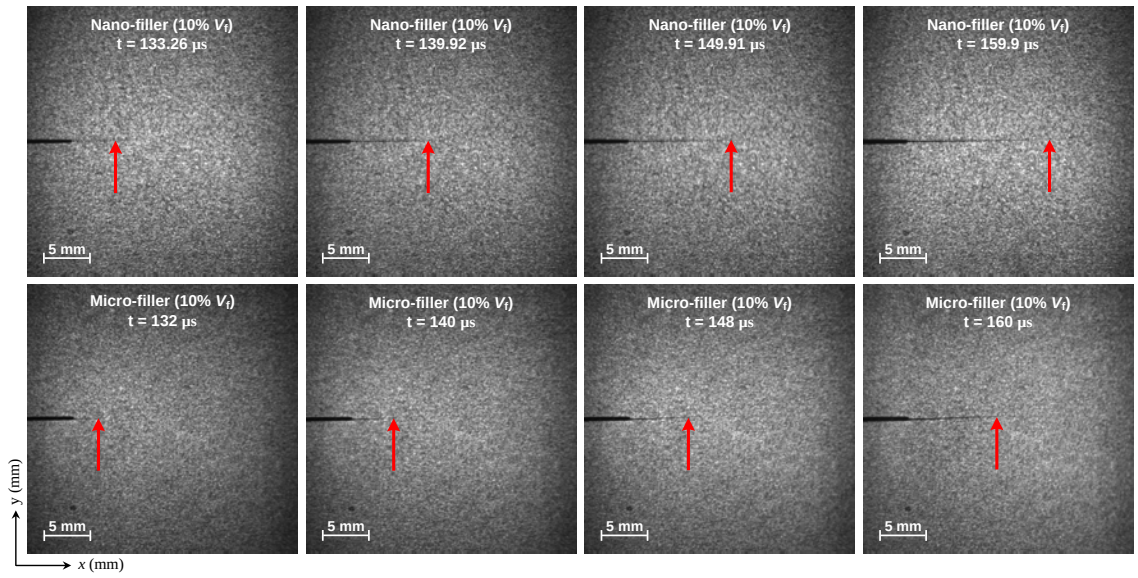

Fig. 4.9: Few selected speckle images of nano- and micro-filler modified epoxy specimens with 10% V_f at approximately same time instants. Each image represents 30 x 30 mm^2 region-of-interest recorded by the high-speed digital camera at framing rates of 300,000 and 250,000 frames per second for nano- and micro-filler modified epoxies, respectively. The moving crack-tip is indicated by an arrow and the dark line is the initial crack in the photographed images.

As described earlier, a sub-image size of 26 x 26 pixels (1 pixel = 30 μm on the specimen) was chosen for image correlation analysis and displacements fields were obtained as 37 x 37 data points for each pair. Subsequently, full-field in-plane displacement contours with 5 μm per contour interval were generated. A few representative speckle images with corresponding crack-opening (v-field or displacement along the y-axis) and crack-sliding (u-field or displacement along the x-axis) displacement contours for nano-filler (10% V_f), micro-filler (10% V_f) and neat epoxy specimens are presented in Fig. 4.10. Here, at a particular time instant, $t \sim 160$ μs, crack extension in nano-filler specimen is larger than neat epoxy and micro-filler specimens, whereas the slowest crack growth is evident in the micro-filler specimen. The v- and u-fields show that contour lines and magnitude of displacement (in μm shown by color-bars) are nearly symmetric relative to the crack path suggesting dominant mode-I

fracture. The contour lines in the *u*-field show a set of isolines emerging from right-hand side of the contour plots due to impact loading on the edge of the specimen facing the initial crack-tip.

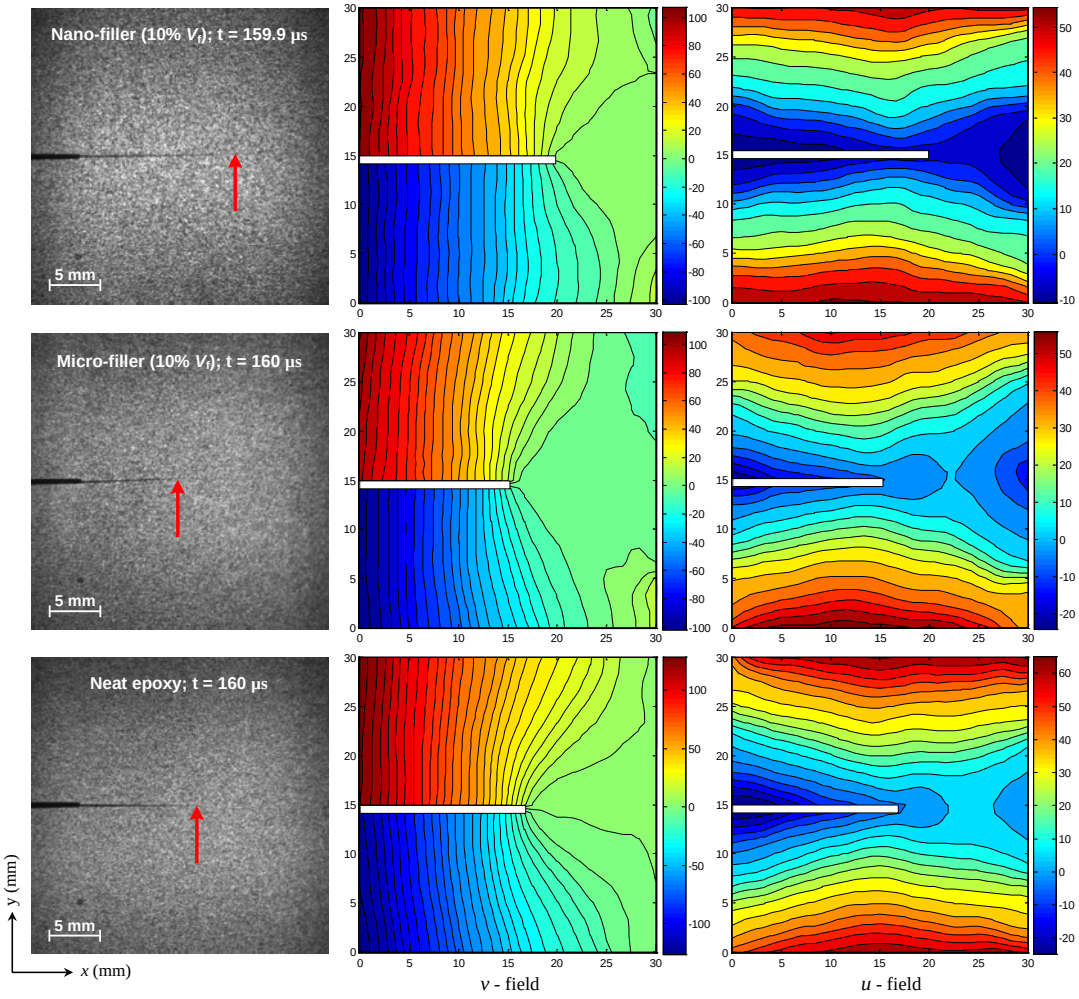

Fig. 4.10: Representative speckle images of 30 x 30 mm^2 region-of-interest at time instant, t ~ 160 μs with corresponding crack-opening (v-field) and crack-sliding (u-field) displacement contours. Contour interval is 5 μm. Color-bars represent displacement in μm. The arrows indicate the current crack-tip position in the speckle images.

4.3.4 Crack tip velocities (V) histories

The crack tip velocity histories were estimated from the smoothed values of instantaneous crack extension data for nano- and micro-filler cases for different volume

fractions and are shown in Figs. 4.11(a) and (b), respectively. It can be seen that following initiation the crack accelerated to a maximum value followed by a modest oscillatory behavior due to the transient nature of impact induced fracture.

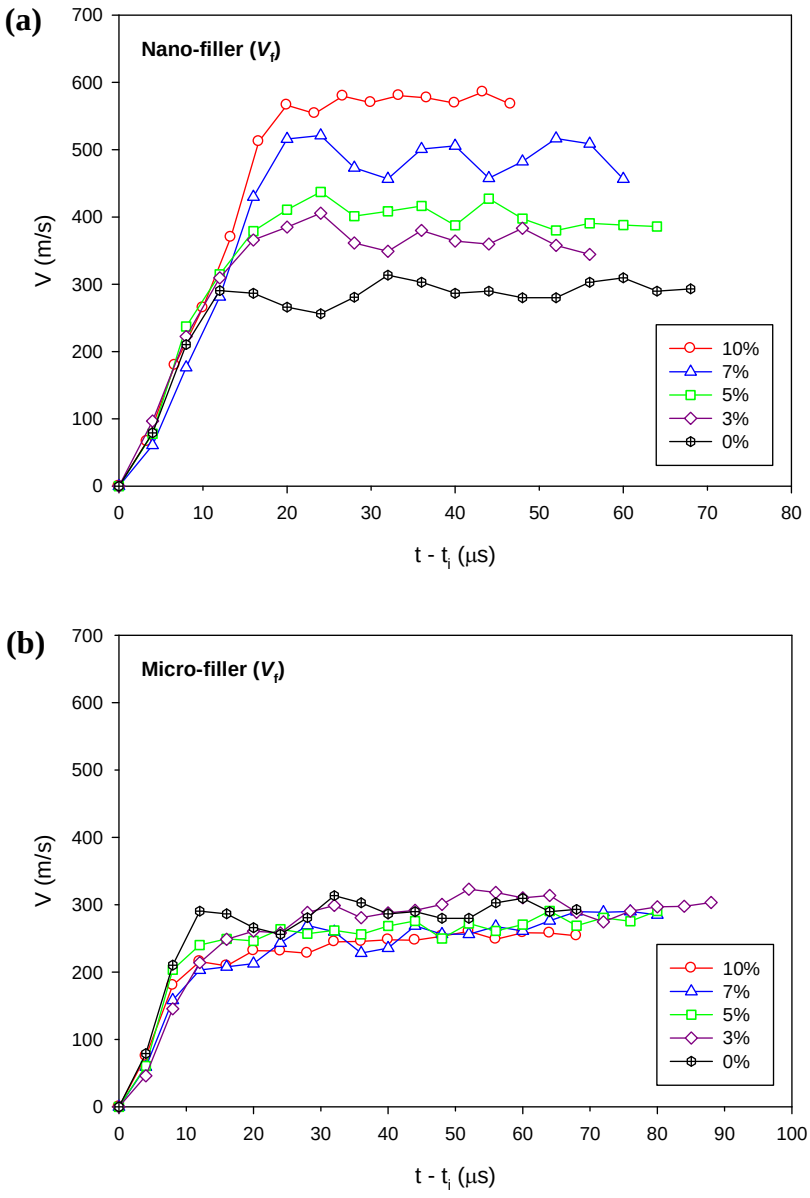

Fig. 4.11: Crack tip velocity histories at different volume fractions: **(a)** Nano-filler modified epoxies, **(b)** Micro-filler modified epoxies.

For nano-particle filled epoxies, as shown in Fig. 4.11 (a), the crack tip velocity shows increasing steady state values as the particle volume fraction increases and the

crack propagates at an average velocity of approximately 300, 370, 400, 490, 570 m/s for 0% (neat epoxy), 3%, 5%, 7%, 10% V_f cases, respectively. On the other hand, the velocity trends are the opposite in micro-particle filled epoxies as shown in Fig. 4.11 (b). It can be noticed that the average crack velocity decreases slightly as the volume fraction of micron-size particles increases.

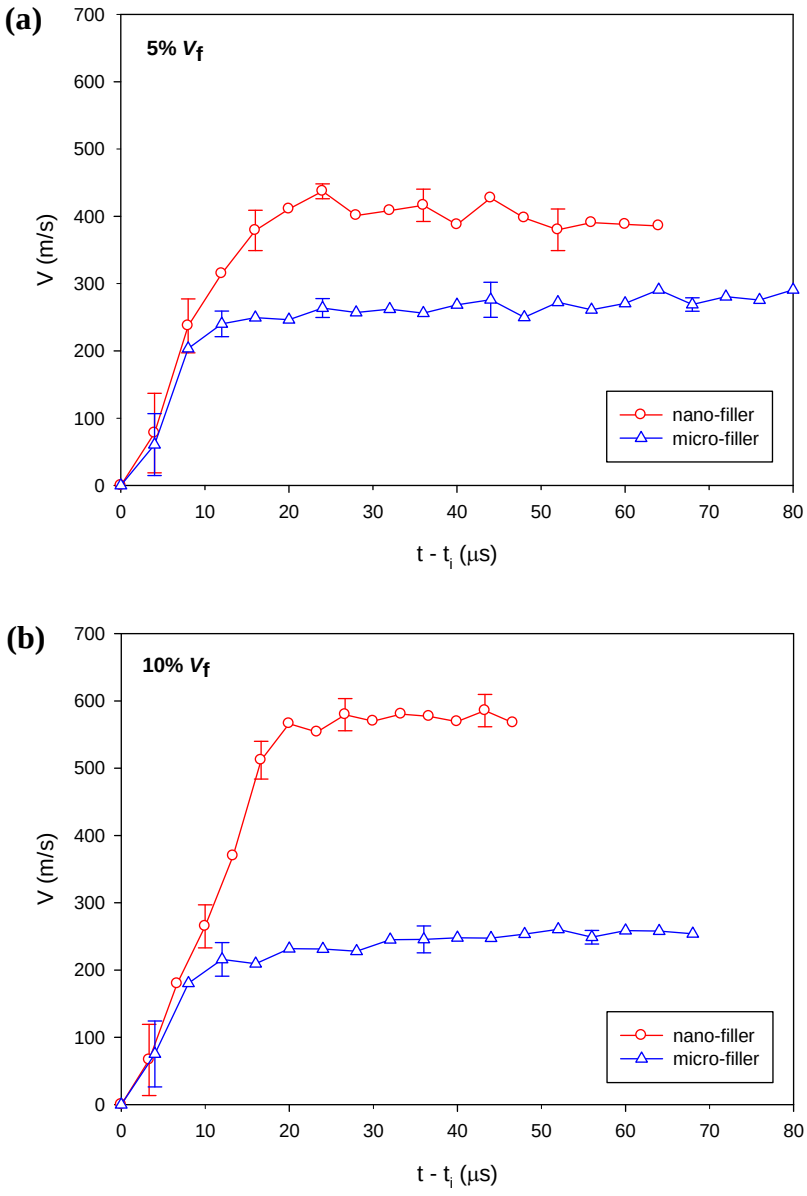

Fig. 4.12: Role of nano- *vs.* micro-fillers on crack-tip velocity histories: **(a)** 5% V_f, **(b)** 10% V_f.

The effect of particle size-scale on the crack-tip velocity can be consistently compared by plotting crack velocity histories for each volume fraction separately and two representative cases for 5% and 10% V_f are shown in Figs. 4.12(a) and (b), respectively. The average crack-tip velocities in the nanocomposites are approximately 60%, 160% higher than that observed in the micro-filler cases for 5%, 10% volume fractions, respectively.

4.3.5 Dynamic mode-I (K_I^d) SIF histories

The optically measured mode-I SIF histories for specimens with nano- and micro-fillers at various volume fractions are shown in Figs. 4.13(a) and (b), respectively. In these plots, the crack-initiation time is denoted by $t - t_i = 0$ μs so that the negative and positive values correspond to the pre-initiation and post-initiation periods, respectively. The pre-initiation data for each specimen in both types of fillers show that the mode-I dynamic SIF, K_I^d, increases gradually until it reaches a threshold value for crack-initiation. Furthermore, the K_I^d values in the pre-initiation regime show increasing trends as the particle volume fraction increases in both nano- and micro-filler specimens. Following initiation, a distinct drop in K_I^d is evident in all specimens (nano- and micro-filler) and it increases subsequently in a nearly steady-state fashion.

For clarity, consistency, and to avoid data clutter, the mode-I SIF behavior for nano- and micro-fillers cases can be systematically compared by plotting SIF histories for two representative cases of 5% and 10% V_f, as shown in Figs. 4.14(a) and (b). These plots clearly reflect the effect of particle size (nano- *vs.* micro-) on the dynamic fracture toughness of particulate composites at crack-initiation as well as in the pre- and post-initiation regimes. For each volume fraction, it can be seen that in the pre-initiation

period, the K_I^d values are in agreement within the measurement accuracy. However, unlike quasi-static counterparts the dynamic crack-initiation toughness values for nanocomposites are lower than the micro-filler counterparts.

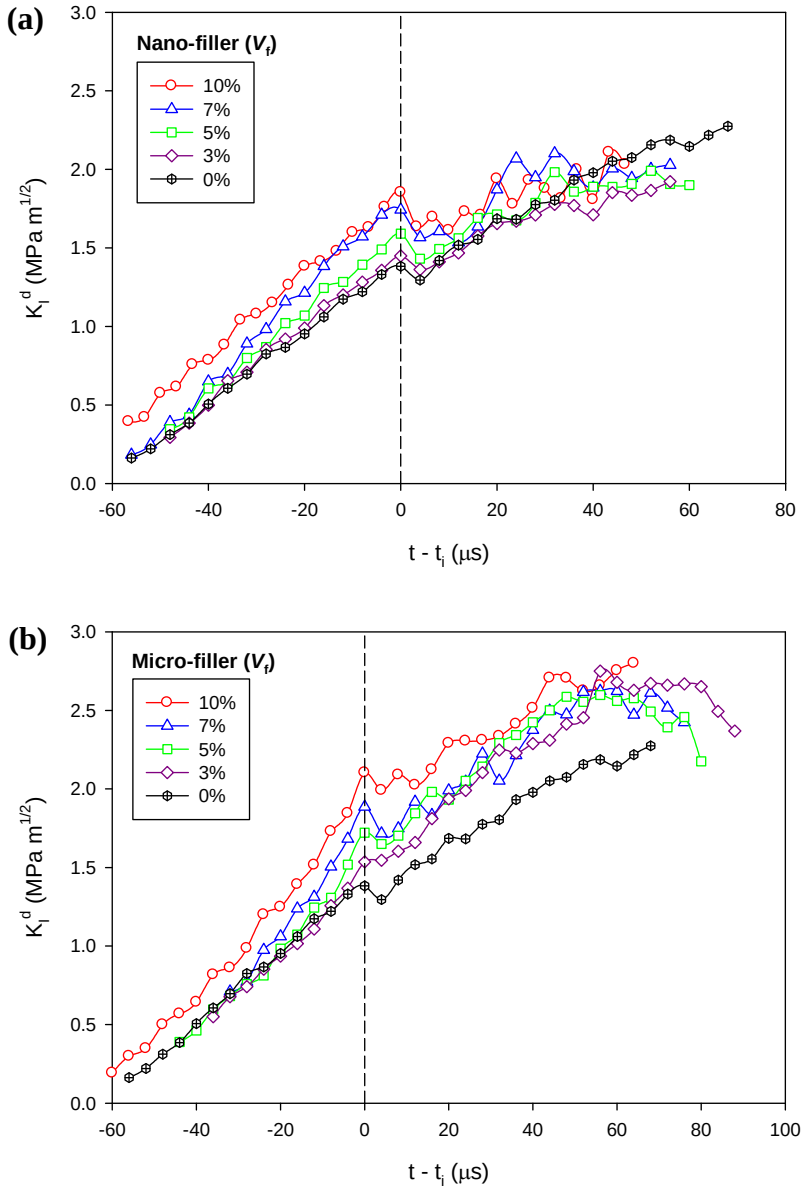

Fig. 4.13: Mode-I dynamic SIF histories at different volume fractions: **(a)** Nano-particle filled epoxies, **(b)** Micro- particle filled epoxies. (Time base is shifted such that $t - t_i = 0$ corresponds to crack-initiation as shown by the vertical dashed line.)

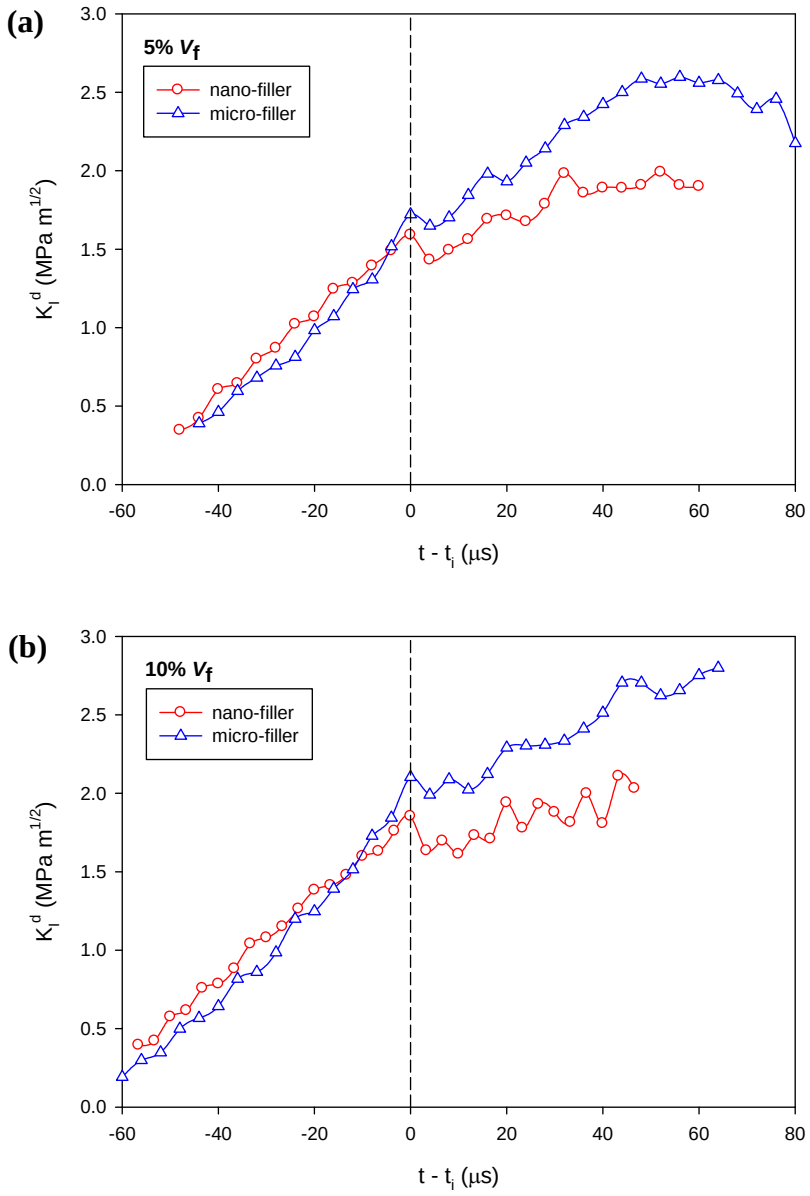

Fig. 4.14: Role of nano- *vs.* micro-fillers on mode-I dynamic SIF histories: **(a)** 5% V_f, **(b)** 10% V_f.

Also note that the post-initiation K_I^d values for nanocomposites are also lower than the micro-filler cases for the volume fractions shown. Hence, it is noteworthy that, *under identical impact loading conditions, the micro-filler particulate composites outperform nano-filler ones at crack-initiation as well as in the post-initiation regimes.* Further note that these observed trends of K_I^d for nano- and micro-fillers are consistent with crack-tip

velocity histories shown in Figs. 4.12(a) and (b), as it can be seen that the apparent macro scale crack growth is the slowest in micro-filler cases suggesting higher crack growth resistance, resulting in higher apparent K_I^d values.

The quasi-static crack-initiation toughness (K_{Ic}) and dynamic crack-initiation toughness (K_{Ii}^d) values for nano- and micro-filler epoxies are tabulated in Table 4.3. It can be seen that the fracture behavior for both types of fillers is loading rate sensitive. For quasi-static loading, nano-filler epoxies show higher crack-initiation toughness than the micro-filler ones and the opposite is seen under dynamic loading conditions.

V_f (%)	Quasi-static crack-initiation toughness K_{Ic} (MPa m$^{1/2}$)		Dynamic crack-initiation toughness K_{Ii}^d (MPa m$^{1/2}$)	
	Nano-filler	Micro-filler	Nano-filler	Micro-filler
0	1.92	1.92	1.38	1.38
3	2.99	2.43	1.45	1.54
5	3.67	2.59	1.59	1.72
7	3.92	2.63	1.74	1.89
10	5.22	2.95	1.85	2.13

Table 4.3: Loading rate effects on crack-initiation toughness of nano- and micro-filler reinforced epoxies

4.3.6 K_I^d-V relationship

The existence of K_I^d-V relationship as a dynamic material characteristic has been a subject of interest [117-122] in the past few decades. Previous studies discuss K_I^d-V characteristics of monolithic materials (neat polymers and steels). In the recent years, the existence of K_I^d-V relations for nanocomposites has been shown in the works of Shukla

et al. [27] and Evora et al. [29]. In the present work, the variation of dynamic mode-I SIF with crack-tip velocity for nano- and micro-fillers at 5% and 10% volume fraction as well as for neat epoxy is presented in Figs. 4.15(a) and (b).

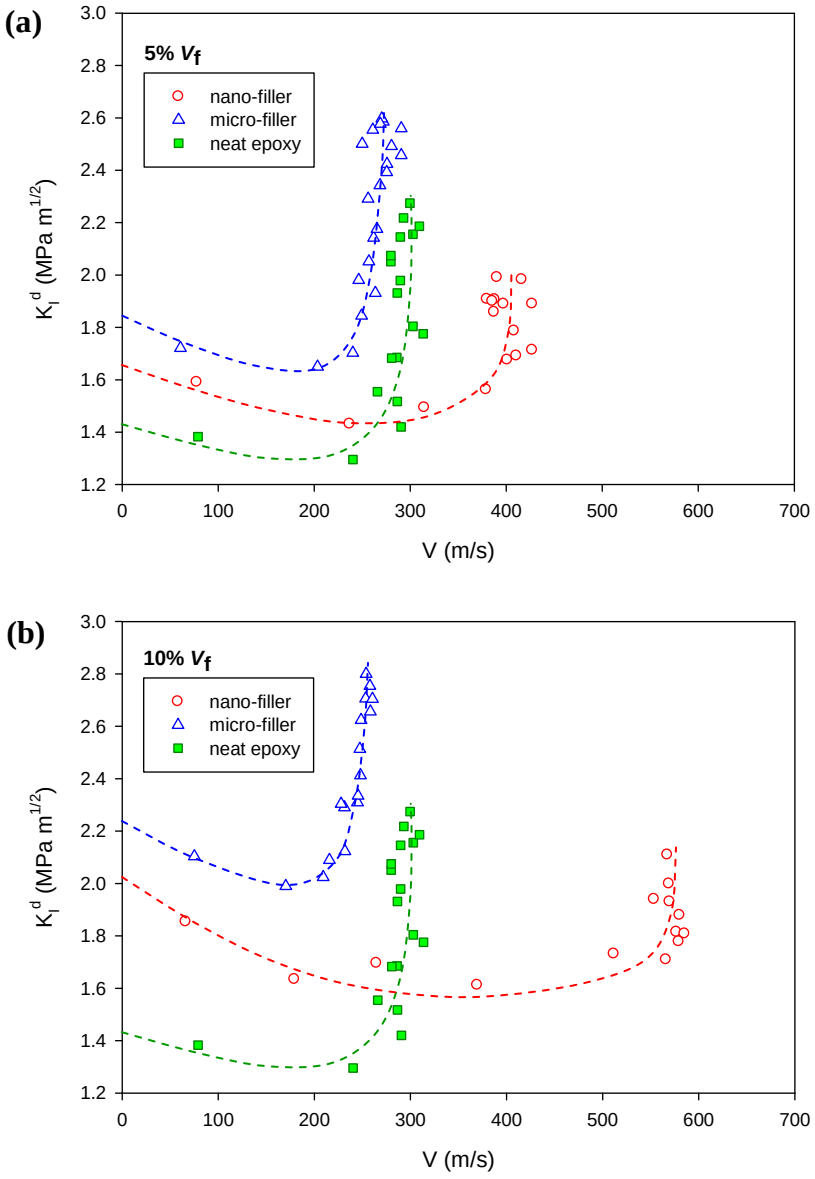

Fig. 4.15: K_I^d-V relationships for particle filled epoxies: **(a)** 5% V_f nano- and micro-filler, **(b)** 10% V_f nano-and micro-filler.

These plots show data points after crack-initiation for all experiments performed under identical impact loading conditions. In these plots, at a given volume fraction, both

types of fillers exhibit a K_I^d-V variation similar to the previously seen ones in monolithic materials. All the specimens indicate a characteristic near-horizontal tail and near-vertical stem. For each case, in the horizontal portion, a small drop in K_I^d value can be seen. The K_I^d-V profiles also suggest that for each volume fraction, the micro-fillesr produce significantly higher crack growth resistance when compared to the ones due to nano-fillers and neat epoxy. The nano-filler specimens show lower K_I^d over a wider range of velocities compared to the micro-filler counterparts and neat epoxy. The terminal velocities in the case of nano-filler specimens are ~400 m/s and ~570 m/s for 5% and 10% volume fractions, respectively, whereas in the case of micro-filler counterparts it is ~250 m/s and ~220 m/s at the same volume fractions, respectively. The K_I^d-V response of neat epoxy in the vertical stem with a terminal velocity of ~300 m/s is, however, bounded by the ones with nano- and micro-filler epoxies. These observations indicate that for the same volume fraction of the filler, nanocomposites fracture at higher crack velocities than the micro-filler and neat epoxy.

4.3.7 Fractography

It has been well recognized that fracture surface topography reveals inherent details of deformation and the associated energy dissipation mechanisms that govern the process of fracture [123-126]. Accordingly, the fracture surfaces were examined both qualitatively and quantitatively. Microscopy was performed for qualitative examination of fracture surfaces of quasi-statically and dynamically failed specimens. Note that the surface features of quasi-statically fractured specimens were evident even to the naked-eye; hence, optical microscope was found suitable for visualizing macro scale surface

features. However, finer details were also captured using a scanning electron microscope (SEM) in these cases. For dynamically fractured surfaces, SEM was used since visual inspection was insufficient as the fracture surface features were mainly confined to a very small spatial domain. To further understand fracture surface morphology, roughness measurements were also performed using a Dektak-150 profilometer with a 2 μm stylus for dynamically fractured specimens. The fracture surface profiles were scanned in a stable crack growth zone as shown in the inset of Fig. 4.18 and will be discussed later in this section. Note that the same region was chosen for SEM analysis of dynamically failed samples.

The optical and SEM micrographs of quasi-statically fractured surfaces of nano- and micro-particle filled epoxies are shown in Fig. 4.16. The top and bottom row represents micrographs of nano- and micro-filler cases, respectively, for 5% and 10% V_f. The arrow in each optical image indicates initial crack front as well as the direction of crack growth. These optical micrographs can be viewed as a global representation of surface features as the images were captured at low magnification in order to cover maximum region of fractured surfaces. The effect of particle size-scale can be clearly seen on the surface roughness. The optical images of nanocomposites show very rough, highly textured/torn surfaces containing a large number of macro as well as microcracks with deep valleys and furrows with steep ridges. These features markedly amplify with 10% V_f of nano-filler loading. However, similar are absent in optical images of micro-filler counterparts indicating lower quasi-static fracture toughness relative to nanocomposites. Interestingly, three distinct zones-‘mirror’, ‘mist’ and ‘hackle’-are also quite evident in optical micrographs of nanocomposite specimens.

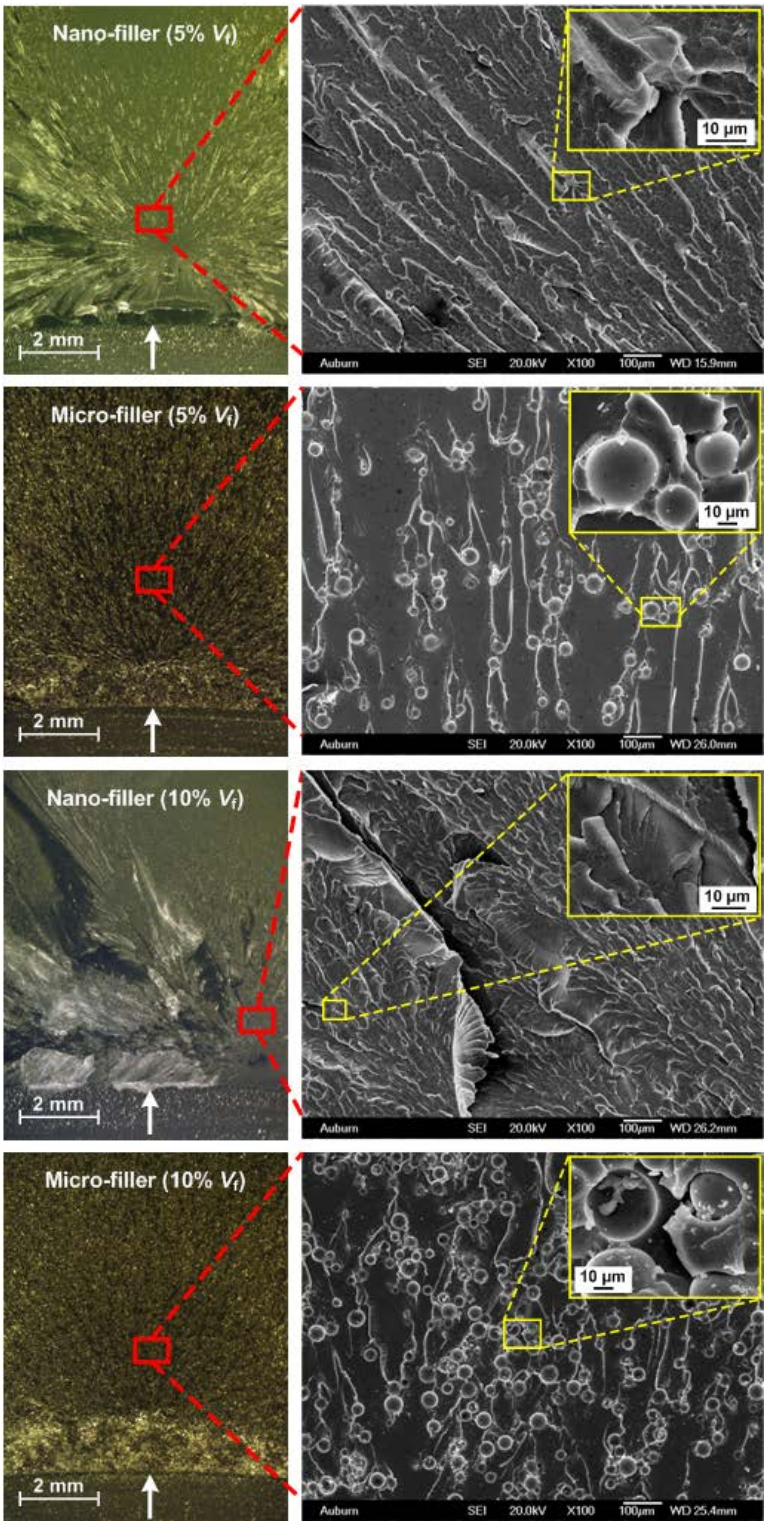

Fig. 4.16: Optical and SEM micrographs of quasi-static fractured surfaces of nano- and micro-filler modified epoxies at 5% and 10% volume fractions (V_f). The arrow in optical images indicates the initial crack-front as well as the direction of crack growth. The 'mirror', 'mist' and 'hackle' zones are clearly visible in optical images of nanocomposites.

The mirror zone can be clearly identified as a flat and smooth region appearing in the lower central portion of 5% nano-filler case close to the initial crack front, whereas it is at the lower right side of 10% nano-filler loading. In each case, surrounding the mirror zone is the mist region appearing with a slight change in the surface texture. The outwardly expanding roughness markings surrounding the mirror and mist zones can be recognized as hackle regions which are generally associated with the violent stage of fracture in which tremendous amount of fracture energy is dissipated through both plastic deformation and by the generation of additional fracture surfaces. However, these features appear to be less prominent in the case of micro-filler specimens. In Fig. 4.16, adjacent to each optical image, SEM micrographs of a select region (the boxed region) is shown. Note that the nanoparticles were hard to detect even at higher magnifications as the nanoparticle size and gold coating layer were of nearly the same order of magnitude. The SEM micrographs for nano-filler cases represent features of the 'mist' region. The micrograph for nano-filler with 5% V_f indicates a nonlinearly deformed (or torn) surface. Furthermore, the surface features resemble microscopic shear bands, seen as a narrow zone of intense slipping and tearing in the inset. The SEM micrograph for 10% nano-filler loading indicates the presence of parabolic markings in addition to all the features seen in the 5% filler case. These parabolic markings are possibly generated by sequential nucleation, growth and coalescence of microcracks (and/or slip bands) resulting in a rougher surface since microcracks or microcrack clusters form far ahead of the main crack and coalesce with it. A close-up view of the zone inside the parabolic marking can be seen in the inset showing microcracking and tearing. On the other hand, the SEM micrographs for 5% and 10% V_f micro-filler loadings show features such as tail lines and

particle-matrix debonding. The fracture surface features from optical and SEM micrographs clearly indicate that nanocomposites with extensive surface features compared to the corresponding micron-filler counterparts. Furthermore, nonlinear deformation and formation of microcracks around the crack-tip reduce the crack-tip stress concentration leading to shielding of the crack-tip. Therefore, the presence of a high concentration of macro and microcracks, slip bands, parabolic markings and high surface roughness suggest greater energy dissipation in the case of nano-filler modified epoxies, consistent with higher fracture toughness when compared to the ones with micro-filler *under quasi-static loading* conditions.

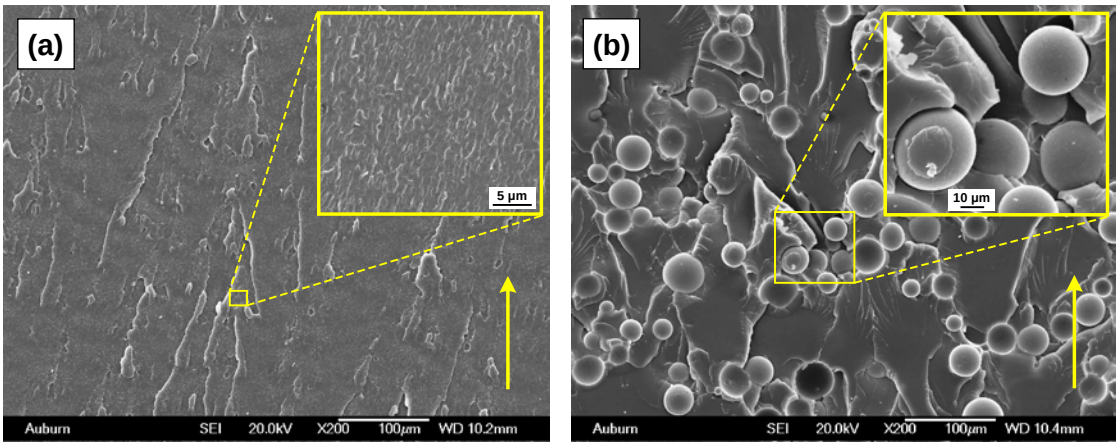

Fig. 4.17: SEM micrographs of dynamically fractured surfaces (*x*-*z* plane): **(a)** Nano-particle filled epoxy (10% V_f), **(b)** Micro-particle filled epoxy (10% V_f). The arrows indicate the direction of crack propagation.

Figures 4.17(a) and (b) show SEM micrographs of dynamically fractured surfaces (*x*-*z* plane) of nano- and micro-filler epoxies at 10% volume fraction, respectively. The arrow in these micrographs indicates crack propagation direction. The differences between the surface roughness features are rather striking. The surface roughness and ruggedness in Fig. 4.17(a) for nano-particle filled epoxy is lower than the micro-filler

one. Some features such as crack front bowing and pinning can be seen but are less prominent than the micro-filler modified epoxy. A higher magnification view of the fracture surface morphology can be seen in the inset. The micrograph in Fig. 4.17(b) reveals particle-matrix debonding (see close-up view in the inset) and particle pullout which results in crack front trapping. It can also be noticed that the crack bows between micron-size particles indicating crack pinning. As micro-cracks leave the pinned positions, tail lines as well as step patterns in the direction of crack propagation appear.

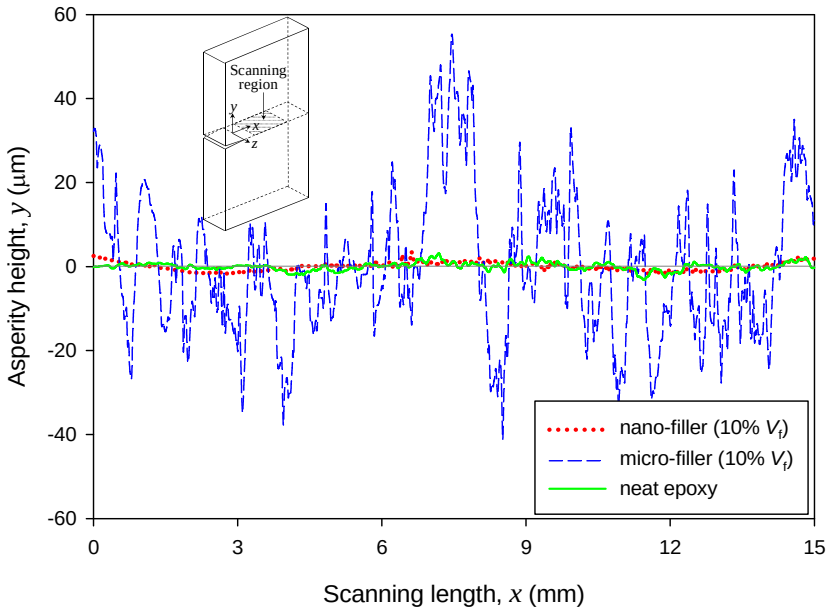

Fig. 4.18: Fracture surface profiles of dynamically fractured nano-particle filled epoxy (10% V_f), micro-particle filled epoxy (10% V_f) and neat epoxy specimens (inset shows schematic representation of crack growth and scanning region chosen for roughness measurements (*x*-*z* plane)).

Figure 4.18 shows fractured surface profiles for nano- and micro-filler cases (10% V_f) and neat epoxy with an inset depicting crack growth and scanned region (*x*-*z* plane). In Fig. 4.18, *x*- represents scanning length and *y*- denotes the asperity height. A scanning length of x = 15 mm was chosen in the stable crack growth region. The data was recorded

at 3-4 different scan lines at different *z*- locations on either side of the centerline within the regions of interest. The scanned data obtained from the surface profiler was processed to get average roughness, R_a, using,

$$R_a = \frac{1}{N}\sum_{1}^{N}\left|y(x)\right| = \frac{1}{L}\int_{0}^{L} y\,dx \tag{4.6}$$

where *N* is the total number of data points collected, *L* is the scan length.

The surface profile of micro-filler case shows longer wavelengths and larger amplitudes relative to the nano-filler counterpart. The nano-particle filled epoxy and neat epoxy, on the other hand, show the least surface amplitude. The fracture-induced surface roughness (after discounting the roughness due to filler particle foot prints or bumps; see Kitey and Tippur [4] was evaluated and found to be approximately 0.78 μm, 12.93 μm, 0.74 μm for nano-filler, micro-filler, and neat epoxy, respectively. Hence, it should be noted that for the same volume percentage of fillers embedded in epoxy, the fracture-induced roughness is higher in case of micro-filler under dynamic conditions. Thus, the qualitative as well as quantitative measurements show higher surface roughness for micro-particle filled epoxy than the nano-filler case suggesting higher energy dissipation and improved dynamic fracture performance in the former relative to the latter.

4.4 Discussion

The striking differences in quasi-static and dynamic fracture behaviors and parameters of nano- and micro-size silica filled epoxies are evident from the results presented above. As the macro scale fracture behaviors are related to events in the process zone [122] in the crack-tip vicinity, plausible explanations for these differences can be offered.

Under quasi-static loading conditions, a relatively smaller crack-tip process zone exists since all material points experience the applied load simultaneously. In case of nano-particle filled epoxy, the net interfacial surface area between the filler particle and the matrix is ~3.3×10^5 times that of the micron-size particles at the same volume fraction. Hence, for similar bond strength between the matrix and the filler, average interfacial stress is substantially lower in case of nanocomposites. The matrix reinforcement offered by the nano-particles, further mitigate crack initiation. On the other hand, the micro-fillers, due to the higher effective interfacial stress (due to lower interfacial area), would locally debond resulting in micro defects ahead of the crack-tip causing fracture at a lower far-field stress. Also, the average inter-particle spacing [127] $l = 2D\left(1-V_{\mathrm{f}}\right)/3V_{\mathrm{f}}$, for a given volume fraction V_{f} with mean particle diameter D, is three orders of magnitude lower for the nano-filler case compared to the micro-filler counterparts. This results in lower interstitial gap reducing stress concentration effects in nano-particle filled epoxy when compared to the micron-size fillers, resulting in improved crack initiation toughness under quasi-static loading conditions.

Under dynamic loading conditions, however, the lower interfacial surface area and higher stress concentration effects present in micro-filler case produces filler-matrix interfacial debonding as stress waves propagate. Moreover, a propagating crack front is attracted and trapped by the weakened particle-matrix interfaces resulting in momentary deceleration and arrest [128]. This requires additional energy for reinitiation and further growth, producing higher apparent dynamic fracture toughness. In the nano-particle case, on the other hand, the lower matrix-filler interfacial stresses promote crack from

deflecting away from interfaces producing sustained matrix crack growth (with the exception of crack pinning sites) at a relatively lower energy expenditure.

CHAPTER 5

FRACTURE BEHAVIOR OF PPCs WITH CARBON NANOTUBES[1]

This chapter presents the fracture responses of epoxy nanocomposites modified with carbon nanotubes (CNTs) and polyol diluent. The synergistic effects of multifunctional reactive polyol diluent and randomly-oriented amino-functionalized multi-walled carbon nanotubes (NH_2-MWCNTs) on the mode-I fracture behavior of two-phase (epoxy/CNT, epoxy/polyol) and hybrid (epoxy/CNT/polyol) epoxy composites were investigated under quasi-static ($\dot{K}_I \sim 10^{-2}$ MPa$\sqrt{\text{m}}/\text{s}$) and dynamic ($\dot{K}_I^d \sim 10^4$ MPa$\sqrt{\text{m}}/\text{s}$) loading conditions to study loading rate effects. The associated toughening mechanisms with respect to loading rates are discussed with the aid of electron microscopy.

5.1 Material Preparation and Characterization

5.1.1 Materials

A low viscosity epoxy system (Applied Poleramics Inc., USA) consisting of unmodified diglycidylether of bisphenol-A (DGEBA) resin cured by cycloaliphatic amine hardener was used as the matrix. An epoxy terminated polyether polyol (triglycidyl ether of propoxylated glycerin) (Applied Poleramics Inc., USA) was used as a reactive diluent and toughener. The amino-functionalized multi-walled carbon nanotubes (NH_2-MWCNTs) synthesized by catalytic chemical vapor deposition (purity>95%,

[1] Parts of this chapter appear in Refs. [129, 130].

average diameter ~10 nm, average length ~1 μm) received from Nanocyl, Belgium, were used as stiff fillers.

5.1.2 Composites Manufacturing Process[2]

Four categories of samples were prepared in this study: neat epoxy, epoxy/CNT(0.3 wt.%), epoxy/polyol(10 phr) and hybrid epoxy/CNT(0.3 wt.%)/polyol(10 phr). Table 5.1 presents the sample codes and formulations of all the epoxy composites used in this work. The choice of 0.3 wt.% CNT and 10 phr polyol was based on our previous study [130] that offered optimum gain in mechanical properties.

Sample nomenclature	DGEBA (phr)	Polyol content (phr)	NH_2-MWCNTs content (wt.%)
EP (Neat epoxy)	100	0	0
EP-CNT (Epoxy + NH_2-MWCNT)	100	0	0.3
EP-POL (Epoxy + Polyol)	90	10	0
EP-CNT-POL (Epoxy + NH_2-MWCNT + Polyol)	90	10	0.3

Table 5.1: Formulation of neat and CNT/polyol modified epoxy samples. (The hardener content was 30 phr for all formulations.)

For EP-CNT system, the 0.3 wt.% NH_2-MWCNTs were dispersed in unmodified DGEBA resin at room temperature using a sonicator probe at 35% amplitude and a 30 seconds 'on'/30 seconds 'off' cycle in pulse mode for 1 h. To overcome the increase in pressure and temperature, the mixture was kept in a cooling bath during sonication. For effective dispersion of CNTs, the sonicated mixture was subsequently subjected to a three-roll shear mixing process, as shown schematically in Fig. 5.1. The rollers 1 and 3 rotate in the same direction and opposite to the middle roller 2 thereby inducing shear to the mixture. A gap setting between the rollers of 20 μm (1st pass), 10 μm (2nd pass) and 5

[2] Composites described in this chapter, were manufactured at Tuskegee University, Tuskegee, AL.

μm (3rd pass) was used to induce a high degree of shear to the mixture. The speed of the rollers was maintained at a ratio of 1:3:9 with a maximum speed of 200 rpm in all the three passes.

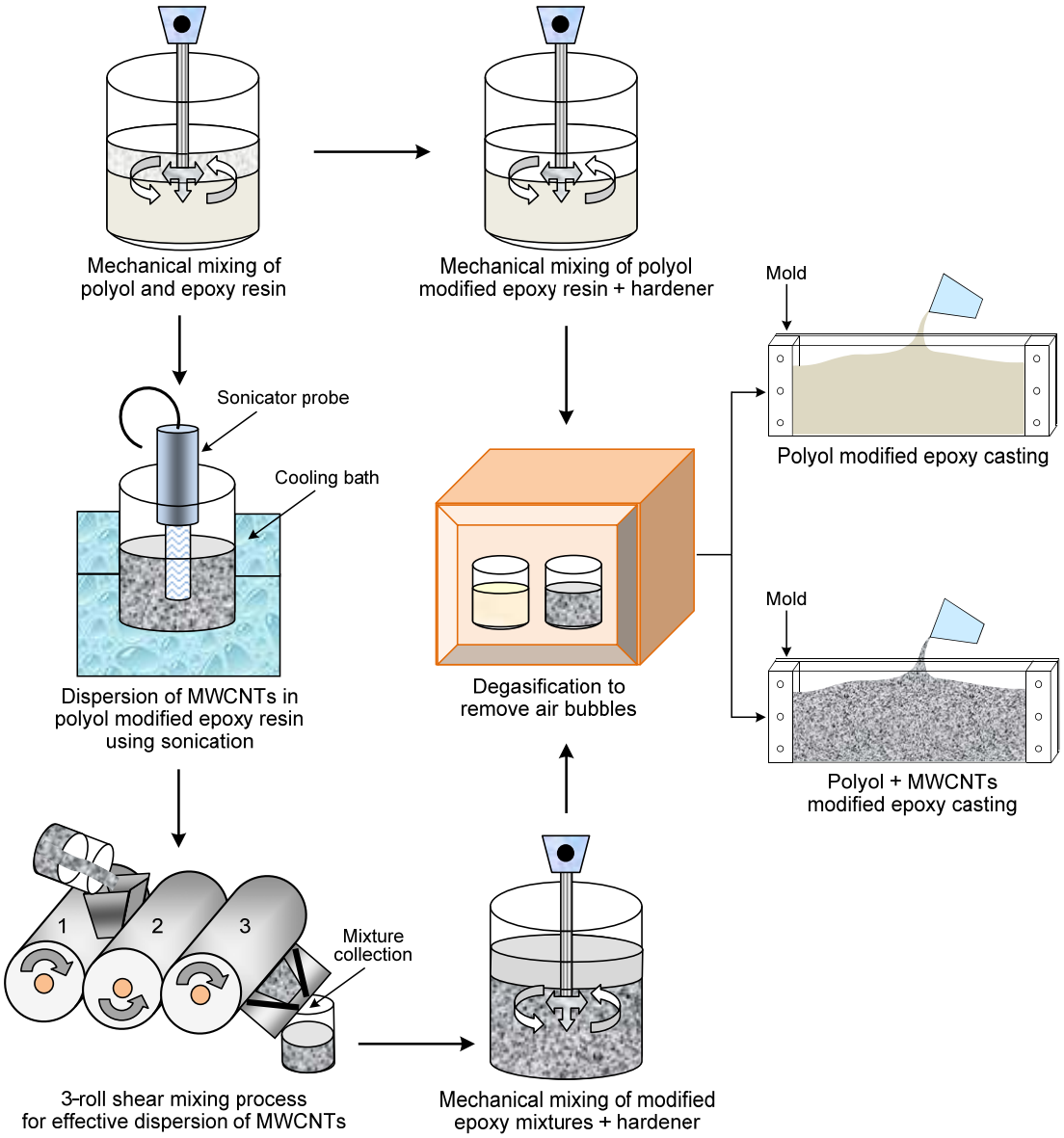

Fig. 5.1: Schematic of the manufacturing process for CNT/polyol modified epoxy composites.

A conventional mechanical mixing technique was used to prepare EP-POL system by blending 10 phr polyol into the unmodified epoxy resin. For hybrid EP-CNT-POL

system, 0.3 wt.% NH_2-MWCNTs were dispersed in 10 phr polyol modified epoxy resin using sonication and three-roll shear mixing process described above. The schematic shown in Fig. 5.1 depicts the manufacturing process for polyol modified epoxy (EP-POL) and epoxy/NH_2-MWCNTs/polyol (EP-CNT-POL) hybrid composites.

The stoichiometric amount of the hardener was added to the neat and modified resin systems and blended using a mechanical stirrer for 10 min. The resulting blends were subjected to degasification to remove any trapped bubbles generated during mixing. After degassing, the mixtures were poured into molds coated with a release-agent and cured for 2 h at 60 ºC followed by post curing at 100 ºC for 5 h. The composite sheets were further rested at room temperature for a week prior to machining and testing.

5.1.3 Material Characterization

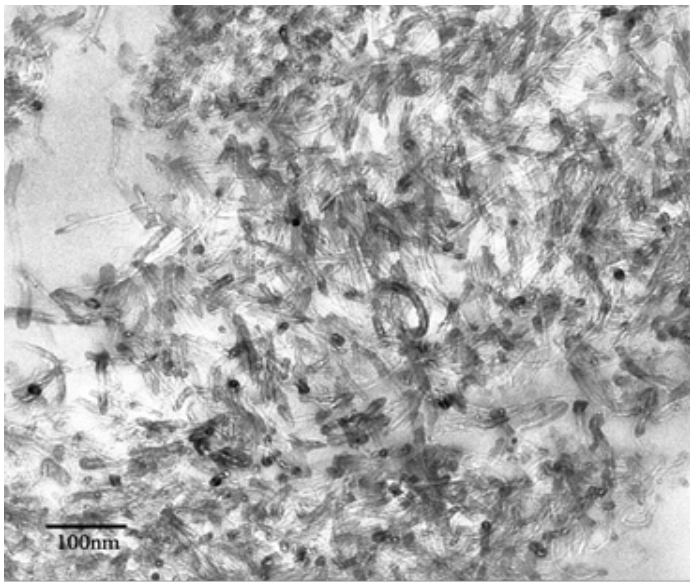

Fig. 5.2 TEM micrograph showing quality of NH_2-MWCNTs dispersion.

The quality of CNT dispersion in the modified epoxy was examined using a ZEISS EM10 transmission electron microscope (TEM). Figure 5.2 shows the state of dispersion

of NH_2-MWCNTs in epoxy/CNT samples manufactured using sonication and 3-roll shear mixing process.

The dynamic elastic characteristics of all the samples were evaluated by indirect means using ultrasonic pulse-echo method. The values of Poisson's ratio in these composites were found to be nearly constant at 0.353±0.011. The measured wave speeds (C_L and C_S) and the dynamic elastic modulus (E_d) for all samples are shown in Fig. 5.3. It can be seen that the epoxy composites show only modest changes in C_L, C_S and E_d relative to the neat epoxy.

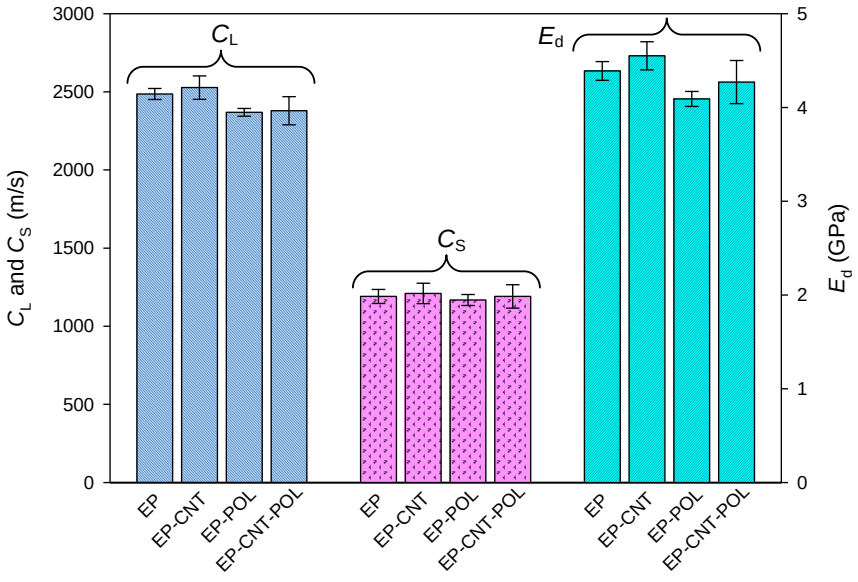

Fig. 5.3: Measured dynamic material properties using ultrasonic pulse-echo method. (EP: neat epoxy, EP-CNT: epoxy/CNT, EP-POL: epoxy/polyol, EP-CNT-POL: epoxy/CNT/polyol.)

5.2 Experimental Procedure

The cured composite sheets were machined into rectangular specimens of nominal dimensions 100 mm x 12.5 mm x 5 mm for quasi-static fracture tests (span 60 mm) and 212 mm x 50 mm x 8 mm for dynamic fracture experiments (span 196 mm). An edge

notch of 3 mm and 10 mm in length was first cut using a diamond impregnated wafer blade (thickness ~300 μm) into the samples for quasi-static and dynamic fracture tests, respectively. The notch tip was sharpened using a razor blade in order to have a sharp crack tip. A random speckle pattern was created on the surface of the specimen to facilitate DIC method for dynamic fracture experiments. The quasi-static and dynamic fracture experiments were performed using the tests setups shown in Figs. 3.1 and 3.2, respectively (see Chapter 3 for testing details). A framing rate of 250,000 frames per second was used to conduct dynamic fracture tests.

5.3 Experimental Results and Discussion

5.3.1 Quasi-static fracture response

The quasi-static fracture response of neat epoxy and modified epoxy composites is shown in Fig. 5.4. Typical load-deflection curves of all formulations are shown in Fig. 5.4(a). It can be seen that the load rises linearly for neat epoxy (EP) and epoxy/ CNT (EP-CNT) systems whereas the epoxy/polyol (EP-POL) and epoxy/ CNT/polyol (EP-CNT-POL) composites show a degree of nonlinear behavior in the initial as well as in the intermediate stages of deformation. Except for neat epoxy, a noticeable nonlinearity is seen in all specimens prior to fracture at which abrupt crack growth ensues causing a sudden drop in the recorded load. Note that the peak loads and the corresponding load-point deflections at break increase after individual as well as simultaneous addition of NH_2-MWCNTs and polyol phases into epoxy. The incorporation of NH_2-MWCNTs as the stiff and polyol as the compliant phase results in increasing and decreasing slopes of the load-deflection curves, respectively, relative to the neat epoxy, whereas the hybrid system containing both stiff and compliant phases show lower stiffness than the EP-CNT

system but higher than the EP and EP-POL counterparts. Further, note that the work needed for crack initiation (area under the load-deflection curve) is the maximum for hybrid EP-CNT-POL system among all the compositions.

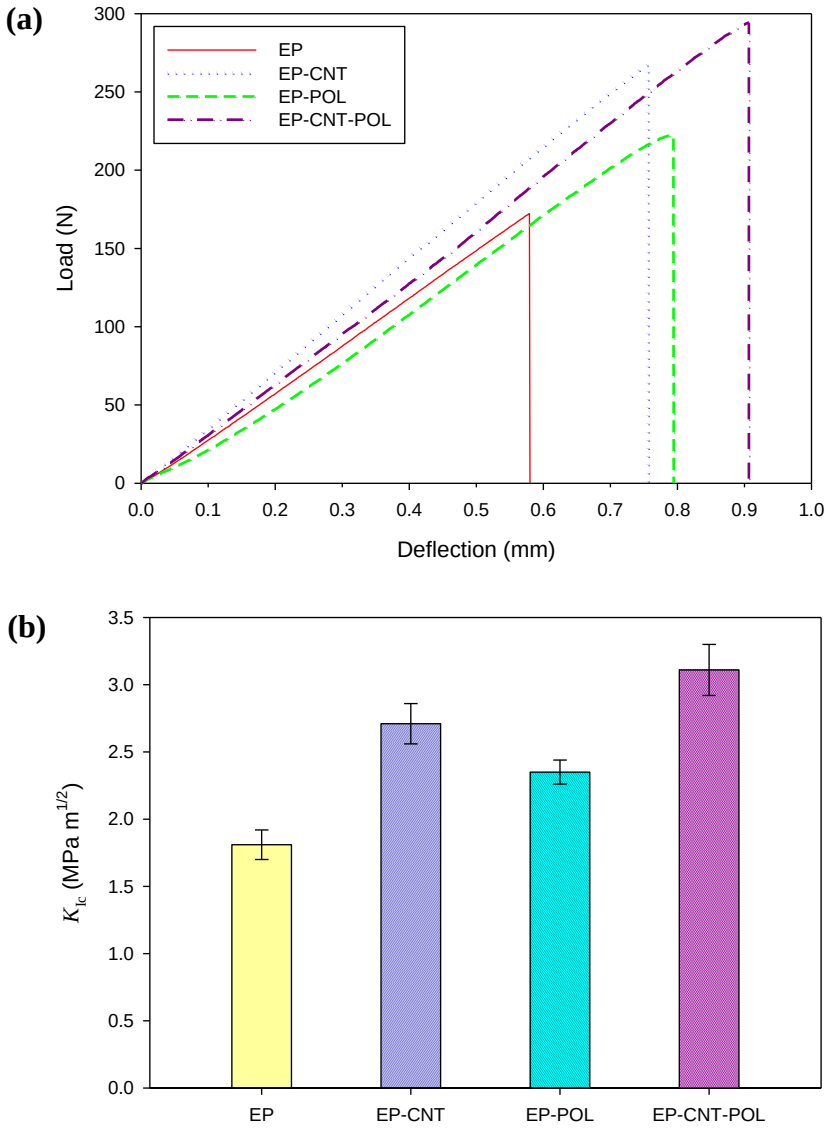

Fig. 5.4: Mode-I quasi-static fracture tests: **(a)** Typical load-deflection responses, **(b)** Quasi-static crack initiation toughness (K_{Ic}) of different formulations.

The measured quasi-static crack initiation toughness (K_{Ic}) values for all formulations are shown in Fig. 5.4(b). Each data represents an average of five measured values of K_{Ic}

and the error bars indicate standard deviations. A significant enhancement in the quasi-static fracture property is quite evident in each modified epoxy system. With respect to neat epoxy, the gain in K_{Ic} values for EP-CNT and EP-POL systems are ~50% and ~30%, respectively, indicating that the 0.3 wt.% addition of NH_2-MWCNTs is more effective than the 10 phr polyol as a toughener. However, the simultaneous incorporation of both phases offers the maximum improvement of ~70% in K_{Ic} value for the hybrid EP-CNT-POL system relative to the neat epoxy. The synergistic effect of stiffening the epoxy with CNTs while toughening with polyol seems to yield the best outcome.

5.3.2 Dynamic fracture experimental repeatability

Due to the transient nature of deformation at elevated loading rates, multiple experiments were first performed in order to verify repeatability in the fracture behavior, and hence, the crack growth measurements. Figs. 5.5(a)-(c) shows the repeatability of dynamic fracture experiments in terms of the impact force, crack length and mode-I SIF histories for hybrid EP-CNT-POL composites. The tup and anvil load histories are shown in Fig. 5.5(a) for the four EP-CNT-POL specimens. (Note that the tup forces are shown as positive instead of negative.) An excellent repeatability in the tup force as well as in the left and right support reaction histories is self evident. In these experiments, the complete fracture of the specimen occurred within ~225 μs after impact. Thus, only the dominant first peak of the tup force history is significant. Note that the supports register reaction force after ~300 μs by which time the crack propagates the entire specimen width. Hence, the reaction forces from support anvils do not contribute to the crack initiation and growth in these specimens, suggesting that a free-free cracked beam model should suffice analytical or computational simulation of these experiments.

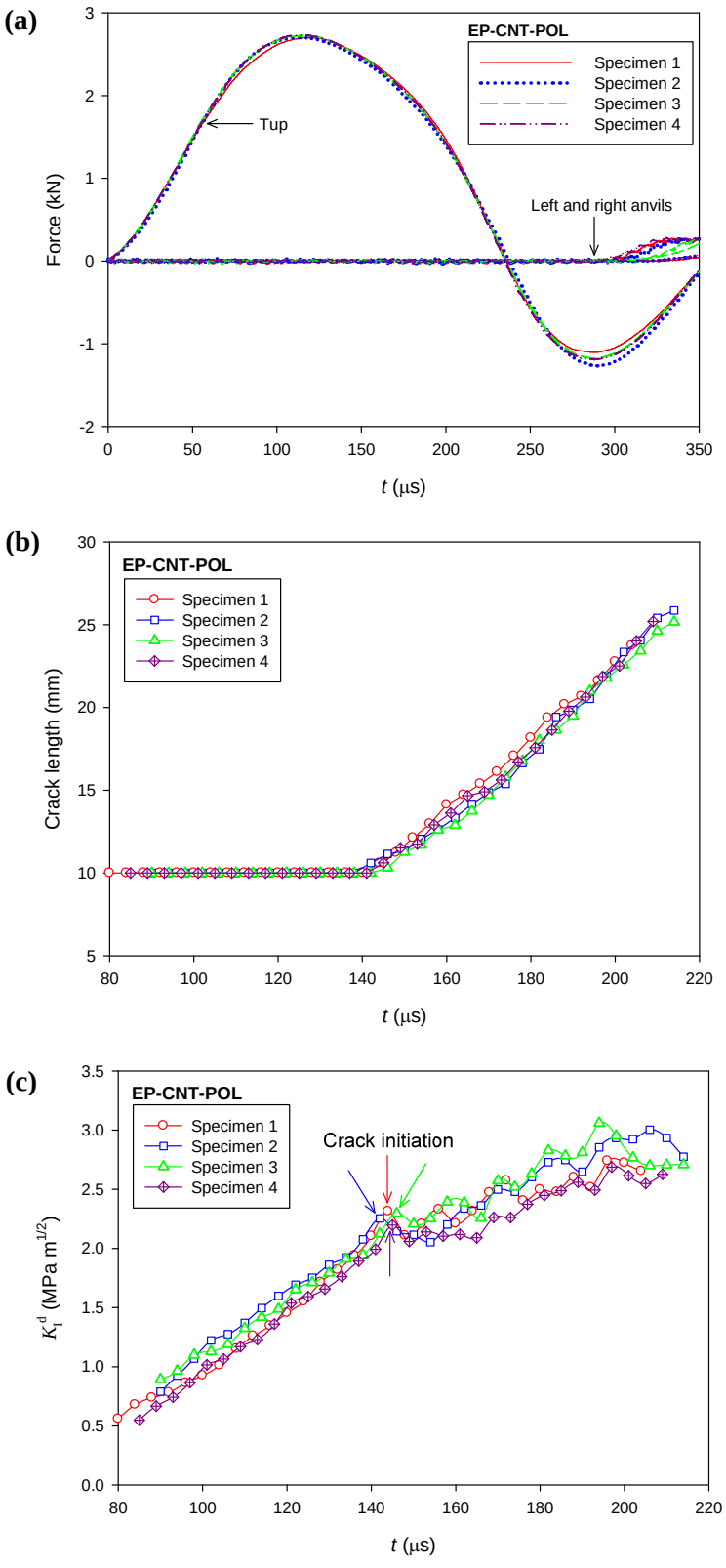

Fig. 5.5: Repeatability of dynamic fracture tests for EP-CNT-POL specimens: **(a)** Impactor force and support reaction histories, **(b)** Crack length histories, **(c)** Mode-I dynamic SIF (K_I^d) histories.

The crack length histories for the same set of specimens are plotted in Fig. 5.5(b). Prior to impact, the specimens had a crack (pre-notch) length of 10 mm. When the impactor contacted the specimen (t = 0), the compressive stress waves propagated the specimen width and took 142-146 μs to initiate the crack. After loading, the compressive stress waves reflect back as tensile waves from the specimen edge opposite to the impact edge, initiating the crack tip in a mode-I fashion. Following initiation, a repeatable and monotonic crack growth is evident in all specimens until complete fracture with minor deviations in the crack length due to the highly transient nature of failure.

The mode-I dynamic SIF (K_I^d) histories for EP-CNT-POL composites are shown in Fig. 5.5(c). The K_I^d value at crack initiation is indicated by an arrow for each specimen. The SIF increases monotonically until crack initiation, followed by a noticeable drop in K_I^d values for all specimens due to elastic unloading. This is accompanied by a gradual increase in K_I^d values until the complete fracture of the specimens. It is important to note that from the perspective of dynamic fracture experiments, the K_I^d profiles show a very good repeatability throughout the fracture event.

5.3.3 Dynamic crack growth responses

A few representative speckle images and the corresponding crack-opening (v-field or displacement along the y-axis) and crack-sliding (u-field or displacement along the x-axis) displacement contours for each sample category are presented in Fig. 5.6. Each speckle image represents 30 x 30 mm^2 region-of-interest recorded by the high-speed camera where surface deformations were monitored optically.

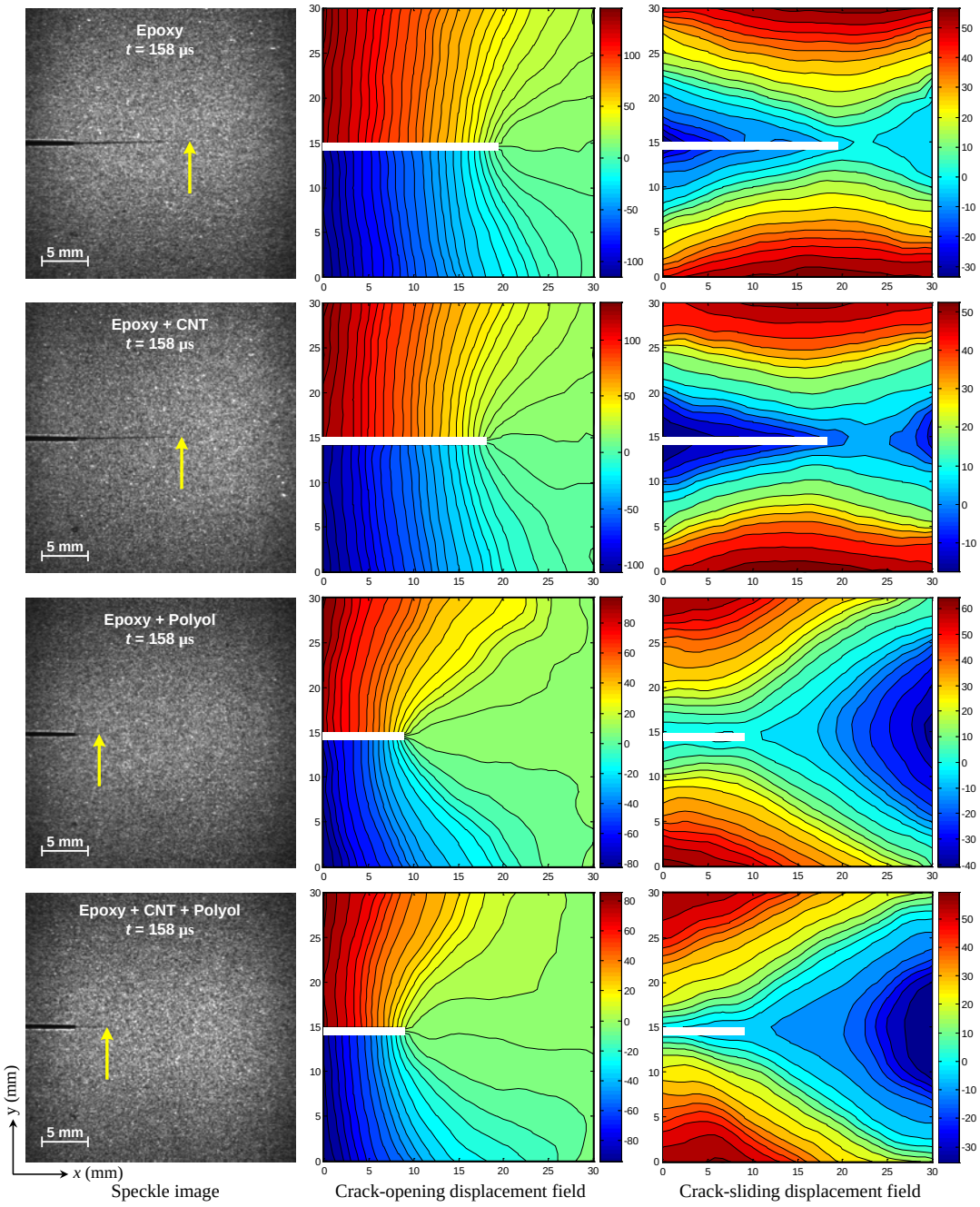

Fig. 5.6: Measured crack-opening and crack-sliding displacement fields at a time instant t = 158 μs corresponding to speckle images (first column) in 30 x 30 mm^2 region-of-interest. The arrows indicate the instantaneous crack tip position in the speckle images. Color bars represent displacement in μm. Contours are plotted in 5 μm increments.

The specimens were subjected to symmetric impact loading and the initial notch as well as the sharp growing crack is visible as indicated by the arrows. In order to compare

the extent of crack growth, the speckle images for each formulation are selected at a particular time instant, t = 158 μs. It can be seen that at this time instant, the crack extension in neat epoxy and epoxy/CNT specimens is nearly equal and larger than the epoxy/polyol and hybrid epoxy/CNT/polyol counterparts. A sub-image size of 26 x 26 pixels was chosen for image correlation analysis and displacement fields were obtained as a 37 x 37 array of data points for each time instant. Subsequently, full-field displacement contours with 5 μm per contour increment were generated. The crack-opening and crack-sliding displacement fields show that contour lines are nearly symmetric relative to the crack, consistent with a dominant mode-I fracture behavior. The crack-sliding displacement field shows a set of isolines emerging from the right side of the contour plots due to impact loading.

5.3.4 Transient load histories

A comparison of dynamic fracture performance in terms of the transient load, crack length and SIF histories for all formulations of modified epoxy composites is made in Fig.5.7-5.9. The tup force and anvils reactions experienced by each type of composite are compared in Fig. 5.7. The peak impact force (compressive) recorded by the piezoelectric tup in case of epoxy/CNT (EP-CNT) system is the maximum indicating higher contact stiffness and peak impact load among all the cases. The hybrid epoxy/CNT/polyol (EP-CNT-POL), neat epoxy (EP) and epoxy/polyol (EP-POL) composites exhibit decreasing trends, successively. However, the dominant peak duration is slightly longer for EP-POL and EP-CNT-POL cases than the EP and EP-CNT counterparts due to a higher crack growth resistance in the former than the latter cases. The left and right anvil support

reactions on the other hand do not register significant values until 300 μs causing a free-free beam condition to prevail during fracture in all the cases.

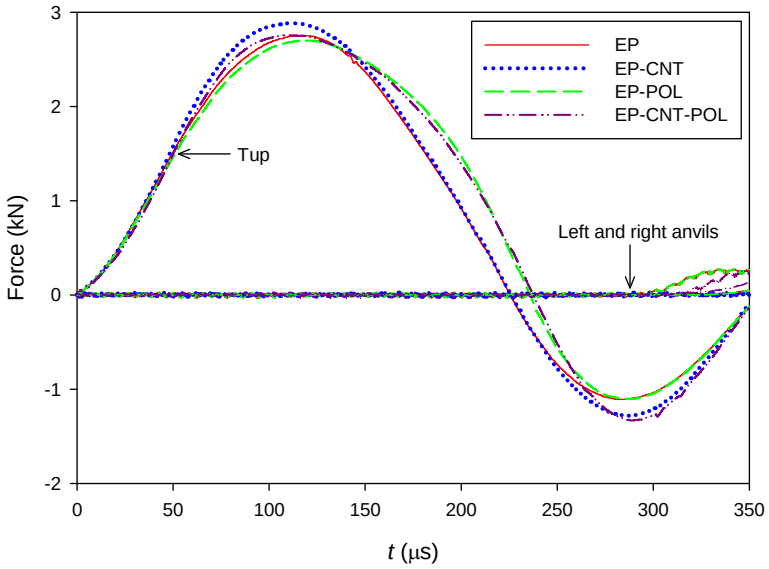

Fig. 5.7: Transient impact force and support reaction histories for all specimens.

5.3.5 Crack length histories

The instantaneous crack length histories for all samples are plotted in Fig. 5.8. The crack initiation occurred much later in the epoxy/CNT (118 μs), epoxy/polyol (144 μs) and hybrid epoxy/CNT/polyol (146 μs) composites when compared to the neat epoxy (98 μs). Following initiation and rapid acceleration (due to sudden release of energy from the initial crack tip), it can be seen that crack growth is essentially continuous in each case during the observation window. In each sample category, minimal deviations can be noted in the crack growth behavior due to the transient nature of stress wave dominant fracture. The slope of crack length histories was used to estimate crack tip velocity and are 325, 313, 210, 227 m/s for neat epoxy, epoxy/CNT, epoxy/polyol, epoxy/CNT/polyol composites, respectively as listed in Fig. 5.8. The crack growth characteristics suggest

that the addition of compliant phase (polyol) siginificanlty retards the crack propagation in polyol modified composites.

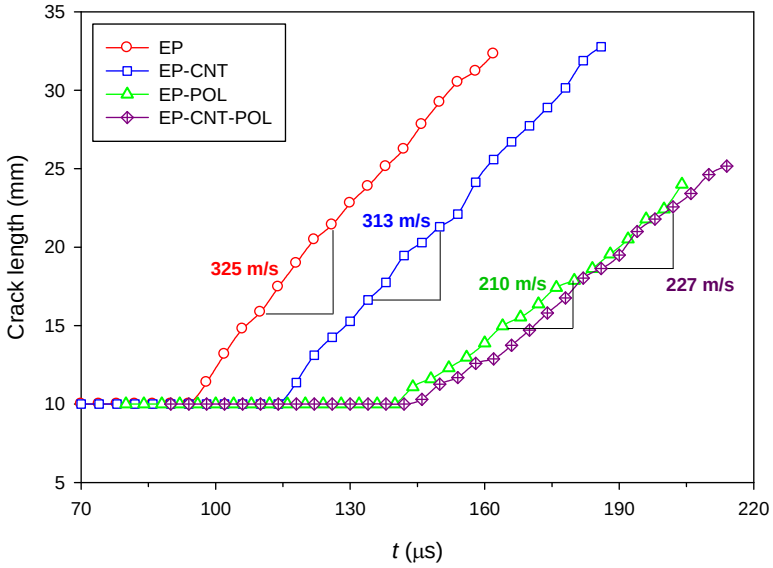

Fig. 5.8: Crack growth histories from dynamic fracture tests.

5.3.6 Stress intensity factor (SIF) histories

The optically measured dynamic mode-I ($K_{\mathrm{I}}^{\mathrm{d}}$) and mode-II ($K_{\mathrm{II}}^{\mathrm{d}}$) SIF histories are shown in Fig. 5.9. Here t_{i} denotes the time at crack initiation after impact and the time base is shifted such that $t - t_{\mathrm{i}} = 0$ corresponds to crack initiation as shown by the vertical dotted line, and hence the negative and positive values represent the pre-initiation and post-initiation periods, respectively. In the pre-initiation regime ($t - t_{\mathrm{i}} < 0$), for each specimen the $K_{\mathrm{I}}^{\mathrm{d}}$ increases monotonically until it reaches a threshold value at crack initiation. Following initiation, a noticeable drop in $K_{\mathrm{I}}^{\mathrm{d}}$ can be seen and the maximum value of $K_{\mathrm{I}}^{\mathrm{d}}$ just before the drop is identified as the mode-I dynamic crack initiation toughness, $K_{\mathrm{Ii}}^{\mathrm{d}}$. One can readily see that the magnitudes $K_{\mathrm{Ii}}^{\mathrm{d}}$ show increasing trend with

the addition of 0.3 wt.% NH_2-MWCNTs, 10 phr polyol and a combination of both into the epoxy matrix. Relative to neat epoxy (EP), the improvements in dynamic crack initiation toughness, K_{Ii}^{d} for EP-CNT, EP-POL and EP-CNT-POL composites are ~37%, ~65% and ~92%, respectively. The K_{I}^{d} values in the pre-initiation ($t - t_i < 0$) and post-initiation ($t - t_i > 0$) regimes are higher for EP-CNT, EP-POL and hybrid EP-CNT-POL composites when compared to that of neat epoxy. After crack initiation, the instantaneous values of K_{I}^{d} steadily rise but with an oscillatory behavior due to stress wave reflections in a finite size specimen. It should be noted that the mode-II dynamic SIF (K_{II}^{d}) values are close to zero throughout the failure event for each experiment, indicating a dominant mode-I fracture behavior.

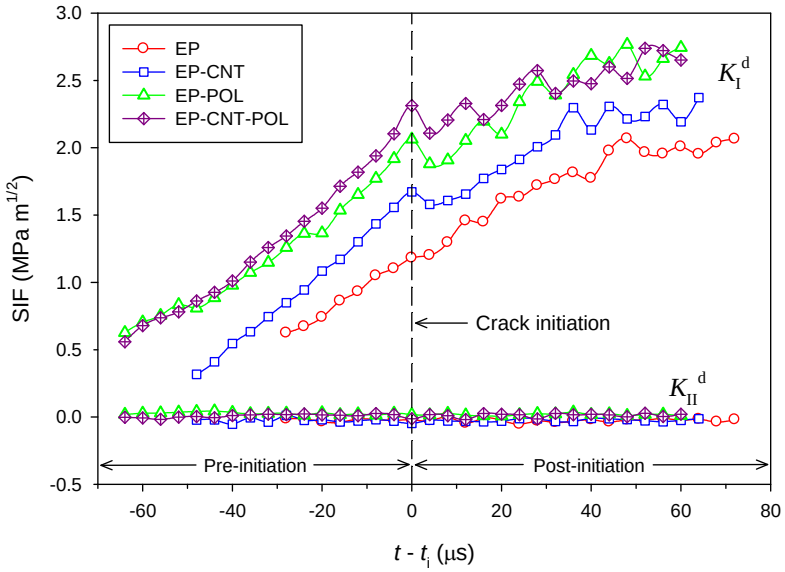

Fig. 5.9: Dynamic mode-I (K_{I}^{d}) and mode-II (K_{II}^{d}) SIF histories.

Sample	Peak impact force (kN)	Crack initiation time t (μs)	Maximum crack velocity V_{max} (m/s)	Steady state crack velocity V_{ss} (m/s)	Dynamic crack initiation toughness K_{Ii}^{d} (MPa $m^{1/2}$)
EP	2.75 ± 0.08	98 - 102	442 ± 56	349 ± 23	1.18 ± 0.07
EP-CNT	2.88 ± 0.07	116 - 118	438 ± 44	323 ± 21	1.62 ± 0.06
EP-POL	2.64 ± 0.04	142 - 146	288 ± 10	214 ± 12	1.95 ± 0.11
EP-CNT-POL	2.71 ± 0.02	142 - 146	281 ± 12	219 ± 15	2.27 ± 0.05

Table 5.2: Measured dynamic fracture parameters for neat and CNT/polyol modified epoxies.

The dynamic fracture performance of modified epoxy composites regarding crack initiation and crack growth parameters is quantified in Table 5.2. Each data is an average of 3-4 experiments, listed along with their standard deviation. The crack initiated in the polyol modified composites (EP-POL and EP-CNT-POL) at the same time range (142-146 μs) after impact and is longer than the initiation time needed for neat epoxy (98-102 μs) and epoxy/CNT (116-118 μs) samples indicating that the crack initiation can be significantly delayed with the incorporation of polyol phase. The maximum (V_{max}) and steady state (V_{ss}) crack velocities are lower for EP-POL and hybrid EP-CNT-POL composites relative to neat epoxy and EP-CNT samples suggesting higher crack growth resistance and dynamic crack initiation toughness in the former cases than the latter.

5.4 Loading Rate Effects

In light of the experimental results discussed above, an obvious question that arises is, are the fracture behaviors of CNT and polyol modified epoxies loading rate dependent? Hence, it is instructive to compare fracture toughness at crack initiation for all cases under quasi-static and dynamic loading conditions. The role of loading rate on fracture parameters of these composites is presented in Fig. 5.10.

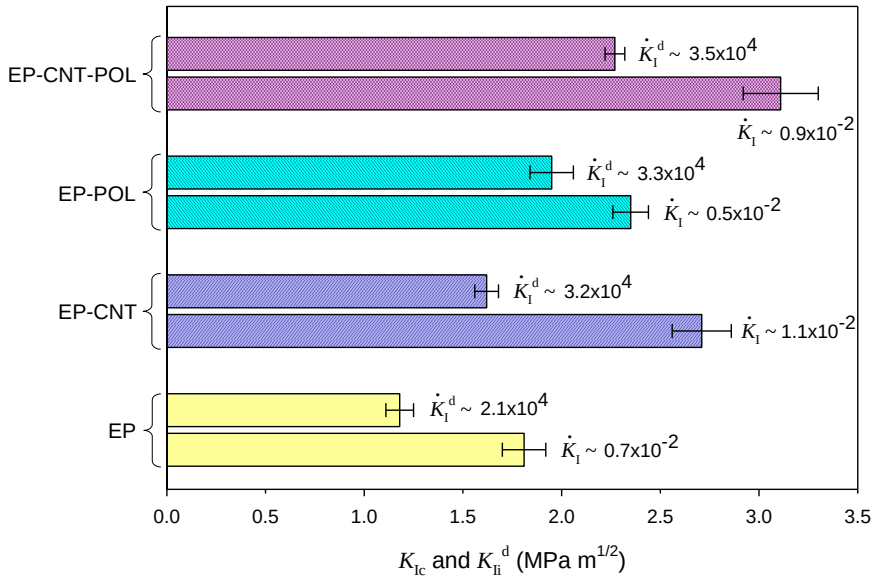

Fig. 5.10: Loading rate effects on mode-I crack initiation toughness of epoxy composites. (Quasi-static loading rate: $\dot{K}_I = dK_I/dt$; dynamic loading rate: $\dot{K}_I^d = dK_I^d/dt$. The $\dot{K}_I$ and $\dot{K}_I^d$ are expressed in $\text{MPa}\sqrt{\text{m}}/\text{s}$.)

In this work, the loading rate for a cracked specimen is defined as the rate of increase of SIF at crack initiation (quasi-static: $\dot{K}_I = dK_I/dt$; dynamic: $\dot{K}_I^d = dK_I^d/dt$) and determined experimentally for each type of composite from a linear fit of 4-5 data points prior to crack initiation. In Fig. 5.10, a systematic comparison is made between quasi-static and dynamic crack initiation toughness (K_{Ic} and K_{Ii}^d) for each material. The respective loading rate $\dot{K}_I$ and $\dot{K}_I^d$ values are listed for each composite as legends, and expressed in $\text{MPa}\sqrt{\text{m}}/\text{s}$. Again, each loading rate is an average of 3-5 experiments for each material category. Note that the dynamic loading rates ($\dot{K}_I^d$ values) are *six orders of magnitude greater* than the quasi-static ($\dot{K}_I$) counterparts. From Fig. 5.10, it can be seen that the fracture toughness values between quasi-static and dynamic cases differ from

each other for the respective composites. At high loading rates ($\dot{K}_I^d \sim 10^4$ MPa$\sqrt{\text{m}}/\text{s}$), the crack initiation toughness values are lower than those corresponding to the quasi-static loading rates ($\dot{K}_I \sim 10^{-2}$ MPa$\sqrt{\text{m}}/\text{s}$). The difference is quite significant for EP-CNT composites, where the fracture toughness value for dynamic case is ~40% lower when compared to the quasi-static counterpart. However, the EP-POL system shows the least difference of ~17% between the toughness values among all the cases.

5.5 Toughening Mechanisms

Fractographic examination was used to study the toughening mechanisms under quasi-static and dynamic loading conditions. The SEM micrographs of quasi-statically fractured surfaces of neat and modified epoxy samples are shown in Fig. 5.11. A relatively smooth fracture surface with a presence of fine lines is seen in neat epoxy case as shown in Fig. 5.11(a) indicating a typical brittle and unstable crack growth behavior accounting for its low fracture toughness among all the cases. Figs. 5.11(b) and (c) depict the highly textured/rough surfaces for epoxy/CNT and epoxy/polyol composites, respectively. The roughness associated with the curved crack front/path indicates significant amount of inelastic deformation and deviation of fracture planes from its original crack plane suggests highly interrupted and deflected crack paths requiring higher amounts of fracture energy. The fractured surface of hybrid epoxy/CNT/polyol composite shown in Fig. 5.11(d) appears to have a higher degree of roughness when compared to the other cases, and can be attributed to micro crack deflections and branched crack propagation in multiple planes caused by CNTs and immiscible polyol domains. The curved and vivid ridges can be seen throughout the fracture surface

suggesting a cumulative contribution of nanotubes and polyol in the fracture toughness enhancement.

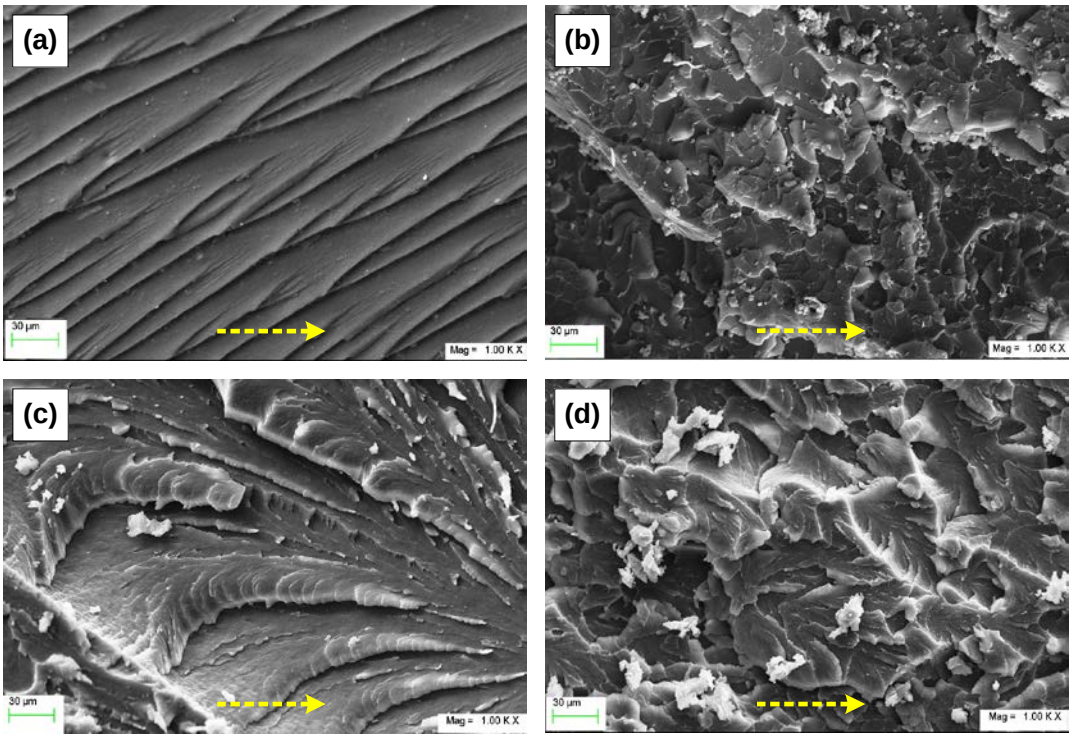

Fig. 5.11: SEM micrographs of quasi-statically fractured surfaces: **(a)** Epoxy, **(b)** Epoxy-CNT, **(c)** Epoxy-Polyol, **(d)** Epoxy-CNT-Polyol. (The dotted arrow indicates the direction of crack propagation.)

As shown in Fig. 5.12, the micrograph for hybrid epoxy/CNT/polyol case shows uniformly dispersed spherical polyol domains and the presence of embedded CNTs is also visible in the magnified view of the highlighted region. The further magnified views of selected regions in the subsequent micrographs show matrix cracking through polyol domains along with the presence of pulled-out CNTs and CNT bridges at various locations on the fracture planes.

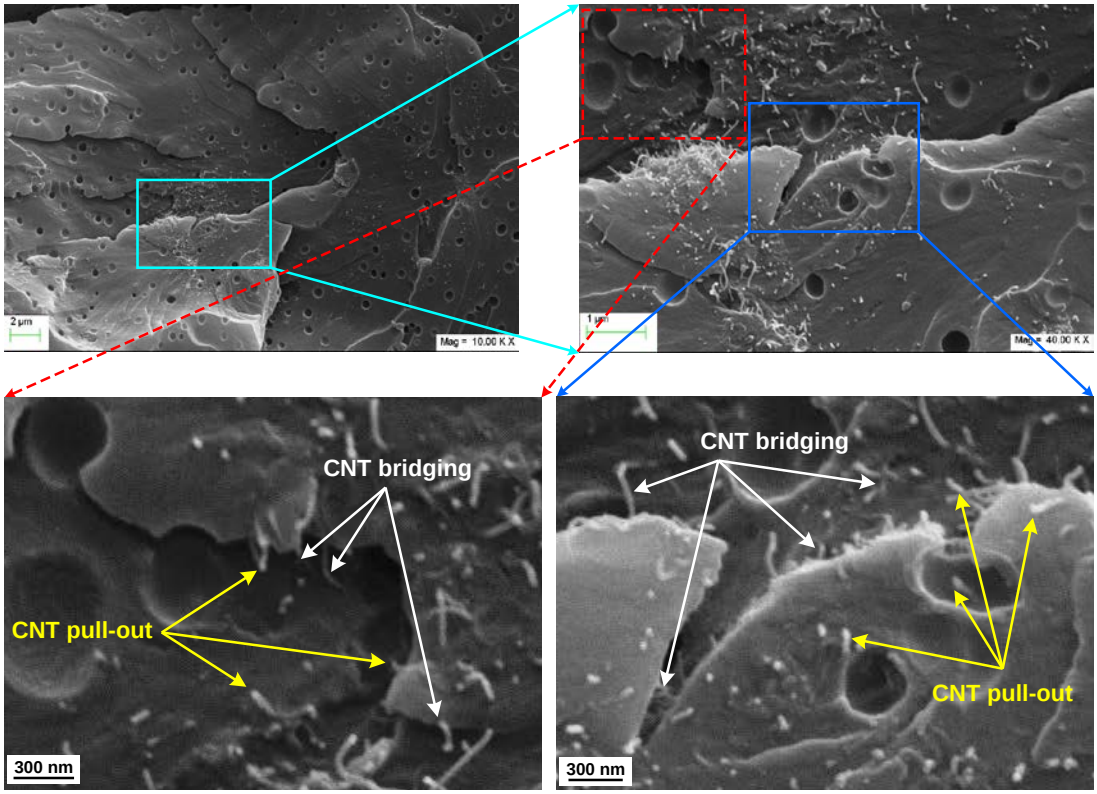

Fig. 5.12: SEM micrographs of quasi-static fracture surface of epoxy-CNT-Polyol hybrid composite showing CNT pull-out and CNT bridging.

The microscopic features of dynamically fractured surfaces are shown in Fig. 5.13 for each material. The broken arrows in these micrographs indicate the direction of crack propagation. The fractured surface of neat epoxy as shown in Fig. 5.13(a), reveals a relatively flat, smooth and featureless surface demonstrating its brittle nature with least energy expenditure among all the cases. In the case of epoxy/CNT composite, the micrograph in Fig. 5.13(b) shows that the surface roughness increased with the addition of CNTs into epoxy thereby forming the stepwise markings and cleavage planes. The magnified view in the inset shows CNT entanglements, pull-out as well as bridges. Fig. 5.13(c) illustrates the fracture surface of epoxy/polyol case showing inelastically deformed matrix with crack branches on various fracture planes. The finely distributed

sub-micron size polyol domains can be observed in the inset along with the presence of micro cracks, riverbed markings and shear band features responsible for strain energy absorption. Fig 5.13(d) shows the fracture surface of the hybrid epoxy/CNT/polyol composites. In addition to shear flow, deep furrows and higher cleavages are visible. The magnified view in the inset shows minor CNT agglomerates associated with dendriform cracks, acting as obstacles for the growing crack leading to deviation from its primary path thereby generating secondary cracks. The CNT pull-out, CNT bridges, matrix cracks, crack bifurcation and crack pining in polyol domains are the major toughening mechanisms in the case of hybrid composites.

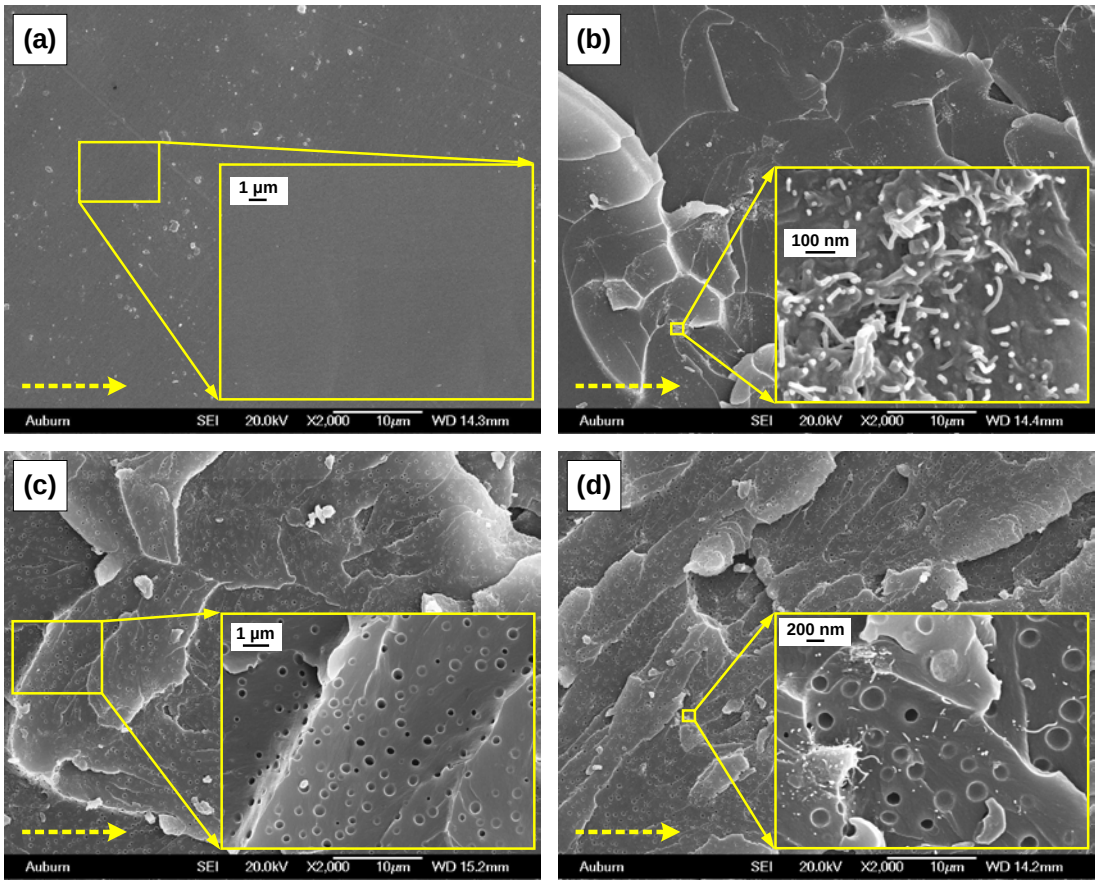

Fig. 5.13: SEM micrographs of dynamically fractured surfaces: **(a)** Epoxy, **(b)** Epoxy-CNT, **(c)** Epoxy-Polyol, **(d)** Epoxy-CNT-Polyol. (The dotted arrow indicates the direction of crack propagation.)

With regards to loading rate effects, the micrographs shown in Figs. 5.11-5.13 reveal higher surface roughness and ruggedness for the quasi-static fractured specimens when compared to dynamic counterparts and accounts for the higher crack initiation toughness in the former cases. Note that the addition of polyols to epoxy increased the fracture energy due to higher ductility of the polyol domains. Additionally, CNTs have a high aspect ratio and elasticity as well as strong interfacial bonding due to ammonia-functionalization, resulting in the nanophase resin systems exhibiting higher absorption of energy. Moreover, CNTs serve as effective crack bridges inducing mechanical interlocking with the matrix material. In addition to bridging, the strongly bonded CNTs significantly absorb fracture energy when pulled-out from the matrix. Moreover, CNTs also add to momentary crack arrest and/or deflection during propagation. These combined effects of both the fillers provide the greatest enhancement in crack initiation toughness in the hybrid composites.

CHAPTER 6

DYNAMIC CRACK-INCLUSION INTERACTIONS[1]

In this chapter, experimental simulations of dynamic crack growth past inclusions of two different elastic moduli, stiff (glass) and compliant (polyurethane) relative to the matrix (epoxy), are described in order to understand the underlying physics of stress-wave dominated fracture in PPCs. As noted earlier, failure of PPCs is intrinsically linked to the fundamentals of matrix crack interactions with a second phase inhomogeneity in or near its path. Thus, some light can be shed on failure mechanisms of PPCs by studying interactions between a dynamically propagating crack and an isolated stiff or compliant inclusion as a function of the inclusion-matrix interfacial strength and its location relative to the crack tip.

6.1 Crack-inclusion Specimen Fabrication and Geometry

A low viscosity epoxy system (Epo-Thin™ from Beuhler, Inc. USA) consisting of Bisphenol-A resin and an amine-based hardener in the ratio of 100:39 was employed as the matrix material. Prior to pouring the mixture into the mold, a cylindrical inclusion of diameter, d = 4 mm and length equal to the specimen thickness (8.6 mm), was positioned at the center of the mold as shown in Fig. 6.1(a). In this study, inclusions of two different elastic moduli, stiff and compliant relative to the matrix, were used. The former was a borosilicate glass inclusion whereas the latter was a polyurethane inclusion.

[1] Parts of this chapter appear in Refs. [128, 131-133].

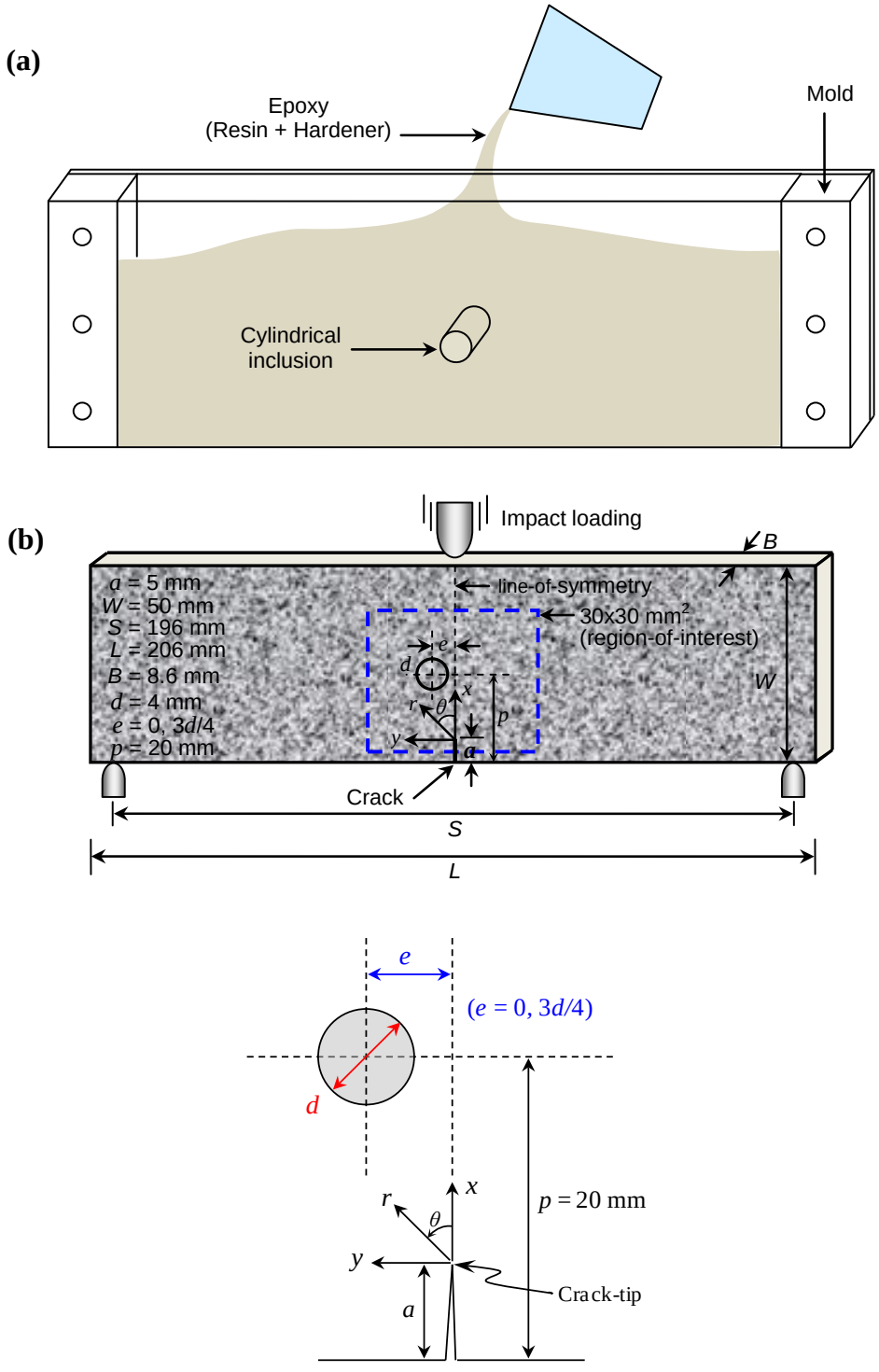

Fig. 6.1: Specimen details: **(a)** Sample preparation, **(b)** Specimen geometry and loading configuration with crack-tip coordinate system and inclusion location with an illustration of random speckle pattern, **(c)** The inclusion location relative to the initial crack tip: symmetrically located inclusion ($e = 0$) and eccentric inclusion ($e = 3d/4$).

Material	Density, ρ (kg/m^3)	Elastic modulus, E (GPa)	Longitudinal wave speed, C_L (m/s)	Impedance, (ρC_L) (MPa.s/m)	Poisson's ratio, υ
Epoxy[a] (matrix)	1124	3.97	2487	2.79	0.368
Glass[b] (stiff inclusion)	2500	69	5800	14.50	0.190
Polyurethane[a] (compliant inclusion)	1030	0.07	1150	1.18	0.384

Table 6.1: Material properties of matrix and inclusion.
[a]In-house measurement (ultrasonic pulse-echo method). [b]Bourne et al. [134].

The physical and measured elastic properties of the matrix and inclusion materials are listed in Table 6.1. A weak inclusion-matrix interface was created by wiping a thin layer of lubricant on both stiff and compliant inclusion cases. In order to achieve a strong inclusion-matrix adhesion, the glass inclusion was treated with amine-based silane (γ-aminopropyltrimethoxysilane) whereas the polyurethane inclusion surface was roughened using a #1000 grit abrasive paper. It should be noted here that the silane is suitable for enhancing organic to inorganic material interface strength and not suitable for organic to organic material interfaces. Hence, the polyurethane inclusion was not silane treated but roughening of the inclusion surface was found to create a strong interface between polyurethane and epoxy (as demonstrated in later sections). To avoid residual stresses, the material was cured slowly at room temperature for over 18 hours and post-cured at room temperature for 7 days. The cured material was then machined into rectangular coupons of dimensions 206 mm x 50 mm x 8.6 mm. An edge notch of 5 mm in length was cut into the sample using a circular saw of thickness ~300 μm and then the notch tip was sharpened carefully by pressing a sharp razor blade to achieve a relatively quiescent crack initiation and a steady growth before crack-inclusion interaction occurs.

The edge cracked fracture specimens were then sprayed with a fine mist of black and white paints alternatively to create a random speckle pattern. Fig. 6.1(b) shows the specimen geometry, dimensions and loading configurations with crack-tip coordinate system and inclusion location with an illustration of random speckle pattern on it. The dotted box represents 30 x 30 mm^2 region-of-interest containing the embedded cylindrical inclusion. The line joining the impact point to the crack tip represents the line-of-symmetry. As shown in Fig. 6.1(c), the location of the inclusion with respect to the initial crack-tip is defined as eccentricity, *e*, the distance between the inclusion center and the line-of-symmetry. In this work, the inclusion was located at two different eccentricities, $e = 0$ and $3d/4$, being referred to as the symmetric and eccentric (or asymmetric) cases, respectively. In both cases, the inclusion was positioned at a constant distance of 20 mm from the lower edge of the specimen containing the initial crack.

6.2 Testing Procedure and Data Analysis

The 2D DIC method and high-speed imaging was employed to record crack tip deformation fields, as described in Chapter 3 (see Fig. 3.2 for experimental setup). In order to capture the entire fracture event, the images in the case of stiff inclusion specimens were recorded at a framing rate of 300,000 frames per second whereas framing rates ranging from 150,000-250,000 frames per second were used for compliant inclusion cases. A total of 32 images were recorded for each undeformed and deformed sets. The corresponding two images of each sensor were paired from undeformed and deformed sets and analyzed. Each resulting image was segmented into sub-images consisting of 24 x 24 pixels for correlation. While analyzing images, no overlapping of sub-images was

used, this resulted in array size of 40 x 40 data points. Further details regarding image analysis can be found in Chapter 2.

6.2.1 Evaluation of crack tip velocity

The position of current crack tip from each digitized image was used to measure the instantaneous values of crack length. The crack velocity (c) was then evaluated from crack length histories using the central difference method by knowing crack growth history from the images,

$$c_i = \left(\frac{da}{dt}\right)_i = \frac{a_{i+1} - a_{i-1}}{t_{i+1} - t_{i-1}} \tag{6.1}$$

where a and t are crack length and time respectively at a given instant i.

6.2.2 Crack tip fields for SIFs extraction

Due to the presence of interface between the inclusion and matrix, the stress intensity factors (SIFs) in this study were extracted using bimaterial crack tip field equations. The mode-I and mode-II stress intensity factors (SIFs) were evaluated by an over-deterministic least-squares analysis of crack-opening and crack-sliding displacements, respectively. The governing asymptotic expressions for crack-opening (v) and crack-sliding (u) displacement fields near the tip of a dynamically loaded stationary or steadily growing bimaterial interface crack are given by Deng [135],

$$\begin{Bmatrix} u(r,\theta) \\ v(r,\theta) \end{Bmatrix} = \sum_{n=0}^{\infty} r^{\frac{n+1}{2}} \frac{\mathrm{Re}\left[\eta_n^I \left(K_I\right)_n r^{i\varepsilon_n}\right]}{\sqrt{2\pi}} \begin{Bmatrix} u_n^I(\theta) \\ v_n^I(\theta) \end{Bmatrix} + \sum_{n=0}^{\infty} r^{\frac{n+1}{2}} \frac{\mathrm{Im}\left[\eta_n^{II} \left(K_{II}\right)_n r^{i\varepsilon_n}\right]}{\sqrt{2\pi}} \begin{Bmatrix} u_n^{II}(\theta) \\ v_n^{II}(\theta) \end{Bmatrix} \tag{6.2}$$

where r and θ are the polar coordinates defined at the current crack-tip, $\varepsilon_n = \varepsilon$, $\eta_n^I = 1$, and $\eta_n^{II} = \eta$ when $n = 0, 2, 4, \ldots$, and $\varepsilon_n = 0$, $\eta_n^I = \eta$, and $\eta_n^{II} = 1$ when $n = 1, 3, 5, \ldots$, ε is

the oscillation index, η is the mismatch parameter. In Eq. (6.2), terms corresponding to n = 0 provide the oscillatory singular crack-tip fields and the coefficients[2] of $\left(K_I\right)_n$ and $\left(K_{II}\right)_n$ of the dominant terms (n = 0) are the dynamic SIFs, respectively. In this work, SIF values were extracted using dominant terms (n = 0) at crack initiation and in the post-initiation regime, therefore, explicit expressions for displacement fields for steadily growing interface cracks in dissimilar isotropic materials were employed [135]:

$$u_n^I(\theta)=\frac{1}{\mu D\left[(n+1)^2+4\varepsilon^2\right]\cosh\pi\varepsilon}\begin{Bmatrix}(n+1)\left[C_1(n+2,\varepsilon,\eta)+C_1(n+2,\text{-}\varepsilon,\text{-}\eta)\right]\\ \text{-}2\varepsilon\left[S_1(n+2,\varepsilon,\eta)\text{-}S_1(n+2,\text{-}\varepsilon,\text{-}\eta)\right]\\ +\alpha_2(n+1)\left[C_2(n+2,\varepsilon,\eta)+C_2(n+2,\text{-}\varepsilon,\text{-}\eta)\right]\\ \text{-}2\alpha_2\varepsilon\left[S_2(n+2,\varepsilon,\eta)\text{-}S_2(n+2,\text{-}\varepsilon,\text{-}\eta)\right]\end{Bmatrix} \tag{6.3}$$

$$u_n^{II}(\theta)=\frac{1}{\eta\mu D\left[(n+1)^2+4\varepsilon^2\right]\cosh\pi\varepsilon}\begin{Bmatrix}(n+1)\left[S_1(n+2,\varepsilon,\eta)-S_1(n+2,-\varepsilon,-\eta)\right]\\ +2\varepsilon\left[C_1(n+2,\varepsilon,\eta)+C_1(n+2,-\varepsilon,-\eta)\right]\\ +\alpha_2(n+1)\left[S_2(n+2,\varepsilon,\eta)-S_2(n+2,-\varepsilon,-\eta)\right]\\ +2\alpha_2\varepsilon\left[C_2(n+2,\varepsilon,\eta)+C_2(n+2,-\varepsilon,-\eta)\right]\end{Bmatrix} \tag{6.4}$$

$$v_n^I(\theta)=\frac{1}{\mu D\left[(n+1)^2+4\varepsilon^2\right]\cosh\pi\varepsilon}\begin{Bmatrix}\alpha_1(n+1)\left[S_1(n+2,\varepsilon,\eta)+S_1(n+2,-\varepsilon,-\eta)\right]\\ -2\alpha_1\varepsilon\left[-C_1(n+2,\varepsilon,\eta)+C_1(n+2,-\varepsilon,-\eta)\right]\\ +(n+1)\left[S_2(n+2,\varepsilon,\eta)+S_2(n+2,-\varepsilon,-\eta)\right]\\ -2\varepsilon\left[-C_2(n+2,\varepsilon,\eta)+C_2(n+2,-\varepsilon,-\eta)\right]\end{Bmatrix} \tag{6.5}$$

[2] Subscripts and superscripts *I* and *II* are used instead of traditional 1 and 2 notation for ease of transitioning from bimaterial fracture mechanics equations to the homogeneous ones.

$$v_n^{II}(\theta)=\frac{1}{\eta\mu D\left[(n+1)^2+4\varepsilon^2\right]\cosh\pi\varepsilon}\begin{Bmatrix}\alpha_1(n+1)\left[-C_1(n+2,\varepsilon,\eta)+C_1(n+2,-\varepsilon,-\eta)\right]\\+2\alpha_1\varepsilon\left[S_1(n+2,\varepsilon,\eta)+S_1(n+2,-\varepsilon,-\eta)\right]\\+(n+1)\left[-C_2(n+2,\varepsilon,\eta)+C_2(n+2,-\varepsilon,-\eta)\right]\\+2\varepsilon\left[S_2(n+2,\varepsilon,\eta)+S_2(n+2,-\varepsilon,-\eta)\right]\end{Bmatrix} \tag{6.6}$$

where,

$$C_1(n,\varepsilon,\eta)=-r_1^{(n-1)/2}e^{\varepsilon(\pi-\theta_1)}\left[2\alpha_2\eta-\left(1+\alpha_2^2\right)\right]\cos\left(\frac{n-1}{2}\theta_1+\varepsilon\ln r_1\right)$$

$$S_1(n,\varepsilon,\eta)=r_1^{(n-1)/2}e^{\varepsilon(\pi-\theta_1)}\left[2\alpha_2\eta-\left(1+\alpha_2^2\right)\right]\sin\left(\frac{n-1}{2}\theta_1+\varepsilon\ln r_1\right)$$

$$C_2(n,\varepsilon,\eta)=-r_2^{(n-1)/2}e^{\varepsilon(\pi-\theta_2)}\left[2\alpha_1-\eta\left(1+\alpha_2^2\right)\right]\cos\left(\frac{n-1}{2}\theta_2+\varepsilon\ln r_2\right)$$

$$S_2(n,\varepsilon,\eta)=r_2^{(n-1)/2}e^{\varepsilon(\pi-\theta_2)}\left[2\alpha_1-\eta\left(1+\alpha_2^2\right)\right]\sin\left(\frac{n-1}{2}\theta_2+\varepsilon\ln r_2\right)$$

$$r_m=\sqrt{x^2+\alpha_m^2y^2},\ \theta_m=\tan^{-1}\left(\frac{\alpha_m y}{x}\right),\quad m=1,2,\quad \alpha_1=\sqrt{1-\left(\frac{c}{C_L}\right)^2},\quad \alpha_2=\sqrt{1-\left(\frac{c}{C_S}\right)^2}$$

$$C_L=\sqrt{\frac{(\kappa+1)\mu}{(\kappa-1)\rho}},\qquad C_S=\sqrt{\frac{\mu}{\rho}},\quad \kappa=\frac{3-\upsilon}{1+\upsilon}\ \text{for plane stress}$$

$$D=4\alpha_1\alpha_2-\left(1+\alpha_2^2\right)^2,\qquad \varepsilon=\frac{1}{2\pi}\ln\frac{1-\beta}{1+\beta} \tag{6.7}$$

In the above equations, (x, y) are the instantaneous Cartesian coordinates situated at the current crack-tip, c is the crack-tip velocity, C_L and C_S are longitudinal and shear wave speeds, ρ is the mass density, β is one of the two Dundurs' elastic mismatch parameters, μ and υ are shear modulus and Poisson's ratio, respectively. Further, Eqs. (6.3) – (6.7) can be reduced to the form of a dynamically loaded stationary crack in the limit the crack velocity $c\to 0$. Moreover, when the oscillation index ε becomes zero, the bimaterial equations reduce to the ones for the homogeneous case. Thus, these equations

can be used to extract crack-tip parameters over the entire history of crack growth during fracture event.

In order to extract SIF history, the crack-opening and crack-sliding displacement fields were digitized by identifying the current crack-tip location. The displacement data used in the analysis was collected in the vicinity of the crack-tip and limited to the region $0.3 < r/B < 1.5$ and ($-150^{\circ} \leq \theta \leq -90^{\circ}$ and $90^{\circ} \leq \theta \leq 150^{\circ}$) as it has been shown that 3D deformations are minimum in this region. At each data point, v and u displacement values as well as the location of these points were stored. The digitized data were used in Eq. (6.2) along with an over-deterministic least-squares analysis scheme in order to estimate the two SIFs. This process was carried out for all 32 image pairs and the SIF histories were generated. Due to mixed-mode crack growth in the inclusion vicinity, the SIFs were used to evaluate an effective SIF, K_e, and mode-mixity, ψ as,

$$K_e = \sqrt{K_I^2 + K_{II}^2} = \sqrt{K_1^2 + K_2^2} \tag{6.8}$$

$$\psi = \tan^{-1}\left(\frac{K_{II}}{K_I}\right) \text{ or } \tan^{-1}\left(\frac{K_2}{K_1}\right) \text{ or } \tan^{-1}\left(\frac{\mathrm{Im}\left(Ka^{i\varepsilon}\right)}{\mathrm{Re}\left(Ka^{i\varepsilon}\right)}\right) \tag{6.9}$$

where a is a length parameter, chosen to be unity in this study, and ε is the oscillation index as defined previously. In this work, the value of ε ranges from 0.096 to 0.156 for the stiff inclusion and -0.0886 for the compliant inclusion for interface crack growth as a function of crack-tip velocity at the inclusion-matrix interface and zero for crack propagation in the matrix.

6.3 Experimental Results

6.3.1 Crack-inclusion interaction scenarios

The pre-notched fracture specimens embedded with weakly and strongly bonded symmetric ($e = 0$) and eccentric ($e = 3d/4$), stiff and compliant inclusions were subjected to symmetric impact loading. Photographs of eight fractured samples from each configuration representing different crack-inclusion interaction scenarios are shown in Fig. 6.2. The impact occurs on the top edge of each image and the initial crack-tip is at the bottom edge as indicated. The location of cylindrical inclusion is shown by a dotted circle and the vertical broken arrow indicates the direction of crack propagation. (In all the photographs in Fig. 6.2, it can be seen that just before the upper edge of the specimens, the crack path deviates noticeably due to a combination of free-edge and impact point interactions). In each configuration, the crack propagates self-similarly until it reached the inclusion-matrix interface vicinity and significant differences in crack paths occur subsequently and are discussed in the following sections.

6.3.1.1 Weakly bonded stiff and compliant inclusion (e = 0)

The crack trajectories for the cases of symmetrically located weakly bonded stiff and compliant inclusions ($e = 0$) are shown in Figs. 6.2(a) and (b). In both cases, it can be seen that once inclusion-matrix interface debonded, the crack was momentarily arrested after it circumscribed the interface covering a distance of approximately half the inclusion circumference. In the case of stiff inclusion, the crack reinitiated in a mode-I fashion with approximately zero offset distance with respect to the initial crack path whereas high frequency irregularity in the crack path can be noticed in the compliant

case. These features in the latter indicate greater energy dissipation for compliant inclusion compared to the stiff one.

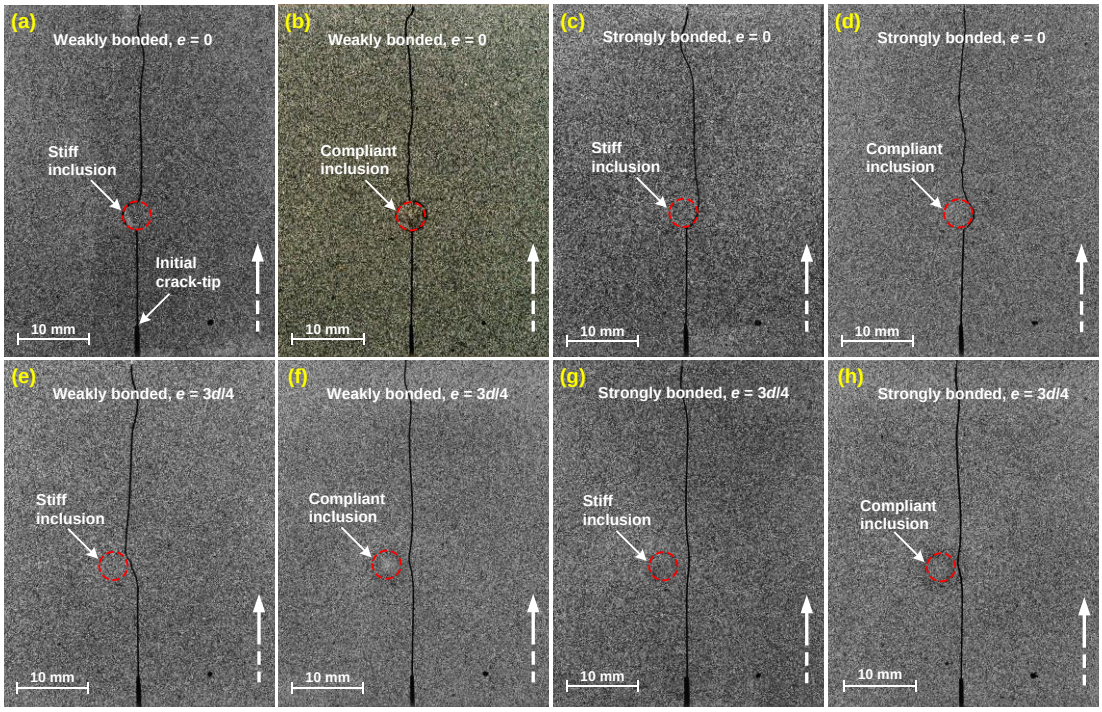

Fig. 6.2: Photographs of fractured stiff and compliant inclusion specimens showing different crack-inclusion interaction scenarios: **(a)** Weakly bonded stiff inclusion (e = 0), **(b)** Weakly bonded compliant inclusion (e = 0), **(c)** Strongly bonded stiff inclusion (e = 0), **(d)** Strongly bonded compliant inclusion (e = 0), **(e)** Weakly bonded stiff inclusion (e = 3d/4), **(f)** Weakly bonded compliant inclusion (e = 3d/4), **(g)** Strongly bonded stiff inclusion (e = 3d/4), **(h)** Strongly bonded compliant inclusion (e = 3d/4). The black dot adjacent to initial crack-tip denotes the reference mark and the broken arrow indicates crack propagation direction.

6.3.1.2 Strongly bonded stiff and compliant inclusion (e = 0)

Figs. 6.2(c) and (d) show crack growth behavior for the cases of symmetrically located and strongly bonded stiff and compliant inclusions (e = 0). Initially, the crack was arrested in both stiff and compliant cases as it approached the inclusion vicinity. The crack circumvented the inclusion in both cases but to a lesser extent in the stiff inclusion compared to the compliant one and then deflected away from inclusion-matrix interface,

nearly tangentially, before propagating in a nearly mode-I fashion. After crack-inclusion interaction, the crack propagated at an offset of about half the inclusion diameter in the stiff inclusion case compared to the compliant one. Similar to the weakly bonded compliant inclusion case, the crack path in the strongly bonded case also shows high frequency irregularity in crack path hinting at a higher energy dissipation (see Figs. 6.2(b) and (d)).

6.3.1.3 Weakly bonded stiff and compliant inclusion (e = 3d/4)

When the inclusion is not in the prospective crack path but positioned eccentrically ($e = 3d/4$), the crack trajectories in the vicinity of the inclusion are different when compared to the symmetrically located inclusion case. Figs. 6.2(e) and (f) show crack paths for weakly bonded stiff and compliant eccentric cases. In case of the stiff inclusion, it is clearly evident that the crack was attracted towards the weak inclusion-matrix interface and left the inclusion vicinity and tended to follow the initial crack path, whereas in the compliant case, as the crack approached the inclusion vicinity, it was attracted by the inclusion and to a lesser extent when compared to the stiff inclusion case. Subsequently the crack propagated along a mode-I path.

6.3.1.4 Strongly bonded stiff and compliant inclusion (e = 3d/4)

The eccentric cases for strongly bonded stiff and compliant inclusions are shown in Figs. 6.2(g) and (h), respectively. It is interesting to note that eccentric cases show opposite crack trajectories when bonded strongly. From Fig. 6.2(g), it can be seen that as the crack approached the inclusion vicinity, the stronger inclusion-matrix interface in the stiff case forced the crack to deflect away from the inclusion before returning to a

nominally mode-I path. On the other hand, as shown in Fig. 6.2(h), the crack was attracted by the compliant inclusion even for a strong inclusion-matrix bonding.

6.3.2 Surface deformation histories

A selected speckle image of 30 x 30 mm^2 region-of-interest from each experiment is shown in Fig. 6.3. The time instant (t) at which the images were recorded after impact is shown on each image and the arrow indicates the current crack-tip position. Note that in Fig. 6, the speckle images are shown at nearly the same time instant (t ~192 μs) except in two cases due to slightly different recording rates used. From Figs. 6.2 and 6.3, it is worth noting the effects of inclusion stiffness, inclusion eccentricity and inclusion-matrix adhesion strength on crack trajectories.

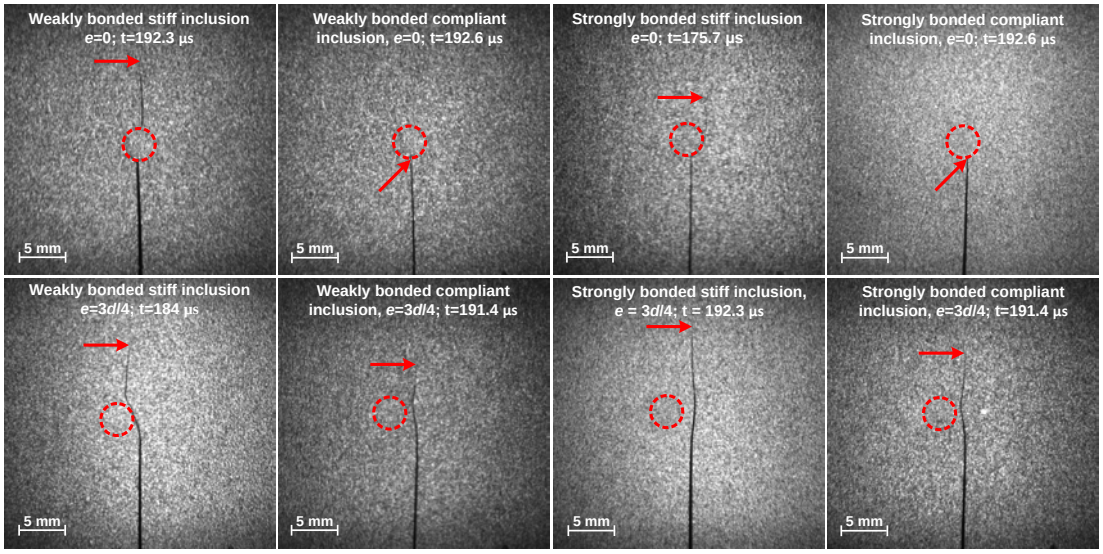

Fig. 6.3: Selected speckle images of 30 x 30 mm^2 region-of-interest at different time instants recorded by Cordin-550 ultra high-speed digital camera. The dotted circle represents inclusion location and arrow indicates current crack-tip position.

For symmetrically located inclusion (e = 0) cases, the crack front was momentarily trapped at the weak interface compared to the stronger one in the stiff inclusion case,

whereas in both weakly and strongly bonded compliant inclusion specimens, the crack experienced a substantial crack arrest event. In the eccentric inclusion (e = 3d/4) cases, the crack was clearly attracted by the weak inclusion-matrix interface whereas the strong inclusion-matrix interface led to crack deflection in the stiff inclusion cases. On the other hand, in the compliant inclusion specimens, the crack was attracted by both weak and strong inclusion-matrix interfaces.

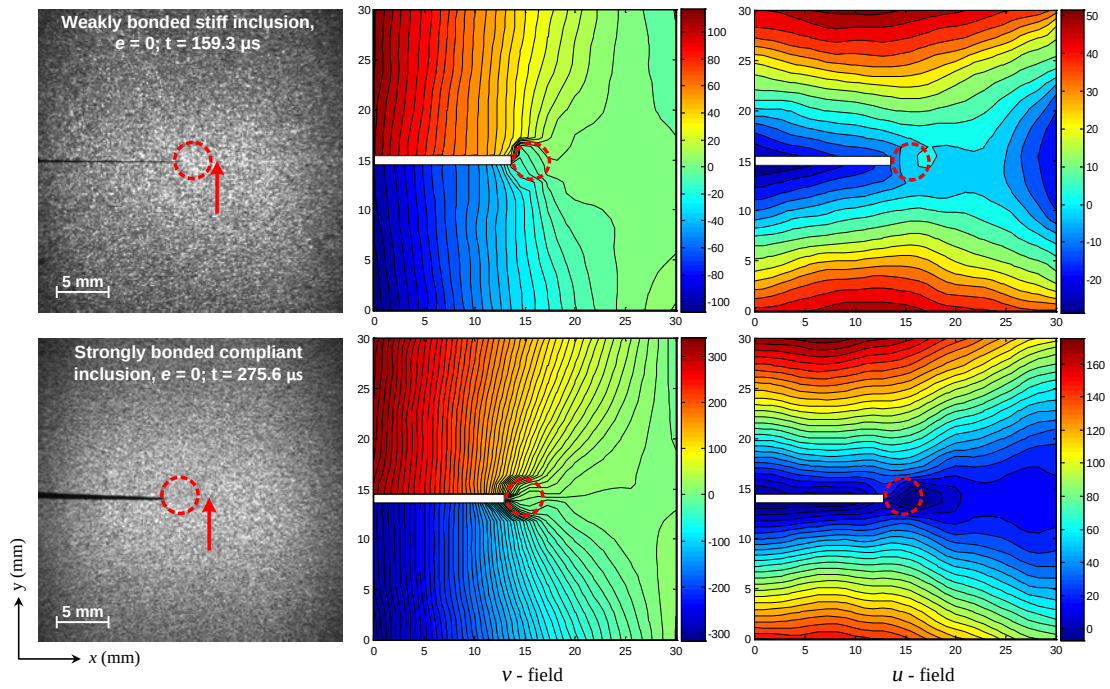

Fig. 6.4: Representative speckle images of 30 x 30 mm^2 region-of-interest for weakly bonded stiff inclusion and strongly bonded compliant inclusion specimens at eccentricity, e = 0 with full-field crack-opening (v-field) and crack-sliding (u-field) displacement contours. (Contour interval: 5μm for stiff and 7μm for compliant inclusion specimens). Color-bars indicate displacements in μm. The location of cylindrical inclusion is represented by dotted circle and arrow indicates the current crack-tip position in the speckle images.

Two representative speckle images (rotated clockwise by 90° relative to Fig. 6.3) along with the corresponding full-field crack-opening (v–field or displacement along the y-axis) and crack-sliding (u-field or displacement along the x-axis) displacement contours

for weakly bonded stiff and strongly bonded compliant inclusion specimens at eccentricity e = 0 are shown in Fig. 6.4. In this work, displacements were obtained as a matrix of 40 x 40 data points in the inclusion-matrix vicinity for each image pair and full-field displacement contours with 5 μm (stiff inclusion) and 7 μm (compliant inclusion) intervals are shown. In the v–field, contour lines (magnitude) are symmetric relative to the crack path before the crack interacts with the inclusion suggesting dominant mode-I conditions. The perturbations in displacements around the inclusion can be seen when the crack reaches the inclusion. Also, perturbations in contour lines in the inclusion vicinity become more prominent as debonding of the inclusion occurs in both cases. It should be noted that the contours lines within the stiff inclusion are nearly parallel to each other and equally spaced implying rigid rotation of the inclusion after debonding, whereas in the compliant inclusion, the isolines show non-uniformity and hence straining of the inclusion due to compliancy. This difference in the inclusion deformations was confirmed by performing quasi-static experiments carried out on three-point bend specimens with stiff and compliant inclusions near a stationary crack. Some of the experimental details are included in Appendix-A for completeness.

6.3.3 Experimental repeatability

To ensure repeatability in the observed fracture behavior multiple experiments (2-3 specimens per configuration) were performed for both stiff and compliant inclusion cases at eccentricities e = 0, 3d/4 as well as the two adhesion strengths. A few cases are shown in Fig. 6.5. Figs. 6.5(a)-(d) show right-half ligaments of two fractured stiff and compliant inclusion specimens for each weakly bonded (e = 0) and strongly bonded (e = 3d/4) configurations. A rather high degree of reproducibility in crack paths including several

macroscale surface features is clearly evident. More importantly, distinctly different crack-inclusion interaction scenarios can be seen in these four configurations. The ligaments holding glass inclusions in Fig. 6.5(a) show good repeatability in the crack path selection. An excellent repeatability in fractured surface ruggedness is also quite evident in weakly bonded compliant inclusion specimens in Fig. 6.5(b). The crack deflection is clearly visible in each ligament shown in Fig. 6.5(c) whereas crack attraction by the compliant inclusion can be seen in Fig. 6.5(d).

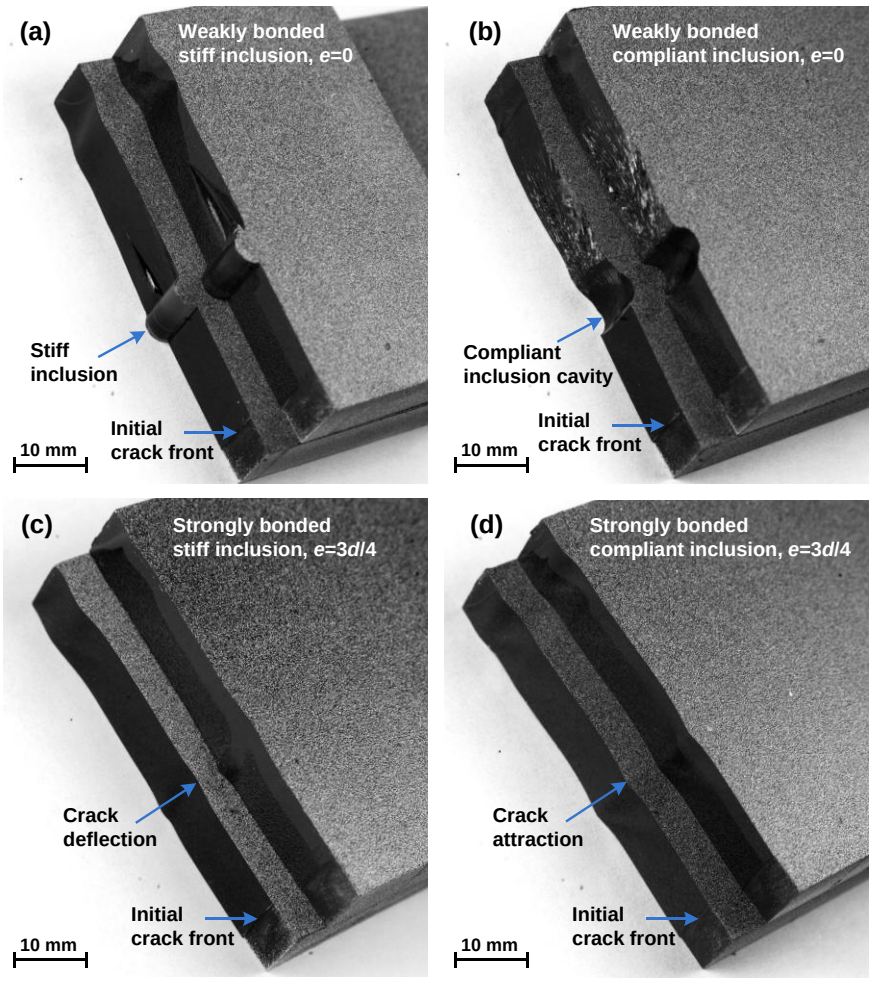

Fig. 6.5: Right-half ligaments of fractured stiff and compliant inclusion specimens from multiple experiments demonstrating experimental repeatability: **(a)** Weakly bonded stiff inclusion (e = 0), **(b)** Weakly bonded compliant inclusion (e = 0), **(c)** Strongly bonded stiff inclusion (e = 3d/4), **(d)** Strongly bonded compliant inclusion (e = 3d/4).

Also, the photographs in Fig. 6.5 demonstrate that the crack propagated in a dominant mode-I fashion *before* and *after* the encounter with the inclusion. Thus, similarity of crack growth behavior, surface roughness, and crack attraction and deflection mechanisms in multiple samples indicates the robustness and repeatability of experiments reported in this study.

6.3.4 Impactor force histories

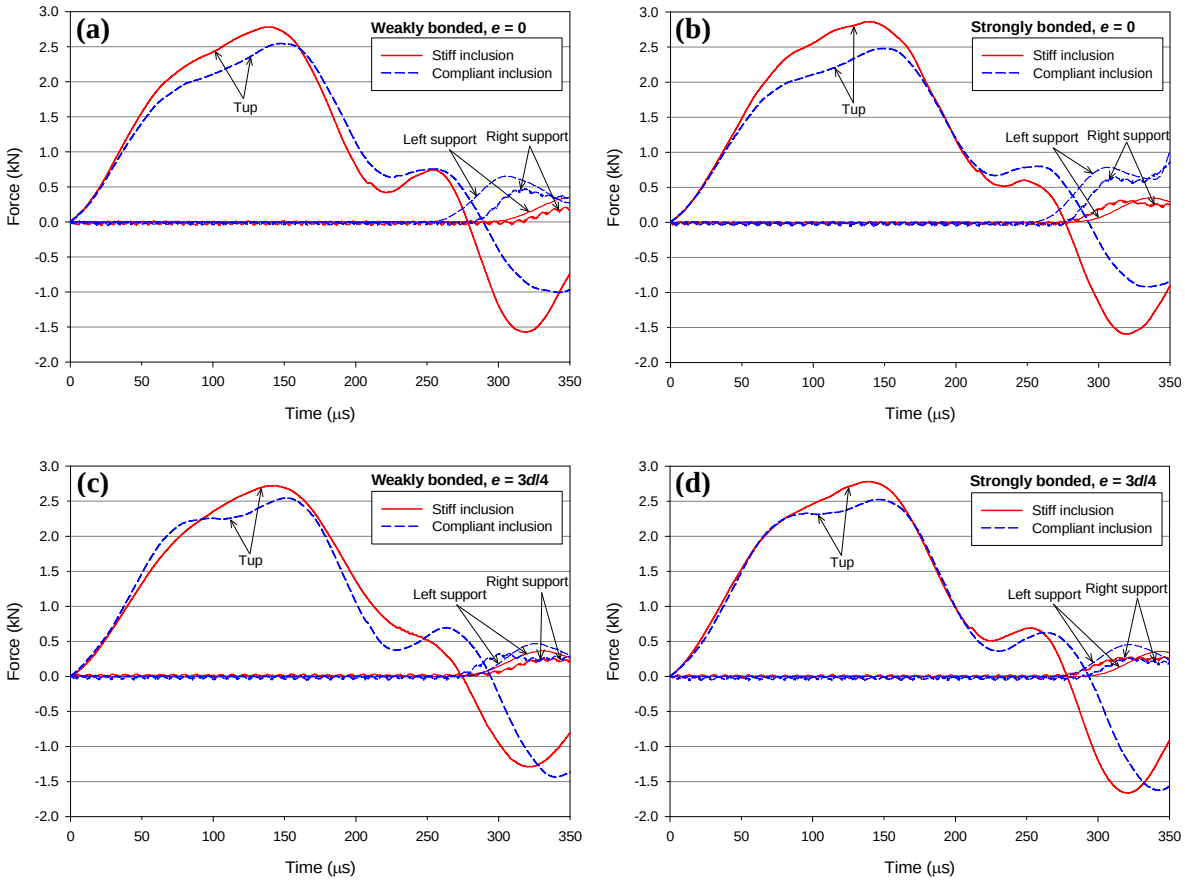

Fig. 6.6: Impactor force and support reaction histories recorded by Instron Dynatup 9250HV drop tower for stiff and compliant inclusion specimens: **(a)** Weakly bonded (e = 0), **(b)** Strongly bonded (e = 0), **(c)** Weakly bonded (e = 3d/4), **(d)** Strongly bonded (e = 3d/4). (Note that the tup forces are shown as positive instead of negative.)

The tup and anvil load histories were recorded for each experiment and are shown in Fig. 6.6 for weakly and strongly bonded stiff and compliant inclusion specimens. The crack initiated at about 120 and 135 μs and complete fracture of the specimen occurred in about 220 and 300 μs after impact in stiff and compliant inclusion specimens, respectively. Thus, only the dominant peak of the tup load history is significant. From Figs. 6.6(a)-(d), note that the peak impact force (compressive) recorded by the tup in the stiff inclusion specimens is higher than the compliant ones. The reaction histories were captured by the two instrumented anvils and it can be seen that supports feel the reaction force only after 300 μs by which time the crack had already traversed the entire specimen width. This shows that reaction forces from support anvils do not contribute to the crack initiation and growth in the specimens, suggesting that a free-free cracked beam should suffice analytical or computational modeling of these experiments in the future.

6.3.5 Effect of inclusion stiffness on crack growth behavior

The crack length histories for each specimen configuration are plotted[3] in Fig. 6.7. In this plot, the crack-initiation is denoted by $t - t_i = 0$ so that the positive and negative values correspond to the post-initiation and pre-initiation periods, respectively. Here t_i indicates the time at crack-initiation after impact. The region between the two vertical broken lines *qualitatively* suggests the duration of crack-inclusion interaction.

Figs. 6.7(a) and (b) show crack length histories for weakly and strongly bonded, symmetrically located ($e = 0$), stiff and compliant inclusion specimens, respectively. In the stiff inclusion case (see Fig. 6.7(a)), following initiation, a monotonic crack growth is

[3] In this work, the inter frame time varies due to different framing rates employed for stiff (300,000 fps) and compliant (150,000 – 250,000 fps) inclusion experiments. Hence, for clarity, the fracture parameters for stiff and compliant inclusion specimens are plotted separately instead of plotting on the same graph.

evident and as the crack approached the inclusion, the rate of crack extension drops modestly before increasing at a much faster rate in the crack-inclusion vicinity as it gets attracted by the interface. Unlike the weakly bonded inclusion case, the crack growth is slower in the region *before* the crack interacts with the strongly bonded inclusion and in the inclusion vicinity an abrupt jump in crack length can be noticed but this jump is lower than the one for the weakly bonded case.

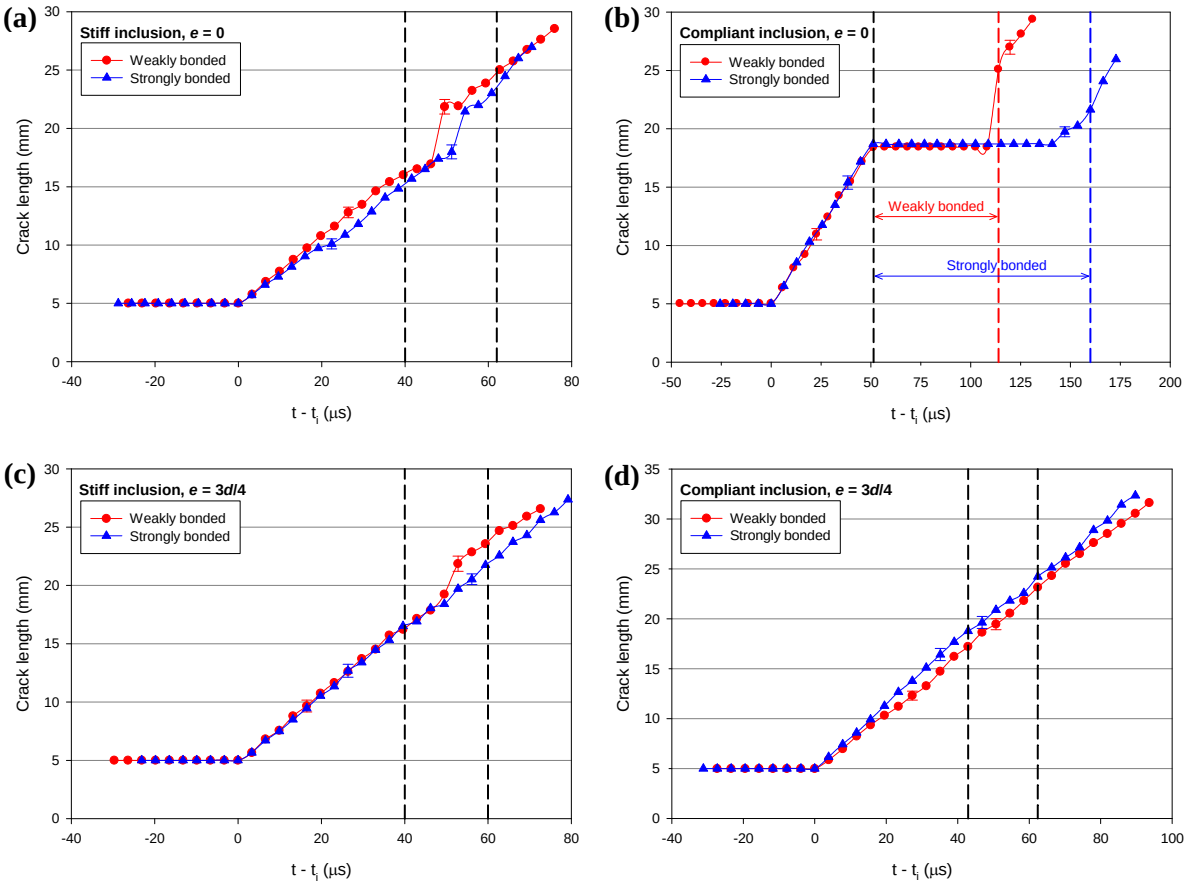

Fig. 6.7: Crack length histories for weakly and strongly bonded inclusion specimens: **(a)** Stiff inclusion (e = 0), **(b)** Compliant inclusion (e = 0), **(c)** Stiff inclusion (e = 3d/4), **(d)** Compliant inclusion (e = 3d/4). The region between vertical broken lines represents crack-inclusion vicinity.

The crack is momentarily arrested at the inclusion-matrix interface before it continues to grow again. As it leaves the inclusion vicinity, the crack grows at the same rate in both

weakly and strongly bonded inclusion cases. On the other hand, in Fig. 6.7(b) it is interesting to note that after initiation the crack propagates steadily before it interacts with the compliant inclusion and then the crack growth ceases at inclusion-matrix interface for about 60 and 100 μs in the case of weakly and strongly bonded compliant inclusion, respectively. Note that, this is about a third to a half of the total observation window. Subsequently, the crack reinitiates much earlier and faster in the weakly bonded case when compared to the strongly bonded one followed by a monotonic propagation until complete fracture.

The crack length histories when the stiff and compliant inclusions are located eccentrically ($e = 3d/4$) are shown in Figs. 6.7(c) and (d), respectively. In Fig. 6.7(c) it can be seen that, in stiff inclusions specimens, before the crack reaches the inclusion vicinity it grows at a constant rate and the crack extension histories for both weakly and strongly bonded inclusion cases coincide. In the crack-inclusion vicinity and beyond, the weakly bonded inclusion shows a faster crack growth compared to the strongly bonded counterpart in which crack growth remains nominally undisturbed. On the contrary, in case of the compliant inclusion specimens as depicted in Fig. 6.7(d), crack growth is slow in the weakly bonded case compared to the strongly bonded one and crack extension histories do not coincide throughout the fracture event.

The instantaneous values of crack lengths were subsequently used to estimate crack velocity histories and are plotted in Fig. 6.8. The effect of the type of inclusion and adhesion strength on crack velocity can be seen in these plots for both inclusion eccentricities. In Fig. 6.8(a), the symmetrically located ($e = 0$) stiff inclusion cases show nearly similar velocity profiles (300 m/s) until the crack encounters the inclusion. A drop

in velocity can be seen in both weakly and strongly bonded inclusions as the crack slows near inclusion-matrix interface just before re-initiation. The crack velocity drops to ~100 m/s and 210 m/s for weakly and strongly bonded inclusions, respectively. Subsequently, velocities in weakly and strongly bonded inclusions reach ~800 m/s and ~600 m/s, respectively, before the crack attains a steady velocity of ~300 m/s in both cases. Fig. 6.8(b) shows crack growth histories of weakly and strongly bonded compliant inclusion specimens. Upon initiation, crack accelerates and reaches a relatively steady velocity of

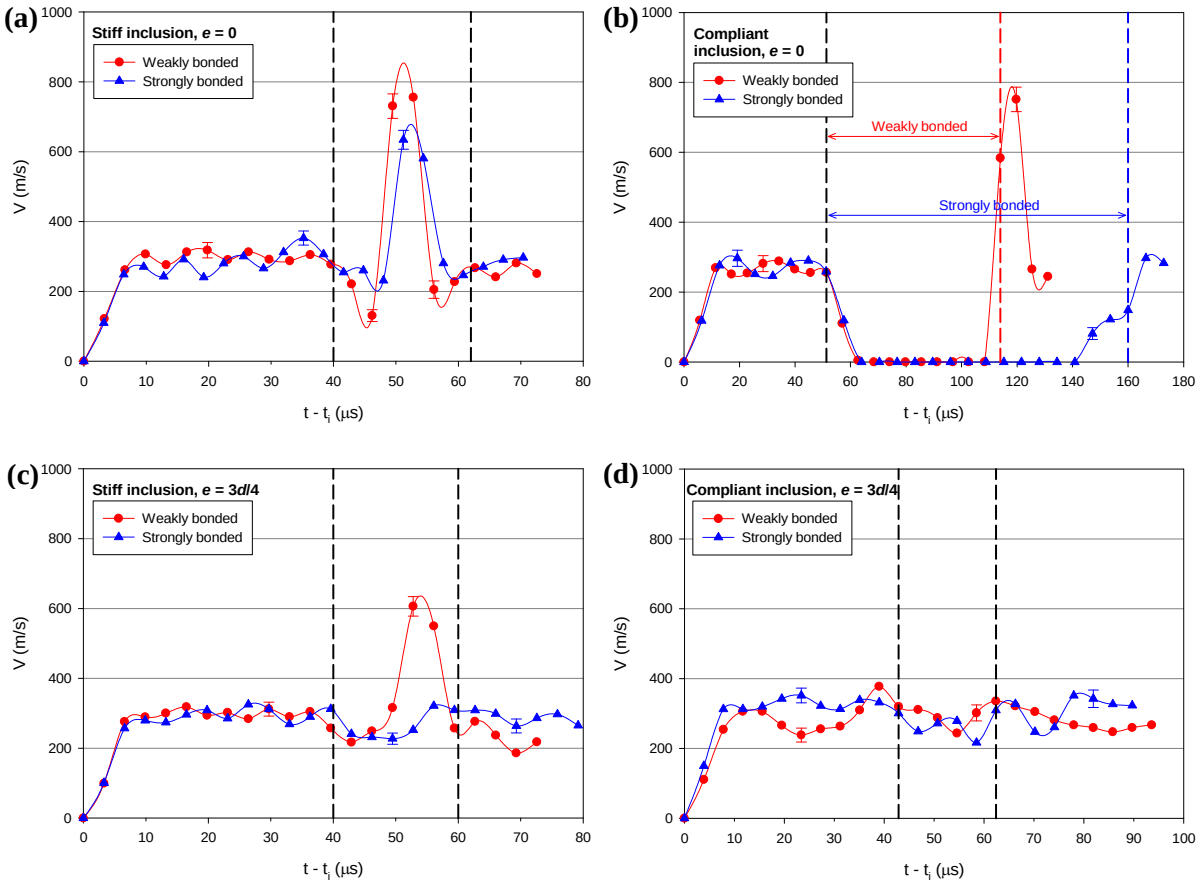

Fig.6.8: Crack tip velocity histories for weakly and strongly bonded inclusion specimens: **(a)** Stiff inclusion (e = 0), **(b)** Compliant inclusion (e = 0), **(c)** Stiff inclusion (e = 3d/4), **(d)** Compliant inclusion (e = 3d/4). The region between vertical broken lines represents crack-inclusion vicinity.

~300 m/s for about 50 μs and then decelerates when it encounters the compliant inclusion and gets completely stalled at the inclusion-matrix interface for about 60 and 100 μs for weakly and strongly bonded inclusions, respectively. Following this, the crack reinitiates with a velocity of ~600 m/s and accelerates to a velocity of ~780 m/s before slowing to ~300m/s in the weakly bonded case. On the other hand, for strongly bonded inclusion, the crack reinitiated more slowly to reach ~300 m/s in the observation window.

Figs. 6.8(c) and (d) show velocity data for weakly and strongly bonded stiff and compliant inclusion specimens, respectively, when the inclusion is placed eccentrically ($e = 3d/4$). Again, the velocity profiles are nearly similar until the crack reaches in the inclusion vicinity. In Fig. 6.8(c) it can been seen that for the weakly bonded case the maximum velocity reaches ~600 m/s as the crack is initially attracted and trapped at the inclusion by the weak interface, whereas a constant decrease in velocity can be seen for the strongly bonded case as the crack circumvents the inclusion. On the other hand, in the case of compliant inclusion specimens (Fig. 6.8(d)), the crack propagates relatively slowly in the weakly bonded inclusion case compared to the strongly bonded one as the crack overcomes the attraction by the inclusion in the former.

6.3.6 Role of inclusion stiffness on stress intensity factor (SIF) histories

The effects of inclusion stiffness and inclusion-matrix adhesion strength on SIFs are presented in Fig. 6.9. Effective SIF histories for weakly and strongly bonded stiff and compliant inclusion specimens are shown in Figs. 6.9(a) and (b), respectively, when the inclusion is located symmetrically ($e = 0$). In Fig. 6.9(a) for both cases, the effective SIF, K_e at initiation is ~1.3 MPa $m^{1/2}$. After initiation, a slight drop in K_e is evident, and it continues to increase modestly until it reaches a steady state value of ~1.8 MPa $m^{1/2}$.

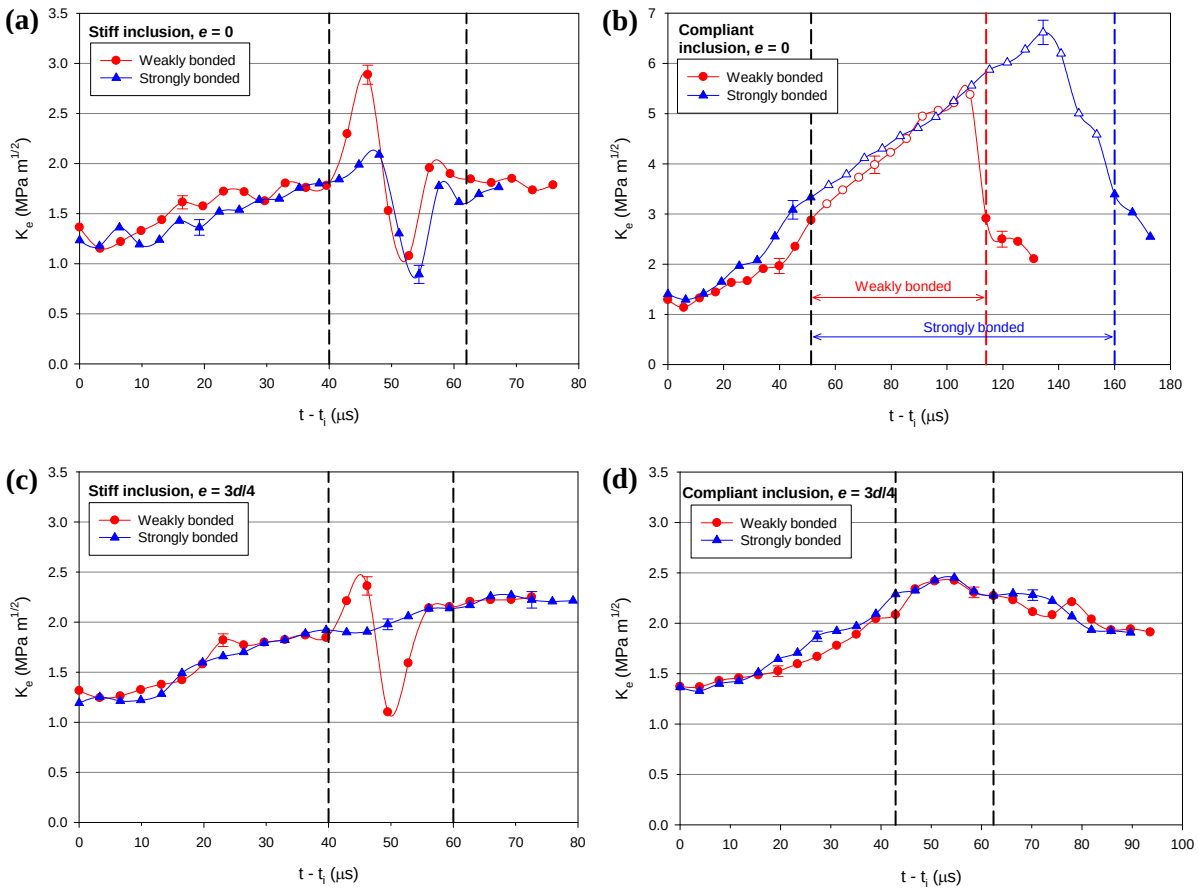

Fig. 6.9: Effective stress intensity factor (K_e) histories for weakly and strongly bonded inclusion specimens: **(a)** Stiff inclusion (e = 0), **(b)** Compliant inclusion (e = 0); (Note that open symbols represent the approximation of data analysis using homogeneous dynamic crack-tip fields due to the lack of asymptotic descriptions at the moment), **(c)** Stiff inclusion (e = 3d/4), **(d)** Compliant inclusion (e = 3d/4). The region between vertical broken lines represents crack-inclusion vicinity.

In the crack-inclusion vicinity, for the weakly bonded case, K_e attains a maximum value of ~2.9 MPa m$^{1/2}$ before dropping to ~1.0 MPa m$^{1/2}$ whereas for the strongly bonded counterpart the maximum value of K_e is ~2.1 MPa m$^{1/2}$ before falling to ~0.9 MPa m$^{1/2}$ followed by a steady value of ~1.7 MPa m$^{1/2}$ in both cases after the crack leaves the inclusion vicinity. A steep drop in K_e is quite evident for both weakly and strongly bonded inclusions due to interfacial debonding. This rise and fall in K_e values in the crack-inclusion vicinity is expected due to interfacial crack growth behavior around the

stiff-compliant inclusion-matrix interface. Fig. 6.9(b) represents effective SIF histories for compliant inclusion specimens at eccentricity e = 0. In this case, as observed previously from the crack-tip velocity histories (see Fig. 6.8(b)), the crack decelerates as it approaches the inclusion vicinity and completely stalls at the interface nearly perpendicular to the inclusion for about 60 and 100 μs for weakly and strongly bonded cases, respectively. It should be noted that when the crack front is perpendicular to the inclusion interface, crack-tip singularity is different from the ones described by Eqs. (6.3) – (6.7). In this scenario, there is a need for dynamic displacement fields of a crack terminating perpendicular to a bimaterial interface. Due to the current unavailability of dynamic field equations, the K_e values for e = 0, have been extracted using those as an approximation for a crack in a homogeneous material ($\varepsilon = 0$ in the Eqs. (6.3) – (6.7)). Hence, for the time instants when the crack-tip is nearly perpendicular to the inclusion interface, the K_e values in Fig. 6.9(b) are distinguished by open symbols. The K_e at initiation for both specimens is ~1.4 MPa $m^{1/2}$ followed by a modest increase before the crack reaches inclusion proximity. As the crack is arrested at the inclusion, there is a small jump in the K_e followed by a monotonic increase until it reaches a maximum value of ~5.5 and ~6.5 MPa $m^{1/2}$ for weakly and strongly bonded inclusions, respectively. Note that these values are 3-4 times higher than the SIF values during crack initiation in the matrix and is attributed to the crack-tip blunting as the inclusion suffers deformation. When the crack departs the inclusion proximity, K_e drops to ~3.0 MPa $m^{1/2}$ in the weakly bonded case whereas K_e decreases monotonically and reaches ~2.5 MPa $m^{1/2}$ for the strongly bonded inclusion in the observation window.

Figs. 6.9(c) and (d) depict effective SIF histories for weakly and strongly bonded stiff and compliant inclusion specimens, respectively, for eccentric inclusion cases. As noted in the symmetric cases, K_e at initiation in Fig. 6.9(c) is ~1.3 MPa $m^{1/2}$ followed by a slight drop and a monotonic increase until it attains a steady state value of ~1.9 MPa $m^{1/2}$ for both specimens. In the inclusion proximity, for the weakly bonded inclusion case, K_e increases up to ~2.4 MPa $m^{1/2}$ and subsequently drops to ~1.1 MPa $m^{1/2}$ whereas for strongly bonded one this remains unperturbed. The K_e values are nearly equal and overlap on each other as the crack propagates away from the inclusion proximity. For the compliant inclusion cases shown in Fig. 6.9(d), it can be seen that K_e is relatively higher in the strongly bonded case compared to weakly bonded counterpart before the crack interacts with the inclusion followed by nearly similar K_e profiles in the inclusion proximity and beyond.

Note that, the crack-tip singularity [136, 137] is affected when the crack front is completely stalled at the compliant inclusion interface and the corresponding K_e values represented in Fig. 6.9(b) are only estimates. Hence, an *ad-hoc* parameter related to crack-tip opening displacement, $\hat{\delta}_y$ (displacement between crack flanks) was calculated. The quantity $\hat{\delta}_y$ was chosen at a location of $r/B = 0.5$ from the *current* crack-tip position before, during, and after crack-inclusion interaction for weakly and strongly bonded compliant inclusion specimens ($e = 0$). The $\hat{\delta}_y(t)$ histories thus obtained are shown in Fig. 6.10. It should be noted that the quantity $\hat{\delta}_y$ is essentially similar to the SIF behavior. It can be seen that $\hat{\delta}_y$ increases monotonically before crack encounters the

inclusion and during crack-inclusion interaction when the crack stops at inclusion interface. Following this, $\hat{\delta}_y$ decreases in a monotonic fashion as the crack recedes from the inclusion. Therefore, it is worth noting that the observed trends in $\hat{\delta}_y$ are very much similar to SIF trends shown in Fig. 6.9(b) for both weakly and strongly bonded compliant inclusions ($e = 0$).

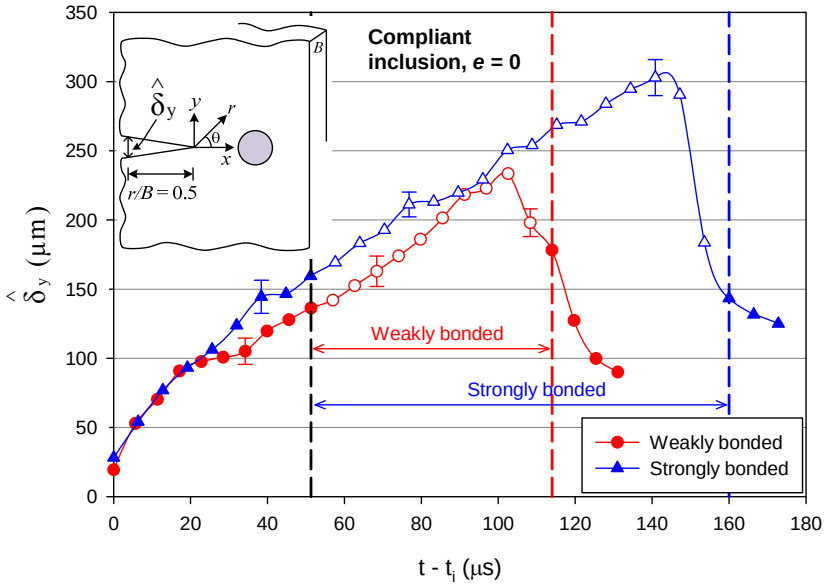

Fig. 6.10. An *ad-hoc* parameter related to crack-tip opening displacement, $\hat{\delta}_y$ at $r/B = 0.5$ from current crack-tip position for compliant inclusion specimens with $e = 0$. The region between vertical broken lines represents crack-inclusion vicinity.

6.3.7 Mode-mixity histories

The mode-mixity (ψ) histories are plotted in Fig. 6.11 for weakly and strongly bonded stiff and compliant inclusion cases ($e = 0$, $3d/4$). In Fig. 6.11(a), following crack initiation, a mildly oscillatory behavior of mode-mixity for about 20 μs can be seen. These oscillations can be attributed to measurement errors and/or transients due to crack initiation. Beyond these initial perturbations, a constant and positive ψ of about 2º is seen

before the crack interacts with the inclusion. (Within the data extraction accuracy, this value can be assumed to be zero.)

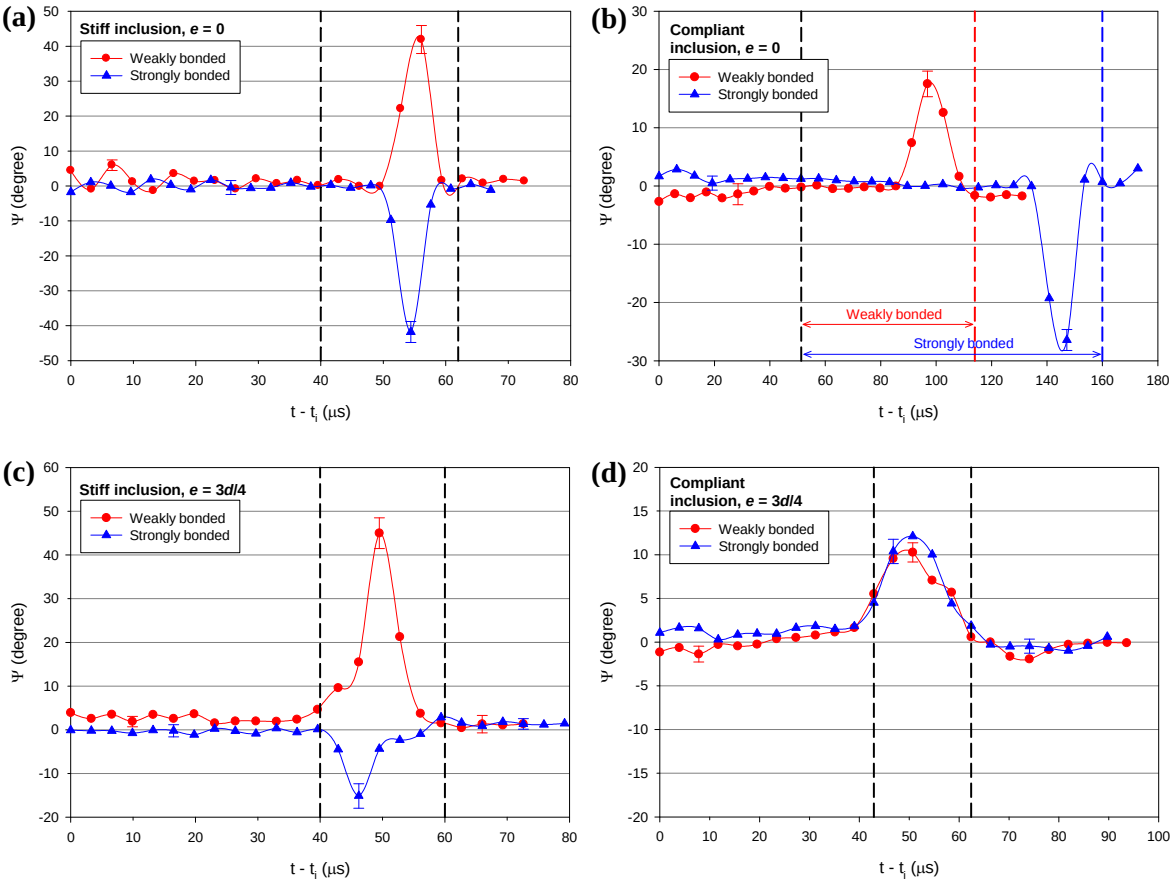

Fig. 6.11: Mode-mixity (ψ) histories for weakly and strongly bonded inclusion specimens: **(a)** Stiff inclusion (e = 0), **(b)** Compliant inclusion (e = 0), **(c)** Stiff inclusion (e = 3d/4), **(d)** Compliant inclusion (e = 3d/4). The region between vertical broken lines represents crack-inclusion vicinity.

When the crack-tip is in the inclusion vicinity a positive mode-mixity of approximately +42º is seen for the weakly bonded inclusion specimen whereas a negative mode-mixity of about -41º is observed for strongly bonded case. No significance is attached to the sign of mode-mixity as the crack can select paths above or below the inclusion with equal probability. In both cases, after the crack leaves inclusion proximity, ψ attains a constant

value of nearly 2º. The mode-mixity histories for compliant inclusion are shown in Fig. 6.11(b). The weakly bonded inclusion specimen shows a positive mode-mixity of about +18° in the inclusion vicinity whereas the strongly bonded counterpart shows a negative mode-mixity of about -28º in the inclusion proximity. The mode-mixity sign changes in these cases are attributed more to the chance associated with the crack path selection.Figs. 6.11(c) and (d) depict mode-mixity behaviors for stiff and compliant inclusion with eccentricity $e = 3d/4$, respectively. In Fig. 6.11(c), after the initial oscillatory period, the weakly bonded inclusion shows a monotonic increase in ψ as the crack approaches the inclusion vicinity whereas ψ remains close to zero in the strongly bonded case. Different mode-mixity behaviors can be seen as the crack nears the inclusion for both weakly and strongly bonded inclusion cases. For weakly bonded inclusion specimen, positive mode-mixity values are seen with a maximum of about +45º, indicating a significant attraction of the crack-tip by the weak interface. Contrary to the weakly bonded case, the negative mode-mixity behavior is noticed with a value of -15º suggesting that the crack is repelled by the strong inclusion-matrix interface. In Fig. 6.11(d), it can be seen that the weakly bonded inclusion specimen shows a positive ψ of approximately +10° in the crack-inclusion proximity, whereas positive mode-mixity is evident in the strongly bonded one throughout the fracture event with a maximum ψ of about +13° in the crack-inclusion vicinity. The positive value of ψ in both compliant specimens is expected as the crack is attracted towards the inclusion in both the specimens.

The positive and negative mode-mixity behaviors are consistent with the crack trajectories shown in Fig. 6.2 for all inclusion eccentricities and bond strengths in stiff

and compliant inclusion specimens indicating that the positive and negative mode-mixities signify crack- attraction and crack-repulsion mechanisms. Once the crack leaves the inclusion vicinity, mode-mixities tend to approach zero and crack propagation occurs under dominant mode-I conditions in both stiff and compliant inclusion specimens.

6.4 Role of Inclusion Stiffness on Fracture Surface Morphology

The fracture surface morphology often controls the process of dynamic fracture and reveals important clues about the underlying failure mechanisms and the associated energy dissipation characteristics. Accordingly, quantitative and qualitative fractographic examination was done to further understand the differences in crack growth behavior as a result of stiff and compliant nature of the inclusion, inclusion location and inclusion-matrix adhesion strength. Quantitative micro-measurements were carried out for the case of stiff inclusion specimens using a Dektak-150 stylus profiler with a stylus of root radius of 12.5 μm. Note that the quantitative measurements were not conducted in the case of compliant inclusion specimens due to the presence of high macroscale surface roughness. The fracture surface profiles were scanned at two different zones, just *before* and just *after* crack-inclusion interaction. Fig. 6.12 represents a schematic of crack growth in a glass inclusion specimen and the regions of interest (x-z plane) for roughness measurements are being highlighted *before* and just *after* crack-inclusion interaction. Here x- represents scanning length along which stylus was moved and y- denotes the asperity height. The scanning length of x = 2 and 5 mm was chosen in the region *before* and *after* crack-inclusion interaction respectively. The data was recorded at 3-4 different scan lines at different z- locations on either side of the centerline within the regions of

interest. The digitized data obtained from the surface profiler was processed to get average roughness *Ra* using,

$$R_a = \frac{1}{N}\sum_{n=1}^{N}\left|y(x)\right| = \frac{1}{L}\int_0^L y\,dx \tag{6.8}$$

where, N is the total number data points collected, L is the scan length and (x, y) are defined as shown in Fig. 6.12.

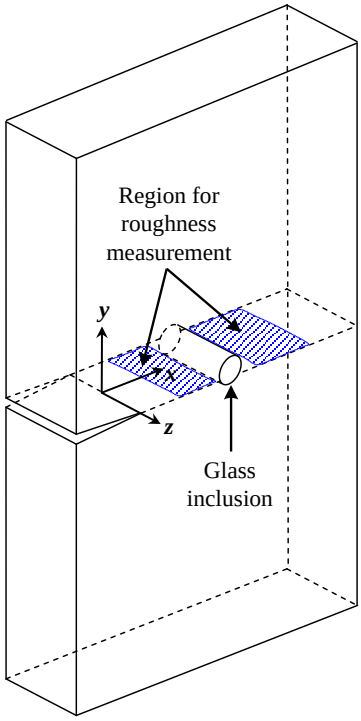

Fig. 6.12: Schematic representing crack growth in a inclusion embedded specimen for roughness measurement (x-z plane) before and after crack-inclusion interaction is also shown.

Fig. 6.13 shows a few representative surface profiles for weakly and strongly bonded stiff inclusion specimens for both eccentricities. (The region between vertical broken lines represents the location of the inclusion where scanning was not performed). The profiles between 0-2 mm and 6-11 mm represent the fracture surfaces just *before* and *after* crack-inclusion interaction. From Fig. 6.13 it can be seen that each surface profile is

qualitatively different from each other. The effects of inclusion-matrix bond strength as well as inclusion location are quite evident from these profiles. In Fig. 6.13(a), for symmetrically located inclusion (e = 0) surface profile amplitudes are much smaller in the region *before* crack interacts with inclusion when compared to the surface profiles *after* crack-inclusion interaction. In the region where the crack leaves the inclusion vicinity surface profiles are different from each other with larger amplitude and higher frequency content for the weakly bonded case when compared to the strongly bonded one. Further, the wavelength is smaller in the former compared to the latter. The surface profiles for $e = 3d/4$ case are shown in Fig. 6.13(b) where similar features can also be noticed. When comparing the surface profiles in the region *after* crack-inclusion interaction for both e = 0 and $3d/4$ cases, the surface profiles in asymmetric case show relatively smaller amplitudes with high frequency content when compared to the symmetric case.

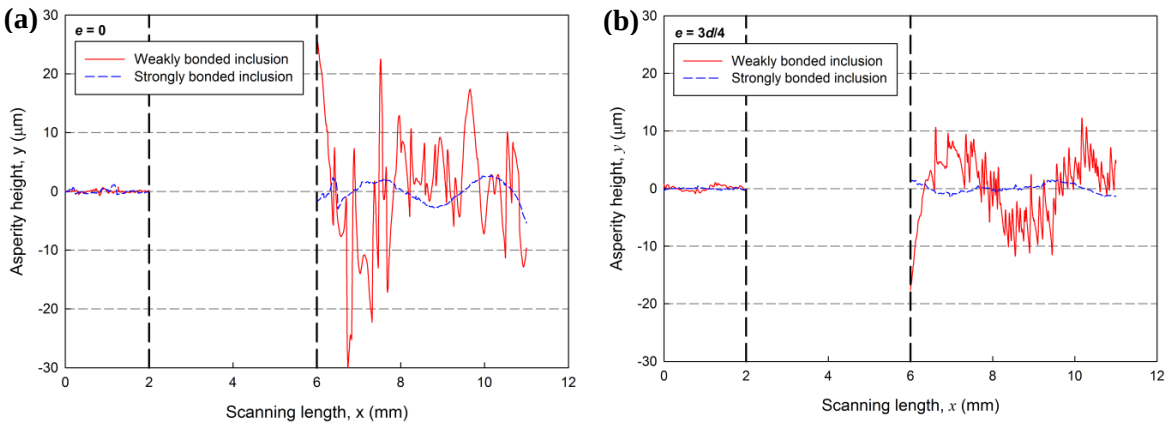

Fig. 6.13: Representative fracture surface profiles for weakly and strongly bonded stiff inclusion specimens for eccentricity: **(a)** e = 0, **(b)** $e = 3d/4$. The region between vertical broken lines represents inclusion location.

In order to quantify the variation of *Ra* along the direction of crack propagation, a longitudinal average roughness parameter Ra_x is used. The Ra_x was obtained by calculating *Ra* from data points collected for every 0.2 mm scan length in the region *before* and 0.5 mm scan length in the region *after* crack-inclusion interface. The Ra_x values thus obtained are plotted against scanning length in Fig. 6.14. The variation of Ra_x along scan length for symmetrically located inclusion (e = 0) is shown in Fig. 6.14(a). The Ra_x values are nearly equal in the region *before* the crack interacts with the inclusion for both bond strengths. On the other hand in the region *after* crack-inclusion interaction Ra_x values are much higher and show a decreasing trend for the weakly bonded inclusion when compared to the strongly bonded one where Ra_x values are almost constant. Similar trends can be seen for the case of $e = 3d/4$ and are shown in Fig. 6.14(b). In this case Ra_x values are relatively smaller than the e = 0 case.

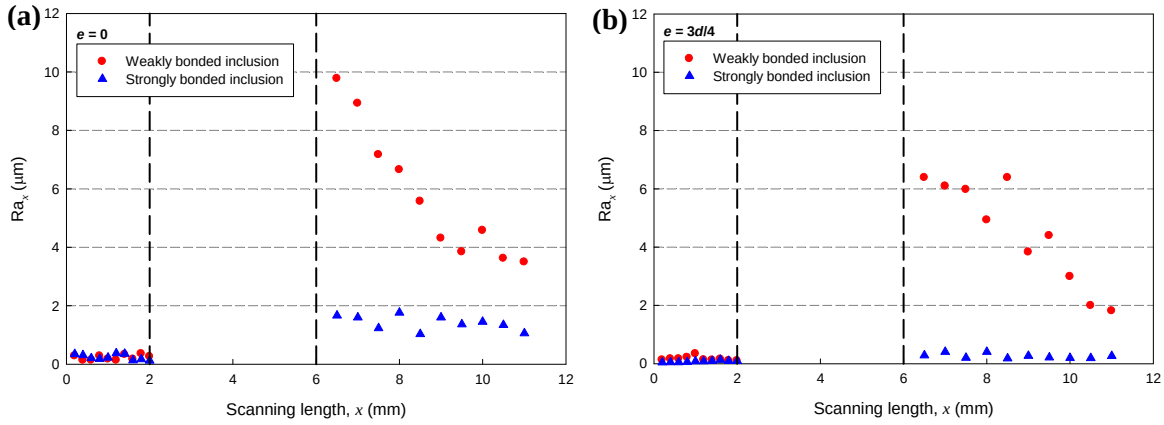

Fig. 6.14: Variation of fracture surface roughness along scanning length for weakly and strongly bonded stiff inclusion specimens with eccentricity: **(a)** e = 0, **(b)** $e = 3d/4$. The region between vertical broken lines represents inclusion location.

From the differences observed in these surface profiles and average roughness parameters shown in Figs. 6.13 and 6.14, it can be concluded that the weakly bonded glass inclusion results in much higher fracture surface roughness when compared to the

strongly bonded counterparts during dynamic crack growth. The average roughness values are nearly equal in the region *before* the crack interacts with the inclusion but the same are higher in the region *after* the crack leaves the inclusion proximity. Considering the effect of the inclusion location on roughness, the specimens with $e = 0$ configuration show relatively higher roughness values compared to $e = 3d/4$. In Figs. 6.13 and 6.14, the surface roughness can be viewed as the combination of the high frequency content indicating local energy dissipation and the low frequency content suggesting the tortuosity in crack path. The tortuosity is present in all cases; however there is always a limit on the amplitude of tortuosity. Therefore, the high frequency content comes into the picture when there is a need of further energy dissipation, that is, in the weakly bonded case. Furthermore, the amplitude of high frequency content depends upon the magnitude of the energy dissipation.

The differences in toughening mechanisms in stiff and compliant inclusions embedded in an epoxy matrix are explained by examining fracture surfaces as shown in Fig.6.15. The photographs of the entire *x*-*z* plane of dynamically fractured weakly and strongly bonded stiff and compliant inclusion specimens with eccentricities, $e = 0$ and $3d/4$ are shown in Figs. 6.15(a)-(h) with both ligaments of the fractured specimens, one ligament showing the inclusion cavity and the other showing the inclusion. The broken arrow indicates the direction of crack propagation. It can be seen that in all these macrographs, the fracture surfaces just before the crack reaches the inclusion are relatively smooth and shiny when compared to the region after it grows past the stiff and compliant inclusions, indicating brittle fracture.

Figs. 6.15(a)-(b) and (c)-(d) depict fracture surface morphology of weakly and strongly bonded stiff and compliant inclusion specimens (e = 0), respectively. In the weakly and strongly bonded stiff inclusion specimens (see Figs. 6.15(a) and (c)), fracture surfaces after crack-inclusion interaction consist of tails lines and river lines with high frequency tail lines in the former compared to the latter. In the compliant inclusion counterparts (see Figs. 6.15(b) and (d)), much higher surface roughness and ruggedness is clearly evident in both weakly and strongly bonded cases with high frequency of tail lines, larger and intensely rough region in the latter compared to the former. Further, it can be seen that the compliant inclusion in the strongly bonded case (see Fig. 6.15(d)) is surrounded by a pool (or pocket) of epoxy showing a strong inclusion-matrix bonding and clearly demonstrates that the roughening of compliant inclusion produced a strong inclusion-matrix interface (as discussed in the sample preparation section). It is interesting to note that this epoxy residue is maximum just before the crack encounters the inclusion. As the crack advances, the epoxy residue diminishes (tapers off) at the other end symmetrically with respect to the center of crack front. The fracture surfaces of both ligaments in case of the compliant inclusion (see Figs. 6.15(b) and (d)) reveal that a highly transient fracture has occurred after the crack front leaves the inclusion, showing very rough, highly textured, surfaces containing a large number of tail lines and deep furrows. Also, the fracture surface morphologies in Figs. 6.15(b) and (d) give an indication of hackle regions [126] which are generally associated with violent fracture in which tremendous amount of fracture energy is absorbed through both plastic deformation and by generation of additional fracture surface areas. Moreover, as crack propagates, the elastic strain energy is released and as the crack driving force increases

along with sufficiently high crack velocity, a single crack front begins to branch into many smaller (micro) crack fronts, increasing energy dissipation by creating new fracture surfaces. On the other hand, the stiff inclusion specimen ligaments indicate much lower roughness, fewer tail lines and river line morphology. The presence of high concentration of tail lines and higher surface ruggedness in case of compliant inclusion specimens suggest greater energy dissipation and accounts for improved fracture toughness compared to the stiff inclusion specimens.

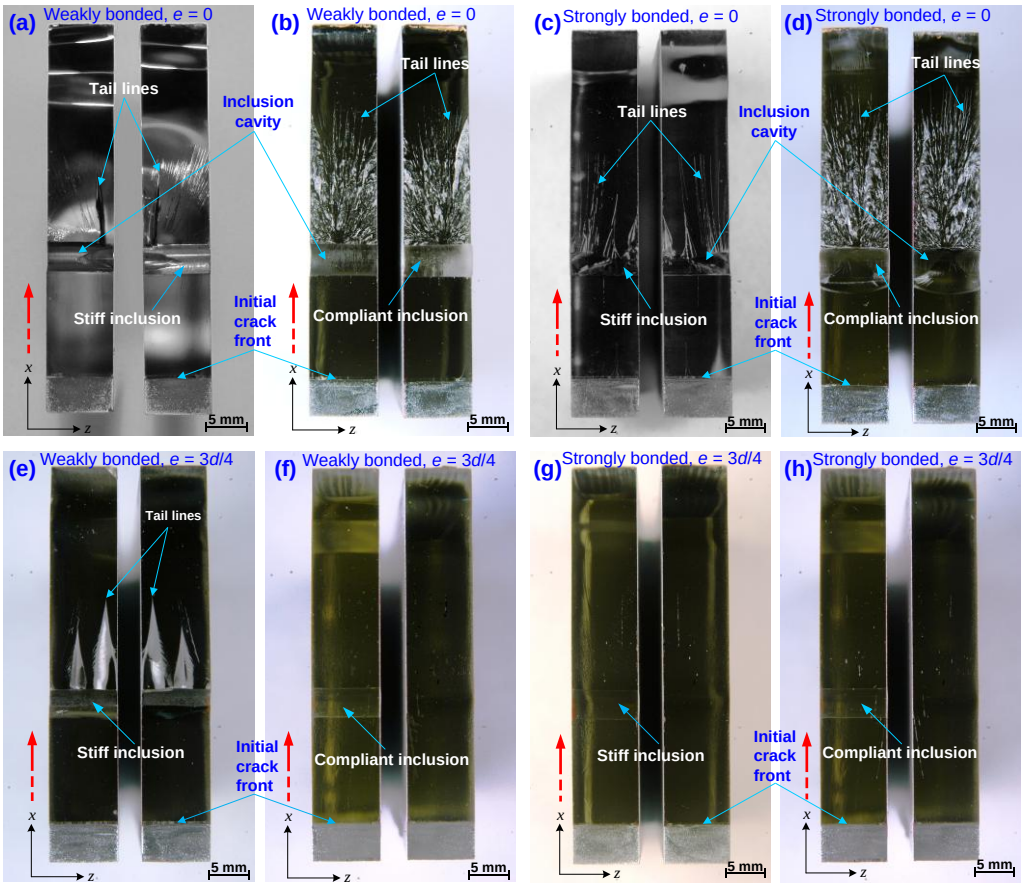

Fig. 6.15: Macrographs of fractured surfaces (x–z plane) of stiff and compliant inclusion specimens showing fracture surface morphologies: **(a)** Weakly bonded stiff inclusion (e = 0), **(b)** Weakly bonded compliant inclusion (e = 0), **(c)** Strongly bonded stiff inclusion (e = 0), **(d)** Strongly bonded compliant inclusion (e = 0), **(e)** Weakly bonded stiff inclusion (e = 3d/4), **(f)** Weakly bonded compliant inclusion (e = 3d/4), **(g)** Strongly bonded stiff inclusion (e = 3d/4), **(h)** Strongly bonded compliant inclusion (e = 3d/4). The broken arrow indicates crack propagation direction.

Figs. 6.15(e)-(f) and (g)-(h) depict fracture surface morphology of weakly and strongly bonded stiff and compliant inclusion specimens ($e = 3d/4$), respectively. In Fig. 6.15(e), as the crack leaves the stiff inclusion, wider pockets of epoxy at the interface are visible. Subsequently these pockets converge into tail lines with further crack propagation, whereas in the case of compliant inclusion no such features are present (Fig. 6.15(f)). In the strongly bonded counterparts as shown in Figs. 6.15(f)-(h) both stiff and compliant inclusion specimens, fracture surfaces are smooth and shiny and macroscopically do not reveal any significant information.

6.5 Implications to Dynamic Fracture of Filler Particle Modified Epoxies

The present study on dynamic crack growth past stiff and compliant inclusions has real world applications involving particulate reinforced polymer composites. In general, filler (stiff/brittle or compliant/ductile) particles in polymeric materials are used to enhance overall strength, impact energy absorption and fracture toughness of the resulting composite system. Hence, in the context of crack-inclusion interaction studies presented here, the dynamic fracture behavior investigations of particle filled-epoxies were also carried out.

The micron-sized soda-lime A-glass particles of average diameter 35 μm (Spheriglass-3000, Potters Industries Inc., USA) were used as stiff fillers in epoxy. Due to the lack of commercial availability of micron size polyurethane particles, the compliant filler employed was CTBN 1300X8 liquid rubber. The CTBN 1300X8 is a carboxyl-terminated butadiene acrylonitrile copolymer, obtained from Hypro™ Reactive Liquid Polymers, Emerald Performance Materials LLC. The CTBN 1300X8 is a reactive

liquid rubber, which precipitates into micron-sized spherical rubber particles in a compatible host matrix upon curing.

Each type of filler/additive was uniformly dispersed at 5% and 10% volume fractions in the same low viscosity epoxy used in the earlier part of the study. Note that both kinds of additives were weakly bonded to the matrix and three types of samples were prepared, namely glass-filled epoxy (V_f = 5% and 10%), CTBN-modified epoxy (V_f = 5% and 10%), and neat epoxy. The glass-filled epoxies were manufactured according to the procedure described in Chapter 4. For the preparation of rubber-filled epoxies, the predetermined amounts of CTBN liquid rubber and epoxy resin were mixed using a magnetic stirrer for 30 min at 60 °C to obtain a homogeneous mixture. While the mixture remained at a relatively low viscosity at 60 °C, degassing was done intermittently until frothing stopped and the mixture became free of air bubbles. After cooling the mixture to room temperature, the stoichiometric amount of the curing agent was added to the mixture, which was again magnetically stirred for 5 min and degassed for 20 min. The mixture was then poured into release-coated molds and the cast material was allowed to gel for 2 h at room temperature, followed by post-curing for 8 h at 90 °C in an oven. After curing, the molds containing the samples were allowed to cool slowly in the oven until it reached room temperature. The cured sheets were then removed from the molds and further rested for a week prior to machining and testing. The physical and elastic properties of neat epoxy, glass-filled and CTBN-modified epoxies are shown in Table 6.2. Evidently, the addition of CTBN generates composites with lower density than those filled with glass particles. Note that the rubber modified epoxies are relatively compliant and exhibit lower wave speeds relative to glass-filled epoxies and neat epoxy. The

dynamic fracture tests on glass and CTBN modified epoxies were conducted to quantify crack-tip deformations and hence crack growth parameters using the experimental methodology described in Chapter 4.

Material	Density, ρ (kg/m^3)	Elastic modulus, E (GPa)	Longitudinal wave speed, C_L (m/s)	Shear wave speed, C_S (m/s)
Neat epoxy	1124	3.97	2487	1136
Glass-filled epoxy (V_f = 5%)	1184	4.76	2569	1216
CTBN-modified epoxy (V_f = 5%)	1098	3.47	2283	1080
Glass-filled epoxy (V_f = 10%)	1279	5.46	2627	1257
CTBN-modified epoxy (V_f = 10%)	1077	3.24	2179	1058

Table 6.2: Material properties of glass-filled and CTBN-modified epoxy composites.

Figures 6.16 and 6.17 show a comparison of dynamic fracture results of the modified epoxies relative to the neat epoxy. The instantaneous crack length histories for all samples are shown in Figs. 6.16(a) and (b) at 5% and 10% V_f, respectively, along with an inset depicting the specimen geometry and loading configuration. For both volume fractions, it can be seen that, the crack initiated later in filled-epoxies than in neat epoxy (116 μs) with a significant delay for CTBN-modified epoxy (144 μs) at 10% V_f. Following initiation and acceleration, the crack growth is essentially continuous in each case during the observation window. The slopes of the crack length histories were used to estimate the crack tip velocity and are shown for each sample category. Relative to the neat epoxy, the crack growth is slower in the modified composites with the slowest propagation speed of ~170 m/s in CTBN-modified epoxy (144 μs) at 10% V_f. The crack growth characteristics suggest that the incorporation of compliant phase delays the crack

initiation time and significantly retards the propagation speeds when compared to the stiff fillers.

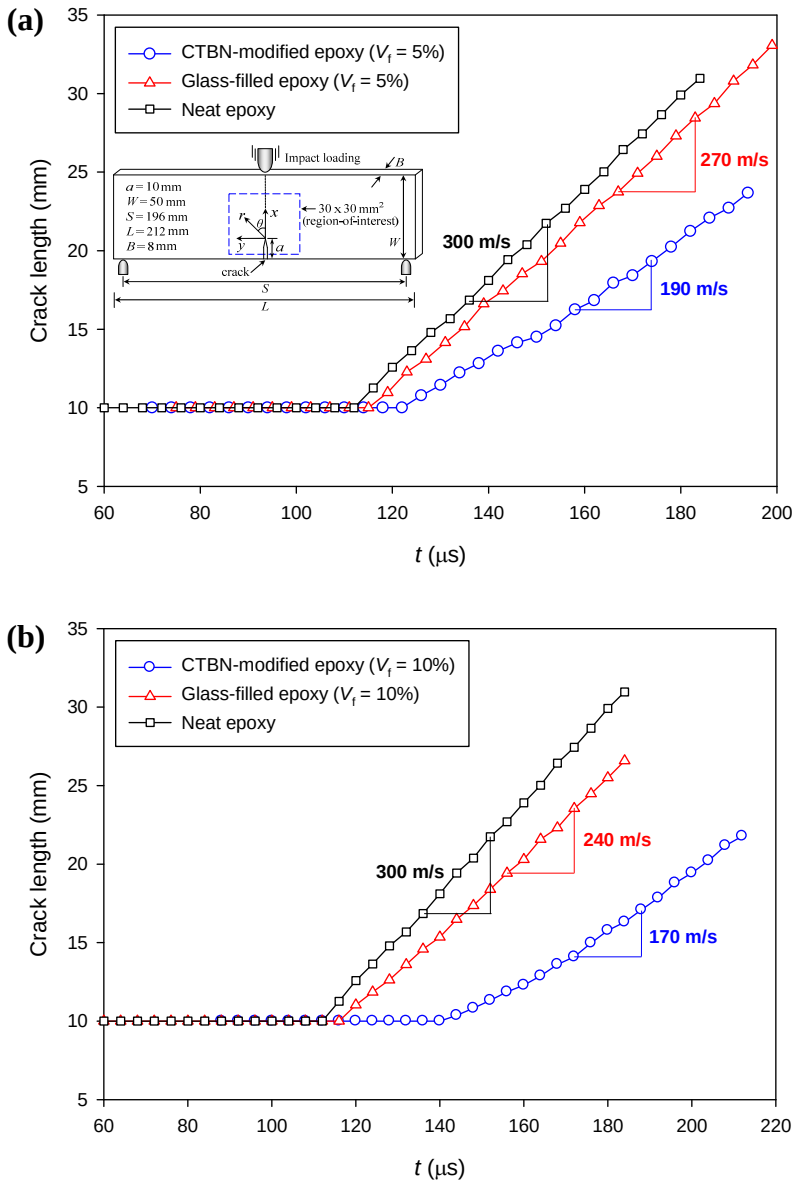

Fig. 6.16: Dynamic fracture of CTBN-modified and glass-filled epoxies: **(a)** Crack length histories at 5% V_f, **(b)** Crack length histories at 10% V_f.

The mode-I SIF (K_I^d) histories for modified composites at 5% and 10% V_f along with the neat epoxy are shown in Figs. 6.17(a) and (b), respectively. Here t_i denotes the

time at crack initiation after impact and the time base is shifted such that $t - t_i = 0$ corresponds to crack initiation, shown by the vertical dotted line, and hence the negative and positive values represent the pre-initiation and post-initiation periods, respectively.

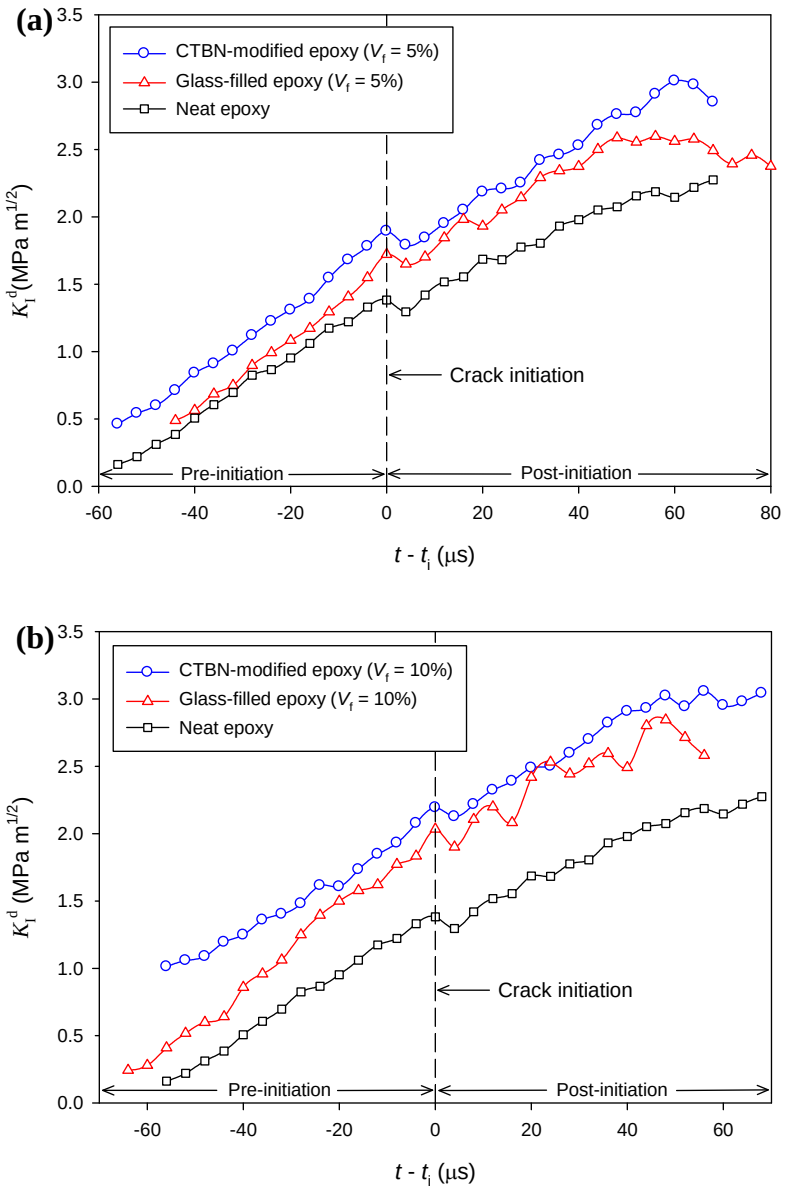

Fig. 6.17: Mode-I SIF (K_I^d) histories for CTBN-modified and glass-filled epoxies: **(a)** 5% V_f, **(b)** 10% V_f.

In the pre-initiation regime, for each specimen the K_I^d increases monotonically until it reaches a threshold value at crack initiation. Following initiation, a noticeable drop in K_I^d can be seen and the maximum value of K_I^d just before the drop is identified as the mode-I dynamic crack initiation toughness, K_{Ii}^d. One can readily see that the magnitudes K_{Ii}^d show increasing trend with the addition of stiff (glass) and compliant (CTBN rubber) phases. When compared to the neat epoxy, the improvements in dynamic crack initiation toughness, K_{Ii}^d values at 5% V_f of glass-filled and CTBN-modified composites are ~25% and ~38%, respectively. The improvements in K_{Ii}^d values for these composites at 10% V_f are ~47% and ~65%, respectively. The K_I^d values in the pre- and post-initiation regimes are higher for both glass-filled and CTBN-modified composites when compared to that of the neat epoxy. It is interesting to note that for both 5% and 10% volume fractions, compliant filler showed higher crack growth resistance than the stiff filler counterparts.

Figs. 6.18(a) and (b) show SEM micrographs of the fractured surfaces (*x*-*z* plane) of 10% V_f glass-filled and CTBN-modified epoxies, respectively. The solid arrow in these micrographs indicates the crack propagation direction. The microscopic examination of glass-filled epoxy in Fig. 6.18(a) reveals toughening mechanisms such as particle pull-out and filler-matrix debonding (as shown in the magnified view) which results in momentary crack front trapping. Also, zigzag micro-crack patterns along the crack growth direction and river bed patterns can be clearly seen. The SEM images of CTBN-modified epoxy in Fig. 6.18(b) shows finer dispersion of rubber particles. It can be noted that CTBN particle size is of the order of 1 μm or smaller and is in the range of particle sizes found in earlier studies on CTBN modified composites [35, 138 139].

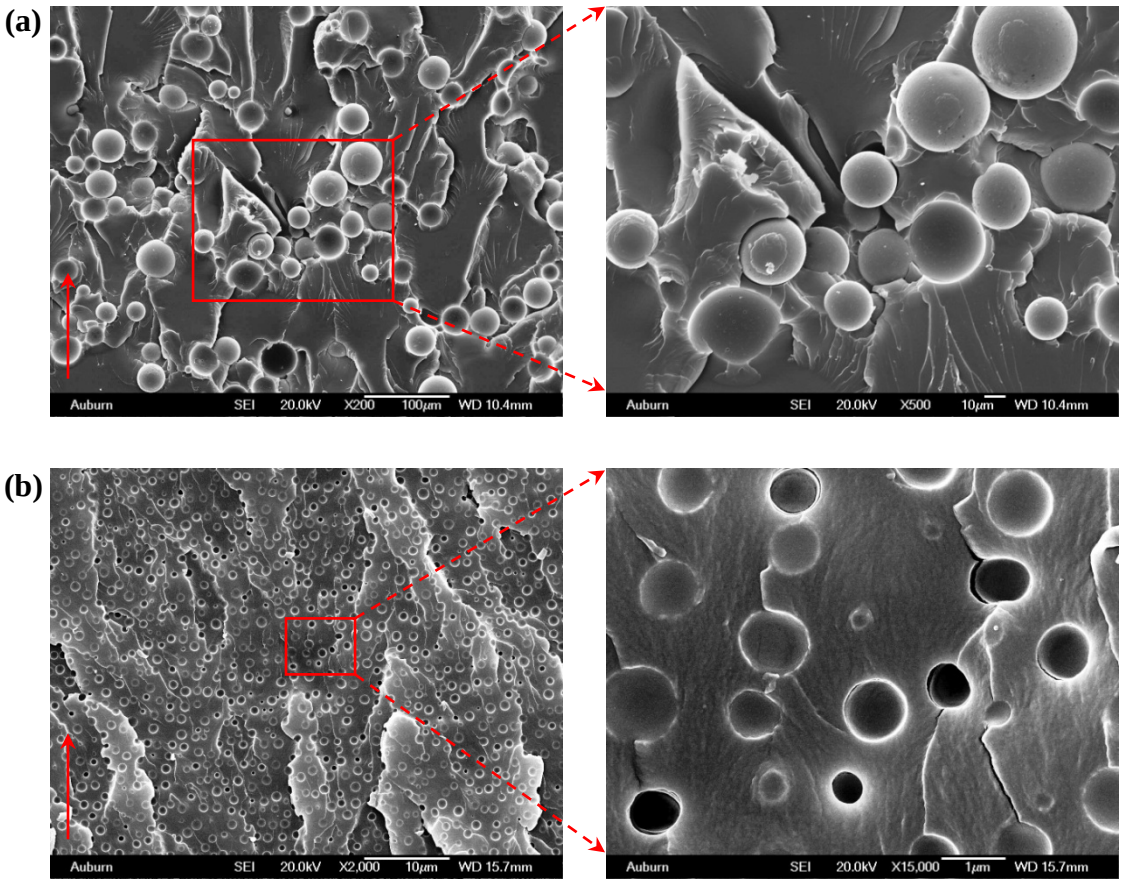

Fig. 6.18: SEM micrographs of fractured surfaces: **(a)** Glass-filled epoxy at 10% V_f, **(b)** CTBN-modified epoxy at 10% V_f. The solid arrow indicates crack propagation direction.

The fracture surface of CTBN modified epoxy shows shear yielding and tail lines generated due to the rubbery domains. The magnified view of the highlighted region shows a scenario where a matrix crack is interacting with the secondary phase rubbery domain. It can be seen that, in addition to filler-matrix debonding, the rubber particles have undergone nonlinear deformations as evident from the departure from the spherical shape due to their high ductility resulting in void formation. The matrix cracks are attracted by the rubber particles which reinitiate at different locations as they continue to be attracted by other neighboring particles. Hence, shear yielding, void formation, and energy dissipation due to distortion of CTBN particles are some of the major toughening

mechanisms responsible for the higher dynamic crack initiation toughness in CTBN modified composites relative to glass-filled ones.

CHAPTER 7

FAILURE BEHAVIOR OF TRANSPARENT IPNs[1]

This chapter presents development and failure characterization of transparent Interpenetrating Polymer Networks (IPNs), synthesized using poly(methyl methacrylate) (PMMA) as the stiff phase and polyurethane (PU) as the tough phase. Several IPNs with varying PMMA:PU ratios in the range of 90:10 to 70:30 were formulated. The resulting molecular composites are *fully* cross-linked IPNs, and characterized in terms of tensile, fracture and energy absorption behaviors. The tests results show that an optimum range of PPMA:PU ratios in the IPNs can produce enhanced fracture toughness and impact energy absorption capability when compared to PMMA.

7.1 IPNs Synthesis and Dynamic Elastic Properties

The reagents used for the PMMA system were: methyl methacrylate (MMA, 99%, ACROS Organics), trimethylolpropane trimethacrylate (TRIM, Sigma-Aldrich) and 2,2´-Azobisisobutyronitrile (AIBN, 98%, Sigma-Aldrich), and the reagents used for the PU system were: poly(tetramethylene ether)glycol (PTMG), 2-Ethyl-2-(hydroxymethyl)-1,3-propanediol (TRIOL, 98%, ACROS Organics), 1,6 diisocyanatohexane (DCH, 99+%, ACROS Organics) and dibutyltin dilaurate (DBTDL, 98%, Pfaltz and Bauer, Inc.). The five different compositions (PMMA:PU ratio) of IPNs were prepared, namely 90:10, 85:15, 80:20, 75:25 and 70:30.

[1] Parts of this chapter appear in Refs. [108, 140-142].

A typical experimental protocol was determined to prepare IPNs of desired PMMA:PU ratios. In this protocol, a homogeneous mixture was prepared at room temperature by dissolving the required amounts of PTMG, TRIOL and DCH in the methacrylic monomer MMA and cross-linker TRIM under vigorous stirring for about 10 minutes. Next, the free-radical initiator, AIBN was dissolved during mixing and finally the desired amount of DBTDL (catalyst) was added followed by further stirring of the mixture for another 5 minutes. This homogeneous mixture was then poured into a closed mold made of Teflon. Care was exercised to avoid evaporation of PMMA from the mixture by sealing the mold interfaces with a thin layer of caulk. The mold containing the PMMA-PU mixture was kept in an oven at 60ºC for 24 hours followed by further curing at 80ºC for another 24 hours. After curing, the mold was left in the oven at room temperature for another 12 hours for complete cooling of the casting. It should be noted that slow cooling from 80ºC to room temperature in the oven prevents warpage of the cured sheets and minimizes residual stresses. A transparent 80:20 (PMMA:PU) IPN sheet of dimensions 170 mm x 80 mm x 8 mm is shown in the inset of Fig. 7.1.

Note that, in this work, the PU-PMMA IPNs were primarily synthesized by sequential route instead of simultaneous mode due to higher gain in transparency in the former than the latter. Additional details regarding IPN synthesis methods, network morphology and transparency measurements are provided in Appendix-B.

The dynamic elastic characteristics of IPNs were determined by indirect means using ultrasonic pulse-echo measurements as described in Chapter 3. The measured values of longitudinal (C_L) and shear (C_S) wave speeds, and dynamic elastic modulus (E_d) are shown in Fig. 7.1. The effect of compositional differences on measured properties is

quite evident. The wave speeds and the dynamic elastic modulus show a monotonic decrease as the PU content increases. The values of Poisson's ratio (ν_d) in these IPNs were found to be nearly constant at 0.351±0.018.

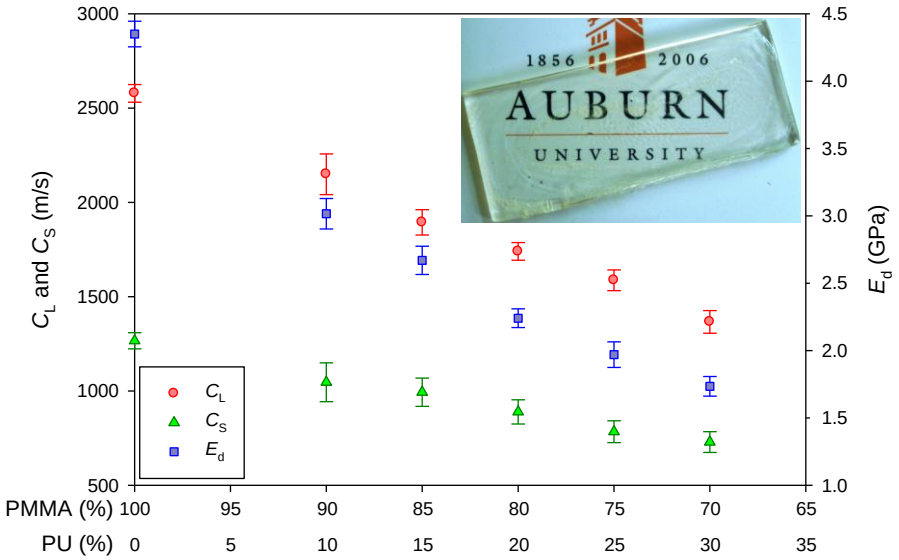

Fig. 7.1: Measured dynamic material properties of PMMA and IPNs using ultrasonic pulse-echo method. The inset shows a PMMA:PU (80:20) IPN sheet (Dimensions: 170 mm x 80 mm x 8 mm).

7.2 Experimental and Testing Procedures

7.2.1 Specimen fabrication and geometry

The cured IPN sheets of thickness 4 mm were machined to dumbbell (dogbone) shaped specimens for tension tests as per ASTM D638-01 standard [109]. The specimens had 115 mm overall length, 19 mm overall width at the two ends of the dumbbell, 65 mm span (distance between grips), 33 mm gage length, 6 mm reduced gage section width, 14 mm fillet radius, and 25 mm outer radius. Note that, prior to testing the machined specimens were inspected at 1000x magnification using an optical microscope and found

to be free from pores. Moreover, the cut sections along the reduced gage and curved (fillet) portions were polished using #1000 and #2000 grit emery papers successively to minimize machining marks, if any, in order to avoid possible failure near the grip ends. This ensured failure of the specimens within the gage length.

For quasi-static fracture tests, the IPN sheets were machined into rectangular beams of nominal dimensions 100 mm x 20 mm x 8-9 mm (span 80 mm). For dynamic fracture experiments, plate-shaped specimens of dimensions 60 mm x 30 mm x 4.5 mm were fabricated. A 6 mm edge notch was first cut into the samples using a diamond impregnated wafer blade for both types of tests. The notch tip was then sharpened using a razor blade in order to have a naturally sharp crack tip. The 3-point bend specimen geometry for quasi-static fracture tests is shown in Fig. 7.2(a). Figure 8.2(b) depicts the specimen geometry, dimensions and loading configuration for dynamic fracture tests. The region in the dotted box represents 28 x 28 mm^2 region-of-interest. For low-velocity impact tests, the specimens were fabricated as circular discs of diameter 110 mm and thickness 6 mm.

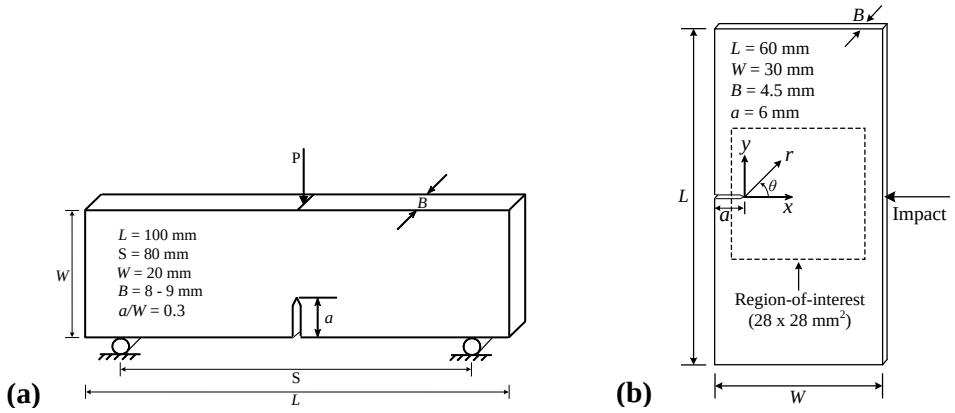

Fig. 7.2: (a) Three-point bend specimen geometry for quasi-static fracture tests, **(b)** Mode-I specimen geometry with crack-tip coordinate system for dynamic fracture tests.

7.2.2 Tensile testing

The uniaxial tension tests were carried out in an Instron testing machine (model 4465) to measure properties such as elastic modulus, tensile strength, and elongation at break. All the experiments were conducted at room temperature under displacement controlled conditions (crosshead speed = 2 mm/min). Typically four specimens were tested for each IPN category.

7.2.3 Quasi-static and dynamic fracture experiments

In order to characterize the fracture toughness of IPNs in terms of the critical stress-intensity factor, K_{Ic}, quasi-static tests were performed. The single edge notched bend (SENB) specimens were loaded in displacement control mode (cross-head speed = 0.25 mm/min) using Instron 4465 testing machine. The mode-I crack initiation toughness, K_{Ic}, was calculated using the peak load. Again, for each category at least four sets of tests were performed.

The dynamic fracture tests were conducted by subjecting IPNs to symmetric 1-point loading using a long-bar impactor and monitoring deformations using 2D DIC technique and high-speed photography. The schematic of the experimental setup used in this study is shown in Fig. 3.5 (see Chapter 3 for experimental setup and testing procedure).

7.2.4 Low-velocity impact tests

Low-velocity impact tests were performed in order to study energy absorption characteristics of INPs. The IPNs were subjected to impact tests using a drop-tower (Instron Dynatup 9250HV). The details regarding experimental setup, testing procedure and energy calculations are described in Chapter 3.

7.3 Tensile Behavior

The tensile responses of transparent IPNs are shown in Fig. 7.3. The insets depict the variation of elastic modulus as a function of IPN composition, and a photograph of a failed dogbone specimen. From the representative stress-strain curves it can be seen that the initial response in each case indicates a linear elastic region with a modest nonlinearity before failure in the case of neat PMMA compared to the IPNs which show a substantial nonlinear response.

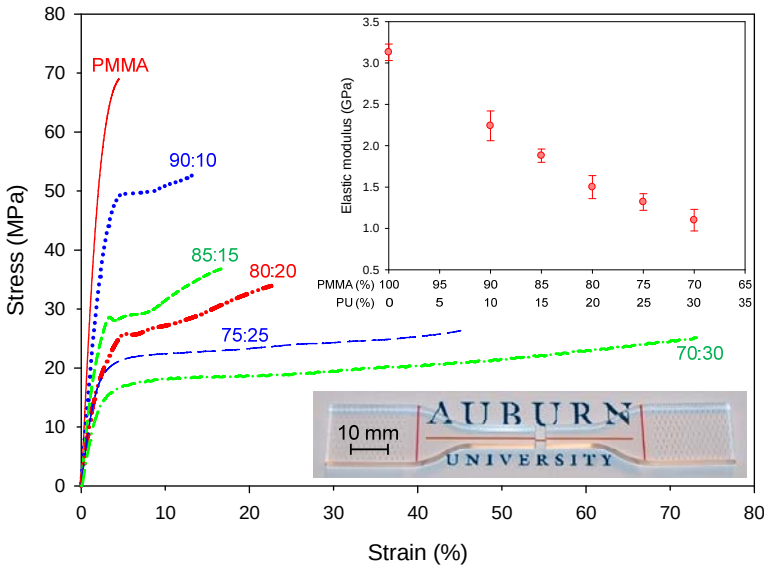

Fig. 7.3: Typical stress-strain response from tension tests. (The insets show the variation of elastic modulus as a function of IPN composition and a photograph of a failed dogbone specimen.)

The IPNs 90:10, 85:15 and 80:20 show yielding at ~50, ~28 and ~25 MPa, respectively, followed by some strain hardening before failure. In 75:25 and 70:30 IPNs, a yield plateau can be seen between ~4 and ~20% strain followed by an appreciable strain hardening until failure. Note that, while the ultimate stresses decrease, a substantial increase in failure strains with increasing PU content occur. The elastic modulus for each

specimen was deterimined by constructing a tangent to the initial part of the stress-strain curve. Each data point respresents an average of four measured values of Young's modulus and the error bars corresponds to their standard deviation. It can be seen that there is a monotonic reduction in elastic modulus as the PU phase increases. The trends of gradual drop in tensile strength and Young's modulus with a substantial gain in failure strain with PU content are similar to those reported in [109, 143]. Furthermore, this behavior is possibly due to the alteration of chain density as a result of stretching of polymer chains by the interpenetration of one network into the other [144].

7.4 Quasi-static Fracture Response

The quasi-static fracture response of IPNs relative to neat PMMA is shown in Fig. 7.4. The normalized load-deflection curves for all compositions are shown in Fig. 7.4(a). It can be seen that the curves are generally linear in the initial stage of deformation for each composition. The PMMA shows a linear response up to a peak load followed by a sudden drop, signalling crack initiation. However, in case of IPNs, as the applied load increases, the specimens respond with a modest nonlinealry before reaching the peak load, and again the extent of nonlinearity increases with PU content. This nonlinearity in the pre-peak load region is attributed to crack-tip blunting and crazing prior to crack initiation. Moreover, propagation of the macro-crack is dependent on the increase in the applied load. Further, the crack may deviate from its original propagation plane. It can also be noted that PMMA and 90:10 IPN indicate brittle unstable crack growth whereas 85:15 and 80:20 IPNs reveal both brittle as well as stable crack grwoth. The extensive crack tip blunting followed by stable crack growth is seen in 75:25 and 70:30 IPNs. Also note that at peak load for each specimen, the corresponding load point deflections

increase as the PU content increases in IPNs. Furthermore, the overall deflection also increases with increasing PU phase and the area under these curves represents the strain energy absorbed.

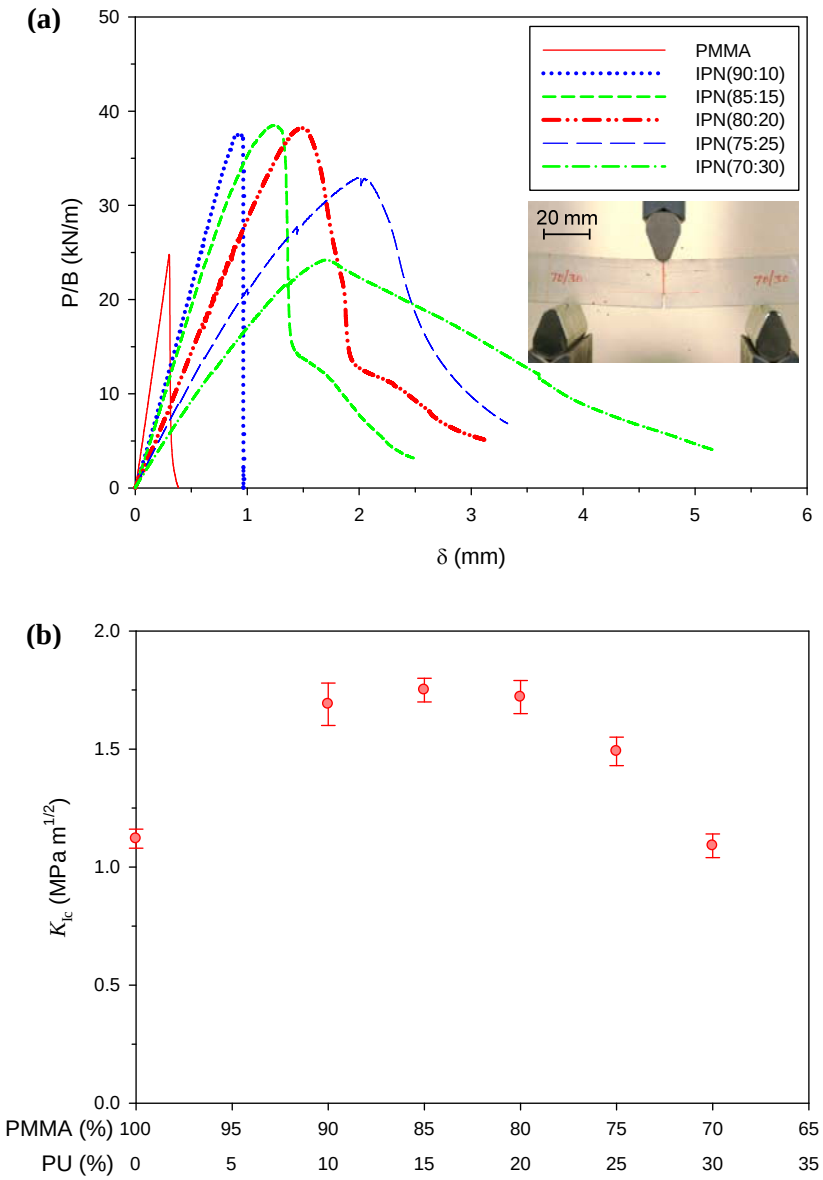

Fig.7.4: Quasi-static fracture response: **(a)** Normalized load-deflection curves, **(b)** Variation of quasi-static crack initiation toughness (K_{Ic}) as a function of IPN composition.

The quasi-static crack initiation toughness, K_{Ic}, was calculated using the load at crack initiation in each case and its variation as a function of IPN composition is shown

in Fig. 7.4(b). Each data point is again an average of four measured values of K_{Ic}. Apporximately 60% improvement in K_{Ic} is evident for IPNs relative to neat PMMA. The trends in K_{Ic} values with increasing PU suggest that there is an optimum range of PMMA:PU ratio for which the quasi-static fracture toughness is the highest. In this work, the 90:10, 85:15 and 80:20 IPNs showed the highest quasi-static crack initiation toughness among all the cases.

7.5 Dynamic Crack Growth Behavior

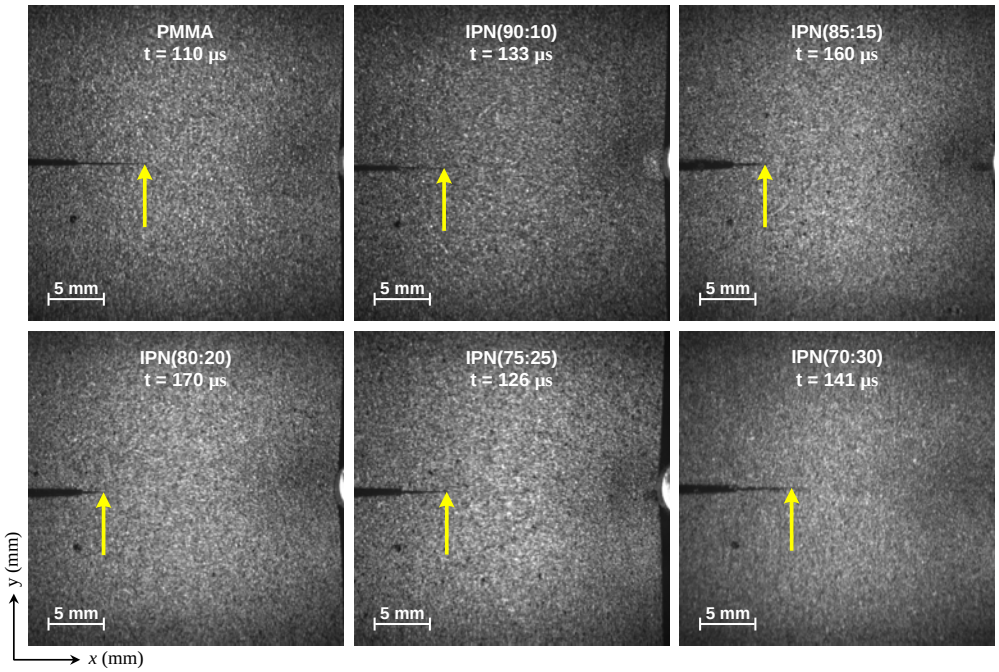

Fig. 7.5: Selected speckle images of 28 x 28 mm^2 region-of-interest for PMMA and IPNs at different time instants recorded by high-speed camera. The arrow in each image indicates the instantaneous crack-tip position.

A few representative speckle images of 28 x 28 mm^2 region-of-interest for PMMA and IPNs where surface deformations were monitored optically during dynamic fracture are shown in Fig. 7.5. The specimens were subjected to symmetric 1-point impact loading on the edge ahead of the initial notch. The time instant (t) after impact at which the

images were recorded is also shown, and the position of the propagating crack-tip is indicated by an arrow. Note that different trigger delays were assigned for each specimen category depending on the time taken by the stress waves to load the crack-tip. This enabled capturing sufficient number of images before and after crack-initiation within the observation window.

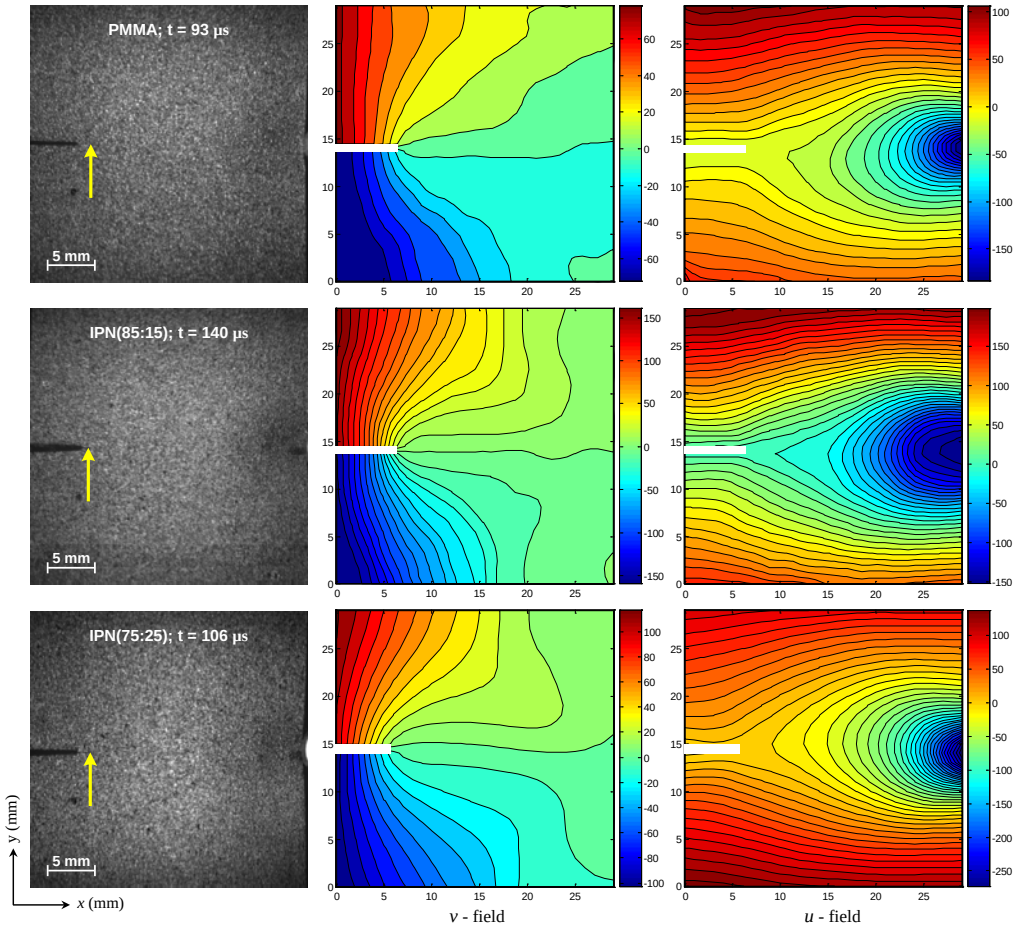

Fig. 7.6: Measured crack-opening (*v*-field) and crack-sliding (*u*-field) displacement contours immediately after crack initiation with corresponding speckle images of 28 x 28 mm^2 region-of-interest. Contour interval is 10 μm. Color-bars represent displacement in μm. The arrows indicate the instantaneous crack-tip position in the speckle images.

As described earlier, a sub-image size of 26 x 26 pixels was chosen for correlation and displacement fields were obtained as 37 x 37 array of data points for each pair.

Subsequently, full-field in-plane displacement contours with 10 μm per contour interval were generated. A few representative speckle images immediately after crack initiation with corresponding crack-opening (v-field or displacement along the y-axis) and crack-sliding (u-field or displacement along the x-axis) displacement contours for PMMA, 85:15 and 75:25 IPNs are presented in Fig. 7.6. The crack-tip is located at the tip of the arrow in each speckle image. The v- and u-fields show that contour lines and magnitude of displacement (in μm shown by color-bars) are nearly symmetric relative to the crack, consistent with mode-I fracture behavior. By comparing the color bars of the v-field, it can be seen that the crack-opening displacement range is higher in IPNs than the one for PMMA with larger deformations in 85:15 IPN case. The u-field plot shows a set of isolines emerging from the right-hand side of the contour plots due to impact loading on the edge of the specimen ahead of the initial crack-tip.

The crack-tip velocity (V) histories were estimated from the instantaneous values of crack extension data and are shown in Fig. 7.7(a). Here t_i denotes the time at crack initiation after impact. It can be seen that following initiation the crack accelerated to attain a maximum speed followed by an oscillatory growth behavior. The steady state crack velocities (average values in the time window after rapid acceleration) for PMMA are the highest (~350 m/s) among all the specimens tested. On the contrary, IPN samples with PMMA:PU ratio of 85:15 and 80:20 show the least crack speeds (~100 m/s). Further, for other compositions, the crack speed drops with increasing PU content up to the composition of 80:20 but begins to rise beyond this. That is, 75:25 and 70:30 ratios show higher crack speeds when compared to 80:20 and 85:15 IPNs suggesting a change in the microstructure and hence the fracture mechanism. The variation of steady state

crack velocity (V_{ss}) as a function of IPN composition is depicted in Fig. 7.7(b). The 85:15 and 80:20 IPNs show the lowest values of V_{ss} among all the cases. The variation of V_{ss} also indicates that further increase or decrease in PU content results in an increase in the V_{ss}.

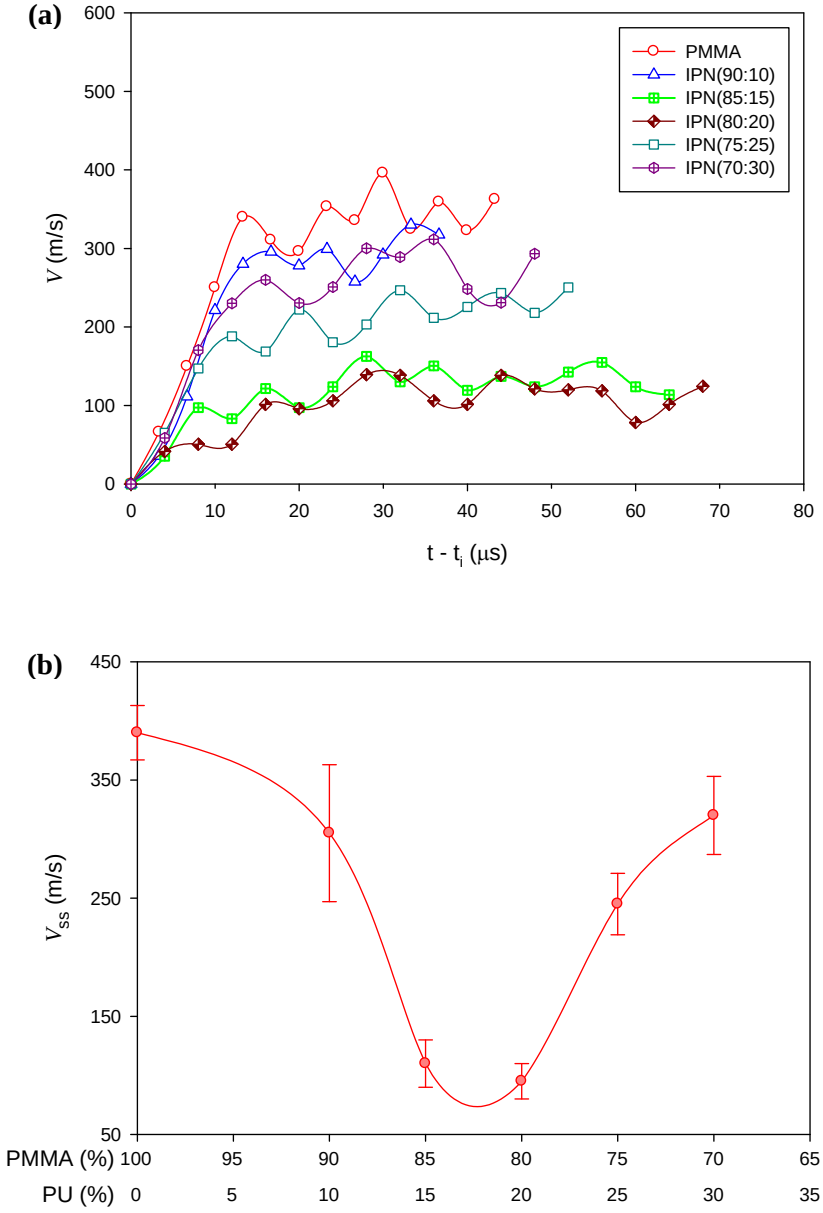

Fig. 7.7: (a) Measured crack-tip velocity (V) histories for PMMA and various IPNs, **(b)** Variation of steady state crack velocity (V_{ss}) as a function of IPN composition.

7.6 Dynamic Crack-initiation Toughness

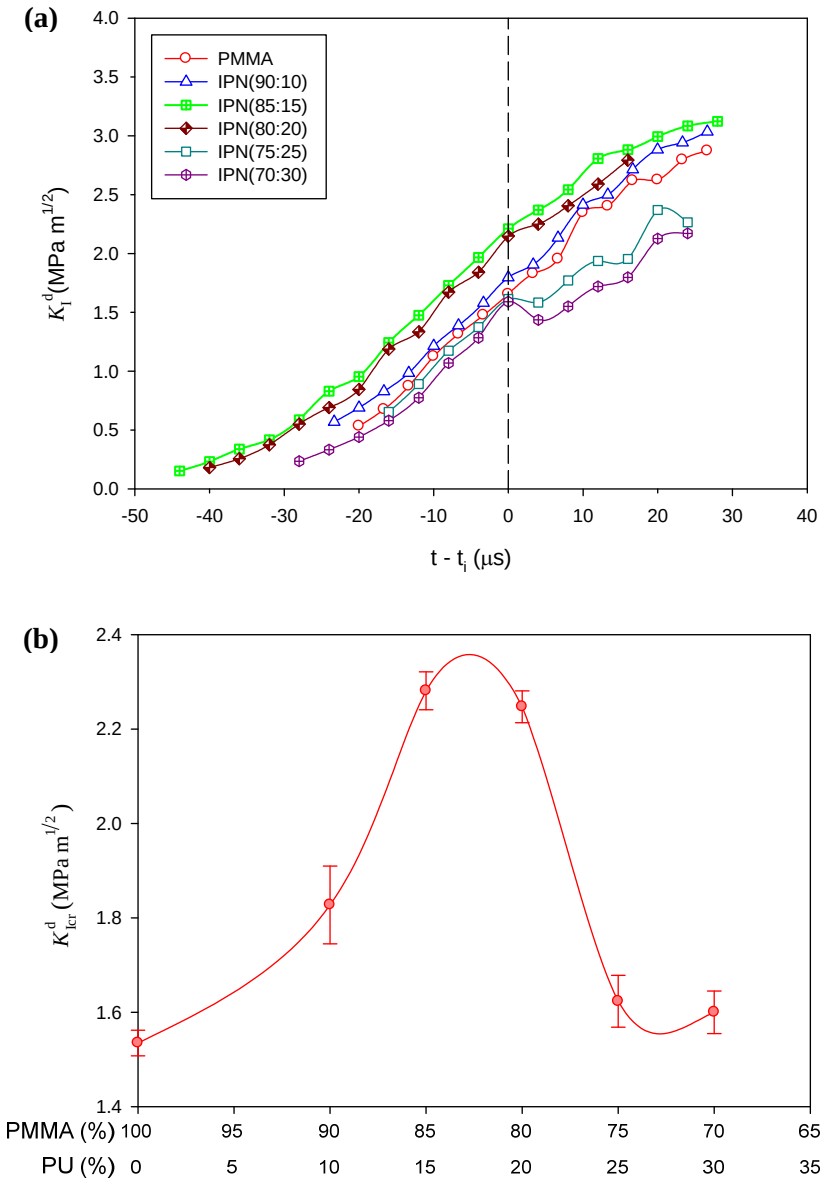

Fig. 7.8: (a) Measured mode-I dynamic stress intensity factor (K_I^d) histories for PMMA and various IPNs. (Time base is shifted such that $t - t_i = 0$ corresponds to crack initiation as shown by the vertical dashed line.) **(b)** Variation of mode-I dynamic crack initiation SIF (K_{Icr}^d) as a function of IPN composition.

The measured mode-I dynamic stress intensity factor (SIF) histories are presented in Fig. 7.8(a). In this plot, the crack initiation time is denoted by $t - t_i = 0$. Hence, the

negative and positive values correspond to the pre- and post-initiation periods, respectively. In the pre-initiation regime, the dynamic SIF, K_I^d, increases monotonically for each specimen until it reaches a threshold for crack initiation. The K_I^d values in the pre-initiation and post-initiation regimes are higher for 85:15 and 80:20 IPNs when compared to other cases. The dynamic mode-I crack initiation SIF (K_{Icr}^d) (corresponding to $t - t_i = 0$ as indicated by the vertical dashed line) initially increases with the PU content. That is, relative to PMMA, a modest improvement in 90:10 IPN can be noted. On the other hand, the 85:15 and 80:20 IPNs show approximately 40% enhancement (from ~1.6 MPa $m^{1/2}$ to ~2.25 MPa $m^{1/2}$) in K_I^d at crack initiation. However, when the PU content is increased further, there is a precipitous drop in values for 75:25 and 70:30 compositions. Furthermore, these trends continue into the post-initiation regime ($t - t_i > 0$). Based on these and the previously discussed velocity histories, an optimum IPN composition appears to be in the neighborhood of 85:15 PMMA:PU ratio. The variation of K_{Icr}^d as a function of IPN composition is shown in Fig. 7.8(b). The 85:15 and 80:20 IPNs show the highest values of K_{Icr}^d among all the cases.

Note that for fracture at elevated loading rates, the crack took longer to initiate in the case of 85:15 and 80:20 IPNs indicating that the crack initiation can be delayed by incorporating an optimum amount of PU phase. Moreover, the fracture toughness of a material being essentially resistance to crack initiation and propagation, the crack velocity histories of 85:15 and 80:20 IPNs shows the slowest crack growth (Fig. 7.7) among all the IPNs.

7.7 Fracture Surface Morphology

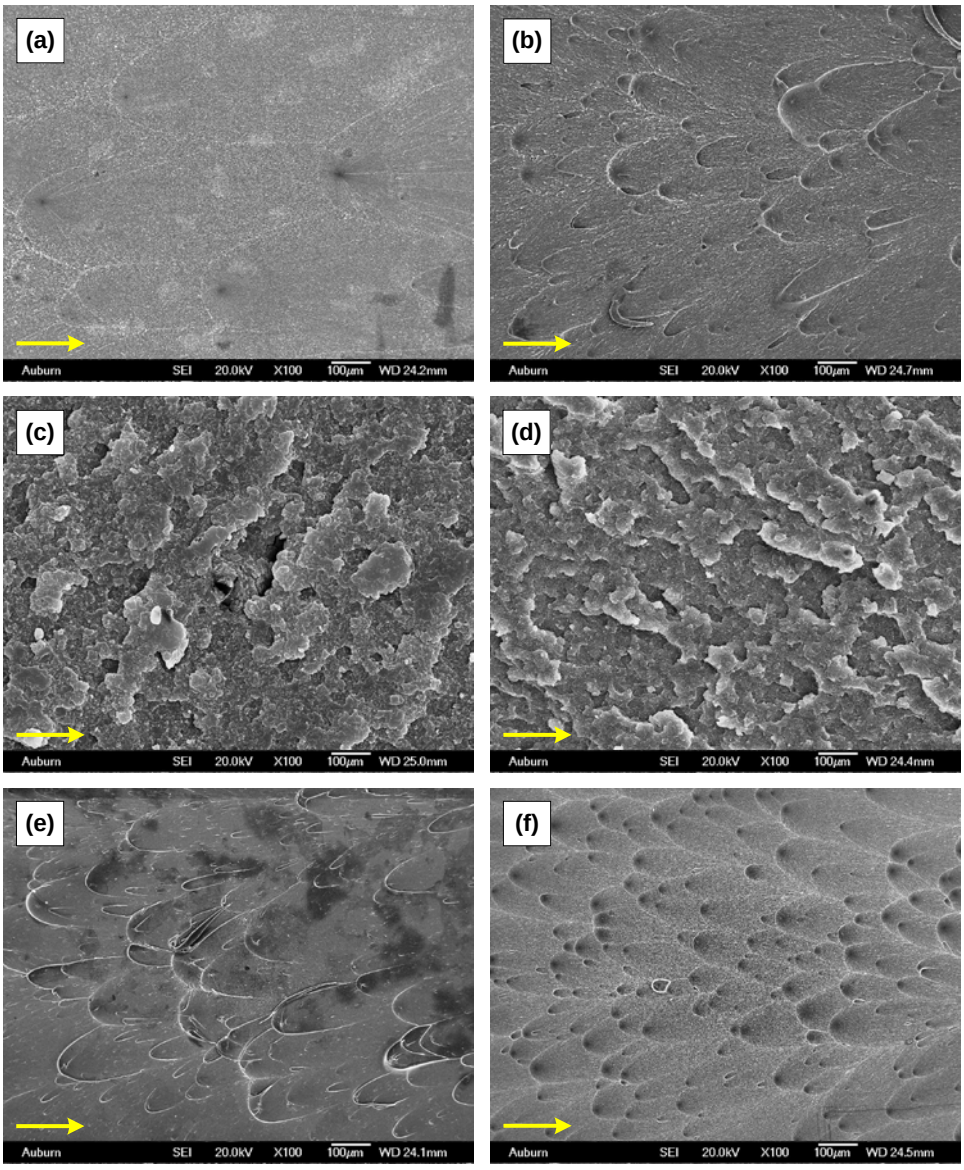

Fig. 7.9: SEM micrographs of dynamically fractured surfaces: **(a)** Neat PMMA, **(b)** 90:10 IPN, **(c)** 85:15 IPN, **(d)** 80:20 IPN, **(e)** 75:25 IPN, **(f)** 70:30 IPN. The arrow in each micrograph indicates the direction of crack growth.

Scanning electron microscopy (SEM) was performed on dynamically fractured surfaces. The SEM micrographs of fracture surfaces are shown in Fig. 7.9. The PMMA fracture surface shown in Fig. 7.9(a) is nearly featureless with a few conic (parabolic)

markings, typical of brittle fracture of neat thermoset polymers signifying low dissipation of fracture energy. Each parabolic marking is associated with radial lines emanating from its focus. In the case of 90:10 IPN (Fig. 7.9(b)) the conic marks become smaller in size and increase in number. On the contrary, 85:15 and 80:20 IPN compositions (Figs. 7.9(c) and (d)) (with high dynamic crack initiation toughness) show noticeably textured/rugged surface with a high degree of roughness. The creation of new surfaces is responsible for greater energy dissipation which explains the higher dynamic crack initiation SIF values seen in these IPNs. However, with further increase of PU content as in the case of 75:25 (Fig. 7.9(e)) and 70:30 (Fig. 7.9(f)) IPNs, a fracture surface that resembles the one corresponding to low energy dissipation case returns. In these cases, with higher PU content, the number and density of conic marks increase with a decrease in their size. These transitions in microscopic features are consistent with the drop in crack initiation toughness measured earlier. Note that the conic marks seen in acrylic-based materials under dynamic fracture are consistent and well documented in the literature [145-147]. These studies indicate that at higher crack speeds ($V \geq 0.4\ C_R$, where C_R is the Rayleigh wave speed for PMMA ~850 m/s), the presence of conic markings is a typical feature. In the present work, the average crack speed for PMMA and IPNs showing conic marks are in the range of 300-400 m/s and satisfy the above criterion of ($V \geq 0.4\ C_R$). The conic marks do not appear in 85:15 and 80:20 cases possibly due to the lower crack speeds (~100 m/s).

7.8 Low-velocity Impact Response

7.8.1 Transient load histories

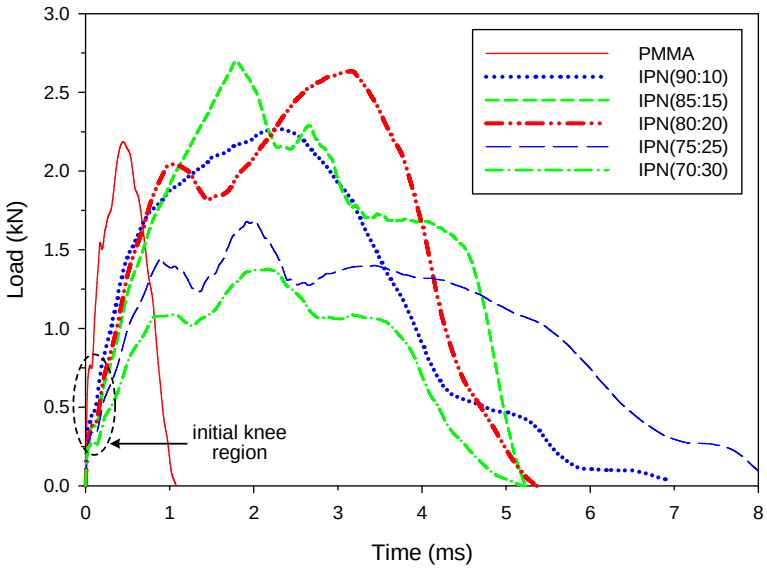

Fig. 7.10 Transient load *vs*. time response from low-velocity impact tests.

The transient load histories from drop-tower tests are presented in Fig. 7.10 dictating how these materials behave during an impact event. The presence of an initial knee in each case, indicated by the dotted region in the load-time curves, is due to the inertial effects, and can be termed as the inertial loading zone indicating initial contact between the tup and the specimen. During this early stage of impact, the specimen deforms elastically and separates from the tup due to elastic wave reflections. Then the tup re-establishes contact with the specimen and continues to deform the specimen elastically until it yields. From the transient load history it can be noted that the slope of the curves relative to PMMA decrease with increasing PU content with nearly equal slopes for 90:10, 85:15 and 80:20 IPNs. Note that in a typical transient event such as an impact test, the slope of the load history in the elastic region represents *contact stiffness* [148]. Following elastic deformation and yielding, the load continues to increase until a peak

value is attained beyond which a drop in the load signals commencement of damage. After reaching an ultimate load value, the IPNs start to suffer plastic deformation whereas PMMA shows a steep drop in the load, qualitatively indicating brittle failure. Also note that among all the cases, 85:15 and 80:20 IPNs sustained maximum peak load before showing a precipitous drop due to failure. Relative to PMMA, the 90:10 IPN shows modest improvement in the load carrying capacity whereas 75:25 and 70:30 IPNs show lower values of peak load. In terms of failure, the IPNs take longer (5-8 ms) to fail than PMMA (1 ms). The longer duration also indicates progressive damage whereas shorter time in the case of PMMA signals catastrophic failure.

7.8.2 Energy absorption characteristics

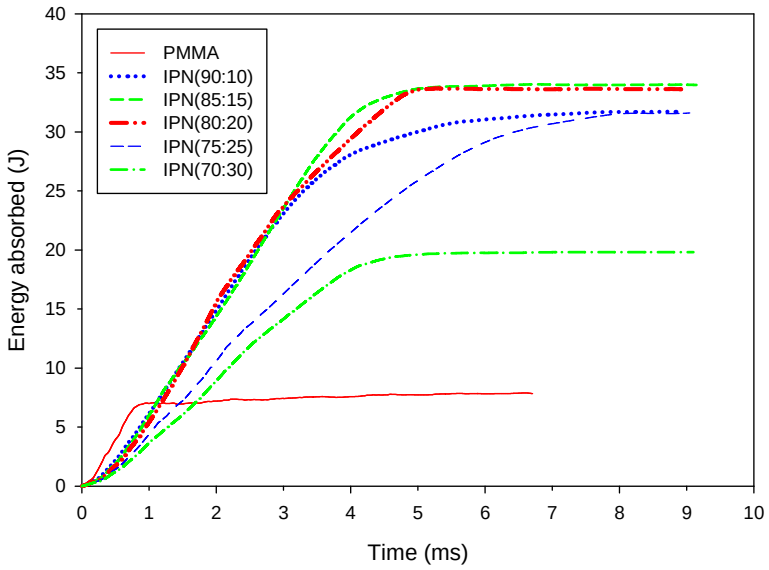

Fig. 7.11: Impact energy absorbed *vs*. time response for various IPNs.

Figure 7.11 shows time histories of impact energy absorbed by various IPNs relative to PMMA. A linear region is evident for all specimens followed by deviations from linearity after which the curves attain a plateau in each case. It should be noted that in the

initial stage of impact loading the energy absorption in the specimens is mainly through elastic deformation. Beyond this regime, the specimen absorbs energy through plastic deformation and various other damage mechanisms. It can be seen that energy absorption rates decrease with increasing PU content. Also note that, the 90:10, 85:15 and 80:20 IPNs again show nearly equal slopes. Further, the duration of energy absorption for elastic deformation is longer in IPN cases (4-5 ms) than for PMMA (0.75 ms). From Fig. 7.11(b), it is worth noting that IPNs show tremendous impact energy absorption capabilities when compared to PMMA. Quantitatively, the energy absorbed by IPNs is 3 to 4 times that of PMMA. The energy absorbed is a measure of the toughness of a material which is further defined as an optimum combination of strength and ductility [149]. Also note that among all IPN compositions, the 85:15 and 80:20 exhibit the highest damage tolerance and energy absorption capabilities under identical impact conditions.

7.8.3 Impact damage features

The photographs depicting macro scale damage features of the front and back surfaces of a few selected specimens are shown in Fig. 7.12. During impact, the front (or top) surface experiences a compressive transient load causing a tensile failure of the back (or bottom) surface. In all the failed specimens through-the-thickness cracks emanate from the impact point. However, the number of cracks, their length and growth behaviors differ from each other. PMMA being a brittle material compared to the IPNs, fails catastrophically, evidenced by a circular opening due to the complete penetration of the indenter. The main failure mode in this case is spallation around the circular opening followed by the growth of radial cracks.

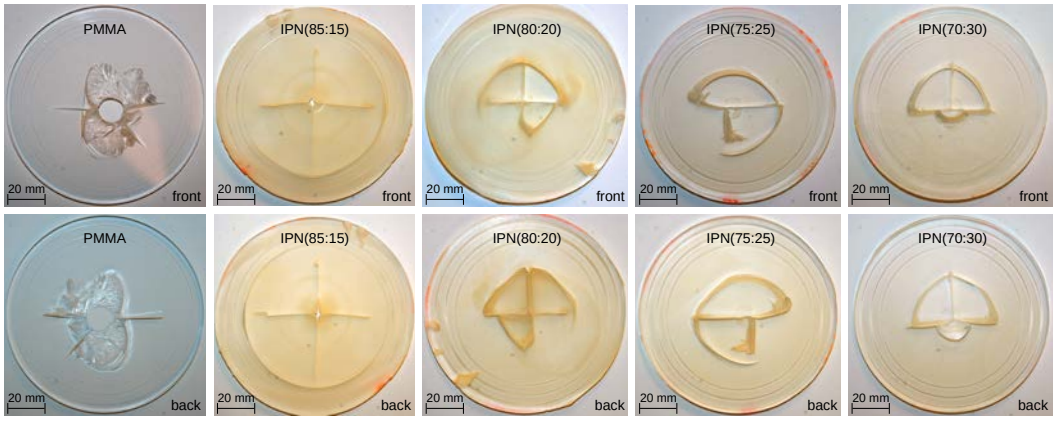

Fig. 7.12: Photographs of front and back surfaces of samples subjected to low-velocity drop-weight impact tests.

In the case of 85:15 IPN, the tup created a small rupture and generated four radial cracks from the impact point. These through-the-thickness cracks made four quadrants on both front and back surfaces of the specimen, propagated ~90° apart relative to each other, and terminated by forming a shear-craze at the terminal points. Interestingly, the length of the cracks in 85:15 IPN is the longest among all the cases shown here. The failure pattern of 80:20 IPN also involved four radial cracks propagated ~90° apart relative to each other. In this case also, the cracks terminated at a (nearly) circular crack due to the flexural failure of the petals. In case of 75:25 and 70:30 IPNs, only three radial cracks are visible confined by a tri-quadrant crack joining the failed petals. The crack lengths in 80:20, 75:25 and 70:30 IPN configurations are shorter than the 85:15 IPN. It should be noted that through-the-thickness cracking and shear-crazing are dominant failure modes in case of IPNs. Furthermore, there was no material spallation in case of IPNs even after impact damage and the size of the damage zone got smaller with higher PU content.

CHAPTER 8

CONCLUSIONS

In this research, the role of filler size, stiffness and loading rate on fracture behavior of particulate polymer composites (PPCs) was investigated experimentally. PPCs made of epoxy matrix with silica nanoparticles, carbon nanotubes, micron-sized glass spheres, polyol diluent and CTBN rubber additives were studied under quasi-static and dynamic loading conditions. To understand the underlying physics of fast fracture in PPCs, experimental simulations of dynamic crack growth past cylindrical inclusions of two very different elastic moduli, stiff (glass) and compliant (polyurethane) relative to the matrix (epoxy), were carried out. Efforts were also made in the development and dynamic failure characterization of interpenetrating polymer networks (IPNs), a relatively new class of transparent materials. The full-field optical technique of 2D digital image correlation coupled with high-speed photography was used to study the mechanics of transient crack growth in PPCs and IPNs under stress-wave dominant loading conditions. The IPNs were also subjected to low-velocity impact tests using a drop-tower for energy absorption studies. Microscopic and quantitative surface measurements were performed in order to understand inherent details of deformation and the associated toughening mechanisms that govern the fracture process. The major conclusions of this research are presented in the following paragraphs.

The study of nano- versus micron-size filler and the loading rate effects on fracture behavior of PPCs shows that the particle size did not produce discernible influence on elastic and physical properties at a given volume fraction in both nano- and micro-filler composites for all volume percentages (3-10%) studied. Both nano- and micro-fillers improved the fracture toughness under quasi-static loading conditions. The quasi-static fracture toughness of nanocomposites was significantly higher than the micro-particle filled epoxies for all volume fractions studied. Nanocomposites containing 10% volume fraction filler yielded the greatest fracture toughness enhancement by ~78% compared to the micro-filler counterparts at the same volume fraction. The dynamic fracture tests showed that with respect to neat epoxy the crack tip velocities increase and decrease in nano- and micro-particle filled composites, respectively, with filler volume fraction. The average crack tip velocities (V) in nanocomposites were approximately 35%, 60%, 90%, 160% higher than that observed in the micro-particle filled specimens for 3%, 5%, 7%, 10% volume fractions, respectively. The mode-I dynamic stress intensity factor ($K_{\mathrm{I}}^{\mathrm{d}}$) and crack initiation toughness values improved consistently with filler volume fraction for both nano- as well as micro-particle fillers when compared to that of neat epoxy. However, contrary to quasi-static fracture tests, the nanocomposites showed a relatively lower dynamic crack initiation toughness than the micro-particle filled counterparts with the same filler volume fraction. Hence, the fracture behavior of both types of composites was found loading rate sensitive. The $K_{\mathrm{I}}^{\mathrm{d}}$-$V$ characteristics for both types of composites were also obtained. Nanocomposites resulted in a lower $K_{\mathrm{I}}^{\mathrm{d}}$ over a wider range of velocities compared to the micro-filler counterparts. The terminal velocities seen in the case of nanocomposites were significantly higher than the micro-filler counterparts under

similar impact loading conditions. Fracture surfaces of quasi-statically failed nanocomposites showed very rough, highly textured surfaces containing mirror, mist and hackle zones, and all these features markedly amplified with filler volume fraction. On the other hand, such features were muted in the case of micro-filler. Micrographs of dynamically fractured surfaces of micro-particle filled epoxy revealed higher surface roughness and ruggedness than the nanocomposites with features consistent with microcracks, crack front bowing, tails lines and crack pinning indicating improved crack growth resistance relative to nano-filler counterparts. Quantitative surface measurements showed that the fracture induced surface roughness was significantly higher in micro-filler composites than the nano-filler counterparts.

In the case of epoxy nanocomposites modified with carbon nanotubes (0.3 wt.% CNT) and polyol diluent, the ultrasonic pulse-echo measurements showed only minor differences in longitudinal (C_L), shear (C_S) wave speeds and dynamic elastic modulus (E_d) among neat epoxy, epoxy/CNT, epoxy/polyol and epoxy/CNT/polyol systems. A significant enhancement in the quasi-static crack initiation toughness (K_{Ic}) was observed in each modified system relative to the neat epoxy. The K_{Ic} was the highest (~70% enhancement) for the hybrid epoxy/CNT/polyol system among all the formulations. Dynamic fracture tests showed the lowest crack speed in epoxy/polyol and hybrid epoxy/CNT/polyol composites when compared to the neat epoxy and epoxy/CNT counterparts. The crack took significantly longer to initiate in epoxy/polyol and hybrid epoxy/CNT/polyol composites than the neat epoxy and epoxy/CNT samples. Relative to neat epoxy, the improvements in dynamic crack initiation toughness values for epoxy/CNT, epoxy/polyol and hybrid epoxy/CNT/polyol systems were ~37%, ~65%, and

~92%, respectively. The fracture behavior in these composites was also loading rate sensitive. At high loading rates ($\dot{K}_I^d \sim 10^4$ MPa$\sqrt{\text{m}}/\text{s}$), the crack initiation toughness values were consistently lower relative to the quasi-static ($\dot{K}_I \sim 10^{-2}$ MPa$\sqrt{\text{m}}/\text{s}$) counterparts. The effect was more significant for epoxy/CNT composites, with dynamic crack initiation toughness value ~40% lower than the quasi-static value. The microscopic examination revealed a combination of toughening mechanisms including plastic deformation, crack deflection, CNT bridges and pull-outs. These features were more pronounced in quasi-static cases that showed higher surface ruggedness compared to the dynamic counterparts, accounting for a higher crack initiation toughness in the former.

To gain additional insight into the toughening mechanisms of PPCs, various dynamic crack-inclusion interaction scenarios were studied. These experiments were aimed at understanding the role of inclusion stiffness (and elastic impedance) mismatch and interfacial strength on dynamic matrix crack growth past embedded inclusions. Two different mismatches – stiff (glass) and compliant (polyurethane) - and adhesion strengths - weak and strong - were investigated for symmetric and eccentric crack growth configurations. In-plane crack-tip deformations were measured in real time optically before, during and after crack-inclusion interactions. Fractured specimens showed different crack trajectories and crack velocities for each inclusion location and inclusion-matrix bond strength. For weakly bonded inclusions, higher crack velocities were observed for both stiff as well as compliant inclusions when compared to the strongly bonded ones. The crack was completely stalled for about a third to a half of the duration needed to complete the fracture of samples in the case of compliant inclusions. The dynamically propagating crack was attracted and arrested by the weak inclusion interface

for both symmetric glass and polyurethane inclusions whereas it was deflected away by the stronger one for glass and attracted by polyurethane inclusion when situated eccentrically. The inclusion elastic moduli and inclusion-matrix interfacial strength also affected the effective stress intensity factor $\left(K_{\mathrm{e}} = \sqrt{K_{\mathrm{I}}^2 + K_{\mathrm{II}}^2}\right)$. The mode-mixity histories captured the physical aspects of crack growth. The compliant inclusion specimens showed much higher fracture toughness for weak and strong bond strengths when compared to the stiff inclusion counterparts. The macroscopic observation of dynamically fractured specimens accounted for greater crack growth resistance in compliant inclusion specimens compared to the stiff inclusion ones. The broader implications of crack-inclusion interaction scenarios were tested by conducting limited dynamic fracture experiments on A-glass and CTBN rubber-modified epoxies. The crack growth characteristics showed that the incorporation of compliant phase delays the crack initiation and significantly reduces the propagation speed when compared to the stiff particles when both fillers are weakly bonded to the matrix. When compared to the neat epoxy, the improvements in mode-I dynamic crack initiation toughness, $K_{\mathrm{Ii}}^{\mathrm{d}}$ values were higher in both glass- and CTBN rubber-modified epoxies with an enhancement of ~65% in $K_{\mathrm{Ii}}^{\mathrm{d}}$ value in the compliant case than the stiff one at 10% volume fraction. The matrix cracking, particle pull-out, filler-matrix interface separation and formation of river bed patterns were major toughening mechanisms observed in glass-filled epoxies. On the other hand, in addition to these toughening mechanisms, the fracture surfaces of CTBN rubber modified epoxies revealed tail lines, shear yielding, void formation, distortion or nonlinear deformation of rubber particles as the primary mechanisms responsible for the

higher dynamic crack initiation toughness enhancements in these composites relative to glass-filled ones.

The tensile, fracture and impact energy absorption studies were performed on transparent IPNs with poly(methyl methacrylate) (PMMA) as the stiff phase and polyurethane (PU) as the ductile phase with varying PMMA:PU ratios in the range of 90:10 to 70:30. Both quasi-static and dynamic elastic moduli gradually decreased as the PU phase increased in IPNs. Static tensile tests showed increasing ductility with a loss of strength and stiffness of IPNs as the PU content was increased. Quasi-static fracture tests indicated brittle unstable crack growth in 90:10 IPN, brittle as well as stable crack growth in the case of 85:15 and 80:20 IPNs, and ductile stable crack growth in 75:25 and 70:30 IPNs. The work up to crack initiation was higher for 85:15 and 80:20 IPNs. The quasi-static fracture toughness was found to be optimum for 90:10, 85:15 and 80:20 IPNs among all the cases. An inverse relationship was found to exist between steady state crack velocities and dynamic crack initiation toughness values as a function of IPN composition. Dynamic fracture tests showed lower crack speeds in IPNs relative to PMMA with the slowest crack growth in 85:15 and 80:20 IPNs. The dynamic crack initiation toughness enhancement was the highest for 85:15 and 80:20 IPNs. The dynamically fractured surfaces of 85:15 and 80:20 IPNs showed highly tortuous fracture surface indicating high energy dissipation during fracture whereas other cases had relatively smooth surfaces with the presence of conic (parabolic) marks. All IPNs showed higher impact energy absorption capability (a 3 to 4 fold increase) relative to PMMA with the highest energy absorbed by 85:15 and 80:20 IPNs among all the cases. The

impact damage features revealed shear-crazing and through-the-thickness cracking as the dominant failure modes responsible for greater impact energy absorption in the IPNs.

8.1 Future Directions

In the early part of this dissertation, nano- and micron- sized stiff fillers were used in as-received form to manufacture epoxy composites in order to study filler size-scale and loading rate effects on fracture behavior of PPCs. The mode-I and mixed-mode fracture behaviors could be studied by fabricating hybrid PPCs with the incorporation of nano- and micro- fillers in different volume fractions. In addition to hybrid PPCs, the loading rate studies can be performed on interfacial crack growth in particulate bimaterials made of nano- and micro-fillers. To accomplish this, two types of bimaterial configurations, one with a discrete jump from nano- to micron-size fillers across the interface and the other with diffused interface (two intermixed particle sizes in the interfacial region), can be considered. Similar objectives can be extended in the case of stiff nano- or micron-fillers with CTBN rubber particles. The effect of stiff and compliant particles on interfacial crack growth in particulate bimaterials is yet to be well understood and could be considered in a future work.

Due to their ease of penetration and flowability between the fibers and/or laminates, the nano-fillers can be incorporated in fiber-reinforced composites and laminates. The laminated composites are commonly used in aerospace structures and automotive components. The fibers in these composites generally provide excellent in-plane (x- and y-directions) reinforcement but very little resistance to failure in the out-of-plane direction. The lack of reinforcement in the through-thickness (z-direction) direction cause *interlaminar* fracture as well as *intralaminar* damage. In the past, several techniques have

been proposed to improve this delamination resistance, such as micro stitching and *z*-pinning. In these techniques, stitches or pins are inserted in the *z*-direction to provide direct closure forces to the interlaminar crack and enhance the delamination resistance. However, these methods degrade the elastic properties and mechanical strength due to fiber damage and weave distortion. Moreover, the brittle matrix materials such as epoxies crack during stitching or pin insertion, further promoting failure during service. In this regard, the carbon nanotubes (CNTs) due to their exceptional strength, stiffness and thermo-mechanical characteristics, can be used to enhance interlaminar fracture toughness of composite laminates by incorporating CNTs in the through-the-thickness direction.

In this dissertation, the experimental simulations of crack-inclusion interactions were studied using a high-speed digital framing camera equipped with CCD sensors of fixed spatial resolution of 1000 x 1000 pixels. It should be noted that despite the camera being a state-of-the-art instrument, the spatial resolution is still far from being optimum for this study. This limits the ability to capture deformation details accurately near the interface without magnifying the image. If magnified, however, the information regarding global deformations will be greatly compromised and hence not used in this work. The spatial resolution, which is one of the constraints in the current experimental setup, can be considered in future in order to capture greater details of deformation within the inclusion and in the crack-inclusion vicinity. Further, in this work, the crack-inclusion interaction experiments were limited for the cases of a propagating crack encountering a single stiff or compliant inclusion embedded in epoxy matrix at symmetric and eccentric locations relative to the initial crack. In reality, however, presence of neighboring

particles, their relative position and inclusion-matrix interfacial strength affect crack growth behavior. Hence, to examine such effects, the current study can be extended to crack-inclusion interaction scenarios with multiple stiff or compliant inclusions and their combinations as a function of interfacial strength.

The current work on transparent IPNs with PMMA-PU networks showed tremendous impact energy absorption capabilities when compared to PMMA. Quantitatively, the energy absorbed by IPNs is 3 to 4 times that of PMMA. It should be noted that the IPNs in the current work were synthesized at ambient pressure conditions. However, in a previous study on IPNs, Lee et al. [91] prepared 50:50 wt% PMMA-PU IPNs under varying pressures of up to 2000 kg/cm^2. They noted changes in phase continuity with synthesis pressure and observed better optical transparency in the IPNs synthesized at higher pressures than the ones at a lower pressure. According to them, the higher pressures decreased the domain sizes of the PMMA and PU phases, thereby enabled them more compatible with one another when compared to synthesis carried out at the atmospheric pressure. Using such an approach in the future may allow better phase continuity in the current IPN system for achieving better optical transparency.

REFERENCES

[1] Fried JR. Polymer Science and Technology. 2 ed: Prentice Hall; 2003.

[2] Owens AT. Development of a split hopkinson tension bar for testing stress-strain response of particulate composites under high rates of loading. M.S. Thesis. 2007.

[3] Kitey R, Tippur HV. Role of particle size and filler-matrix adhesion on dynamic fracture of glass-filled epoxy. I. Macromeasurements. Acta Materialia. 2005;53(4):1153-65.

[4] Kitey R, Tippur HV. Role of particle size and filler-matrix adhesion on dynamic fracture of glass-filled epoxy. II. Linkage between macro- and micro-measurements. Acta Materialia. 2005;53(4):1167-78.

[5] Spanoudakis J, Young RJ. Crack propagation in a glass particle-filled epoxy resin. Journal of Materials Science. 1984;19(2):473-86.

[6] Roulin-Moloney AC, Cantwell WJ, Kausch HH. Parameters determining the strength and toughness of particulate-filled epoxy resins. Polymer Composites. 1987;8(5):314-23.

[7] Nakamura Y, Yamaguchi M, Okubo M, Matsumoto T. Effects of particle size on mechanical and impact properties of epoxy resin filled with spherical silica. Journal of Applied Polymer Science. 1992;45(7):1281-9.

[8] Nakamura Y, Okabe S, Iida T. Effects of particle shape, size and interfacial adhesion on the fracture strength of silica-filled epoxy resin. Polym Polym Compos. 1999;7(3):177-86.

[9] Spanoudakis J, Young RJ. Crack propagation in a glass particle-filled epoxy resin. Journal of Materials Science. 1984;19(2):487-96.

[10] Hsieh TH, Kinloch AJ, Masania K, Taylor AC, Sprenger S. The mechanisms and mechanics of the toughening of epoxy polymers modified with silica nanoparticles. Polymer. 2010;51(26):6284-94.

[11] Reynaud E, Jouen T, Gauthier C, Vigier G, Varlet J. Nanofillers in polymeric matrix: a study on silica reinforced PA6. Polymer. 2001;42(21):8759-68.

[12] Boesl BP, Bourne GR, Sankar BV. Insitu multiscale analysis of fracture mechanisms in nanocomposites. Composites Part B: Engineering. 2011;42(5):1157-63.

[13] Liu H-Y, Wang G-T, Mai Y-W, Zeng Y. On fracture toughness of nano-particle modified epoxy. Composites Part B: Engineering. 2011;42(8):2170-5.

[14] Rosso P, Ye L, Friedrich K, Sprenger S. A toughened epoxy resin by silica nanoparticle reinforcement. Journal of Applied Polymer Science. 2006;100(3):1849-55.

[15] Wetzel B, Rosso P, Haupert F, Friedrich K. Epoxy nanocomposites - fracture and toughening mechanisms. Engineering Fracture Mechanics. 2006;73(16):2375-98.

[16] Liang YL, Pearson RA. Toughening mechanisms in epoxy-silica nanocomposites (ESNs). Polymer. 2009;50(20):4895-905.

[17] Tsai JL, Hsiao H, Cheng YL. Investigating Mechanical Behaviors of Silica Nanoparticle Reinforced Composites. Journal of Composite Materials. 2010;44(4):505-24.

[18] Kwon S-C, Adachi T, Araki W. Temperature dependence of fracture toughness of silica/epoxy composites: Related to microstructure of nano- and micro-particles packing. Composites Part B: Engineering. 2008;39(5):773-81.

[19] Johnsen BB, Kinloch AJ, Mohammed RD, Taylor AC, Sprenger S. Toughening mechanisms of nanoparticle-modified epoxy polymers. Polymer. 2007;48(2):530-41.

[20] Jordan J, Jacob KI, Tannenbaum R, Sharaf MA, Jasiuk I. Experimental trends in polymer nanocomposites--a review. Materials Science and Engineering A. 2005;393(1-2):1-11.

[21] Sun L, Gibson RF, Gordaninejad F, Suhr J. Energy absorption capability of nanocomposites: A review. Composites Science and Technology. 2009;69(14):2392-409.

[22] Fu S-Y, Feng X-Q, Lauke B, Mai Y-W. Effects of particle size, particle/matrix interface adhesion and particle loading on mechanical properties of particulate–polymer composites. Composites Part B: Engineering. 2008;39(6):933-61.

[23] Singh RP, Zhang M, Chan D. Toughening of a brittle thermosetting polymer: Effects of reinforcement particle size and volume fraction. Journal of Materials Science. 2002;37(4):781-8.

[24] Adachi T, Osaki M, Araki W, Kwon S-C. Fracture toughness of nano- and micro-spherical silica-particle-filled epoxy composites. Acta Materialia. 2008;56(9):2101-9.

[25] Ng CB, Ash BJ, Schadler LS, Siegel RW. A study of the mechanical and permeability properties of nano- and micron-TiO_2 filled epoxy composites. Adv Compos Lett. 2001;10(3):101-11.

[26] Ng CB, Schadler LS, Siegel RW. Synthesis and mechanical properties of TiO_2-epoxy nanocomposites. Nanostructured Materials. 1999;12(1-4):507-10.

[27] Shukla A, Parameswaran V, Du Y, Évora V. Dynamic crack initiation and propagation in nanocomposite materials. Rev Adv Mater Sci. 2006;13(1):47-58.

[28] Evora VMF, Shukla A. Fabrication, characterization, and dynamic behavior of polyester/TiO_2 nanocomposites. Materials Science and Engineering A. 2003;361(1-2):358-66.

[29] Evora VMF, Jain N, Shukla A. Stress intensity factor and crack velocity relationship for polyester/TiO2 nanocomposites. Experimental Mechanics. 2005;45(2):153-9.

[30] Lavengood RE, Nicolais L, Narkis M. A deformational mechanism in particulate-filled glassy polymers. Journal of Applied Polymer Science. 1973;17(4):1173-85.

[31] Mallick PK, Broutman LJ. Mechanical and fracture behaviour of glass bead filled epoxy composites. Materials Science and Engineering. 1975;18(1):63-73.

[32] Moloney AC, Kausch HH, Stieger HR. The fracture of particulate-filled epoxide resins. Journal of Materials Science. 1983;18(1):208-16.

[33] Moloney A, Kausch H, Kaiser T, Beer H. Parameters determining the strength and toughness of particulate filled epoxide resins. Journal of Materials Science. 1987;22(2):381-93.

[34] Hussain M, Nakahira A, Nishijima S, Niihara K. Fracture behavior and fracture toughness of particulate filled epoxy composites. Materials Letters. 1996;27(1-2):21-5.

[35] Kinloch AJ, Shaw SJ, Tod DA, Hunston DL. Deformation and fracture behaviour of a rubber-toughened epoxy: 1. Microstructure and fracture studies. Polymer. 1983;24(10):1341-54.

[36] Kinloch AJ, Shaw SJ, Hunston DL. Deformation and fracture behaviour of a rubber-toughened epoxy: 2. Failure criteria. Polymer. 1983;24(10):1355-63.

[37] Kinloch AJ, Yuen ML, Jenkins SD. Thermoplastic-toughened epoxy polymers. Journal of Materials Science. 1994;29(14):3781-90.

[38] Geisler B, Kelley FN. Rubbery and rigid particle toughening of epoxy resins. Journal of Applied Polymer Science. 1994;54(2):177-89.

[39] Tirosh J, Nachlis W, Hunston D. Strength behavior of toughened polymers by fibrous (or particulate) elastomers. Mechanics of Materials. 1995;19(4):329-42.

[40] Yee AF, Pearson RA. Toughening mechanisms in elastomer-modified epoxies. Journal of Materials Science. 1986;21(7):2462-74.

[41] Ratna D. Phase separation in liquid rubber modified epoxy mixture. Relationship between curing conditions, morphology and ultimate behavior. Polymer. 2001;42(9):4209-18.

[42] Wong DWY, Lin L, McGrail PT, Peijs T, Hogg PJ. Improved fracture toughness of carbon fibre/epoxy composite laminates using dissolvable thermoplastic fibres. Composites Part A: Applied Science and Manufacturing. 2010;41(6):759-67.

[43] Di Pasquale G, Motto O, Rocca A, Carter JT, McGrail PT, Acierno D. New high-performance thermoplastic toughened epoxy thermosets. Polymer. 1997;38(17):4345-8.

[44] Lange F, Radford K. Fracture energy of an epoxy composite system. Journal of Materials Science. 1971;6(9):1197-203.

[45] Tsai J-L, Huang B-H, Cheng Y-L. Enhancing fracture toughness of glass/epoxy composites by using rubber particles together with silica nanoparticles. Journal of composite materials. 2009;43(25):3107-23.

[46] Isik I, Yilmazer U, Bayram G. Impact modified epoxy/montmorillonite nanocomposites: synthesis and characterization. Polymer. 2003;44(20):6371-7.

[47] Harani H, Fellahi S, Bakar M. Toughening of epoxy resin using hydroxyl-terminated polyesters. Journal of Applied Polymer Science. 1999;71(1):29-38.

[48] Iijima S. Helical microtubules of graphitic carbon. nature. 1991;354:56-8.

[49] Yu M-F, Lourie O, Dyer MJ, Moloni K, Kelly TF, Ruoff RS. Strength and Breaking Mechanism of Multiwalled Carbon Nanotubes Under Tensile Load. Science. 2000;287(5453):637-40.

[50] Thostenson ET, Ren Z, Chou T-W. Advances in the science and technology of carbon nanotubes and their composites: a review. Composites Science and Technology. 2001;61(13):1899-912.

[51] Geng Y, Liu MY, Li J, Shi XM, Kim JK. Effects of surfactant treatment on mechanical and electrical properties of CNT/epoxy nanocomposites. Composites Part A: Applied Science and Manufacturing. 2008;39(12):1876-83.

[52] Kathi J, Rhee K-Y, Lee JH. Effect of chemical functionalization of multi-walled carbon nanotubes with 3-aminopropyltriethoxysilane on mechanical and

morphological properties of epoxy nanocomposites. Composites Part A: Applied Science and Manufacturing. 2009;40(6):800-9.

[53] Ma P-C, Mo S-Y, Tang B-Z, Kim J-K. Dispersion, interfacial interaction and re-agglomeration of functionalized carbon nanotubes in epoxy composites. Carbon. 2010;48(6):1824-34.

[54] Kim M-G, Moon J-B, Kim C-G. Effect of CNT functionalization on crack resistance of a carbon/epoxy composite at a cryogenic temperature. Composites Part A: Applied Science and Manufacturing. 2012;43(9):1620-7.

[55] Srikanth I, Kumar S, Kumar A, Ghosal P, Subrahmanyam C. Effect of amino functionalized MWCNT on the crosslink density, fracture toughness of epoxy and mechanical properties of carbon–epoxy composites. Composites Part A: Applied Science and Manufacturing. 2012;43(11):2083-6.

[56] Spitalsky Z, Tasis D, Papagelis K, Galiotis C. Carbon nanotube–polymer composites: Chemistry, processing, mechanical and electrical properties. Progress in Polymer Science. 2010;35(3):357-401.

[57] Gojny F, Wichmann M, Köpke U, Fiedler B, Schulte K. Carbon nanotube-reinforced epoxy-composites: enhanced stiffness and fracture toughness at low nanotube content. Composites Science and Technology. 2004;64(15):2363-71.

[58] Fidelus J, Wiesel E, Gojny F, Schulte K, Wagner H. Thermo-mechanical properties of randomly oriented carbon/epoxy nanocomposites. Composites Part A: Applied Science and Manufacturing. 2005;36(11):1555-61.

[59] Zhou Y, Pervin F, Lewis L, Jeelani S. Experimental study on the thermal and mechanical properties of multi-walled carbon nanotube-reinforced epoxy. Materials Science and Engineering: A. 2007;452–453(0):657-64.

[60] Seyhan AT, Tanoğlu M, Schulte K. Tensile mechanical behavior and fracture toughness of MWCNT and DWCNT modified vinyl-ester/polyester hybrid nanocomposites produced by 3-roll milling. Materials Science and Engineering: A. 2009;523(1):85-92.

[61] Hsieh T, Kinloch A, Taylor A, Kinloch I. The effect of carbon nanotubes on the fracture toughness and fatigue performance of a thermosetting epoxy polymer. Journal of Materials Science. 2011;46(23):7525-35.

[62] Tang L-C, Wan Y-J, Peng K, Pei Y-B, Wu L-B, Chen L-M, et al. Fracture toughness and electrical conductivity of epoxy composites filled with carbon nanotubes and spherical particles. Composites Part A: Applied Science and Manufacturing. 2013;45:95-101.

[63] Yang L, Zhang C, Pilla S, Gong S. Polybenzoxazine-core shell rubber-carbon nanotube nanocomposites. Composites Part A: Applied Science and Manufacturing. 2008;39(10):1653-9.

[64] Tamate O. The effect of a circular inclusion on the stresses around a line crack in a sheet under tension. International Journal of Fracture. 1968;4(3):257-66.

[65] Evans AG. The role of inclusions in the fracture of ceramic materials. Journal of Materials Science. 1974;9(7):1145-52.

[66] Erdogan F, Gupta GD, Ratwani M. Interaction between a circular inlcusion and an arbitrarily oriented crack. Journal of Applied Mechanics-Transactions of the Asme. 1974;41(4):1007-13.

[67] Bush MB. The interaction between a crack and a particle cluster. International Journal of Fracture. 1998;88(3):215-32.

[68] Kitey R, Phan AV, Tippur HV, Kaplan T. Modeling of crack growth through particulate clusters in brittle matrix by symmetric-Galerkin boundary element method. International Journal of Fracture. 2006;141(1-2):11-25.

[69] Li R, Chudnovsky A. Variation of the energy release rate as a crack approaches and passes through an elastic inclusion. International Journal of Fracture. 1993;59(4):R69-R74.

[70] Li R, Chudnovsky A. Energy analysis of crack interaction with an elastic inclusion. International Journal of Fracture. 1993;63(3):247-61.

[71] Mantic V. Interface crack onset at a circular cylindrical inclusion under a remote transverse tension. Application of a coupled stress and energy criterion. International Journal of Solids and Structures. 2009;46(6):1287-304.

[72] O'Toole BJ, Santare MH. Photoelastic investigation of crack-inclusion interaction. Experimental Mechanics. 1990;30(3):253-7.

[73] Li R, Wu S, Ivanova E, Chudnovsky A, Sehanobish K, Bosnyak C. Finite element model and experimental analysis of crack–inclusion interaction. Journal of Applied Polymer Science. 1993;50(7):1233-8.

[74] Savalia PC, Tippur HV. A study of crack-inclusion interactions and matrix-inclusion debonding using Moire interferometry and finite element method. Experimental Mechanics. 2007;47(4):533-47.

[75] Kitey R, Tippur HV. Dynamic crack growth past a stiff inclusion: Optical investigation of inclusion eccentricity and inclusion-matrix adhesion strength. Experimental Mechanics. 2008;48(1):37-53.

[76] Millar JR. Interpenetrating polymer networks. Styrene-divinylbenzene copolymers with two and three interpenetrating networks, and their sulphonates. Journal of the Chemical Society. 1960:1311-7.

[77] Vasile C, Kulshreshtha AK. Handbook of Polymer Blends and Composites, 3A. Shawsbury: Rapra Technology Ltd.; 2003.

[78] Lipatov YS, Alekseeva TT. Phase-Separated Interpentrating Polymer Networks. Berlin: Springer; 2007.

[79] Sperling LH, Mishra V. The current status of interpenetrating polymer networks. Polymers for Advanced Technologies. 1996;7(4):197-208.

[80] Frisch HL, Klempner D, Frisch KC. A topologically interpenetrating elastomeric network. Journal of Polymer Science Part B: Polymer Letters. 1969;7(11):775-9.

[81] Sperling LH, Friedman DW. Synthesis and mechanical behavior of interpenetrating polymer networks: Poly(ethyl acrylate) and polystyrene. Journal of Polymer Science Part A-2: Polymer Physics. 1969;7(2):425-7.

[82] de Moura MR, Aouada FA, Guilherme MR, Radovanovic E, Rubira AF, Muniz EC. Thermo-sensitive IPN hydrogels composed of PNIPAAm gels supported on alginate-Ca2+ with LCST tailored close to human body temperature. Polymer Testing. 2006;25(7):961-9.

[83] Frisch KC, Klempner D. Advances in Interpenetrating Polymer Networks. Lancaster, PA, USA: Technomic Publishing Company Inc.; 1990.

[84] Gupta N, Srivastava AK. Interpenetrating polymer networks: A review on synthesis and properties. Polymer International. 1994;35(2):109-18.

[85] Suthar B, Xiao HX, Klempner D, Frisch KC. A review of kinetic studies on the formation of interpenetrating polymer networks. Polymers for Advanced Technologies. 1996;7(4):221-33.

[86] Cascaval CN, Rosu D, Rosu L, Ciobanu C. Thermal degradation of semi-interpenetrating polymer networks based on polyurethane and epoxy maleate of bisphenol A. Polymer Testing. 2003;22(1):45-9.

[87] Kim SC, Klempner D, Frisch KS, Radigan W, Frisch HL. Polyurethane Interpenetrating Polymer Networks. I. Synthesis and Morphology of Polyurethane-Poly(methyl methacrylate) Interpenetrating Polymer Networks. Macromolecules. 1976;9(2):258-63.

[88] Kim SC, Klempner D, Frisch KC, Frisch HL. Polyurethane Interpenetrating Polymer Networks. II. Density and Glass Transition Behavior of Polyurethane-Poly(methyl methacrylate) and Polyurethane-Polystyrene IPN's. Macromolecules. 1976;9(2):263-6.

[89] Kim SC, Klempner D, Frisch KC, Frisch HL. Polyurethane Interpenetrating Polymer Networks. 3. Viscoelastic Properties of Polyurethane-Poly(methyl methacrylate) Interpenetrating Polymer Networks. Macromolecules. 1977;10(6):1187-91.

[90] Kim SC, Klempner D, Frisch KC, Frisch HL. Polyurethane Interpenetrating Polymer Networks. 4. Volume Resistivity Behavior of Polyurethane-Poly(methyl methacrylate) Interpenetrating Polymer Networks. Macromolecules. 1977;10(6):1191-3.

[91] Lee DS, Kim SC. Polyurethane interpenetrating polymer networks (IPN's) synthesized under high pressure. 1. Morphology and Tg behavior of polyurethane-poly(methyl methacrylate) IPN's. Macromolecules. 1984;17(3):268-72.

[92] Rosu L, Cascaval CN, Rosu D. Effect of UV radiation on some polymeric networks based on vinyl ester resin and modified lignin. Polymer Testing. 2009;28(3):296-300.

[93] Djomo H, Morin A, Damyanidu M, Meyer G. Polyurethane-poly(methyl methacrylate) interpenetrating polymer networks: 1. Early steps and kinetics of network formation; intersystem grafting. Polymer. 1983;24(1):65-71.

[94] Widmaier JM, Bonilla G. In situ synthesis of optically transparent interpenetrating organic/inorganic networks. Polymers for Advanced Technologies. 2006;17(9-10):634-40.

[95] Bonilla G, Martinez M, Mendoza AM, Widmaier JM. Ternary interpenetrating networks of polyurethane-poly(methyl methacrylate)-silica: Preparation by the sol-gel process and characterization of films. European Polymer Journal. 2006;42(11):2977-86.

[96] Akay M, Rollins SN. Polyurethane-poly(methyl methacrylate) interpenetrating polymer networks. Polymer. 1993;34(9):1865-73.

[97] Chen S, Wang Q, Wang T. Hydroxy-terminated liquid nitrile rubber modified castor oil based polyurethane/epoxy IPN composites: Damping, thermal and mechanical properties. Polymer Testing. 2011;30(7):726-31.

[98] Chou YC, Lee LJ. Mechanical properties of polyurethane-unsaturated polyester interpenetrating polymer networks. Polymer Engineering & Science. 1995;35(12):976-88.

[99] Chakrabarty D, Das B, Roy S. Epoxy resin–poly(ethyl methacrylate) interpenetrating polymer networks: Morphology, mechanical, and thermal properties. Journal of Applied Polymer Science. 1998;67(6):1051-9.

[100] Chakrabarty D. Interpenetrating polymer networks: Engineering properties and morphology. Polymer Gels and Networks. 1998;6(3–4):191-204.

[101] Harismendy I, Del Río M, Marieta C, Gavalda J, Mondragon I. Dicyanate ester–polyetherimide semi-interpenetrating polymer networks. II. Effects of morphology on the fracture toughness and mechanical properties. Journal of Applied Polymer Science. 2001;80(14):2759-67.

[102] Peters WH, Ranson WF. Digital imaging techniques in experimental stress-analysis. Opt Eng. 1982;21(3):427-31.

[103] Sutton MA, Wolters WJ, Peters WH, Ranson WF, McNeill SR. Determination of displacements using an improved digital correlation method. Image and Vision Computing. 1983;1(3):133-9.

[104] Dally JW, Riley WF. Experimental Stress Analysis. 4 ed: College House Enterprises; 2005.

[105] Tippur HV. Lecture notes: Experimental Mechanics: Auburn University, Auburn, AL; 2013.

[106] Kirugulige MS, Tippur HV, Denney TS. Measurement of transient deformations using digital image correlation method and high-speed photography: application to dynamic fracture. Applied Optics. 2007;46(22):5083-96.

[107] Jajam KC, Tippur HV. Quasi-static and dynamic fracture behavior of particulate polymer composites: A study of nano- vs. micro-size filler and loading-rate effects. Composites Part B: Engineering. 2012;43(8):3467-81.

[108] Jajam KC, Bird SA, Auad ML, Tippur HV. Tensile, fracture and impact behavior of transparent Interpenetrating Polymer Networks with polyurethane-poly(methyl methacrylate). Polymer Testing. 2013;32(5):889-900.

[109] ASTM, D638-01. Standard test method for tensile properties of plastics: Annual Book of ASTM Standards (2001) 45-57.

[110] ASTM, D5045-96. Standard test methods for plane-strain fracture toughness and strain energy release rate of plastic materials: Annual Book of ASTM Standards (1996) 325-333.

[111] ASTM, D5628-96. Standard test method for impact resistance of flat, rigid plastic specimens by means of a falling dart (tup or falling mass): Annual Book of ASTM Standards (1996) 242-251.

[112] Impact testing. Materials Testing eBook. 50 ed: Instron; 2011. p. 61-67.

[113] Jajam KC, Tippur HV. Is nano always better? Static and dynamic fracture study of particulate polymer composites. Dynamic Behavior of Materials. 2012;Vol.1:537-544. doi:10.1007/978-1-4614-4238-7_69.

[114] Prautzsch H, Boehm W, Paluszny M. Bézier and B-spline techniques: Springer-Verlag Berlin Heidelberg New York; 2002.

[115] Nishioka T, Atluri SN. Path-independent integrals, energy release rates, and general solutions of near-tip fields in mixed-mode dynamic fracture mechanics. Engineering Fracture Mechanics. 1983;18(1):1-22.

[116] Tippur HV, Krishnaswamy S, Rosakis AJ. Optical mapping of crack tip deformations using the mehods of transmission and reflection coherent gradient sensing: a study of crack tip *K*-dominance. International Journal of Fracture. 1991;52(2):91-117.

[117] Irwin G, Dally J, Kobayashi T, Fourney W, Etheridge M, Rossmanith H. On the determination of the *å-K* relationship for birefringent polymers. Experimental Mechanics. 1979;19(4):121-8.

[118] Dally JW, Fourney WL, Irwin GR. On the uniqueness of the stress intensity factor-crack velocity relationship. International Journal of Fracture. 1985;27(3):159-68.

[119] Kobayashi T, Dally JW. Dynamic photoelastic determination of the *å-K* relation for 4340 alloy steel. Crack Arrest Methodogy and Applications, ASTM STP 711, GT Hann and MF Kanninen, editors, American Society for Testing Materials. 1980:189-210.

[120] Knauss WG, Ravi-Chandar K. Some basic problems in stress wave dominated fracture. International Journal of Fracture. 1985;27(3):127-43.

[121] Shukla A, Nigam H. A note on the stress intensity factor and crack velocity relationship for homalite 100. Engineering Fracture Mechanics. 1986;25(1):91-102.

[122] Broberg KB. Crack and fracture: Academic Press, Cambridge; 1999.

[123] Arakawa K, Takahashi K. Relationships between fracture parameters and fracture surface roughness of brittle polymers. International Journal of Fracture. 1991;48(2):103-14.

[124] Takahashi K, Kido M, Arakawa K. Fracture Roughness Evolution During Mode I Dynamic Crack Propagation in Brittle Materials. International Journal of Fracture. 1998;90(1):119-31.

[125] Sharon E, Gross SP, Fineberg J. Energy Dissipation in Dynamic Fracture. Physical Review Letters. 1996;76(12):2117.

[126] Lampman S. Characterization and failure analysis of plastics: ASM International, Materials Park, OH, USA; 2003.

[127] Fullman RL. Measurement of particle sizes in opaque bodies. Transactions of the American Institute of Mining and Metallurgical Engineers. 1953;197(3):447-52.

[128] Jajam KC, Tippur HV. An experimental investigation of dynamic crack growth past a stiff inclusion. Engineering Fracture Mechanics. 2011;78(6):1289-1305.

[129] Jajam KC, Rahman MM, Hosur MV, Tippur HV. Fracture behavior of epoxy nanocomposites modified with polyol diluent and amino-functionalized multi-walled carbon nanotubes: A loading rate study. Composites Part A: Applied Science and Manufacturing. 2013 (submitted).

[130] Rahman MM, Hosur M, Zainuddin S, Jajam KC, Tippur HV, Jeelani S. Mechanical characterization of epoxy composites modified with reactive polyol diluent and randomly-oriented amino-functionalized MWCNTs. Polymer Testing. 2012;31(8):1083-93.

[131] Jajam KC, Tippur HV. Role of inclusion stiffness and interfacial strength on dynamic matrix crack growth: an experimental study. International Journal of Solids and Structures. 2012;49(9):1127-1146.

[132] Jajam KC, Tippur HV. Interaction between a dynamically growing crack with stiff and compliant inclusions using DIC and high-speed photography. Application of Imaging Techniques to Mechanics of Materials and Structures. 2013;Vol.4:63-69. doi:10.1007/978-1-4419-9796-8_9.

[133] Jajam KC, Tippur HV. A study of dynamic crack-inclusion interactions using digital image correlation and high-speed photography. Proceedings of the Society of Experimental Mechanics Inc. 2009;390-396.

[134] Bourne NK, Millett JCF, Field JE. On the strength of shocked glasses. Proceedings of Royal Society of London A. 1999;455:1275-1282.

[135] Deng X. General crack tip fields for stationary and steadily growing interface cracks in anisotropic biomaterials. Journal of Applied Mechanics. 1993;60:183-189.

[136] Zak AR, Williams ML. Crack point stress singularities at a bimaterial interface. Journal of Applied Mechanics. 1963;30:142-143.

[137] Bogy DB. On the plane elastostatic problem of a loaded crack terminating at a material interface. Journal of Applied Mechanics. 1971;38(4):911-918.

[138] Wise CW, Cook WD, Goodwin. CTBN rubber phase precipitation in model epoxy resins. Polymer. 2000;41:4625-4633.

[139] Ramos VD et al. Modification of epoxy resin: a comparison of different types of elastomer. Polymer Testing. 2005;24:387-394.

[140] Bird SA, Clary D, Jajam KC, Tippur HV, Auad ML. Synthesis and characterization of high performance, transparent interpenetrating polymer networks with polyurethane-poly(methyl methacrylate). Polymer Engineering & Science. 2013;53(4):716-723.

[141] Jajam KC, Bird SA, Auad ML, Tippur HV. Development and characterization of a PU-PMMA transparent Interpenetrating Polymer Networks (IPNs). Dynamic Behavior of Materials. 2011;Vol.1:117-121. doi:10.1007/978-1-4614-0216-9_16.

[142] Jajam KC, Tippur HV, Bird SA, Auad ML. Dynamic fracture and impact energy absorption characteristics of PMMA-PU transparent Interpenetrating Polymer Networks (IPNs). Proceedings of the SEM International Conference & Exposition on Experimental and Applied Mechanics. 2013 (submitted).

[143] Morin A, Djomo H, Meyer GC. Polyurethane-poly(methyl methacrylate) interpenetrating polymer networks: some mechanical properties. Polymer Engineering & Science. 1983;23(7):394-398.

[144] Zhao X. A theory for large deformation and damage of interpenetrating polymer networks. Journal of the Mechanics and Physics of Solids. 2012;60(2):319-332.

[145] Fineberg J, Marder M. Instability in dynamic fracture. Physics Reports. 1999;313:1-108.

[146] Scheibert J, Guerra C, Célarié F, Dalmas D, Bonamy D. Brittle-quasibrittle transition in dynamic fracture: an energetic signature. Physical Review Letters. 2010;104:045501.

[147] Guerra C, Scheibert J, Bonamy D, Dalmas D. Understanding fast macroscale fracture from microcrack post mortem patterns. Proceedings of the National Academy of Sciences. 2012;109:390-394.

[148] Hosur MV, Chowdhury S, Jeelani S. Low-velocity impact response and ultrasonic NDE of woven carbon/epoxy-nanoclay nanocomposites. Journal of Composite Materials. 2007;41:2195-2212.

[149] Ritchie RO. The conflicts between strength and toughness. Nature Materials. 2011;10:817-822.

[150] Kato KJ. Osmium tetroxide fixation of rubber lattices. Journal of Polymer Science Part B: Polymer Letters. 1966;4(1):35-38.

APPENDIX A

QUASI-STATIC CRACK-INCLUSION INTERACTIONS

The crack-inclusion interaction was studied statically in greater detail (higher spatial and grayscale resolutions). A digital SLR camera with 2000 x 3008 pixel resolution and 10 bit (0 – 1023) grayscale digitization was used to capture details within the inclusion and in the inclusion vicinity. A few selected crack-opening (v–field) and crack-sliding (u–field) displacement contours for a symmetrically located (e = 0) strongly bonded stiff and compliant inclusion specimens are shown in Fig. A.1 *before* and *after* debonding of the inclusion. Figs. A.1(a) and (b) show displacement contours depicting crack-inclusion interaction *before* debonding and Figs. A.1(c) and (d) show the same *after* debonding for stiff and compliant inclusion specimens. From Figs. A.1(a)-(d) it can be seen that the contours are symmetric near the crack-tip, indicating dominant mode-I conditions and contours around the inclusion discontinuous after debonding occurs. After debonding, the contour lines within the stiff inclusion in Fig. A.1(c) are parallel to each other and equally spaced showing rigid rotation of the inclusion relative to the matrix. This is similar to the observation made by Savalia and Tippur [74] using moiré interferometry. On the other hand, for the compliant inclusion, the non-uniform deformations within the inclusion can be clearly seen in Figs. A.1(b) and (d), suggesting substantial straining of the inclusion. The contours are denser near the top/bottom edges of the inclusion in Fig. A.1(d) is indicative of large strains compared to the mid-portion of the inclusion.

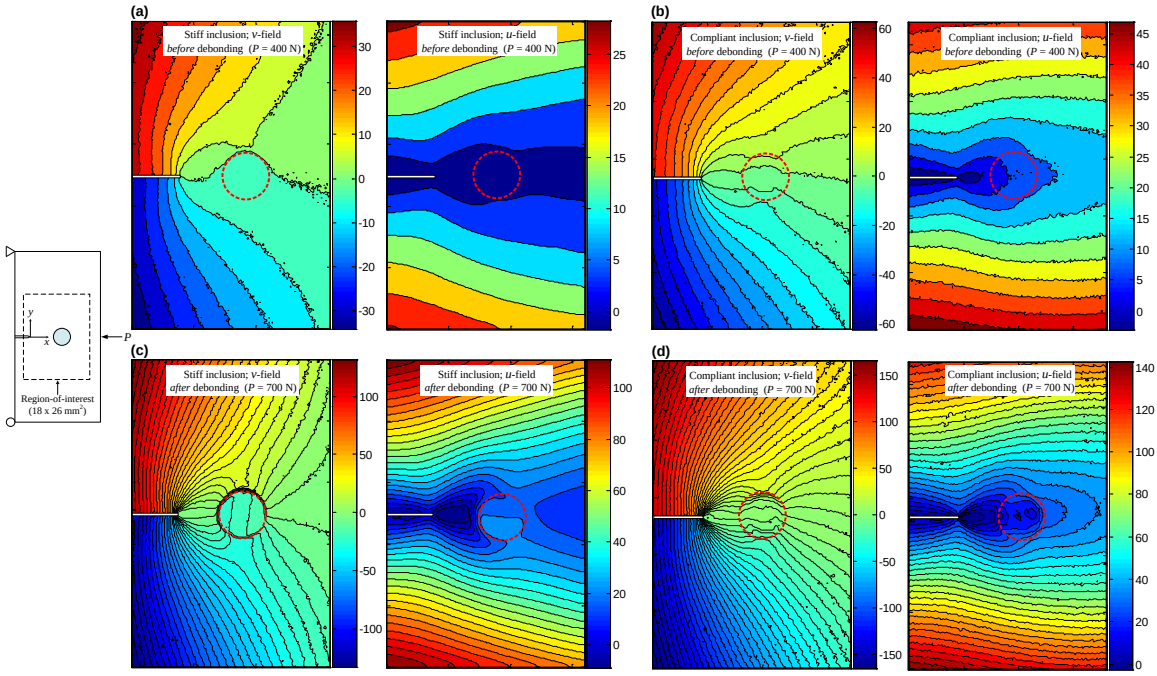

Fig. A.1: Crack-opening (*v*-field) and crack-sliding (*u*-field) displacement contours from quasi-static fracture tests for strongly bonded stiff and compliant inclusion specimens at eccentricity, e = 0. (Contour interval: 5μm). Color-bars indicate displacements in μm. The location of cylindrical inclusion is represented by dotted circle. **(a)** Stiff inclusion, *before* debonding at P = 400 N, **(b)** Compliant inclusion, *before* debonding at P = 400 N, **(c)** Stiff inclusion, *after* debonding at P = 700 N, **(d)** Compliant inclusion, *after* debonding at P = 700 N.

The measured crack-tip normal strains (ε_y, ε_x) and shear strains (ε_{xy}) for symmetrically located (e = 0) strongly bonded stiff and compliant inclusion specimens are shown in Fig. A.2 *after* the inclusion debonds from the matrix. The concentration and symmetry of ε_y, ε_x, and ε_{xy} contours around the crack-tip can be seen in these figures. A high strain concentration in ε_y field is quite evident for both stiff and compliant inclusion specimens in the debonding region. As expected, a nearly zero ε_y strain can be seen over the stiff inclusion, whereas the contours ranging from ~2000 to ~7000 micro-strains are quite evident within the compliant inclusion with least strain at the center of the inclusion. The redistribution of strains can also be seen ahead of the crack-tip and in the inclusion vicinity when the inclusion debonds from the matrix. In the case of ε_x strains,

the contours within the compliant inclusion are compressed and elongated in the *x* and *y*-directions, respectively, due to straining of the inclusion whereas no such features are evident in the case of stiff inclusion. Further, ε_x strains are tensile and concentrated on the opposite ends of the inclusion in the stiff and compliant cases. The ε_{xy} strains show skew symmetry in strain contours around the crack-tip and in the inclusion vicinity. The ε_{xy} contours are tangential around the inclusion in both stiff and compliant inclusions with nearly zero shear strain within the stiff case and a relatively large shear deformation in the compliant counterpart.

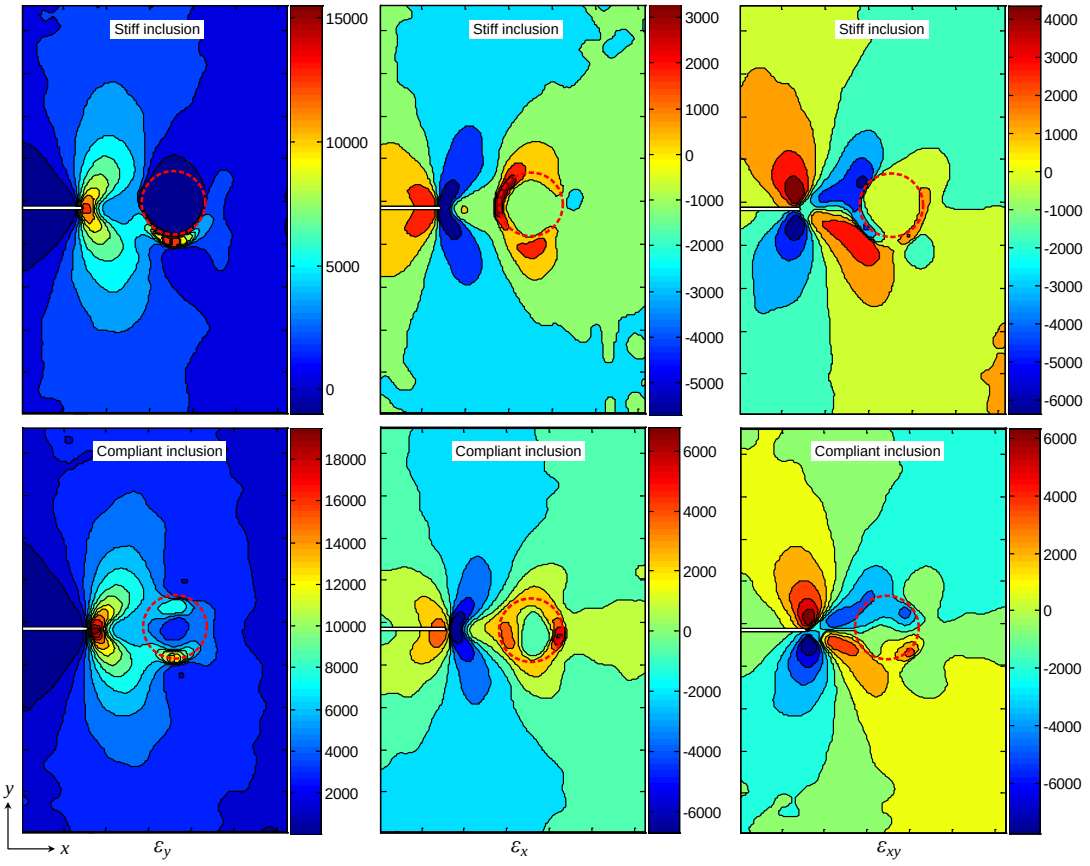

Fig. A.2: Crack-tip normal strains (ε_y, ε_x in $\mu\varepsilon$) and shear strains (ε_{xy} in $\mu\varepsilon$) from quasi-static fracture tests for strongly bonded stiff and compliant inclusion specimens *after* debonding at eccentricity, e = 0 and, at a load level, P = 700 N. (Contour interval: 1500 $\mu\varepsilon$). Color-bars indicate strains in $\mu\varepsilon$. The location of cylindrical inclusion is shown by dotted circle.

APPENDIX B

NETWORK MORPHOLOGY AND TRANSPARENCY OF IPNs

B.1 Synthesis Methods of IPNs

Interpenetrating polymer networks (IPNs) can be synthesized in many different ways. Figure B.1 shows two popular methods of preparing IPNs. The schematic in Fig. B.1(a) illustrates the synthesis method for sequential IPNs. The term 'sequential' refers to

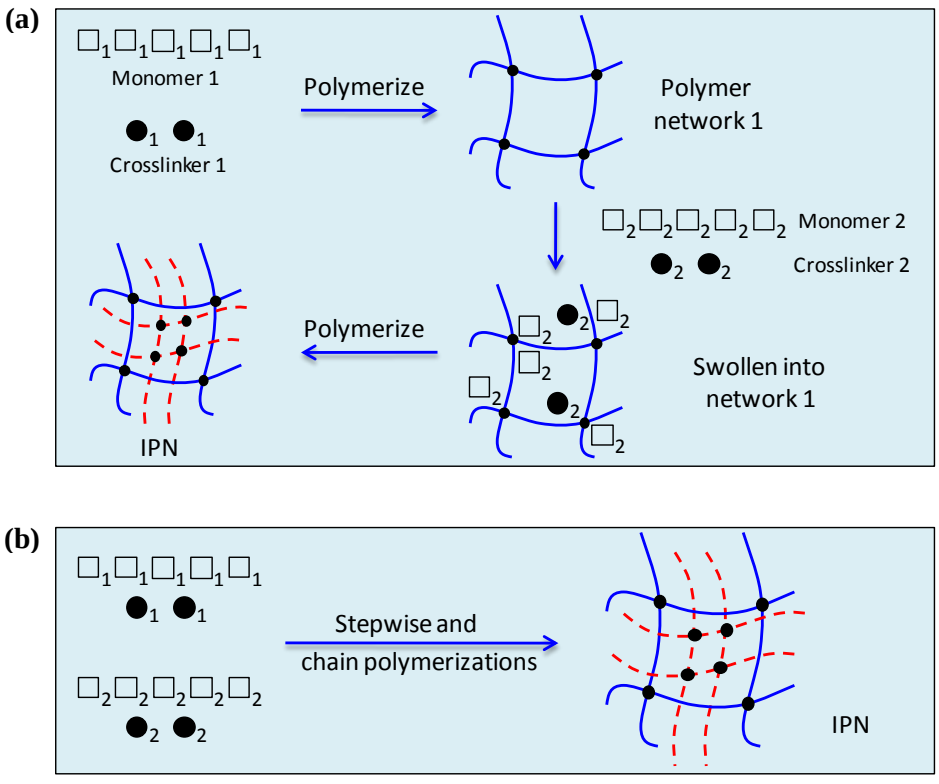

Fig. B.1: Schematics showing IPN synthesis routes: **(a)** Sequential IPNs, **(b)** Simultaneous IPNs. (Reproduced from [79].)

the history of polymerization. The monomer 1 and crosslinker 1 polymerize first to form a polymer network 1. Next, monomer 2 together with requisite crosslinker 2 and activator are swollen into polymer network 1 and polymerized in situ and form network 2 (shown by dashed lines) resulting into a full-IPN. The solid curves denote the polymer chains of network 1 and dashed lines represent polymer chains of network 2, and heavy dots are crosslinkg points. Hence, in the sequential route the synthesis of one network follows the other and their polymer networks interpenetrate into each other without forming covalent bonds with each other. On the other hand, the simultaneous method refers to the mixing of monomers plus the corresponding crosslinkers and initiators of both the polymers, followed by simultaneous polymerizations via independent, non-interfering reactions such as step and chain polymerization kinetics.

B.2 Network Morphology

In order to study phase morphology of the PMMA-PU components in IPNs, the sample preparation for TEM was done using Kato's osmium tetroxide (OsO_4) staining technique [150]. Prior to microtoming the samples for TEM, the specimens were exposed to a dye for about 48 h. This enabled PU system turn dark due to the absorption of the dye while PMMA remained unaffected, thereby facilitating distinction between PMMA and PU domains as well as phase separation processes in the IPN. Figure B.2 shows TEM images of stained 80:20 IPN samples and illustrates the effect of two different diisocyanates (DCH and TDI), and MMA monomers with and without inhibitor on the network morphologies. In these micrographs, the dark zones represent the PU phase whereas the clear domains correspond to the PMMA phase.

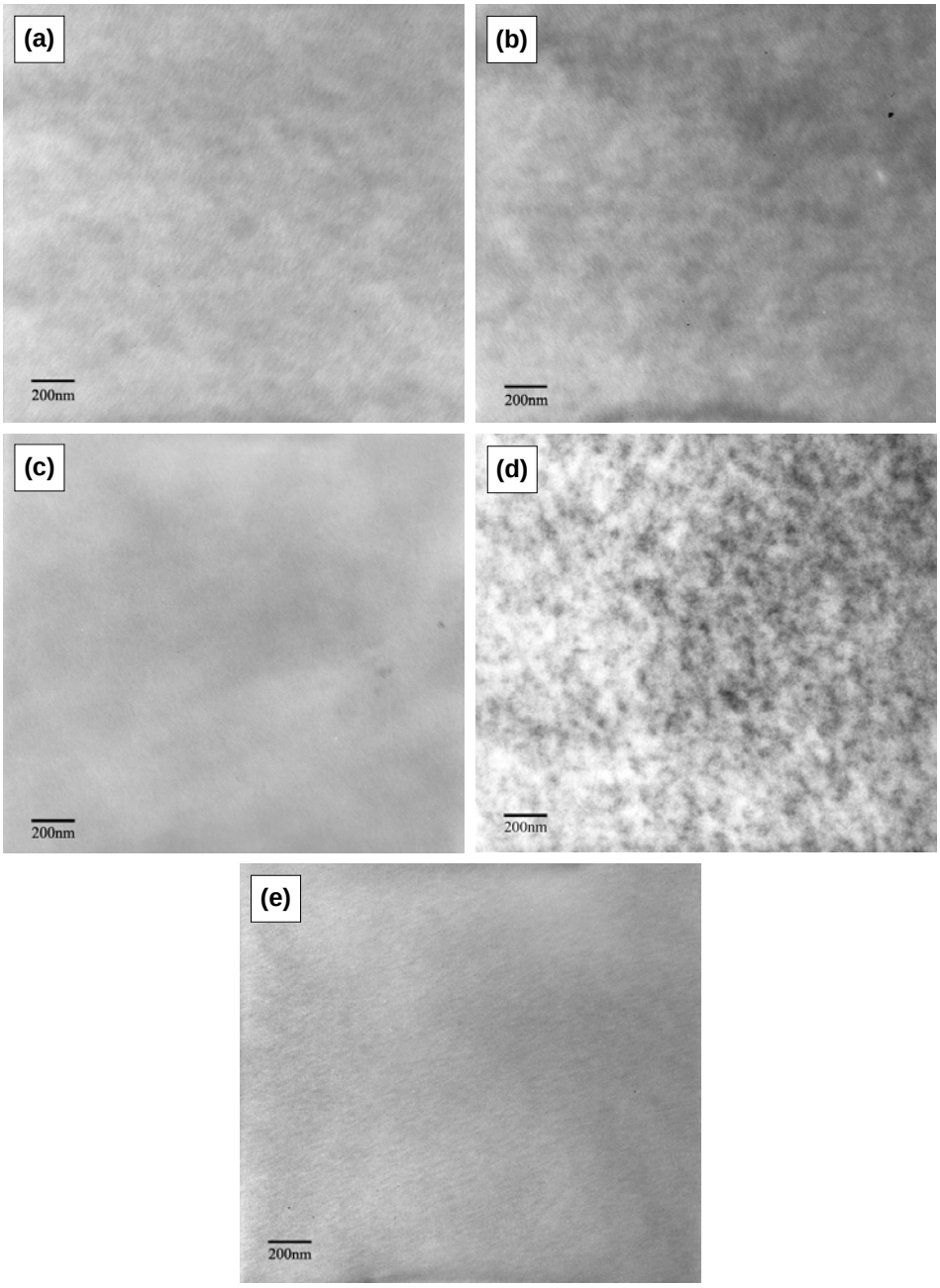

Fig. B.2: TEM micrographs showing network morphology of: **(a)** 80:20 IPN with an inhibitor and DCH, **(b)** 80:20 IPN with an inhibitor and TDI, **(c)** 80:20 IPN with no inhibitor and DCH, **(d)** 80:20 IPN with no inhibitor and TDI, **(e)** pure PMMA with inhibitor. (Reproduced from [140].)

Figures B.2(a) and (b) depict network morphology of 80:20 sequential IPNs with an inhibitor using DCH and TDI, respectively. The fine dispersion of PMMA and PU components indicates interpenetration of both polymer networks at the molecular level.

Figures B.2(c) and (d) show micrographs of 80:20 IPNs without inhibitor synthesized via simultaneous route using DCH and TDI, respectively. However, the effect of the type of diisocyanates (DCH and TDI) can be clearly seen on the network morphology. IPNs synthesized using DCH generally show a homogeneous gray color, indicating that phase separation was minimal whereas the samples consisting of TDI clearly display patches of dark gray or white, especially in Fig. B.2(d), the larger spherical domains indicate extreme phase separation within the IPN. Hence, in this study, DCH, an aliphatic diisocyanate was used for IPN preparation instead of TDI where aromatic rings could be the possible source of discoloration and substantial phase separation. From Fig. B.2, it can also be noted that the network morphology shown in Fig. B.2(a) is very similar to the one shown in Fig. B.2(e) for the case of pure PMMA with inhibitor. Therefore, the sequential route of IPN synthesis was adopted in this work due to least phase separation and better transparency (to be discussed in the following section) compared to the ones synthesized via simultaneous method.

B.3 Transparency Measurements

In order to study the effects of the type of diisocyanate (DCH vs. TDI) and IPN syntheses methods (sequential vs. simultaneous) on the degree of transparency, a UV-visible 2450 spectrophotometer (Shimadzu Scientific Instruments) was used for transparency analysis of IPN samples. Figure B.3 shows the results from transparency measurements performed on relatively thick (3.5 mm) 80:20 PMMA:PU IPN samples. It can be seen that samples containing DCH or TDI display approximately similar percent

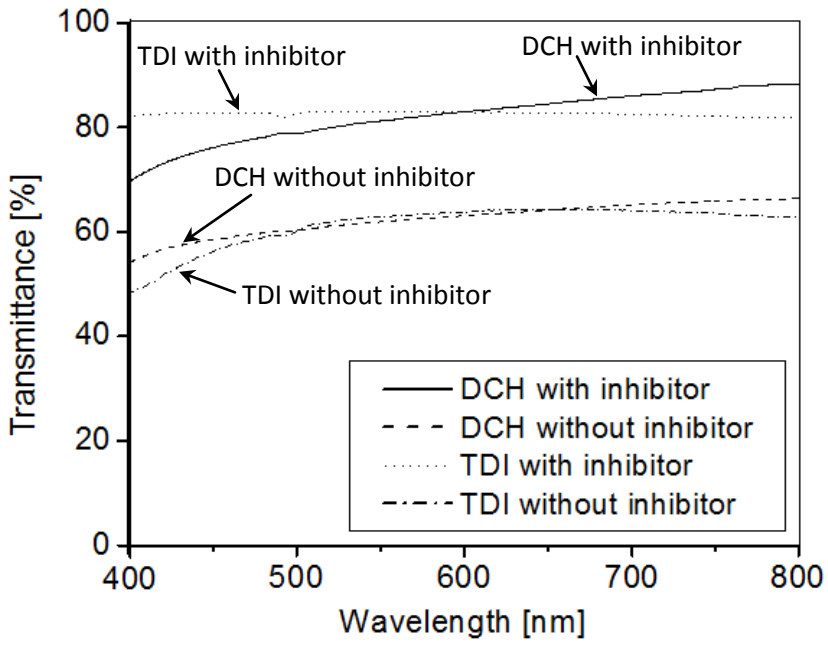

Fig. B.3: Effect of DCH and TDI with and without inhibitor on percentage transmittance of 80:20 PMMA-PU IPNs. (Reproduced from [140].)

transmittance values (~82%) and (~60%) in the IPNs with and without inhibitor, respectively. (However, visual inspection of the samples showed that IPNs based on DCH (aliphatic diisocyanate) resulted clear samples. On the other hand, samples prepared using TDI (aromatic diisocyanate) produced a yellow-orange coloration in the IPNs.)

The effect of IPN synthesis modes can be clearly noted from Fig. B.3. It can be seen that IPNs prepared via sequential route (samples with inhibitor) exhibited higher degree of transparency than the counterparts synthesized using simultaneous mode (samples without inhibitor). In view of this, the sequential method of IPN synthesis was followed in this work in order to achieve better transparency.